Rat Optic Nerve Head Anatomy within Three-Dimensional Histomorphometric Reconstructions of Normal and Early Experimental Glaucoma Eyes

Marta Pazos

Rat Optic Nerve Head Anatomy within Three-Dimensional Histomorphometric Reconstructions of Normal and Early Experimental Glaucoma Eyes

Thesis submitted for the degree of Doctor of Philosophy (PhD)
with International Research Component as compendium of publications

by
Marta Pazos MD
to
the department of surgery of the Universitat Autònoma de Barcelona (UAB)

Supervisors
Claude F. Burgoyne, MD
Alfonso Antón, MD, PhD
Miguel Castilla-Céspedes, MD, PhD

Institutions
Hospital de l'Esperança-Parc de Salut Mar. Barcelona, Spain
Devers Eye Institute, Portland, Oregon, USA

Claude F.Burgoyne, Alfonso Antón, Miguel Castilla-Céspedes Marta Pazos

Rat Optic Nerve Head Anatomy within Three-Dimensional Histomorphometric Reconstructions of Normal and Early Experimental Glaucoma Eyes

Abstract

Purpose: To Three-Dimensionally (3D) reconstruct rat optic nerve heads (ONHs) with varying stages of unilateral early experimental glaucoma (EG), so as to provide the first histomorphometrical description of nomal controls and early EG ONH anatomy in this species.

Methods: Hypertonic saline was unilaterally injected into the episcleral veins of 8 Brown Norway rats and animals were sacrificed 4 weeks later by perfusion fixation. Orbital optic nerve (ON) cross-sections from were graded (1 normal, 5 extensive injury) by 5 masked observers. ONH's with peripapillary ONH sclera were 3D reconstructed, visualized, delineated, and parameterized. Overall and animal-especific EG versus control eye ONH parameters differences were assessed globally and regionally by linear mixed effect models with significance criteria adjusted for multiple comparisons.

Results: The rat ONH consists of 2 scleral openings (a superior neurovascular and inferior arterial) separated by a scleral sling. Within the superior opening, the nerve abuts a prominent extension of Bruch's Membrane (BM) superiorly and is surrounded by a vascular plexus. Expansions of the ON and anterior scleral canal opening (ASCO) achieved statistical significance overall and in 7 of 8 EG eyes. In at least 5 EG eyes, significant expansions in Bruch's Membrane Opening (BMO) (3-10%), the ASCO and Posterior Scleral Canal Openings (PSCOs) (8-21% and 8-41%, respectively) were detected. ON expansion was significantly correlated to ON damage (R^2=0.668, $p<0.05$).

Conclusions: The 3D complexity of the rat ONH and the extent to which it differs from the primate have been under-appreciated within previous 2D studies. In the rat ONH, the ON ansd surrounding BMO and neurovascular canal expand early in their response to chronic experimental IOP elevation. These findings provide phenotypic landmarks and imaging targets for detecting the development of EG optic neuropathy in the rat eye.

Claude F.Burgoyne, Alfonso Antón, Miguel Castilla-Céspedes Marta Pazos

Anatomía de la Cabeza del Nervio Óptico de Rata a través de Reconstrucciones Histomorfométricas 3D de Ojos Normales y con Glaucoma Experimental Temprano

Resumen

Objetivo: Reconstruir en 3D cabezas del nervio óptico (CNOs) de rata con glaucoma experimental (GExp) precoz unilateral, para proporcionar la primera descripción histomorfométrica de la CNO de controles normales y GExp precoz en esta especie.

Métodos: Se inyectó suero salino hipertónico unilaterlamente en las venas epiesclerales de 8 ratas noruegas que se sacrificaron 4 semanas después (fijación-perfusión). Cinco observadores enmascarados graduaron el daño de secciones del nervio óptico (NO) orbitario (1 Normal-5 Extenso). Se reconstruyeron en 3D, se visualizaron, delinearon y parametrizaron las CNOs junto con la esclera peripapilar. Los parámetros globales y específicos por ojo fueron evaluados conjuntamente y regionalmente con un modelo de efectos lineares mixtos con criterios de significación ajustados para comparaciones múltiples.

Resultados: La CNO de la rata consiste en 2 aperturas esclerales (una superior neurovascular y otra inferior arterial) separados por una cincha escleral. Dentro de la apertura superior, el nervio se apoya en una prominente extensión de la Membrana de Bruch's (MB) superiormente y está rodeado de un plexo vascular. El NO y la Apertura Anterior del Canal Escleral (ASCO) se expandieron significativamente en 7 de 8 ojos con GExp. En al menos 5 ojos con GExp se detectaron expansiones significativas de la apertura de la MB (BMO) (3-10%), de la ASCO y de la Apertura Posterior del Canal Escleral (PSCO) (8-21% y 8-41% resp.). La expansión del NO se correlacionó significativamente con el grado de daño (R^2=0.668, $p<0.05$).

Conclusiones: La complejidad 3D de la CNO de rata y el grado en el que se diferencia de la del primate han sido infravalorados en los estudios previos en 2D. En la CNO de rata, el NO, el BMO que lo rodea y el canal neurovascular se expanden de manera temprana en respuesta a la elevación experimental crónica de PIO. Estos hallazgos proporcionan nuevos puntos de referencia y objetivos de imagen para detectar el desarrollo de la neuropatía glaucomatosa experimental en ojos de rata.

Claude F.Burgoyne, Alfonso Antón, Miguel Castilla-Céspedes Marta Pazos

Anatomia del Cap del Nervi Òptic de la Rata a través de Reconstruccions Histomorfométriques d'Ulls normals i amb Glaucoma Experimental Primerenc

Resum

Objetciu: Reconstruir en 3D caps del nervi òptic (CNOs) de rata camb glaucoma experimental (GExp) precoç unilateral, per proporcionar la primera descripció histomorfomètrica del CNO de controls normales i amb GExp primerenc en aquesta espècie.

Métodos: Es va injectar sèrum salí hipertònic unilateralment en les venes epiesclerals de 8 rates noruegues que van ser sacrificades 4 setmantes després (fixació-perfusió). Cinc observadors enmascarats graduaren el dany de seccions del nervi òptic (NO) orbitari (1 Normal-5 Extens). Es van reconstruir en 3D, es van visualitzar, deliniar i parametritzar els CNOs i l'esclera peripapil·lar. Els paràmetres globals i específics per ull van ser avaluats conjuntament i regionalment amb un model d'efectes linials mixtes amb criteris de significació ajustats per a comparacións múltiples.

Resultats: El CNO de la rata consisteix en 2 obertures esclerals (una superior neurovascular i una altra otra inferior arterial) separades por una cingla escleral. Dins l'obertura superior, el nervi es recolza un una prominent extensió de la Membrana de Bruch's (MB) superiorment i està rodejat d'un plexe vascular. El NO i l'Obertura Anterior del Canal Escleral (ASCO) van expandir-se significativament en 7 dels 8 ulls amb GExp. En almenys 5 ulls amb GExp van detectar-se expansions significativae de l'Obertura de la MB (BMO) (3-10%), de l'ASCO y de l'Obertura Posterior del Canal Escleral (PSCO) (8-21% i 8-41% respectivament). L'expansió del NO va correlacionar-se significativament amb el grau de dany (R^2=0.668, $p<0.05$).

Conclusions: La complexitat 3D del CNO de rata y el gau en el què es diferencia de la del primat han estat infravalorats en estudis previs en 2D. En el CNO de rata, el NO, el BMO que el rodeja I el canal neurovascular s'expandeixen de manera precoç en resposta a l'elevació experimental crònica de PIO. Aquestes troballes aporten nous punts de referència i objectius d'imatge per detectar el desenvolupament de la neuropatia glaucomatosa experimental en ulls de rata.

"And now here is my secret, a very simple secret: It is only with the heart that one can see rightly; what is essential is invisible to the eye."

– Antoine de Saint-Exupéry- in Le Petit Prince

To our wonderful son Quim and our future addition Maria

Acknowledgements/ Agradecimientos/Agraïments

Al Doctor Miguel Castilla Céspedes, por creer en mí desde el principio y facilitar todas y cada una de mis aventuras profesionales.

Al Doctor Alfonso Antón, por inculcarme la pasión por la investigación. Por todas las oportunidades y enseñanzas que me has dado y por hacer realidad el sueño de poder ir a formarme a Estados Unidos. Sin tí esto no habría sido posible.

To George "Jack" A. Cioffi to give me the opportunity to be his glaucoma fellow at Devers Eye Institute in Portland. It was, without any doubt, the best professional experience I have ever had.

To Claude F. Burgoyne for being the most inspiring mentor possible. Opening the doors of one of the best Research laboratories to that tenacious Spanish girl was the first step for this project to come true. Thank you for all the research opportunities you have given to me, for your generosity, your valuable taughts and your friendship.

To Hongli Yang for her patience as a teacher and her commitment to this piece of work.

To John Morrison, Elaine Johnson and Bill Cepurna for their unconditional support and participation in the project.

To the great Discoveries in Sight Team at Devers Eye Institute: To Juan Reynaud for his assistance improving the visibility of the rat ONH anatomy within the green channel (Gracias Juan, sin tí no hubiera sido posible ver más allá del pigmento…) and, together with Johnatan Grimm, for their assistance with software for volumetric and thickness quantification. To Brad Fortune for his careful review of the manuscripts and data interpretation. To Stuart Gardiner for his tremendous statistical support. To Galen Williams and Christy Hardin for their performance of the serial section staining and imaging.

A tot l'equip del Servei d'Oftalmologia de l'Hospital de l'Esperança, pel recolzament, motivació i suport que rebo cada dia des de ja fa uns quants anys. Perquè amb il·lusió i amb ganes de fer bé la feina, tot sempre acaba sortint.

A mi padre, por enseñarme el valor del trabajo bien hecho.
A mi madre, por apoyarme siempre y hacer de mí todo lo que soy hoy.
Al meu marit Quim, pel seu suport incondicional, per entendre tot el temps de dedicació a la meva professió. No pot existir en el món un millor company de viatge. Gràcies per estar sempre al meu costat.
Al nostre fill Quim, per obrir-me els ulls al més important de la vida.

Directors Certificate

Dr. **Claude F. Burgoyne MD**, Senior Scientist and Research Director of the Optic Nerve Head Research Laboratory at Devers Eye Institute and Clinical Ophthalmology Professor at Oregon Health and Science University, Portland, United States of America (USA);

Dr. **Alfonso Antón, MD, PhD** Senior Consultant at Hospital de l'Esperança- Parc de Salut Mar, Glaucoma Service and Research Department Director at Institut Català de la Retina, Professor of Ophthalmology at Universitat Internacional de Catalaunya, Barcelona, Spain;

Dr. **Miguel Castilla Céspedes, MD, PhD.** Chairman of Ophthalmology. Hospital de l'Esperança-Parc de Salut Mar. Professor of Ophthalmology at Universitat Autònoma de Barcelona and Universitat Pompeu Fabra, Barcelona, Spain;

We CERTIFY that the following research dissertation entitled "Rat Optic Nerve Head Anatomy within Three-Dimensional Reconstructions of Normal and Early Experiemental Glaucoma Eyes" has been made by Dr. Marta Pazos López under our supervision and it is suitable to be read and defended publicly as a compendium of publications.

November, 2015

Contents

0

Overview

0.1-Thesis Approach

This thesis is presented as compendium of publications as regulated by the Doctorate Committee of the Universitat Autònoma de Barcelona (UAB).

To achieve the purpose of the project, two complementary experiments have been performed and two papers have been published. The first describes our conceptual framework for understanding the normal rat ONH anatomy. The second describes changes in experimental early glaucomatous eyes within the same conceptual framework and parametrization scheme

0.2.- List of Abbreviations/Definitions

Abbreviation/Term	Meaning/Definition
AGIS	Advanced Glaucoma Intervention Study
ANOVA	Analysis of Variance
ASCO	Anterior Scleral Canal Opening
ASCO-ON-ASCO	Gap distance measured radially between the ASCO and the ON-ASCO
BM	Bruch's Membrane
BMO	Bruch's Membrane Opening
CCT	Central Corneal Thickness
CI	Confidence Interval
CNTGS	Collaborative Normal Tension Glaucoma Study
CRA	Central Retinal Artery
CRV	Central Retinal Vein
3D	Three-Dimensional
EG	Experimental Glaucoma
EMGT	Early Manifest Glaucoma Trial
Eye-specific results	Parameters related to an individual eye
GLS	Generalized Least Square
GON	Glaucomatous Optic Neuropathy
H/V	Horizontal/Vertical Ratio
I	Inferior
ICC	Intraclass Correlation Coefficient
IOP	Intraocular Pressure
LM	Light Microscopy
LPCA	Long Posterior Ciliary Artery
N	Nasal
NA	Not Available or Not Applicable
NTG	Normal-Tension Glaucoma
OA	Ophthalmic Artery
OD	Right Eye
OHT	Ocular Hyertension

OHTS	Ocularl Hypertension Treatment Study
ON	Optic Nerve
ON-ASCO	Optic Nerve at the level of ASCO
ON-PSCO	Optic Nerve at the level of PSCO
ONH	Optic Nerve Head
OR	Odds Ratio
OS	Left Eye
Overall results	Data from all rats considered together
POAG	Primary Open Angle Glaucoma
PSCO	Posterior Scleral Canal Opening
PSCO-ON-PSCO	Gap distance measured radially between the PSCO and the ON-PSCO
RGC	Retinal Ganglion Cell
RNFL	Retinal Nerve Fiber Layer
SD	Standard Deviation
SD-OCT	Spectral-Domain Optical Coherence Tomography
SPCA	Short Posterior Ciliary Artery
T	Temporal
TEM	Transmission Electron Microscopy

0.3- List of Tables

0.4.-List of Figures

Fig. 3.1. Perineural vascular plexus

Fig. 3.2. The CRA passes perpendicularly and the LPCAs pass obliquely through the arterial scleral opening

Fig. 3.3. Summary of the 3D relationships between BMO, the ASCO and PSCO, the Optic Nerve, the Central Retinal Vein, the Central Retinal Artery and the Long Posterior Ciliary Arteries (with and without their intrascleral branches) as visualized within the 3D Point Clouds in a representative normal control eye

Fig. 3.4. Eye-specific comparisons of *BMO* (red), *ASCO* (blue) and *PSCO* (black) for the 8 normal control eyes

Fig. 3.5. Within and between-eye comparisons of *BMO* (red), *ASCO* (blue) and *PSCO* (purple) for the Control (solid lines) and EG (dotted lines) eye of each animal

Fig. 3.6. EG (dotted line) versus Control (solid line) eye *Bruch's Membrane Opening (BMO*) comparison for each animal

Fig. 3.7. EG (dotted line) versus Control (solid line) eye *Anterior Scleral Canal Opening (ASCO*) comparison for each animal

Fig.3.8. EG (dotted line) versus Control (solid line) eye *Posterior Scleral Canal Opening (PSCO)* comparison for each animal

Fig. 3.9. EG (dotted line) versus Control (solid line) eye *Optic Nerve within the Anterior Scleral Canal Opening* (*ON-ASCO)* comparison for each study animal

Fig. 3.11. EG (dotted line) versus Control (solid line) eye *Optic Nerve within the Posterior Scleral Canal Opening* (*ON-PSCO)* comparison for each study animal

Fig. 3.11. Animal-specific, EG (dotted line) versus Control Eye (solid line) comparisons of *Anterior Scleral Canal Opening* (*ASCO* - blue) and *Optic Nerve – ASCO* (*ON-ASCO* - green) and the *ASCO-to- Optic Nerve ASCO Gap Distance* (*ASCO-ON-ASCO*) (green arrow upper left)

Fig. 3.12. Animal-specific, EG (dotted line) versus Control Eye (solid line) comparisons of Posterior Scleral Canal Opening (PSCO – Purple) and Optic Nerve–PSCO (ON-PSCO - green)

Fig. 3.13. Correlation between EG Eye *ON-PSCO Area* Expansion and EG eye Optic Nerve Damage Grade (Table 3.6)

Fig. 4.1. Principal Scleral Openings in the Normal Control Rat Eye (A) and a Schematic Overlay of Optic Nerve and Surrounding Neurovascular Scleral Canal Expansion in Early Experimental Glaucoma (EG)

"It always seems impossible until it's done"
– Nelson Mandela

1

Introduction

1.1- The Normal Optic Nerve

The optic nerve, also known as cranial nerve II, is a paired nerve that transmits visual information from the light sensitive cells (photoreceptors) of the retina to the brain. In humans, the optic nerve extends from the optic disc to the optic chiaasm and continues as the optic tract to the lateral geniculate nucleus, pretectal nuclei, and superior colliculus. As a paired cranial nerve, the optic nerve is technically part of the central nervous system because it is derived from an out-.pouching of the diencephalon (optic stalks) during embryonic development. As a consequence, the fibers of the optic nerve are covered with myelin produced by oligodendrocytes, rather than Schwann cells of the peripheral nervous system, and are encased within the meninges. The optic nerve is ensheathed in all the three meningeal layers (dura,

arachnoid and pia mater) in its intraorbital and intracanalicular portions; these sheaths are continuous with those that line the brain (Hogan et al.; 1971)

The optic nerve is composed of retinal ganglion cells (RGCs) axons and glial cells. Each human optic nerve contains between 1.2-2.0 million fibers (Jonas et al 1999), which are axons of the RGCs of the retina. In this region, axons bend through 90 degrees to start their exit from the eye.

The optic nerve leaves the orbit via the optic canal, running postero-medially towards the optic chiasm, where there is a partial decussation of fibers from the temporal visual fields (the nasal hemi-retina) of both eyes. Most of the axons of the optic nerve terminate in the lateral geniculate nucleus from where information is relayed to the visual cortex, while other axons terminate in the pretectal nucleus and are involved in reflexive eye movements. Other axons terminate in the suprachiasmatic nucleus and are involved in the sleep-wake cycle regulation (Vilensky et al. 2015).

Based on this anatomy, the optic nerve is traditionally divided into four portions (Bron et al., 1997; Ritch et al., 1989) (Fig.1.1): 1) Intra-scleral or ONH portion or ONH (which is where the RGC axons pass through the connective tissues of the posterior eye wall to achieve the orbit); 2) Intraorbital portion (which is the part that runs within the orbit); 3) Intracanalicular Portion (the part within a bony canal known as the optic canal) and 4) Cranial Portion (the part within the cranial cavity, which ends at the optic chiasm). The first of these is approximately 1-3 mm in length and it is the major site of axonal damage in glaucoma. The intraorbital component length is approximately 25 mm long, and has a sigmoidal course to allow extreme ocular movements. The intracanalicular portion is approximately 10 mm in length. Upon exiting the optic canal, the nerve runs an intracranial course for approximately 16 mm, until it reaches the optic chiasm.

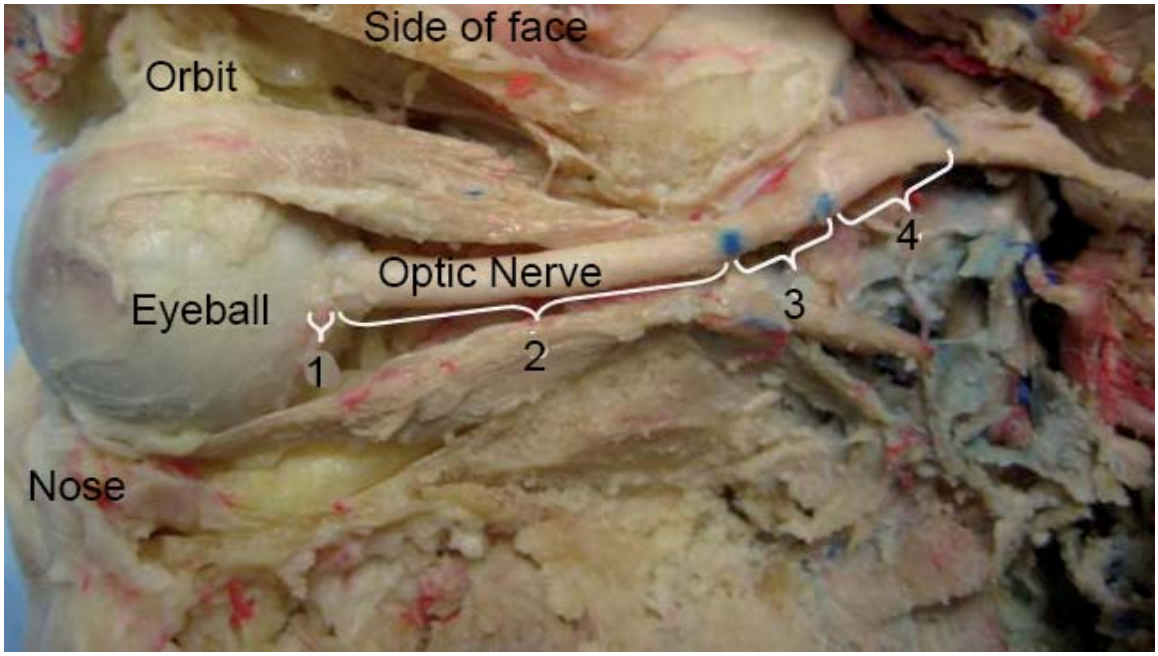

Figure 1.1. Anatomical dissection of the Optic Nerve showing its different components (superior view): 1)Intraocular portion; 2) Intraorbital portion; 3) Intracanalicular portion and 4) Intracranial portion. Courtesy Dr. John B.Selhorst (Creative Commons International License).

1.1.1.- General Macroscopic Anatomy of the Optic Nerve Head (ONH)

The ONH comprises of RGC axons, blod vessels, glia and connective tissue. It is thought to be the primary site of damage in glaucoma (Anderson et al 1974; Quigley et al 1976; Quigley et al 1981). It can be divided into three regions - the retinal, the choroidal and the scleral (Anderson and Hoyt, 1969; Hogan et al., 1971), as the nerve passes throught each of these structures. An other alternative is to divide it into distinct regions, based on their association with the connective tissue lamina cribrosa (Fig. 1.2): 1) *Prelaminar zone* (equivalent to the retinal and choroidal portions); 2) *Laminar zone* (equivalent to the scleral region wherein the sclera is continuous with the lamina cribrosa) and 3) the *Retrolaminar zone* (equivalent to the scleral region posterior to the lamina that extends to the posterior scleral opening where the optic nerve exits the eye) (Bron et al., 1997; Ritch et al, 1989). The differences among these regions reflect the changing conditions to which the axons are exposed as they pass through the ONH. These differences include axonal myelination just posterior to the lamina cribrosa, distinct arteriolar sources of blood supply (although capillaries from prelaminar through lamina and retrolamina are continuous), and an abrupt increase in tissue pressure from the intraocular pressure (IOP) to that of the cerebrospinal fluid (Morgan et al, 1998).

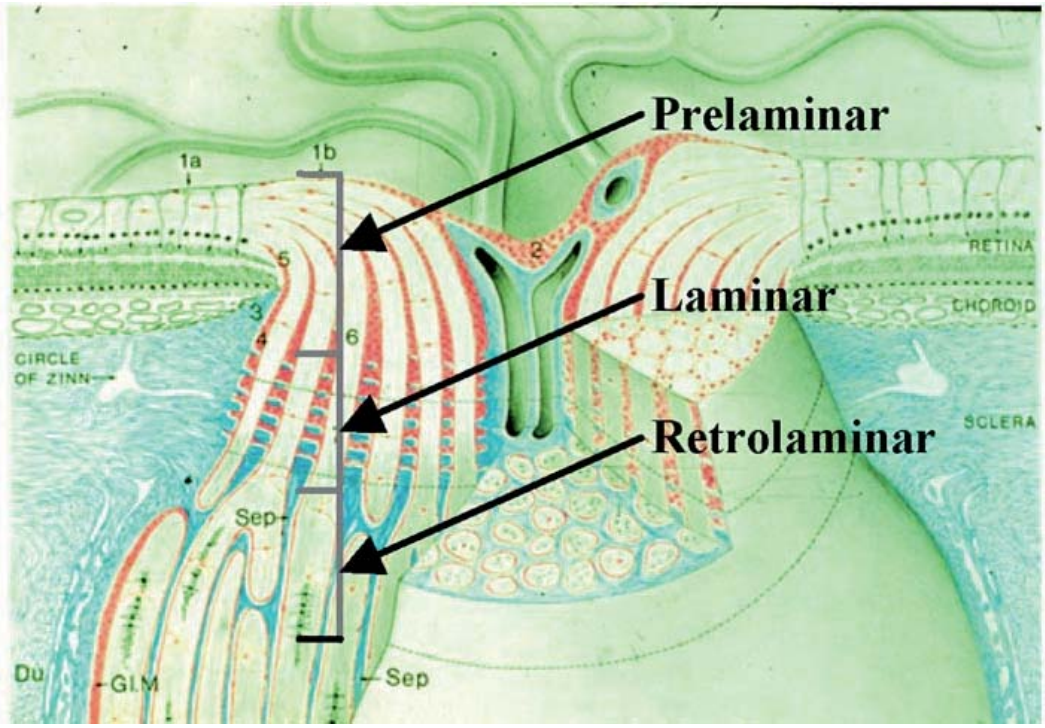

Figure 1.2. Subdivision of the ONH. Adapted from Anderson and Hoyt, 1969.

Clinicians often use the term **optic disc** to refer to the part of the ONH that is visible by ophthalmoscopy. This refers to all the neural tissues that extend from the anterior surface of the disc to the lamina cribrosa (prelaminar zone). This optic disc is slightly verticaly oval and its size is very variable measuring approximately 1.75 mm high and 1.50 mm wide (Jonas et al 1988). The optic disc contains a peripheral "rim" composed primarily of neural tissue (as well as blood vessels and supporting cells) and a more central excavation (without neural tissue). The optic disc margin is a key clinical landmark that is traditionally defined to be the inner edge of the scleral lip or crescent (a whitish reflective halo at the innermost boundary of the neuroretinal rim, also know as "Elschnig's ring") (Hogan et al. 1971) (figure 1.3). In this context, optic disc margin has been thought to be a single and consistent anatomic structure around the entire ONH and a true outer border of the retinal rim, and therefore the landmark from which the width of the rim can be measured.

However, recent findings with Spectral-Coherence Tomography (SD-OCT) have challenged the basis and accuracy of current rim evaluation proposing a paradigm change for clinical assessment of the ONH (Chauhan and Burgoyne, 2013) (Fig.1.4).

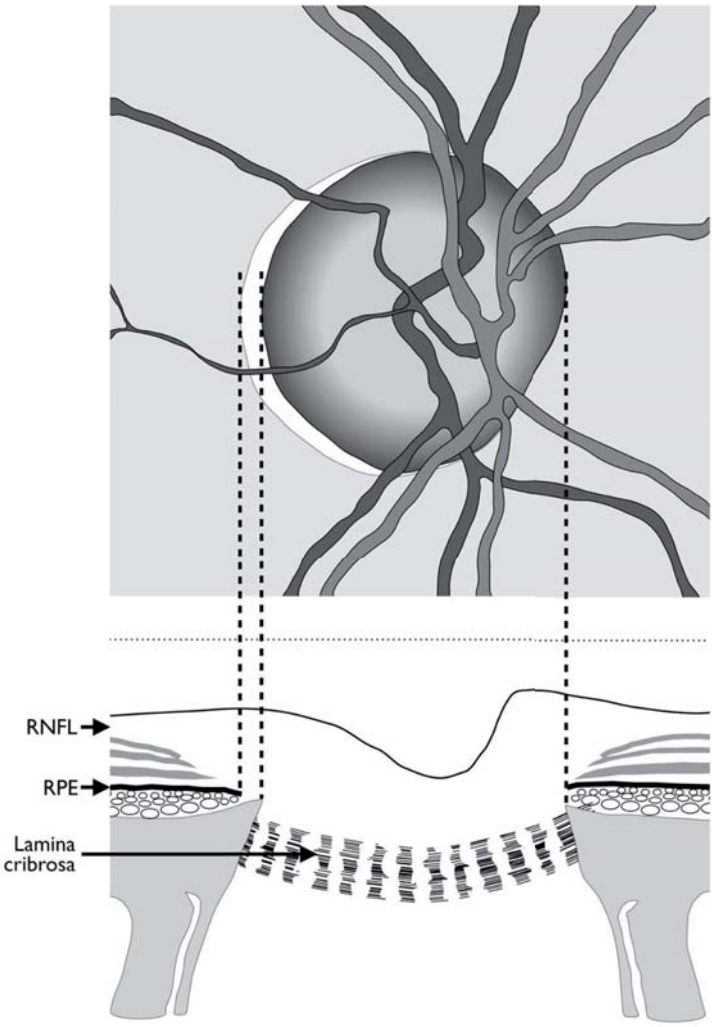

Figure 1.3. Current concepts of optic disc margin anatomy. Top: Optic disc appearance of a right eye. Bottom: Corresponding view of the optic nerve head. In this example, the temporal disc margin is defined by the inner edge of the scleral lip or crescent (dotted lines) while the nasal disc margin corresponds to the termination of retinal pigment epithelium, which also coincides with the inner edge of the sclera. In both instances, the disc margin is depicted as the true outer border of the neuroretinal rim. RNFL = retinal nerve fibre layer; RPE = retinal pigment epithelium. Modified from Hogan, Alvarado Wedell.

Adapted from Chauhan and Burgoyne, 2013.

The termination of the Bruch's membrane (BM) at the ONH (termed BM opening BMO-) represents the entrance to the neural canal which extends from BMO, through the Border Tissues of Elschnig and sclera. BMO is thus a true border for RGC axons and is thus an accurate landmark from which to make ONH neuroretinal rim tissue measurements. Moreover, BMO is a structure consistently identified with SD-OCT (Strouthidis et al 2009; Reis et al 2012a; Hu et al 2010), but not always clinically visible. The clinically visible disc margin is therefore an unreliable outer border of rim tissue due to clinically invisible extensions of BM (Chauhan and Burgoyne, 2013).

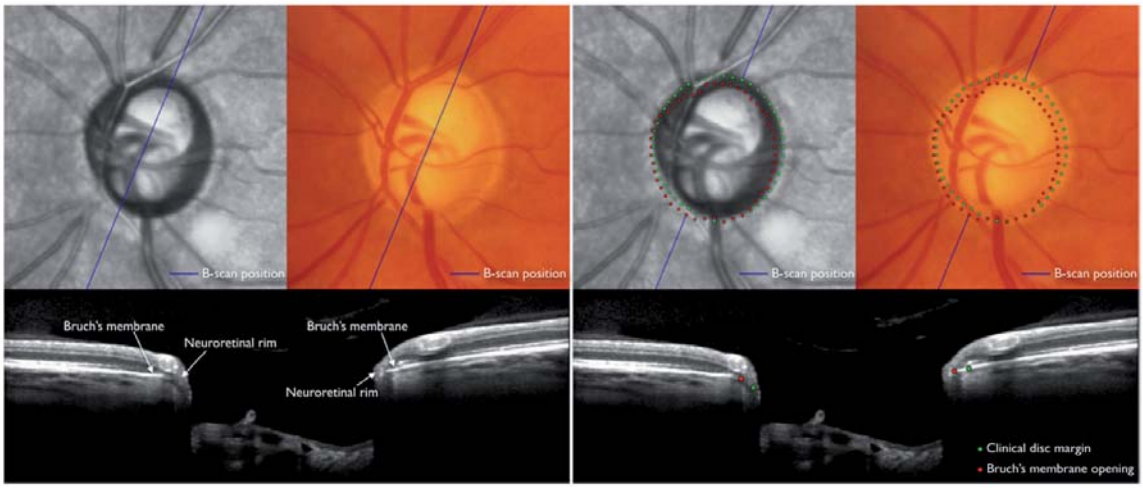

Figure 1.4. Optic disc margin anatomy with conventional optic disc photography and spectral domain coherence tomography (SD-OCT) in the left eye of a patient with glaucoma. Top: optic disc with infrared illumination (first and third columns) with SD-OCT imaging and photography (Second and four columns) precisely co-localised. Bottom: Co-localised B-Scan images corresponding to the position (blue line) indicated in the fundus images. Clinically visible optic disc margin (green dots; top right) traced in the disc photograph projected to the B-scan (bottom right), and Bruch's membrane opening identified in the B-scan (red dots; bottom right) projected to the fundus photograph (top right). In this case, there is a clinically invisible overhang of Bruchps membrane in the superior temporal quadrant resulting in a significant overstimation of the neuroretinal rim width with disc margin based evaluation, while in the inferior nasal quadrant the rim is actually wider than perceived clinically. Adapted from Chauhan and Burgoyne, 2013.

1.1.2- ONH Microscopic Anatomy

The "optic nerve head" is commonly used to refer to the tissues within and around the passage of the RGC axons through the wall of the eye. While there is no agreement upon usage for "optic nerve head", we use this term to refer to not just the RGX axons or optic nerve but the surrounding Bruch's Membrane, Border Tissues of Elschnig, lamina cribrosa, peripapillary sclera and choroid. There are good reasons for taking this conceptual approach to these tissues. In the primate, the sclera and the lamina cribrosa are biomechanically linked. Their connective tissues are an embryological, anatomical, physiological and biomechanical continuum. The astrocytes of the ONH exist in a synctytium extending from the prelaminar to the retrolaminar nerve in the same fashion. There are no clean borders and boundaries anatomically, physiologically, embryologically or biomechanically.

For the one to two million axons that comprise the optic nerve the ONH is an environment of transition and vulnerability. Axons have to rotate through 90º to exit the eye and,

in so, rearrange themselves to achieve a new topographic organization within the optic nerve (Morrison and Pollack, 2003). Axons are supported in this passage by a complex three-dimensional arrangement of glial supportive tissue, which in the prelaminar ONH forms a continuum with the astrocytes which line the laminar beams and pores. This continuum of astrocytes is linked by gap junctions and has been termed a syncium, that along with the capillaries, are continuous throughout the ONH and retrolaminar nerve (Hogan et al. 1971). Ultrastructurally, there are differences in each of the anterior optic nerve regions described below e table 1.1).

Region	Prominent Features
Retinal nerve fiber layer	Unmyelinated ganglion cell axons converge on the ONH
Prelamina	Axons segregate into bundles and begin to turn into the ONH Bundles separated and supported by astrocyte processes
Lamina cribrosa	Connective tissue sheets with holes aligned to transmit the axonal bundles at the level of posterior sclera Astrocyte processes support axons with intimate contacts within the axonal bundles
Retrolaminar optic nerve	Myelination begins at the posterior limit of the lamina cribrosa

Table 1.1. Regions of the anterior optic nerve and their ultrasctructural characteristics.
Adapted from Morgan and Morrison, 2003. In: Morrison and Pollack, 2003.

Astrocytes surround the RGC axons as they leave the RGC soma and contribute significantly to axon organization in the nerve fiber layer (Stone et al, 1995). The axons are separated into bundles by the processes of Müller glial cells, whose endfeet, together with the less numerous astrocytes, form the internal limiting membrane between the retina and vitreous (Ramirez et al, 1996). It is likely that processes from both the astrocytes (Ramirez et al 1996)

and the Müller cells underlie the striations seen in the healthy neve fiber under red free illumination (Quigley et al, 1986).

The glial tissue provides a continuous layer between the nerve fibers and blood vessels in the ONH (Anderson et al, 1967). In the rhesus monkey, astrocytes occupy 5% of the nerve layer , increase to 23% of the laminar region, and then decrease to 11% in the retrolaminar area (Minckler et al, 1976). The astroglial tissue also provides a covering for portions of the ONH. The internal limiting membrane of Elschnig separates the ONH from the vitreous and it is continuos with the internal limiting membrane of the retina (Anderson et al, 1967; Anderson et al 1970; Anderson et al 1969). The central portion of the internal limiting membrane is referred to as the central meniscus of Kuhnt (Anderson et al. 1970). The Müller cells are a major constitutional element of the intermediary tissue of Kuhnt (Hirata et al, 1991, which separates the nerve from the retina, whereas the border tissue of Jacoby separates the nerve from the choroid (Anderson et al, 1969a and 1969b).

Astrocytes also play a major role in the remodeling of the extracellular matrix of the ONH and synthesizing growth factors for the RGCs axons (Hernandez, 2000).

1.1.3- Lamina Cribrosa

The main physical support for axons appears at the level of the sclera, in the form of approximately 10 connective tissue sheets (Anderson et al 1969; Elkington 1990). These sheets, the scleral lamina cribrosa, span the scleral opening at the back of the eye, inserting into the outer half of the sclera. Each of these sheets, or plates, is perforated to provide room for the axons to pass in bundles approximately 100 μ m wide (Ogden et al 1988). The openings in the cribiform plate, through which the optic nerve fascicles pass, are called laminar “pores”. There are 500 to 600 in human optic nerves (Ogden et al, 1988). The number of pores increases by approximately 50% from the choroidal to the scleral lamina and as a result the pores are not vertically aligned in successive cribiform plates (Emery et al, 1974; Ogden et al, 1988). Digest studies in which the cellular components and the glial prelamina are removed by enzymatic or chemical digestion have revealed that the plates have abundant connections between each other and form a compact three-dimensional array of pores through which the axon bun-

dles run (Quigley et al, 1983). In contrast to the more conventional view of axons following a relatively direct course through the lamina, more recent studies examining its 3D microstructure throught cadaveric monkey optic nerves digital reconstructions (Roberts et al, 2009) have shown a much more complex architecture (see figure 1.5).

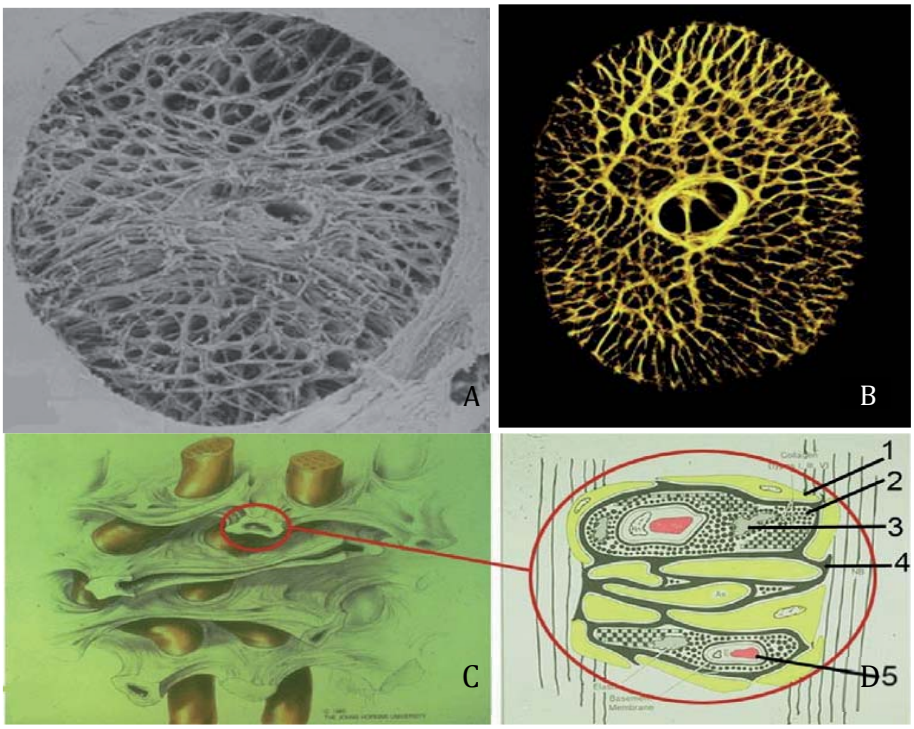

Figure. 1.5. The Lamina Cribrosa and its connective tissue arrangement. The structural architecthure of the lamina cribrosa is very complex: A) Electron micrograph showing the arrangement of interconnecting laminar beams enclosing the laminar pores, after a trypsin digest of a normal human cadaveric ONH (Quigley et al 1990); and B) 3D digital reconstruction of a cadaveric normal monkey ONH (Roberts et al. 2009). The arrangement of connective tissues and capillaries within the lamina cribroa is shown in C) passage of nerve fiber bundles through a section of the lamina; and D) Ultrastructural components representation of a magnified area of a laminar beam:1) Astrocytes (yellow cells), 2) Collagen fibrils, 3) Elastin fibrils, 4) basement membranes of astrocytes and 5) Capillary. Adapted from (Morrison et al 1989; Quigley, 1995)

Astrocytes in the lamina cribrosa form a thin mantle that separates the nerve bundles from the laminar connective tissue and from the connective tissues around the central retinal vessels (Hogan et al, 1971). The astrocytes also separate the nerve from scleral collagen at the edge of the scleral canal. Capillaries, very similar to those found in the sclera, run through the connective tissue of the lamina where they have thin adventitial connective tissue (see figure 1.5).

The lamina should be seen more like a sponge through which pores channel from anterior to posterior with opening and connectivity existing between adjacent pores. The scleral lamina can thereforte be regarded as a meshlike structure that effectively acts as a connective tissue "scaffold" that serves to anchor the bundles of optic nerve axons to each other and to the scleral canal. The connective tissue of the peripapillary sclera and the lamina cribrosa represents the chief load-bearing tissue of the ONH (Burgoyne et al, 2005).

1.1.4- ONH Vasculature

1.1.4.1. Arterial Supply

Posterior ciliary artery (PCA) circulation is the main source of blood supply to the ONH (Onda et al, 1995), except from the nerve fiber layer, which is supplied by the retinal circulation. The arterial supply of the ONH has been shown to have a sectorial distribution (Hayreh et al, 2001), in which the four divisions of the ONH correlate roughly with a four-part vascular supply (Fig.1.6):

- The *Surface nerve fiber layer* is mainly supplied by arteriolar branches of the central retinal artery (CRA) (Onda et al, 1995) which anastomose with vessels of the prelaminar region (Lieberman MF et al, 1976) and are continuous with the peripapillary retinal and long radial peripapillary capillaries (Hayreh et al, 1974). The temporal region may be also supplied by one or more of the ciliary-derived vessels from the PCA circulation in the deeper prelaminar region, which may occasionaly enlarge to form cilioretinal arteries (Hayreh et al, 1974).

- The *prelaminar and laminar regions* are supplied primarily by short posterior ciliary arteries (SPCAs), which create a perineural, circular anastomosis at the level of the sclera called the circle of Zinn-Haller (Hayreh et al, 1974; Onda et al, 1995). Branches of this circle penetrate the ON to supply the prelaminar and laminar regions and the peripapillary choroid (Onda et al, 1995). This circle is not present in all eyes in which case direct branches from the SPCAs supply the anterior optic nerve. The peripapillary

choroid may also make a minimal contribution to the anterior ON (Hayreh et al, 1974; Onda et al, 1995; Lieberman MF et al, 1976).

- The *Retrolaminar Region* is supplied by both the ciliary and retinal circulations, with the former coming from recurrent pial vessels. Medial and lateral perioptic nerve short posterior ciliary arteries anastomose to form and elliptical arterial circle around the optic nerve, which has also been referred to as the circle of Zinn-Haller (Olver et al, 1994; Ko et al, 1999). This anastomosis was found to be complete in 75% of 18 human eyes in one study (Olver et al, 1994). The CRA provides centripetal branches from the pial system and frequently, but not always, gives off centrifugal vessels (Hayreh et al, 2001).

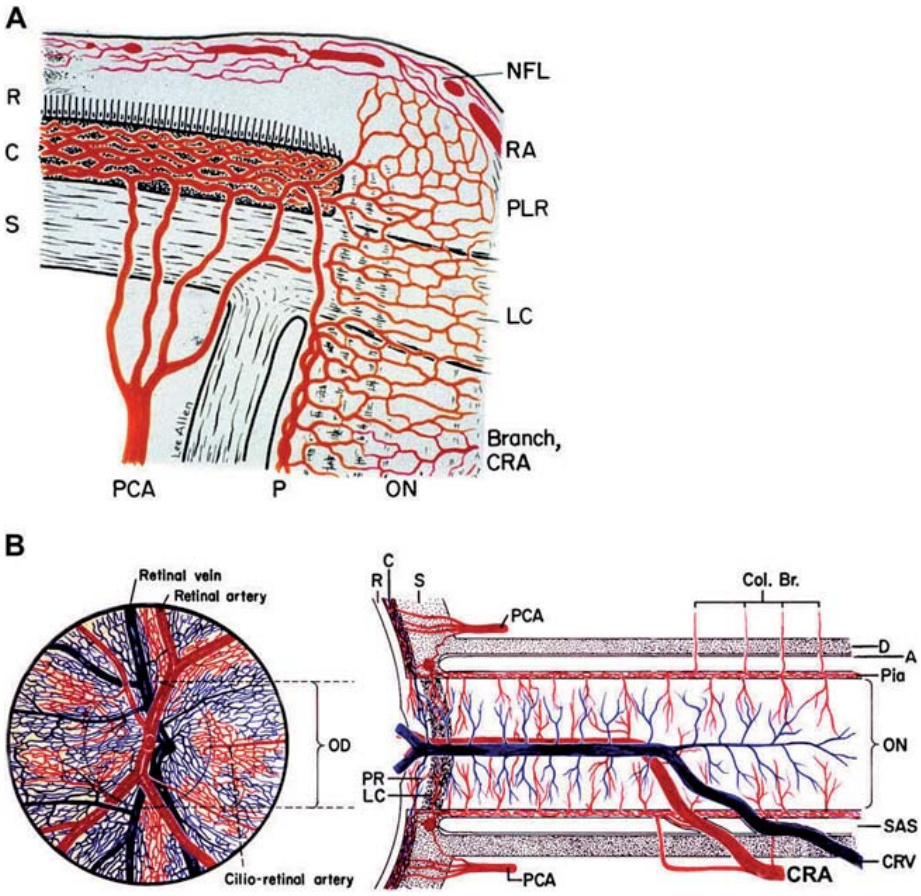

Fig. 1.6 Schematic representation of blood supply of: (A) the optic nerve head and (B) the optic nerve. A reproduced from Hayreh [B modified from Hayreh et al, 1974. Abbreviations used: A = arachnoid; C = choroid; Col. Br. = Collateral branches; CRA = central retinal artery; CRV = central retinal vein; CZ = Circle of Zinn and Haller; D = dura; LC = lamina cribrosa; NFL = surface nerve fiber layer of the disc; OD = optic disc; ON = optic nerve; P = pia; PCA = posterior ciliary artery; PR and PLR = prelaminar region; R = retina; RA = retinal arteriole; S = sclera; SAS = subarachnoid space

1.1.4.2. Venous Drainage

The venous drainage from the ONH is almost entirely through the central retinal vein (CRV) (Onda et al, 1995), although a small portion may occur through the choroidal system (Hayreh et al, 2001).

1.1.5. Influence of Age

The ON cross-sectional area reaches 50% of the adult size by 20 weeks gestation, 75% at birth, and 95% before 1 year of age (Rimmer et al, 1993). At birth, the optic nerve is nearly unmyelinated (Dolman et al, 1980), and myelination, which comes from the brain to the eye during gestation, is largely completed in the retrolaminar region of the ON by the first year of life (Magoon et al, 1981). The connective tissue of the lamina cribrosa is also incompletely developed at birth, which may account for the greater susceptibility of the infant nerve head to glaucomatous cupping, as well as its potential for reversible cupping (Quigley, 1977). With increasing age, the pores of the cribriform plates enlarge and there is increase in the apparent density of collagen types I, II, and IV and elastin (Hernandez, 1989 and 1992). Not only does elastin increase wih age, but elastic fibers become thicker, tubular, and surrounded by densely packed collagen fibers (Hernadez et al, 1992). Proteoglycan filaments in the human lamina cribrosa also decrease in length and diameter with age (Sawaguchi et al, 1993). Also with increasing age, there appears to be a progressive loss of axons with a dercrease of the nerve fiber layer thickness (Alamouti and Funk, 2003; Toprak and Yilmaz, 2000), and a corresponding increase in the cross-sectional area occupied by the leptomeninges and fibrous septa (Mikelberg, 1991a and 1989; Repka and Quigley, 1989; Jonas et al, 1995). The loss of axons has been estimated to be between 4,000 and 12,000 per year (Mikelberg et al, 1989; Mikelberg et al, 1991; Jonas 1992). All this connective tissue changes wil undoubtedly alter the biomechanical behavior of the ONH and may help to explain why the risk of glaucoma increases with ageing.

1.2- Glaucoma

1.2.1. Definition and Context

Glaucoma describes a group of ocular disorders of multi-factorial aetiology in which the common clinical feature is a characteristic optic neuropathy with potentially progressive, clinically visible changes at the ONH, comprising focal or generalized thinning of the neuro-retinal rim with excavating and enlargement of the optic cup and an a corresponding defect in the visual field (Casson et al, 2012).

Glaucoma is a major cause of irreversible blindness worldwide. Recent work estimates that in 2013, the number of people (aged 40-80 years) with glaucoma worldwide was 64.5 million, and that this number will increase to 76 million in 2020 and 111.8 million in 2040 (Tham et al. 2014). The prevalence of glaucoma in caucassian subjects over the age of 40 in Europe varies from 1.1-2.5% (Anton et al, 2004; Bonomi et al, 1998; Coffey et al, 1993; Dielemans et al, 1994). The prevalence of glaucoma is low before the age of 40 and increases exponentially with age (Leske et al, 2007). Glaucoma is a major public concern and its prevalence will likely continue to as life expectancy continues to rise.

In the past, elevated intraocular pressure (IOP) was usually included in the definition of glaucoma as the main cause of the neuropathy. Epidemiology studies have considered a normal IOP upper limit of 21 mmHg (mean of 15-16 mmHg + 2 standard deviations) (Armaly, 1965; Kahn et al, 1977; Klein et al, 1992). However, at present, while IOP has been shown to be the most important risk factor for the disease, at all levels of pressure, all ages, and all stages of the neuropathy, glaucoma is diagnosed based on the presence of an optic neuropathy without regard or the level of IOP at which it has occurred. Depending upon the study, between 30 and 50% of all subjects who are found to have glaucoma do not demonstrate elevated IOP (Sponsel, 1989; Iwase et al, 2004). This “normal” IOP in some patients with glaucoma has given rise to a clinical distinction between “Normal-Tension Glaucoma (NTG)”, where basal IOP is less than 21 mmHg, and “High-Tension Glaucoma”, where untreated IOP is greater than 21 mmHg. There is ongoing disagreement as to whether these are two separate clinical entities or if they are a continuum of ONH susceptibility within the same disease.

There are some characteristical features of NTG that may indicate an associated vascular dysregulation of the ONH, such as history of vasospasm (migraines, Raynaud's phenomenon), increased frecuency of optic disc hemorrhages and a more focal distribution of nerve loss (focal rim loss and focal RNFL defects). However, given that lowering IOP remains the only proven treatment strategy for delaying glaucomatous progression in both high-tension glaucoma and NTG (Kass et al, 2002; CNTGS, 1998; Hejil et al, 2002) IOP clearly plays a central role in the development of GON, regardless of the level of IOP at which it occurs.

Perhaps the most clinically useful classification of the glaucomas is that devised by Barkan which divides glaucoma into angle-closure or open angle based on the presence or absence of an obstruction to aqueous outflow at the trabecular meshwork within the iridocorneal angle (Barkan et al, 1938). Open angle glaucoma refers to the presence of glaucoma in the absence of significant iridotrabecular contact. A further subdivision produces either primary or secondary glaucomas. In the latter, the clinician detects an elevated IOP during the disease and finds a cause; in the former, if the IOP is elevated, no cause is found. Primary Open Angle Glaucoma (POAG) is the commonest form of glaucoma in white populations of European descent. Angle closure refers to the situations where ther is greater than 180º of iridotrabecular contact. In primary angle closure, the angle is closed owing to an anatomical predisposition. In secondary angle-closure glaucomas, the cause for the iridotrabecular contact is secondary to an associated pathologic process, rather than a primary anatomic abnormality.

It is important to note that the optic disc and visual field changes are similar between open angle and angle closure glaucoma, especially in cases of chronic duration. Nevertheless, an acute IOP elevation clinically often produces pallor without excavation wich, by definition, is not glaucoma. In such circunstances, the neuropathy has more in keeping with an ischaemic aetiology (Douglas et al. 1975). In order for the work contained in this PhD to be clinically applicable to all forms of glaucoma, it was important to identify an experimental model with chronic sustained IOP elevation to avoid sudden extreme increases in IOP that could result in an ischemic neuropathy. The rationale for selecting the rat model of experimental glaucoma is discussed later in section 1.3.

1.2.2. Major Risk Factors

Risk factors are clinically useful to assess the risc of glaucoma based on the characteristics of the patient, and may also give some indication as to the pathogenesis of glaucoma.

1.2.2.1. IOP

The evidence for a causal association between IOP and glaucoma is robust and has already been mentioned in the previous section. In addition, there is support for at least one plausible biologic mechanism that links elevated IOP to apoptosis of neurons (Kerrigan et al, 1997) of the optic nerve through blockage of retrograde axonal transport (Quigley et al, 1981). A discussion on ONH biomechanics is included in a later section (1.2.6).

The most decisive evidence is the demonstration by randomized clinical trials that IOP lowering decreased the incidence and progression of glaucoma compared to no treatment (The AGIS Investigators, 2000; Heijl A, et al 2002). In the Baltimore survey, the prevalence of POAG increased with IOP. Compared to those with an IOP ≤ 15 mmHg the prevalence of POAG was over 40 times in those with an IOP of 35 of greater. In addition, 10.3% of individuals with an IOP greater than 22 mmHg were found to have glaucoma, whereas only 1.2% of individuals had glaucoma with an IOP less than 21 mmHg (Sommer et al, 1991). The incidence of POAG was found to increase steadily with IOP in the Barbados Eye Study to a realitve risk o 25 for an IOP of more than 25 mmHg compared to a reference group with an IOP less than 17 (Leske et al, 2001). In the population of the Melbourne Visual Impairment Project (Heijl, 2002) it was estimated that for every 1 mmHg, the risk of depeloping glaucoma increased 10%. Importantly, the OHTS also demonstrated that lowering the IOP by an average of 23% decreased the incidence of malnifest POAG at 5 years by 60% (Kass et al, 2002). In POAG, the EMGT and the CNTGS have shown that an IOP reduction of 25% and greater than 30% cut the risk of progression by 33% and 50%, respectively, compared to no treatment (Heijl, 2002; CNTGS, 1998).

It has also been shown that that the higher the basal IOP, the more severe the visual field loss is at presentation (Jay and Murdoch, 1993). Even in NTG subjects, the eye with

more severe visual field loss is most commonly the eye with the higher IOP (Cartwright and Anderson, 1988) and the magnitude of IOP (even though is within the normal range) is a risk factor for disease progression (Crichton et al, 1989; Orgul and Flammer, 1994).

1.2.2.2. Age

Population-based studies of prevalence and incidence consistently show a steady increase with age. The prevalence of glaucoma approximately doubles for each decade over 40, and is about 10-fold higher in the 80+ group compared to the 40-49 year-old group (Mukexh et al, 2002; Bengtsson et al, 1989; Lestke et al, 2001). In the OHTS, the relative risk of developing POAG was lower at 1.2 decade of age, possibly as a result of excluding glaucoma suspects (Gordon et al, 2002). In the EMGT, the relative risk of progression of early glaucoma was 1.5 times greater for those 68 of age and older compared to those younger than 68 years (Leske et al. 2003). In a study carried out using data from the Beaver Dam Eye Study, an increase in optic disc cupping with high IOP was more likely to be found in subjects over 75 years of age as compared to younger subjects with high IOP or subjects over 75 with lower IOP (Klein et al, 2006).

The mechanisms by which ageing influences the susceptibility of the ONH are multiple (Burgoyne, 2011). The aged ONH is more likely to have stiff connective tissues and a compromised blood supply (Albon et al 2007, Hernandez et al, 1989; Quigley 1989). However, age-related increases in laminar beam thickness, laminar astrocyte basement membrane thickness and laminar extracellular matrix should not only increase laminar beam stiffness, but also diminish nutrient diffusion from the laminar capillaries into the adjacent axons (Burgoyne, 2011). While the concepts of age-related optic nerve axon loss and an optic neuropathy of aging remain controversial, we believe that the range of physiologic stress and strain within the ONH connective tissues experienced over a lif-time are likely to be of central importance to both (Burgoyne, 2011). Both normal and elevated levels of IOP-related strain can be expected to induce synthesis of extracellular matrix by the laminar astrocytes, which alters the material properties of the adjacent laminar trabeculae (for more information see section 1.2.6, ONH Biomechanics). Additionaly, the laminar astrocytes and laminar capillary endothelial

cells may thicken their basement membranes as a secondary response to the physical distortion induced by laminar deformation (Burgoyne, 2011).

1.2.2.3. Myopia

An association between myopia, particulary high myopia, and open-angle glaucoma has long been reconginzed and is supported by numerous case series (Fong et al, 1990; Podos et al, 1966; Perkins et al, 1982) and case-control studies (Daubs et al 1981, Wilson et al, 1987). This association is also supported by large population-based prevalence surveys (Mitchell et al, 1999a; Weih et al, 2001; Wong et al, 2003) that reported an elevation of prevalence of POAG in those with any myopia of 48% (Quigley et al, 1999), 60% (Wong et al, 2003), and 70% (Weih et al, 2001) after adjustment for age and gender. Another survey reported a twofold to threefold higher prevalence of glaucoma in individuals with myopia (Mitchell et al, 1999b). However, individuals with myopia were not found to have a higher incidence or progression of glaucoma in the OHTS or EMGT (Leske et al, 2003). Other longitudinal studies have previously shown high myopia to be a risk factor for progression (Phelps et al, 1982; Chihara et al, 1997).

One potential detection-bias is the fact that myopic eyes tend to have larger optic discs, and as such will have larger cup-to-disc ratios. It is possible that, at least in some population-based studies, there is this potential confounding factor, with myopic eyes being more likely to be flagged as glaucomatous because thay have increased cupping. Furthermore, it is perhaps easier to detect glaucomatous changes in a larger myopic disc. In myopia, the axial length of the eye is increased and it is likely that, as with ageing, there are connective tissue changes at the ONH and peripapillary sclera that may influence how the nerve responds to IOP. This may explain the predisposition of myopic ONHs to develop glaucomatous damage.

1.2.2.4. Central Corneal Thickness (CCT)

CCT has been shown to vary in different populations. For example, results from the Barbados Eye Study (Nemesure et al, 2003) and the OHTS (Brandt et al, 2001) have shown that Blacks have thinner CCT compared to Whites. CCT also ifluences the accuracy of the

measurement of IOP. The gold standard for IOP measurement is currently the Goldmann applanation tonometer, which assumes a standard CCT. Thicker corneas are associated with erroneous measurements that are higher than the actual IOP and thinner corneas with measurements that are lower than actual IOPs (Ehlers, 1970; Li et al, 2004; Shimmyo et al, 2003).

However, separate from the effect of CCT on IOP measurement accuracy, the results of OHTS indicated that a thin CCT is one of the strongest risk factors for conversion to glaucoma in ocular hypertensive subjects, and that this risk is over and above what might be expected through measurement error only (Gordon et al, 2002). This finding was confirmed independently in the European Glaucoma Prevention Study (EGPS) and the combined OHTS/EGPS risk model features CCT as a major component of glaucoma risk (Gordon et al, 2007; Miglior et al, 2007; Pfeiffer et al, 2007). Numerous investigators have further explored the role of CCT in patients with existing glaucoma and in general they have found that CCT has a significant impact in glaucoma progression (Congon et al, 2006; Herndon et al, 2004; Hong et al, 2007; Jonas et al, 2005). Randomized controlled trials have yet to confirm the role of CCT in established glaucoma. The EMGT initially found no association between CCT and incident glaucoma or disease progression. However, with longer follow-up a moderate relationship was found between CCT and progression but only in those subjects with higher IOPs (Leske et al, 2007).

One possible reason for a relationship between thin CCT and glaucoma is that, patients with higher IOPs are perhaps treated more aggressively compared to those with lower IOPs and thinner corneas. As such, progression may be more likely to occur in those with thinner corneas. However, an indication, that CCT exerts an independent influence over glaucomatous progression is the fact that a relationship, albeit modest, was found in the EMGT, a study in which tonometry was not used as inclusion or treatment criteria (Brandt, 2007; Leske et al, 2007).

An alternative explanation is the possibility that CCT may be in some way a surrogate marker for the connective tissue behavior of the peripapillary sclera and lamina cribrosa. After all, the cornea contains the same biological agent (collagen), encoded by the same genes, as found in the connective tissues within the ONH. It should be noted, however, that CCT

alone is only one component of structural stiffness and therefore cannot alone be used to determine the biomechanical behavior of the cornea without knowing its material properties. Any potential links between CCT and the biomechanical response of the ONH remains speculative. Studies that have tried to link CCT with movement of the ONH surface (assumed to be a proxy for lamina cribrosa displacement) following IOP-lowering have found uncertain results (Leske et al, 2006; Nicolela et al, 2006).

1.2.2.5. Family History

The data on family history as a risk factor in POAG is inconsistent. A family history of POAG is generally considered to be an important risk factor for POAG. Having a first-degree relative (parent, sibling, or child wih glaucoma has been consistently associated with an increased risk of POAG inprevalence surveys (Rosenthal and Perkins, 1985; Tielsch et al, 1994; Nemesure et al, 1994; Wolf et al, 1998; Mitchell et al, 2002). The odds ratio (OR) for a family history of glaucoma are higher if based on patients with previously diagnosed glaucoma (Baltimore OR=4.7; Blue Mountain Eye Eye Study OR=4.2) than if based on newly diagnosed cases (Baltimore ORE=2.3; Blue Mountains Eye Study OR=2.4). This suggests that having a diagnosis of POAG leads to a greater awareness of glaucoma in the family. The association between POAG and family history may be stronger when the affected relative is a sibling (OR=3.7) rather than a parent (OR=2.2) or child (OR=1.1) (Tielsch et al, 1994). Family history has been shown to be a risk factor for glaucoma in one population-based prospective study (RR=2.1) (Le et al, 2003), while in clinically assembled OHTS population no association was found. In prospective studies of established glaucoma, family history hasnot been shown to be a significant predictor of progression (Leske et al, 2003; Drance et al, 2001).

Mutations in multiple genes and genomic regions contribute to open angle glaucoma (Wiggs, 2007), or may be associated with the development of pseudoexfolitaion, a condition with a high risk of developing secondary open angle glaucoma (Grodum et al, 2005; Thorleifsson et al, 2007).

1.2.3. Morphology of Glaucomatous Optic Neuropathy

The disc changes in glaucoma are typically progressive and asymmetric and present in a variety of characteristical clinical patterns. –The main clinical feature present in glaucoma is neuroretinal rim thinning that can be focal or diffuse. Other important features are: increase of the excavation or "cupping", deepening of the cup, retinal nerve fiber layer defects, peripapillary atrophy and presence of optic disc hemorrhages.

Typically there is a widely accepted sequence of sectoral rim loss in glaucoma (local or diffuse): the inferotemporal, followed by the superotempral, then the temporal, inferonasal and superonasal sectors (Airaksinen et al, l992; Jonas et al, 1993; Tuulonen and Airaksinen, 1991). The final neuroretinal sector affected in glaucoma is usually the nasal region, corresponding to the preservation of a temporal island of vision. A number of studies have characterized the phenotype of "cupping" in glaucoma using the four classic types represented in figure 1.7. (Nicolela and Drance, 1996; Nicolela et al, 2003; Spaeth 1994; Spaeth et al, 1976):

- Type 1 or *Focal Glaucomatous disc:* Selective loss of neural rim tissue that occurs preferentially at the superior and inferior poles (Caprioli and Spaeth, 1985); Hitchings and Spaeth, 1976). Where a focal notch extends to the edge of the disc, a "sharpening" of the rim is observed (no visible neural rim remains in that area). A deep notch, extending to the edge of the disc can also appear as a round or oval, gray or white depression in the optic disc. This is called "acquired disc pit". This focal rim loss progresses by notch area enlargement, deepening and sharepening of the polar edge and eventually leading to narrowing and loss of neuroretinal rim.

- Type 2 or *Myopic Glaucomatous disc*: They are typically tilted and shallow optic discs with a myopic temporal crescent of peripapillary atrophy. Damage usually appears in the form of superior and inferior rim narrowing (Nicolela et al, 1996b).

- Type 3 or *Senile Sclerotic or Atrophic Glaucomatous disc:* They are characterized by a diffuse rim loss resulting in rim narrowing and a "moth-eaten" appearance of the rim (Geijssen and Greve, 1987). Usually, a complete ring of peripapillary atrophy is also present. Rim

loss is characterized by a gentle sloping, "shallow" cupping leading to a central pale area of the disc cup, a process known as "saucerization" of the disc.

- Type 4 or *General Enlargement*: These discs demonstrate enlarged round cups without focal rim loss and healthy-looking residual neuro-retinal rim. Atrophy of the neuroretinal rim occurs in a concentric, circular fashion with the cup enlarging in an inferotemporal, superotemporal or horizontal direction (Spaeth et al. 1976).

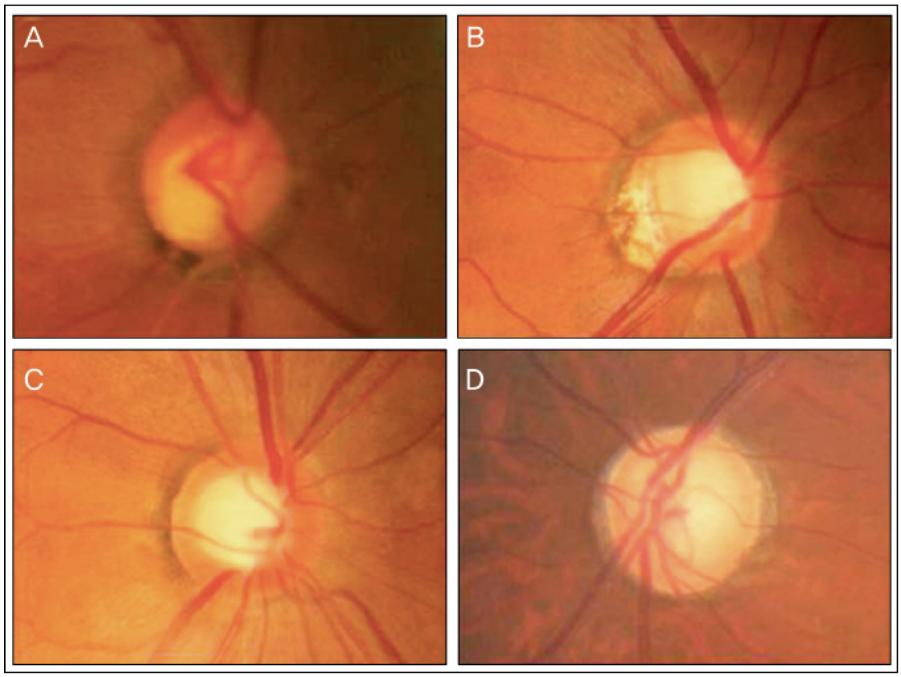

Fig. 1.7. Optic disc photographs showing the appearances of the four types of glaucomatous optic dis damage (reproduced from Kim G, et al, 2013): A) Type 1: Focal disc pattern; B) Type 2: Myopic disc pattern; C)General enlargement disc pattern and D)Senile sclerotic pattern.

Deepening of the cup is present in most forms of glaucoma and it is due to a combination of neuroretinal rim loss and connective tissue remodeling, resulting in a posterior movement of the lamina cribrosa. Advanced loss of the prelaminar neural tissue in severe glaucoma results in the laminar pores becoming visible (Read and Spaeth, 1974). The characteristic "bean pot cupping" of end stage glaucoma occurs when the cup enlarges to form a bowl behind Bruch's Membrane Opening (BMO) or the anterior scleral canal opening (Hitchings and Spaeth, 1976; Spaeth et al, 1976).

There are also some vascular signs of glaucoma, which are a consequence of the loss of surrounding neuroretinal tissue or connective tissue remodeling. As the cup progressively enlarges, the central retinal vessels may migrate towards the nasal edge of the disc. Loss of rim tissue may cause a vessel to appear exposed or "bared" (Herschler and Osher, 1980) or to "bayonette" as it turns 90º to course up a steep cup slope or undermined rim.

Peripapillary atrophy (alpha and beta) are both significantly larger in glaucomatous optic nerves, however they are a second order variable, being less useful than features based on the neuroretinal rim (Jonas et al, 2005). Alpha zones atrophy is less specific (being more commonly present in normal eyes) than Beta zone. The location of this atrophy is larger in the sector with the more marked rim thinning (Jonas et al, 1992). A larger beta zone and small neuroretinal rim have been identified as significant risk factors for glaucomatous progression (Jonas et al, 2004).

Optic disc hemorrhages occur within the margin of the optic nerve head, extend to variable lengths on either side, and are a common feature of glaucomatous damage (Drance et al, 1977; Susann R et al, 1979; Hendricx et al, 1994; Jonas and Xu, 1994). They occur more commonly in patients with normal-tension glaucoma and glaucoma suspects, with cumulative incidences of 35.3%, 10.3% and 10.4%, respectively (Hendricx et al 1994). Disc hemorrhages occurring in POAG are most frequently seen at the inferior and superior poles (Sonsjo et al, 2002). They usually take place in the prelaminar region of the ONH and in the superficial nerve fiber layer, appearing thin and radial (splinter hemorrhage) when located at the disc margin and round when occurring more centrally on the disc. If extravasation is more extensive, then a flame-shape appearance may be seen. The presence of a disc hemorrhage has been found to be a significant prognostic factor in glaucoma (Ishida et al, 2000), being associated with notching of rim tissue (Ahn and Park, 2002; Airaksinen and Tuulonen, 1984; Jonas and Xu, 1994), focal nerve fiber loss (Airaksinen et al 1981; Sugiyama et al 1997; Sugiyama et al, 1999), lamina cribrosa defects (Takayama et al, 2013) and progression of visual field loss (De Moraes et al, 2011; Rasker et al, 1997; Siegner and Netland, 1996).

The loss of axonal bundles, which leads to the neural rim changes of glaucomatous optic neuropathy, also produces visible defects in the retinal nerve fiber layer (nerve fiber bundle

defects). These appear either as dark stripes or wedge-shaped defects of varying width in the peripapillary area, paralleling the normal retinal striations, or as diffuse loss ot the striations, usually first in the supero-temporal or infero-temporal arcuate regions (Sommer et al, 1977; Sommer et al, 1979; Quigley et al, 1980; Jonas et al, 1994). With disease progression, localized wedge defects will increase in size and become more diffuse. RNFL loss has been detected up to five years before visual field loss in glaucoma patients and has been found to be be at least as predictive of future damage as changes within the optic disc itself (Quigley et al, 1982; Sommer et al 1977; Sommer et al 1979).

1.2.4. Histopathological Changes in Glaucoma

Postmortem changes at the lamina cribrosa in eyes with glaucoma include a posterior bowing of the lamina and posterior compression of the laminar sheets (Emery et al, 1974; Quigley et al, 1983) (Fig.1.8). The laminar pores become more elongated as glaucoma progresses (Emery et al, 1974), losing their typically round shape. Histopathological studies of glaucomatous ONH have shown persistent glial activation accompanied by increased synthesis of extrcellular matrix (Hernandez et al, 1990; Morrison et al 1990, Quigley et al, 1991; Varela and Hernandez, 1997). Astrocytes located within the cribiform plate have been found to migrate towards de laminar pores in glaucoma. This migration is activated by IOP in vitro (Tezel et al, 2001). These changes hightlight the important role astrocyte activation has in the remodeling of ONH and the consequent depelopment of GON.

Axons of larger diameter have been identified as being more susceptible to glaucomatous damage, both in humans and in animal models (Quigley, 1998; Quigley et al, 1987). Although axons are lost throughout the whole optic disc, they appear to be most susceptible within are the superior and inferior sectos of the nerve (Quigley et al, 1982; Quigley et al, 1983). However, the question of whether large axons and RGCs are most susceptible to early damage in glaucoma is controversial, with a series of more recent studies that have challenged Quigley's original observations (Morgan et al, 2000).

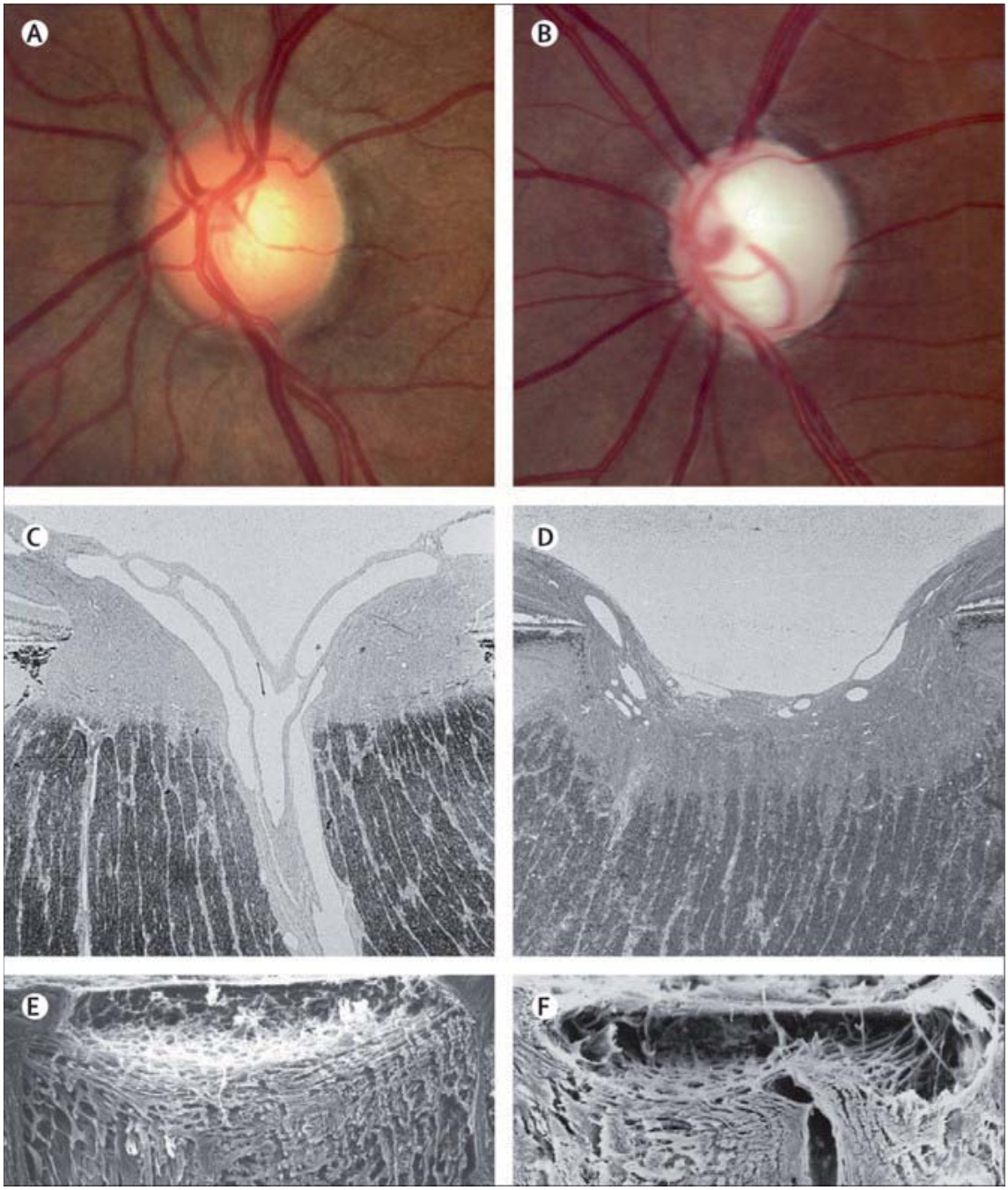

Fig. 1.8. Histopathological changes in Normal (A, C, E) and advanced glaucoma (B, D,F). In the glaucomatous nerve there is a posterior displacement of the lamina, accompanied by a loss of the overlying neural tissues and an increase in the size of the cup. In figures E and F, the connective tissues of the ONH following trypsin digest are compared between normal and glaucoma. A fixed deformation, with compression and deep excavation can be seen in the glaucomatous lamina (F). Adapted from Quigley, 2011.

Researchers within the Devers Eye Institute, where the experimental work for this PhD was undertaken, have pioneered a technique for digitally reconstruction ONH histological sections in Three-Dimensions (3D Digital Histomorphometry). Using this technique that allows 3D visualization and mapping of ONH connective tissues, connective tissue alterations in the earliest stages of a monkey model of experimental glaucoma (EG) have been identified (Burgoyne et al, 2004; Downs et al, 2007; Yang et al, 2007a; Yang et al 2009a; Yang et al, 2007b; Yang et al, 2011a). Using these 3D Histomorphometrical techniques, after moderate chronic IOP elevations in this model, posterior laminar deformation and neural canal expansion was found to be the underlying histopathological mechanism behind what is perceived clinically as "cupping" (see figure 1.9).

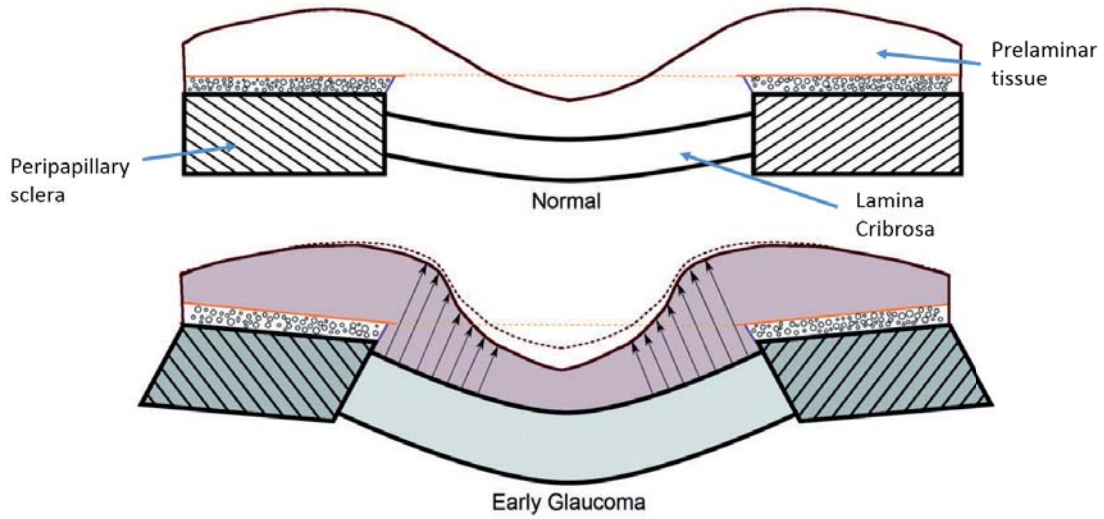

Fig. 1.9. ONH changes seen in Early Experimental glaucoma in a monkey eye, as shown by 3D histomorphometric reconstruction. Changes include expansion of the scleral canal opening, posterior displacement and thickening of the lamina cribrosa and thickening of the preliminar tissue and LC. Adapted from (Yang et al, 1997a).

These changes were more prominent within the superotemporal and/or inferonasal quadrants and was accompanied by laminar thickening of the prelaminar tissue, suggesting that early-onset cupping is due to laminar and not pre-laminar changes (Yang et al, 2007a; Yang et al, 2007b). Interestingly, there is some evidence to indicate that the laminar beams become thicker and there is effective recruitment on retrolaminar septae into the load bearing (Roberts et al, 2009). However, as glaucomatous damage progresses with continued exposure to a biomechanically driven insult, the prelaminar tissues begin to thin (Yang, Downs et al,

2007). In most cases, glaucomatous cupping is a combination of these two components (prelaminar and laminar cupping), reflecting both damage to and remodeling of the laminar connective tissues and progressive loss of RGC axons (Downs, Roberts and Sigal, 2011).

Separate from this, the lamina appears to effectively migrate beyond its scleral insertion (outward migration) and into the pia in more severely affected eyes, with complete "pialization" in some of them (Yang et al, 2011b)

1.2.5. Pathogenesis of Glaucoma

The exact site of injury in glaucomatous damage is not completely known, and pathophysiological changes have found to occur within the RCG body (Asai et al, 1987; Garcia-Valenzuela et al, 1995; Quigley et al, 1995; Weber et al, 1998; Quigley et al, 2000; Quigley et al, 1995), photoreceptors (Wygnanski T et al, 1995; Panda et al, 1992; Kendell et al, 1995; Nork et al 2000; Janssen P et al, 1996), lateral geniculate body (Yucel et al, 2000; Yucel et al, 2001; Yucel et al, 20033) and visual cortex (Yucel et al 2003) However, there is strong evidence to suggest that the central pathophysiology is damage to the RGC axons at the lamina cribrosa (Bellezza et al, 2003; Burgoyne et al, 2004. Gaasterland et al, 1978; Minckler et al, 1977; Quigley et al, 1981; Quigley and Green, 1979).

There are a number of observations that support the hypothesis that the changes driving RGC death are IOP-mediated and take place at the level of the lamina cribrosa. Axonal transport is known to be compromised at the level of the lamina in eyes with acute and chronic elevation of IOP (Quigley and Anderson, 1976; Quigley and Anderson, 1977). Various damaging effects with anterograde and retrograde blocking of axonal transport lead to axonal injury of the ONH (Anderson and Hendrickson, 1974). Responses mediated by this axonal injury likely transmit to the ganglion cell body in the retina and to the brain, explaining the observed changes in distal areas to the ONH as RGCs depend on neurotrophic support provided by the target neurons in the brain and the retinal interactions (Quigley, 2011). If survival mechanisms do not succeed, then apoptosis is triggered with early axonal loss by Wallerian degeneration followed by somal death after an abortive attempt at regeneration (Buckingham et al, 2008). Secondary degeneration of RGCs may be the result of a toxic environment after

primary apoptosis, in which excitotoxicity (glutamate-mediated) (Hare et al, 2001), free radical generation (Ko et al, 2000) and immune responses (Bakalash et al, 2005) play an important role. Glia cells that support the RGCs and their axons are also important in both protecting and damaging the RGC axons and its soma.

A number of studies support the fact that vascular factors play a significant role in the development of GON. The vascular theory of glaucomatous ONH damage proposes that there is either a primary insufficiency in the blood supply to the ONH, or that vascular compromise is an early component of IOP-related alteration to the ONH tissues. Vascular insufficiency produces a reduction of nutrient delivery to the RGC axons which is presumed to be mediated by the ONH astrocytes. This is thought to be more important within Normal Tension Glaucoma (NTG), in which there is a clinically observed association between nocturnal "dipping" of arterial blood pressure and disease progression (Graham and Drance, 1999; Graham et al, 1995; Hayreh et al, 1999; Hayreh et al 1994) and vascular dysregulation/vasospasm that cause damage to the ONH through reperfusion injury (Flammer et al, 2001). Further evidence is provided by several other works that have found a relationship between reduced ocular blood flow (measured in an indirect way) and glaucoma (Fontana et al, 1998; Hitchings and Spaeth 1977; Kerr et al, 2003; Michelson et al, 1996; Nicolela et al, 1996b).

Most likely, this theoretical distinction between mechanical (IOP-related) and vascular pathophysiologies is artificial. The biomechanical theory (discussed in more detail in next section) hypothesizes that glaucoma damage is a consequence of the IOP mechanical action on the tissues of the eye, producing deformations, strain and stress within the tissues that could directly induce alterationsin the connective tissues or indirectly alter blood flow and delivery of nutrients in the laminar regions (Burgoyne 2005; Burgoyne 2011; Burgoyne 2008; Downs, Roberts and Sigal, 2011).

1.2.6. ONH Biomechanics

1.2.6.1. Basic Engineering concepts

Biomechanics refers to the application of mechanical principles to biological systems. The ONH is of particular interest from a biomechanical perspective as it represents a relative weak point in the otherwise strong corneoscleral coat of the globe. Further more, the ONH (in particular LC) has been assumed to be the principal site on damage to RGC axons in glaucoma (Anderson and Hendrickson, 1974; Quigley et al 1981) and IOP, essentially a mechanical entity, is the primary risk factor for the development of the glaucomatous neuropathy. Given these observations, it is reasonable to suggest that biomechanics of the ONH may play a role in the development of glaucoma. Before discussing the biomechanical theory of glaucoma (1.2.6.2), the engineering terminology and basic principles used in biomechanics will be explained.

Engineering *stress* is a measure of the load applied to, transmited through, or carried by a tissue or material (Downs et al, 2008; Sigal and Ethier, 2009). It can be defined as the amount of force applied to a tissue divide by the cross-sectional area over which it acts. Stresses can be compressive, tensile (pulling) or shearing (forces in tangentially opposite directions). When used in a biomechanical context with a mathemactical description of mechanical load, engineering stress is distinct from "physiologic" which a typically describes cellular responses to alterations in their environment (i.e. ischemic or oxidative stress)

Strain is a measure of local deformation induced by stress (Downs et al, 2008; Sigal and Ethier, 2009). It is usually expressed as the percentage of change in the length of the original shape. As with stress, it can comprise normal (compressive or tensile) and shear (distortional) components. It is important to recognize that strain, unlike stress, may be observed and measured. It is also important to appreciate that strain is a measure of local tissue deformation. It is related to overall tissue deformation, but it is concerned only with quantifying local deformation of the environment which cells experience. It is therefore possible for a tissue to displace substantially and contain regions with little local deformation (and consequently contain regions of low strain). It is therefore also possible for a tissue to demonstrate minimal overall

deformation yet experience large local strains. . Hence, strain is a measurable indicator of the level of micro-deformation experienced by a tissue and this is important in biomechanics as it is strain, not stress, that damages tissues that cells respond to via mechanoreceptors embedded within their cytoarchitecture and outer membranes (Sigal et al, 2007).

Stress and strain in a tissue are therefore different things and they should not be interchanged. They are however, related to each other thorugh the material properties of the tissue in question (Downs et al, 2008; Sigal and Ethier 2009). Material properties may be classified according to the naure of the relationship between load and deformation (linear or non-linear), the time-dependent response to loading (elastic or viscoelastic) and the level of material symmetry (isotropy or anisotropy)

In linear materials, the stress is directly proportional to the strain by a constant (Young's modulus). In non-linear materials, there is a variable relationship between stress and strain and therefore the absence of single Young's modulus. *Viscoelastic* materials exhibit higher resistance when loaded quickly; by contrast the stiffness of *elastic* materials is not dependent on the rate of load application. *Isotropic* materials exhibit identical resistance to loading in all directions, whereas *anisotropic* materials vary in stiffness in different directions. *Structural stiffness* is a concept that incorporates both material properties and geometry of a load-bearing structure to create a combined measure of structure's resistance to deformation.

In the ONH, the geometry and material properties of the sclera and lamina cribrosa contribute to the stiffness of the ONH, thereby determining its ability to endure strain when exposed to IOP (Downs et al, 2008; Sigal and Ethier 2009). The biomechanics of an individual ONH will therefore be determined by the tissue geometry (including features such as scleral canal size and shape, scleral thickness, laminar beam density and orientation) and the material properties (stiffnesses) of the lamina cribrosa and sclera. Using these definitions, the simplest d material property would be that of an isotropic, linearly elastic material, such as steel. Unfortunately, this is not applicable whn trying to explain and measure the biomechanics of the ONH. Biological tissues such as sclera and lamina are usually non-linear, anisotropic and have viscoelastic properties. Consequently, measuring the material properties of the ONH is very challenging. However, once experimental characterization of the material properties is ac-

complished, they can be used together with descriptions of the tridimensional geometry of the structure (lamina cribrosa) and loading conditions (IOP) to model the stress and strain fields experienced by the ONH.

When a tissue is strained beyond its elastic limit, *mechanical yield* will occur and it will be unable to return to its undeformed shape (Downs et al, 2008; Sigal and Ethier 2009). A material or tissue that has "yielded" in response to high strains is permanently damaged and deformed and is usually less resistant to further loading (hypercompliance). *Mechanical failure* occurs at even higher strain, typically follows yield, and generally manifests in soft tissues as catastrophic rupture or pulling apart. In any ONH, there will likely be an IOP that induces yield in laminar beams but no visible failure; at higher IOPs it is possible that failure may occur in some individual beams, while a new population of beams may now demonstrate yield. Yield and failure in the ONH likely induce a chronic cellular remodeling response that results in restructuring the ONH, altering its future load-bearing capacity. Early connective tissue damage leads to astrocyte remodeling which may make the remaining connective tissues more susceptible to future damage at all leves of IOP (Hernadez, 2000; Hernandez et al, 1990; Morrison, 2006; Quigley et al, 1991a; Quigley et al, 1991b). This concept is key to understanding how chronic IOP elevation leads to glaucoma and also how ageing changes may predispose to GON.

1.2.6.2. The Biomechanical Theory of Glaucoma

The biomechanical thery of glaucoma proposes that ONH biomechanics may explain how IOP-induced stress and strain (a measure of tissue deformation) of the load bearing tissues of the ONH (sclera and lamina cribrosa) influence their physiology and pathophysiology, and of the adjunctive tissues (astrocytes, glia, endothelial cells, vascular pericytes and their basement membranes) and the RGC axons (Burgoyne et al, 2005; Burgoyne and Morrison, 2001; Strouthidis and Girard; 2013). ONH biomechanics is the "link" by which IOP can influence such apparently non-IOP factors such as ischemia, inflammation autoimmunity, astrocytic and glial cell biology (Burgoyne, 2011; Strouthidis and Girard, 2013). The interplay between IOP, biomechanics and RGC loss is outlined in fig. 1.10. The interaction of these factors with laminar and peripapillary scleral connective tissue geometry and material proper-

ties may be used to explain the physiology of ageing in normal ONH, the susceptibility of the ONH to IOP and the clinical appearance of GON at any level of IOP (Burgoyne et al, 2005).

The likely factors that will influence and individual ONH's will include the magnitude of IOP and the geometry and material properties of the ONH and peripapillary scleral tissues. Furthermore the volume flow and perfusion pressure of blood within the laminar capillaries will influence the diffusion of nutrients to astrocytes. The way astrocytes and glia respond either to strain and/or changes in localized nutrient diffusion (the 2 being linked within the biomechanical paradigm) will also play a role. Finally, there may be other features within the RGC itself that may lead to an increased susceptibility to apoptosis in response to localized distress (Burgoyne and Downs, 2008).

From an engineering point of view, they eye may be considered a vessel with inflow and outflow facilities that regulate IOP. In normal conditions, IOP exerts normal load to the surface of the wall of the eye, generating an in-wall circumferential stress known as "hoop stress" that is primarily undertaken by the relatively stiff sclera. The stress of IOP at the level of ONH is taken by the connective tissues of the lamina cribrosa and is this this in-wall hoop stress transferred form the peripapillary sclera that leads laminar biomechanics.

This hoop stress has been measured to be up to 15 times greater than the stress generated by the translaminar pressure gradient (differential between the compressive force of the IOP and the inverse force of the retrolaminar cerebrospinal fluid pressure) (Bellezza et al, 2000). Our ability to study ONH biomechanics is complicated by a number of factors. First, the 3D geometry of the connective tissues is very intricate and difficult to measure, with the thickness of the monkey sclera varying up to four times from the equator to the peripapillary region (Downs et al, 2002; Downs et al, 2001) and the microarchitecture of the lamina being highly complex and individual. Secondly, the cornea, sclera, and lamina cribrosa have extremely complex extracellular matrix microstructures with highly anisotropic (fiber orientation of the tissue has a principal direction) collagen and elastin fibrin orientations. As a result, the experimental characterization and theoretical description of their material properties are difficult to obtain. Thirdly, the cells that maintain the ocular connective tissues are biologically active. As such, the geometry and material properties of the sclera and lamnina cribrosa change in re-

sponse to both physiologic (age) and pathologic (IOP-related damage) factors. Fourthly, the eye is exposed to ever changing loading conditions because IOP undergoes acute, short-term and long-term fluctuations ranging from blinks and eye rubs to circadian rhythms.

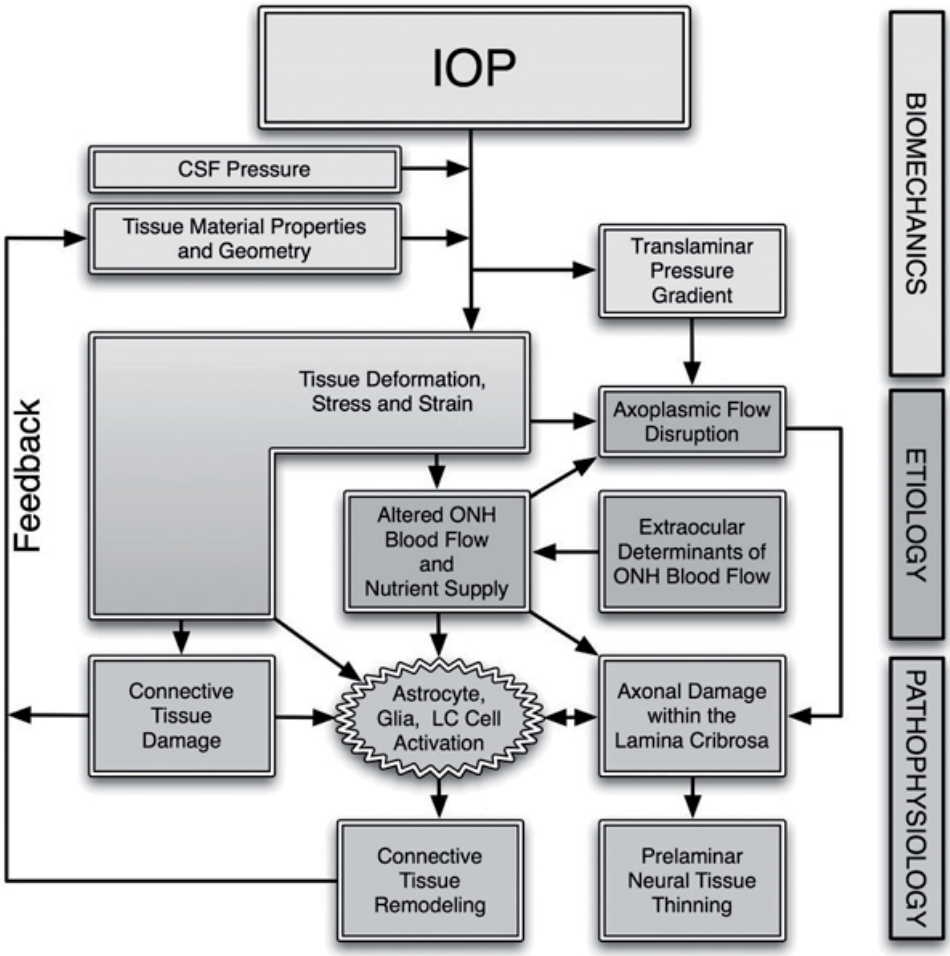

Fig. 1.10. The Biomechanical paradigm of Glaucoma. IOP acts mechanically on the ocular tissues, producing deformations strain and stress. Local tissue deformations dependo n the geometry and material properties of an individual eye. In a biomechanical paradigm, stress and strain alters the blood flow (primarily), and the delivery of nutrients (secondarily) through remodeling-driven alterations in connective tissue stiffness and diffusion properties. IOP-related stress and strain also cause connective tissue damage directly, or indirectly through celular mechanisms, which induces connective tissue remodeling that alters the ONH's responses to loading via feedback mechanism. These effects are pertinent at all tiime sclales, and combine to cause axonal damage in the laminar región. Reproduced from Downs, Roberts and Sigal, 2011.

Finally, IOP-related stress generates strain patterns in the ONH and peripapillary sclera that are not only dependent on differing connective tissue geometries and material properties but also are influenced by complex loading conditions (Downs et al, 2008; Sigal and Ethier 2009). The important factors contributing to this biomechanical component include the alignment and density of collagen fibrils in each tissue (stiffness and anisotropy), the rate of change in IOP (via tissue viscoelasticity), and the level of IOP-related strain and the time of altered loading (via tissue nonlinearity). In broad terms, the ONH connective tissues should be stiffer when there is already considerable strain present and/or if the load is applied quickly. Conversely, the ONH should be more compliant in response to slow changes in IOP and/or at low levels of strain.

1.3- Rodent Models of Glaucoma

1.3.1.General Aspects of Animal Models

As we have seen in previous sections of this dissertation, the precise mechanisms by which ocular hypertension induces glaucomatous optic nerve and retinal damge are not completely understood. Because we currently lack non-invasive methods for assaying cellular function in humans, it is not yet possible to study these possibilities directly in human glaucoma. Therefore, relevant animal models will remain essential to better understand the mechanisms involved in GON-induced RGC degeneration (Morrison, Johnson and Cepurna, 2008).

Most animal models of glaucoma use experimental elevation of IOP. Although IOP is only one of several known glaucoma risk factors (as we have seen in section 1.2), large multicentric clinical trials have demonstrated that aggressive IOP lowering is beneficial in a wide spectrum of open angle glaucomas, including normal-tension glaucoma, ocular hypertension, and early and late glaucoma (Drance, 1999; Kass et al, 2003; Leske et al, 2003). From this, it is reasonable to expect that models based on elevated IOP will be highly relevant to ON damage in open-angle glaucoma.

Experimental models of pressure-induced ON damage have some advantages over spontaneous models, First, unilateral pressure elevation leaves the fellow eye available as a control against the effects of inter-animal variability. Second, the more predictable onset of the pressure elevation makes it possible to determine sequential events of the optic nerve and retina damage (Morrison, Johnson and Cepurna, 2008).

Anatomically, non-human primates should be the most relevant experimental glaucoma model, due to their closer anatomy to human. However, these animals are are expensive and at present cannot be easily genetically manipulated, making them impractical for studies that require large animal numbers.

For these and other reasons mouse and rat (Dai et al, 2012; Howell et al, 2007; Johnson and Tomarev, 2010; Mabuchi et al, 2003; 2004; May, 2008; Morrison et al, 2011; 2008; Pang and Clarck, 2007; Ruiz-Ederra and Verkman, 2006; Vidal-Sanz M, 2011) experimental glaucoma models are increasingly utilized to study the mechanisms of chronic intraocular pressure-induced ONH and RGC axon injury. A large body of knowledge on cell biology of neuropathology based on rats already exists, thus providing a collection of tools for studying pressure-induced optic nerve damage when produced in these animals (Morrison, Johnson, Cepurna; 2008).

This section will discuss the current status of rat models (Morrison, Cepurna and Johnson, 2015; Morgan and Tribble, 2015 and Pang, Millar and Clark, 2015), including a comparison of the major methods for measuring IOP in rats as well as strategies for assessing damage.

1.3.2. Anatomy of the rodent ONH

1.3.2.1. Normal rat ONH

The anatomy of the rodent ONH is widely recognized to differ from the human and non-human primate (Dai et al, 2012; Morrison et al, 2011; Sugiyama et al. 1999b). Post-mortem histologic measurements in fixed and processed tissues suggest that the rat eye is approximately 6.29 mm in axial length and 6.41 mm in diameter, with a posterior sclera that is about 5 to 10 times thinner and a circular scleral canal that is about 4 times smaller than the human eye. Normal rat optic nerve axons counts range from 0.11 to 0.14 million axons compared to 1.2 to 2.0 milliion in the human eye and from 0.9 to 1.4 million in monkeys.

Viewed from within the eye, the rat ONH is dominated by spoke-like retinal arteries and veins that obscure the rat optic disc (Fig.1.11A) (Morrison et al, 2015). These vessels actually enter the posterior sclera just inferior to the neural portion of the ONH. This is a fundamental difference from the primate ON, in which the retinal vessels are already within the nerve when they enter the eye. Histologically, in cross-section, the optic nerve of the rat is oval at the level of BM and sclera, with its short axis oriented vertically (Fig.1.11B). This means that, in longitudinally-prepared anterior to posterior cuts when looking at one single section, differences in orientation will provide very different appearances (Morrison et al, 2015). A horizontal section (Fig.1.11C) will show the neural tissue adjacent to BM and the sclera at either edge (simillary to what is usually seen in the primate), however a vertical section (fig. 1.11D) will show a much different appearance with a narrower neural tissue at the level of the sclera (short axis of the oval) and only superior contact of the nerve with the BM, as the retinal artery and vein, along with other vessels lie inferior, separating the ON from the sclera and the BM (Morrison et al, 20015). All previous charactherizations of the rat ONH have been based upon this traditional histologic sections or 2D photos of 3D vascular casts. These studies have therefore lacked the ability to digitally sample and visualize the same reconstruction from multiple viewpoints at the same time so as to confront, understand and characterize its principal organizing relationships. These broad aspirations have driven much of the research undertaken for this PhD.

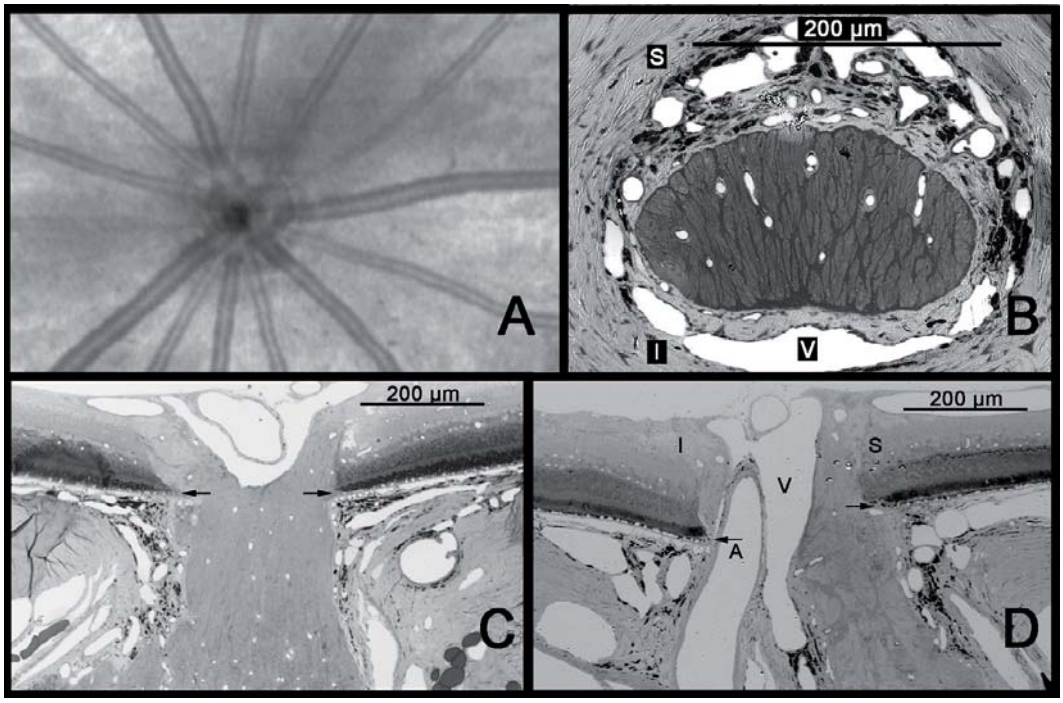

Fig. 1.11 Anatomy of the rat ONH. A. An anterior view of the rat fundus as seen by Scanning Laser Ophthalmoscopy (CSLO). The rat ONH is obscured by the retinal arteries and veins. B. Cross-sectional view of the ONH at the level of the sclera. Th enerve is horizontally oval and densely surrounded by vessels, including the CRV (V), which runs inferior to the nerve. C. Horizontal longitudinal section shows the ON contecting the BMO at either extreme. D. A vertical longitudinal section shows thatt only the superior aspect of the nerve is in contact with the edge of Bruch's membrane, while inferiorly, the ONH is separated from BM by the CRA as well as the CRV. Arrows=BM; S=Superior; I=Infeiror; A: CRA; V=CRV (Adapted from Morrison et al, 2015)

Reported differences in normal rat ONH anatomy include a lack of a robust collagenous lamina cribrosa (Morrison et al, 1995a-b), a cellular lamina-like structrure with a basket-like distribution formed by sparse connective tissue associated with blod vessels lined with astrocytes (Dai et al, 2012; Li et al, 2015). Due to the similarity in their orientation to the collagenous lamina this has been referred to, in both mice and rats, as a "glial lamina" (Sun et al, 2009). In the rat lamina, the astrocytes are oriented, as in the primate, across the scleral canal and perpendicular to the axon bundles (Johnson et al, 2000; Tehrani et al, 2014). Its connective tissue is composed of extracellular matrix materials which are themselves similar in composition to those within the primate lamina cribrosa (Fujita et al, 2000; Johansson, 1987; Morrison et al, 1995a, 2001). Astrocytes in the rat ONH are in intimate contact with blood vessels and pial membranes of the ONH with their nuclei arranged in columns, similar to those in the anterior portions of the primate ONH (Anderson, 1969b; 1970). Their processes also appear to surround axon bundles, and send numerous, actin-filled processes into the nerve

bundles themselves (Morrison, 2005; Morrison et al, 2011; Tehrnai et al, 2014). These considerations indicate that, despite the lack of a collagenous connective tissue component, the glial lamina cribrosa of the rat contains many relationships that will allow us to understand how the cell biology of the ONH responds to increases in IOP and affects axonal damage in human glaucoma (Morrison et al, 2015).

1.3.2.2. Rat ONH blood supply

Regarding the ocular blood supply of the rat, it is primarily from the ophthalmic artery, which typically splits posterior to ghe globe into the CRA and three LPCAs (Morrison et al, 1999; Sugiyama et al, 1999). The CRA then enters the globe inferior to the passageway for the optic nerve, from which it supplies capillary beds of the RNFL and anterior portion of ONH. Capillaries in more posterior portions of the ONH arise from arterioles emanating from the proximal portions of encircling branches of thet LPCAs, and are continuous with those of the anterior ONH and retrobulbar optic nerve. All of these capillary beds drain into either the CRV, which lies inferiorly, between the nerve and the CRA, or veins that reside within the optic nerve sheath.

Another feature of the vascular distribution of the rat ONH is a perineural vascular plexus that surrounds the optic nerve within the scleral canal (Morrison et al, 1999; Sugiyama et al, 1999), which is not present in the primate ONH.

1.3.2.3. Anatomy of the rat aqueous humour ouflow

Most experimental models of induced IOP elevation rely on producing increased resistance to aqueous humor ouflouw. In the rat, as in the primate, conventional outflow occurs through the trabecular meshwork, into Schlemm's canal, and through the limabal sclera via collector channels to the episcleral venous circulation (Morrison et al, 1995a, 1995b). This episcleal plexus as well as Schlemm's canal, is continuous, and can be accessed by retrograde injection into the radially-oriented episcleral veins that drain this plexus (fig. 1.12). This anatomy is important for the hypertonic saline injection model of experimental glaucoma model which was used the work presented in this PhD thesis.

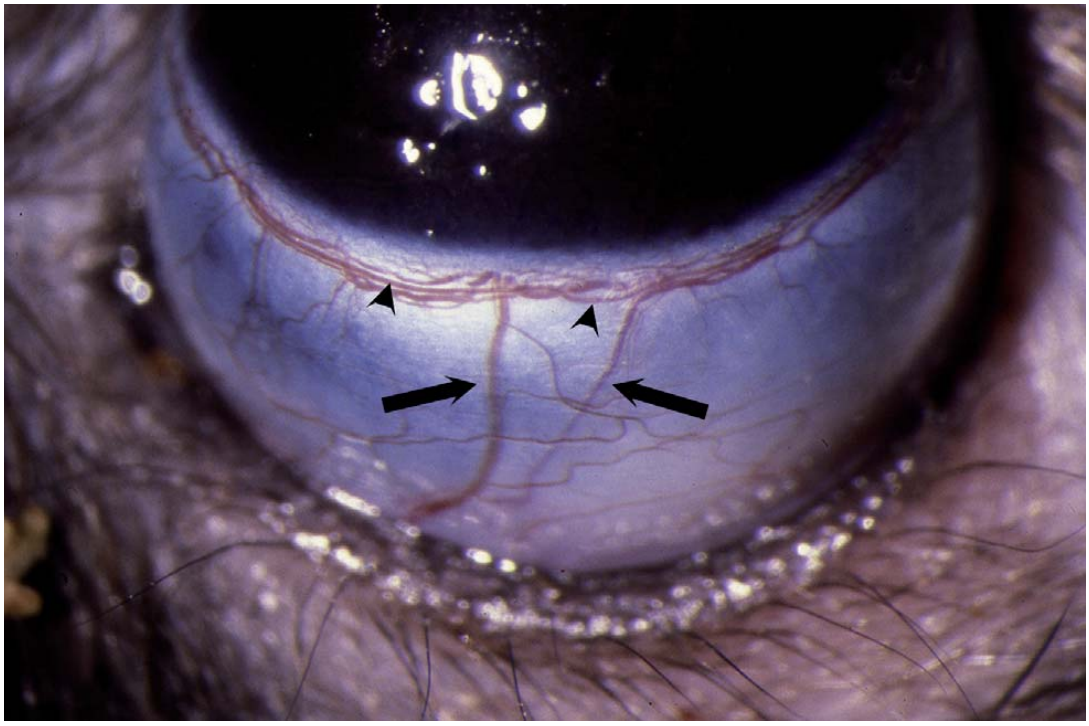

Fig. 1.12. External view of the rat limbus from the perspective of the operator. Note the radial episcleral veins (arrows) that drain in the limbal plexus, one of which would be injected with hypertonic saline. Limbal artery (arrowheads) within the plexus can be differentiated from veins as it is relatively straight, and does not branch. Reproduced from Morrison et al, 2015.

1.3.3. Suitability of the rat for models of optic nerve damage in glaucoma

The suitatbility of rodent models is based upon several lines of reasoning.

First, a series of previous reports have determined that early (if not the earliest) damage to the RGC axons occurs within the ONH tissues in all induced and spontaneous forms of rodent (Morrison 2005; Morrison et al, 2011; Morrison et al, 2008; Morrison et al, 1997; Morrison et al, 1998, Schlamp et al, 2006) chronic IOP elevation.

Second, to a certain degree, and as we have seen in a previous section, the rodent ONH demonstrates charactheristics that are analogues to the primate ONH (Morrison et al, 2011). These include: A) similar ultrastructural relationships between astrocytes and axons (Morrison et al, 1995; Morrison et al, 1997). Ultrastructurally, rat ONH processes lie within axonal bundles, providing intimate contact with all axons, a situation that also exists in the

primate (Morrison et al, 2005). B) Similar cellular changes (Hernandez et al 1990; 2000; Johnson et al 1996; Morrison et al, 1990), that include disorganization of the normal columnar structure of astrocytes and aberrant deposition of collagen and laminin within spaces normally occupied by axon bundles; C) Neural canal expansion (Chauhan et al, 2002; Guo et al, 2005); D) And posterior deformation of the ONH surface in response to chronic IOP elevation (Chauhan et al, 2002); The most useful feature that the rat eye offers for POAG research lies in the close association between astrocytes and axons within the ONH (Morrison, Johnson and Cepurna, 2008. This provides a potential link by which IOP-generated forces in the load-bearing tissues of the ONH can get translated into axonal damage (see the section 1.2.6.2. of this thesis for the Biomechanical Theory of Glaucoma). In this way, the rat eye presents an opportunity to understand the specific cellular mehcanisms leading to glaucomatous optic nerve damage. Likewise, chronic models of IOP elevation in rats have also demonstrated a predilection for early superior optic nerve injury (Dai et al, 2012; Huang and Knighton, 2009; Li et al, 2015; Morrison, 2005; Morrison et al, 1997; WoldeMussie et al, 2001) (Morrison JC et al. IOVS 2002; ARVO E-abstract #2885). Understanding this regional susceptibility in rats may provide insight intro mechanisms of regional susceptibility in humans.

Third, the anatomy of the rodent ONH is also very different from the human and non-human primate (Morrison et al, 2011; Morrison et al, 2015). Understanding these differences and recognizing how they contribute to species-related differences in age-related RGC loss (Cepurna et al, 2005) and age-related differences in the susceptibility of axon transport to acute (Kong et al, 2009) and chronic IOP elevation (Morrison et al, 1997) (Morrison JC et al. IOVS 2007; 48:ARVO E-Abstract #3662; Johnson EC et al. IOVS 2008; 49:ARVO E-Abstract #4059) should provide important knowledge about these same phenomena in human eyes.

1.3.4. Rat Animal models for studying glaucoma

Animal models developed for studying the cellular events of GON can be broadly separated in those that are independent of IOP and those that rely on IOP elevation. The latter all rely on elevation of IOP to reproduce a major risk factor for glaucoma, and its effects on the visual system. These will be briefly presented in the next subsection. The former are gener-

ally based on specific hypotheses of the mechanism of glaucomatous RGC death. These methods are beyond the scope of this dissertation and briefly include transient retinal ischemia (selective ligature of the ophahlmic vessels) (Naskar, 2002), endothelin (Chauhan, 2004; Murphy 2010; Prasanna, 2011) or immune system alteration (Wax et al, 2008; Joachim SC et al, 2013) (…), among others.

1.3.4.1 "Pressure-Dependent" Models

Elevated IOP is a weidely recognized and well-documented glaucoma risk factor (Sommer 1989; Klein et al, 1992). As we have seen in previous section 1.2.2 (Glaucoma risk factors), several large multicentric trials have demonstrated that reducing IOP has a beneficial effect in the progression of GON (Drance 1999; AGIS-Investigators, 2000; Hijl e tal, 2002; Kass et al, 2002) without regard for the level of IOP at which the neuropathy has occurred. Therefore, models of elevated IOP should provide useful insights into evaluating glaucomatous damage.

Rodent models of elevated IOP can either be spontaneously or produced experimentally. Spontaneus models of high IOP in mice have the advantage of causing a progressive, moderate IOP rise, similar to what occurs in POAG. These models, when combined with mouse genetics to manipulate specific cellular pathways, represent a powerful tool for understanding the importance of specific pathways in the production of ON damage. The problem of these models is that IOP is generally bilateral, and since it is not possible to perform continuous IOP monitoring, the exact level and duration of IOP elevation is unkwown (Morrison et al, 2011). One of these models is the DBA/2J mouse line (John et al, 1998; Schlamp et al 2006).

Other IOP-dependent rodent models rely on experimental production of elevated IOP. With this approach, the experimenter knows when the IOP induced insult is applied, making it easer to determin the timing of the cellular responses to high IOP (Morrison et al, 2011). In adition, since IOP increase is unilateral, the fellow eye can be used as an internal control. However, the exact onset of pressure elevation may still be uncertain, and the level of IOP obtained can be hard to control.

The most important rodent models of experimental glaucoma (EG) are those that obstruct aqueous humor outflow. In rats, this can be done by retrograde injections of hypertonic saline into the aqueous humor outflow pathways via episcleral veins (Morrison 1997) or using external laser to the anterior chamber angle (Ueda et al, 1998; WoldeMussie et al, 2001; Levkovitch-Verbin et al, 2002). Although these two approaches have their individual strengths and weaknesses, both result in a combination of trabecular meshwork scarring and anterior chamber angle closure, and produce a similar extent and pattern of ON damage (Morrison et al, 2005). Other methods of elevating IOP obstructing aqueous outflow include intracameral injections of foreign substances, including hyaluronic acid and latex microspheres (Urcola et al, 2006; Sappington et al, 2009).

1.3.4.2. Hypertonic saline injection method for modeling glaucoma in rats

Since this is the model used in the experiments that are included in this PhD, we will explain this method in some detail.

The animals typically used for this model are adult (6-8 months, 300-400g) Brown Norway rat, which are generally docile, requiring, in general, only a brief period of handling in ordering to obtain reliable awake IOPs (see next section 1.3.5, methods for measuring IOP in rats for more details) (Morrison et al, 2015). The basic challenge of this model is to gain access to one of the radial episcleral veins and confine the injection to the limbus. The instruments required for this procedure are listed in table 1.2. and pictured in figure 1.13.

The surgical procedure is as follows (Morrison et al, 20015): Animals are anasthetized with an intraperitoneal injection of anesthetic cocktail (ketamine, xylazine and acepromazine) and positioned under an operating microscope with the target vessel pointing toward the limbus, away from the operator. Because each eeye has several radial episcleral veins draining the limbal venous plexus, hypertonic saline simply injected into one vein is likely to exit an adjacent vein, and not enter the entire limbal plexus, Schlemm's canal or trabecular meshwork. To prevent this, a plastic ring is fited around the equtor of the eye to temporarily block flow in all of the episcldral venous veins, except the one being injected. After completely dissecting the conjunctiva, the microneedle is brought up to the vessel with the bevel up, and

while grasping only the vessel with the jewelers forceps, the needle is carefully inserted into the vessel just anterior to the forceps. Then, with the needle in place, an assistant can inject the hypertonic saline either manually ofr with the aid of a syringe pump. Following injection, the needle is removed and the vein occluded with the forceps for 30 seconds. After removal of the plastic ring the anterior chamber will remain deeper, with posterior concavity of the iris.

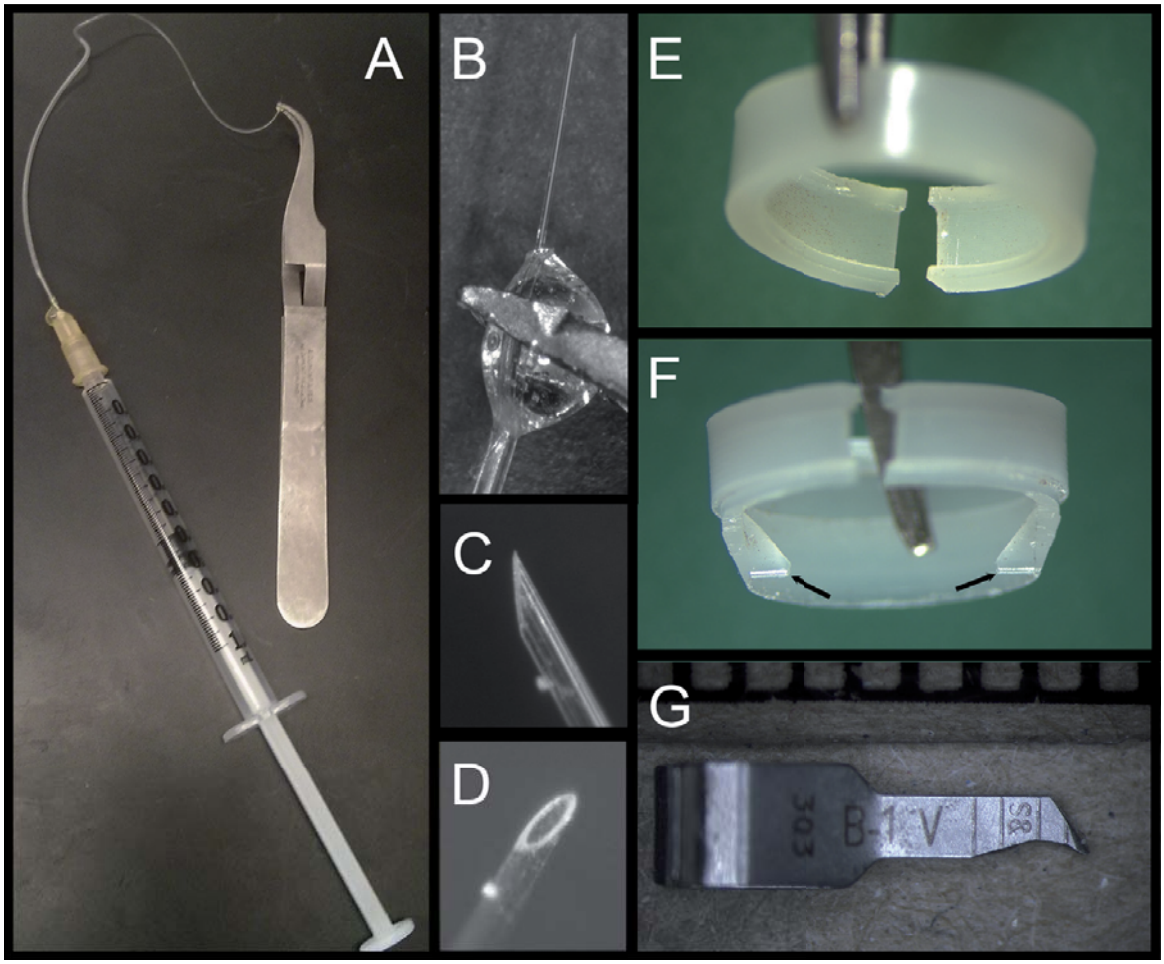

Figure 1.13. Specialized equipment for hypertonic saline injection. A)The entire microneedle assembly with self-locking forceps; B) Detailed view of tubing: microneedle junction held at the gluo joint by forceps, along with beveled needle tip (C and D). E. Standard plastic ring used to compress episcleral veins to confine injected saline to the limbus. F) Irregular ring cast to form internal projections (arrows) that apply focal pressure to constrict Schlemm's canal and lmit circumferencial flow of injected saline. G) Vascular microclip (viewed next to a millimeter scale), sharpened to constrict vessels not occlude d by the ring. Reproduced from Morrison JC et al, 2015.

Fine tip jeweler's fórceps Dumont #5SF Forceps Fine Science Tools 11252-00 (Foster City, CA)
Fine –tipped Vannas Capsulotomy Scissors Curved Storz E3387 Bausch&Lomb Surgical, Inc (Rancho Cucamonga, CA)
Microneedle with attached, tapered tubing
Dumont Self-Closing #7 Curved Forceps Fine Science Tools 11267-30 to hold microneedle
Hypertonic saline (1.5-2.0 M) filtered through a millipore filter into 1 cc siringe
Plastic Limbal ring
Fine vessel clamps, S&T Vascular Clamps Fine Science Tools 00396-01

Table 1.2. Instruments for hypertonic saline injection (Adapted from Morrison et al, 2015)

1.3.5. Methods for measuring IOP in rats

The use of rodent OHT models has been advanced by the availability of reliable devices to register IOP in these animals-the tonometers TonoPen (Tono-Pen® XL Reichert® Ophthalmic Instruments Depew, NY, USA) (Moore et al, 1993; 1996) and TonoLab (Tono-Lab®, Tiolat, OY, Helsinki, Finland) (for review see Morrison et al, 2005; 2009). The TonoPen tonometer (Moore et al, 1993; 1995; 1996) was the method of choice to measure IOP in adult rats fore many years. More recently the rebound tonometer, Tonolab (Kontiola, 2000; 2001; Danias et al, 2003) which was designed specifically for rodents (Wang WH et al, 2005; Pease et al, 2006) has become the preferred tool to measure IOP in adult rats (Jia et al, 200; Pease et al, 2006) and mice (Filippopoulos et al, 2006; Pease et al 2006).

In its initial evaluation (Moore et al, 1993; Fig.1.14) IOPs measured by the Ton-Pen in cannulated eyes connected to a pressure transducer correlated well with the actual IOP. However, due to its design it needs to be held exactly centered and perpendicular to the cornea to tobtain good readings, needing an experienced operator. On the other hand, TonoLab, designed for rodents is easier to use. However, they noted that readings with this instrument over time were more variable than with the Tono-Pen. In addition, their calibrations indicate that,

in Brown Norway rats, reading with the TonoLab tend to underestimate the actual IOP and flatten out below an actual IOP of 20 mmHg, suggesting that instrument readings below 10 mmHg will be difficult to interpret (fig. 1.14b). In rat eyes, with experimental glaucoma, they found that the TonoLab, unlike the Tono-Pen, was not able to detect significant pressure elevations in eyes with minimal optic nerve damage, most likely due to the greater variability of readings with this instrument (Jia et al, 2006).

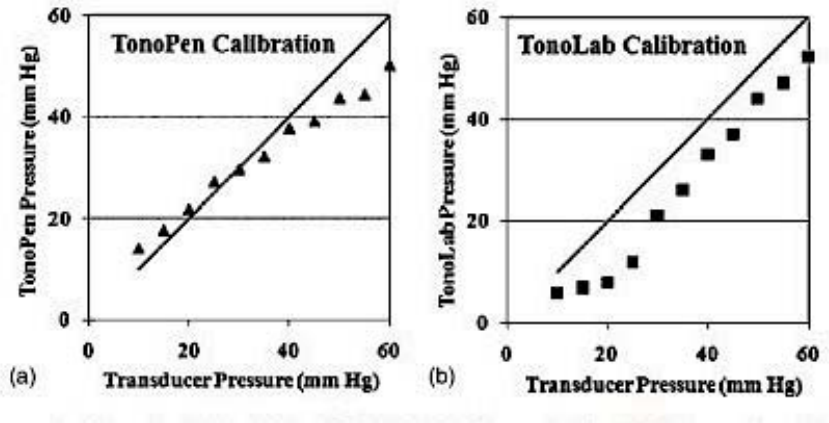

Fig. 1.14. Calibration curves for Tono-Pen (a) and Tono-Lab (b). Note the liniar relationship between Tono-Pen readings and actual transducer pressure. Tono-Lab pressure readings are consistently below transducer pressures, with flattening of this relationship below transducer pressure of 20 mmHg (adapted from Moore et al, 1993; Morrison, Johnson and Cepurna, 2008).

In the experiments performed for the purpose of this PhD (see section 2: Material and Methods), IOP was measured under topical anesthesia with the TonoPen tonometer.

1.3.5.1 General considerations for measuring IOP in rats

A reliable, unbiased method of measuring IOP is indispensable for working with any glaucoma model. Because IOP fluctuation is common in glaucoma and in animal glaucoma models, IOP measurements must be non-invasive and repeatable.

While it is possible to monitor IOP repeatedly under time using general anesthesia, daily IOP measurements can result in progressive weight loss and even in a reduction of IOP

(Moore et al, 1995; Jia et al, 2000). Because of these problems, it is recommended to use topical anesthesia and measure IOP in awake animals.

Obtaining an accurate IOP assessment also requires understanding of the normal, daily circadian fluctuations of IOP. When rats are housed in a standard 12-hours light: dark cycle IOP is significantly lower in the light phase and higher in the dark (Moore et al, 1996). When superimposed on experimental obstruction of aqueous outflow, this circadian fluctuation can become exaggerated. Over 30% of eyes with experimental IOP elevation develop a significant IOP elevation over the fellow control eyes only in the dark phase, all of which have significant optic nerve injury (Jia et al, 2000). Light and dark pressures in these conditions can be around 19-21 mmHg and 28-30 mmHg (Moore et al, 1996; Morrison et al, 2005; Pang et al, 2005). These results suggest that when experimental obstructed animals are housed in standard lighting conditions, IOP must be monitored in both the dark and light phases (Morrison, Johnson, Cepurna, 2008). This approach is inconvenient, since the resulting IOP fluctuations may make it difficult to correlate pressure history with optic nerve damage. For these reasons, it is important to minimize these underlying circadian IOP fluctuations. In Dr. Morrison's lab, where the experimental aqueous obstruction of the rats studied in this dissertation was performed, animals are kept in a low-level constant light environment. When animals are housed in constant fluorescent light conditions (40-90 lux), IOP in normal eyes will consistently measure between 27 and 28 mmHg by the Tono-Pen, regardless of the time of the day. This approach eliminates the IOP effects of circadian rhythm without altering the physiological IOP fluctuations. It has been shown to produce no evidence of neural or retinal damage in normal controls and provides close correlations between EG mean IOP measurements and different measures of injury, such as degree of optic nerve damage, RGC loss and measures of altered cellular function (Jia et al, 2000; Johnson et al, 2000; 2006; 2007; Schlamp et al, 2001; Ahmed et al, 2004; Fortune et al, 2004; Morrison et al, 2005; Pang et al, 2005).

1.3.6. Assessing ONH and retinal damage in the rat

Assessing damage in any glaucoma model can be done examining either the optic nerve or the retina.

1.3.6.1. Assessing Nerve damage

Nerve damage can be measured by evaluating a single cross section of the optic nerve, which contains the entire output of the RGCs. At the light microscopic (LM) level, standard staining of plastic-embedded sections readily allows identification of normal axons by staining the myelin sheaths. Semiatutomated image analysis methods can count and determine axon density within specific areas (Quigley et al, 1987).

Optic nerve counts can also be determined in cross-sections by transmission electron microscopy (TEM) (Chauhan et al, 2002; Cepurna et al, 2005). Here, tissue sections from experimental and control nerves are pictured randomly, and axon counts are performed manually (axons can be identified by their myelin sheaths and contained microtubules). These two methods do not provide identical results, and in some comparison studies, the LM method underestimates the axon counts in about 19-43% (Cepurna et al, 2005; Morrison et al, 2005).

Another way to assess optic nerve damage is to develop a qualitative LM grading scale for optic nerve degeneration (Jia et al, 2000). This avoids the potential flaws of LM axon counting noted above and is faster than the TEM method. This approach depends on recognizing axonal degeneration at the LM level by the appearance of swollen axons that lack apparent axoplasm and dark axons due to collapsed myelin sheaths. The extent of injury is then graded, based on a stereotypical pattern of injury that has been observed in rats with elevated IOP due to aqueous humor outflow obstruction (Table 1.2). In this system, each ON cross-section is assigned a grade, based on a 5-point scale, ranging from grade 1 (normal) to 5 (extensive damage- degeneration involving the entire cross-section).

Grade	Qualitative characteristics at LM
Grade 1	Normal
Grade 2	Focal Degeneration (generally superior)
Grade 3	Degeneration spreading beyond the focal region
Grade 4	Degeneration involving the entire cross-section of the nerve, with approximately equal numbers of apparently normal and degenerating axons
Grade 5	Apparent degeneration of nearly all axons

Table 1.3. Light Microscopy (LM) qualitative grading system for optic nerve damage due to elevated IOP secondary to aqueous humor outflow obstruction. Adapted from Jia et al, 2000; Morrison, Johnson and Cepurna, 2008)

To support the reliability of this grading system, a comparison to actual nerve counts by TEM in the same nerve reveals a linear relationship between the two methods, representing approximately 12,000 axons per grade (Morrison et al, 2005; Figure. 1.13)

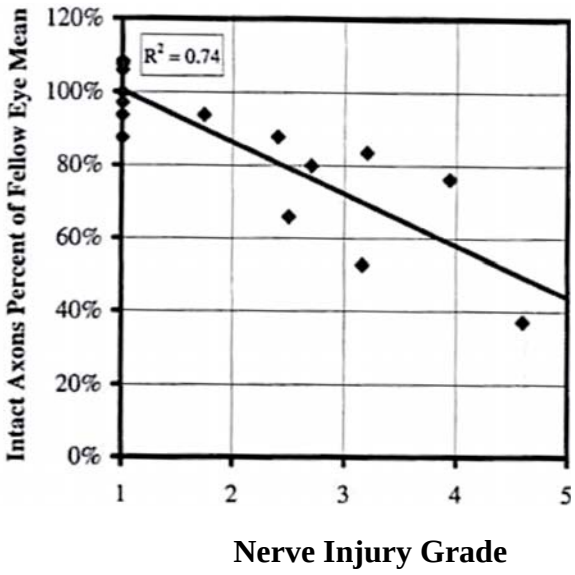

Fig. 1.15. Graph comparing damage from experimental and fellow eye optic nerves from 8 animals as determined by ultrastructural assessment of axon counts and a qualitative, light microscopic grading system. Axons counts (expressed as percent of the mean counts of normal fellow eyes) appear on the y-axis and mean optic nerve injury grade of 5 masked observers i son the x-axis. Linear correlation between the two methods was good (R^2=0.74) (Adapted from Morrison et al, 2005).

For the animals studied in this dissertation (see section 2: Material and Methods), glaucomatous damage to the optic nerve was assessed using the above qualitative damage grading scale (Jia et al, 2000).

1.3.6.2. Assessing Retinal Damage

Other investigators evaluate damage by documenting loss of RGCs. A detained description of these retinal techniques is beyond the scope of this thesis. Briefly, this usually involves placing a tracer, such as fluorogold, into the superior colliculus of the severed optic nerve. The tracer, which is then transported by retrograde axoplasmic flow, will accumulate in RGCs, which can then be counted, usually in flat mount preparations. Generally, these counts are performed systematically in representative regions of the retina and RGC losses determined as a reduction of of RGC density or by calculating total RGCs based on the total retinal area (Morrison, Johnson and Cepurna, 2008).

Because this technique relies on axonal transport, it allows the examiner to assess viable cells, although it depends on uniform uptake of the tracer by axons, which may not always happen and can result in an underestimate of actual RGC count. Also, the fact that the technique relies on sampling of different regions of the retina increases the change that regional injury may not be adequately or reproducibly detected (Morrison, Johnson and Cepurna, 2008).

2

Materials and Methods

2.1. Animals and Eyes

All animals were treated in accordance with the ARVO Statement for the Use of Animals in Ophthalmic and Vision Research. Both the Control and EG eyes of 8 adult male brown Norway rats, between 9.5 and 10.5 months of age, were studied (Table 2.1).

2.1.1.- Induction of chronic unilateral experimental IOP elevation and its measurement in rats.

Animals were housed initially in standard lighting conditions, with lights automatically turned on at 6 AM and off at 6 PM. One week before the hypertonic episcleral vein injection in one eye (the treated eye), each animal was placed in constant light conditions (24 hours exposure to 40-90 lux) (Morrison et al. 2005; Pang et al. 2005). Following injection, each animal was followed for 4 weeks, then sacrificed (see below). IOP readings in both the Control and EG eyes of each animal were made while awake (using 0.5% proparacaine hydrochloride as topical anesthesia to avoid the effects of general anesthetics) using a hand-held TonoPen tonometer. IOP was measured at least every other day, with a minimum of 14 IOP readings over the 4 weeks post saline injection. Mean IOP for both eyes of each animal was calculated as the

area under the curve of an IOP vs days plot divided by the number of days. The Mean IOP Difference for each animal was defined to be the difference between the mean IOP of the EG versus the Control eye. The Peak IOP for each animal was defined to be the highest IOP in the EG eye.

Rat Number	ID	Age at sacrifice *(months)*	Eye	Status	Mean IOP *(mmHg)*	Mean IOP difference *(mmHg)*	EG Eye Peak IOP *(mmHg)*	Optic Nerve Damage Grade	Number of Serial Section Images
1	MR8	9.5	OD	C	28.5	5		1	400
			OS	EG	33.5		42.3	1.22	383
2	MR10	9.5	OD	EG	29.2	0.4	45	1.6	465
			OS	C	28.8			1	313
3	MR1	9.5	OD	EG	33.3	5	39.1	2	696
			OS	C	28.3			1	398
4	MR9	9.5	OD	EG	35	6.6	45.8	2.36	430
			OS	C	28.4			1	307
5	MR12	10.5	OD	EG	29.6	1.1	36	2.47	500
			OS	C	28.5			1	275
6	MR11	10.5	OD	EG	32.1	3.8	41	2.9	230
			OS	C	28.3			1	375
7	MR5	9.5	OD	C	28.8	3.7		1	484
			OS	EG	32.5		40.9	3	480
8	MR4	9.5	OD	C	28.4	6.2		1	501
			OS	EG	34.6		42.3	3.28	455

ID – Laboratory Rat Identification Number; **Age**- in months; **Eye** - OD-Right eye, OS-left eye**; Status**- C- Control, EG-Experimental Glaucoma; **Mean IOP** (mmHg)- Mean IOP of all IOP measurements taken AM and PM for each eye**; Mean IOP difference**- Mean IOP of the EG eye minus Mean IOP of the Contol eye (mmHg). **EG Eye Peak IOP** - Maximum IOP in mmHg obtained in the EG eye; **Optic Nerve Damage Grade:** average score of orbital optic nerve cross section grading performed by 5 masked observers using a previously published scale (Morrison *Exp.Eye Res*.1997). **Number of Digital Serial Section Images**- number of serial digital section images required to reconstruct each optic nerve head.

Table 2.1. Animal and Eye Data.

2.1.2.- Rat Euthanasia, Fixation and Injury Grade Analysis

All animals were sacrificed 4 weeks post-initial saline injection to the treated eye under isoflurane anesthesia by transcardial injection of heparin (1 ml/kg) containing 10 mg ml sodium nitroprusside followed by 1 liter of 5% glutaraldehyde in 0.1 M phosphate buffer (pH 7.2). Optic nerves were dissected, washed, dehydrated and embedded in Spurr's resin as previously described (Morrison et al. , 1998). Using light microscopy, 5 masked observers graded the orbital optic nerve cross-section from each eye using a previously published scale from 1 (no injury) to 5 (active degeneration involving the whole nerve area) (Jia et al. 2000) and their grades were averaged to obtain the final injury grade for each nerve.

2.2. 3-D Histomorphometric reconstruction of the ONH

The ONH and peripapillary sclera of each eye were trephined (3-mm-diameter), embedded in paraffin, mounted to a microtome (RM2165; Leica, Wetzlar, Germany) and serial sectioned at 1.5 μm thickness from the vitreous surface through the optic nerve head into the orbital optic nerve (Burgoyne et al, 2004). After each section was cut, the block surface was stained with a 1:1 (v/v) mixture of Ponceau S and acid fuchsin stains, then imaged at a resolution of 1.5 x 1.5 μm per pixel using a custom device (Burgoyne et al., 2004). For each ONH 275 to 501 serial digital transverse section images were thus generated, aligned and stacked into a digital 3-D reconstruction (Burgoyne et al, 2004; Downs et al, 2007; Yang et al. 2007a; 2009a; 2007b; 2011a).

2.2.1. Initial qualitative 3D visualization of each ONH reconstruction and comparison to existing light and electron microscopy

To gain an initial understanding of the anatomy (Figs. 2.1 and 2.2) and to design a landmark and parameterization scheme appropriate to the rat ONH (Figs. 2.6-2.9), 40 radial digital sagital sections from each ONH reconstruction (Fig. 2.3A and B) were viewed by the authors (as a group) using our custom Multiview 3D visualization software (based on the Visualization Toolkit [VTK], Clifton Park, NY) (Burgoyne et al., 2004; Downs et al., 2007; Morrison et al., 1999; Yang et al., 2007a, 2007b, 2009b). Where indicated, selected comparisons were made to existing stained histologic sections, electron micrographs and vascular casting photographs from normal rat eyes that had been studied as part of a series of previous reports (Morrison et al., 2011, 1995b, 2005, 1997). With the basic macroscopic and microscopic relationships thus established (Figs. 2.1 and 2.2), strategies for delineation (Figs. 2.3 and 2.4) and parameterization (Appendix Figs.2. 1-2.4) were developed and executed. Final qualitative 3D visualization of the delineated point clouds (Figs. 2.3-2.5) were then performed to confirm the anatomic relationships described herein.

2.2.2. 3-D Delineation of the Rat ONH and Peripapillary Scleral Landmark Points (Fig.2.3)

We have previously published our 3D delineation method in detail (Downs et al., 2007; Yang et al., 2007b, 2011). In summary, each 3D ONH reconstruction was loaded into Multiview memory and the delineator assigned the approximate center of the optic nerve

(Figs. 2.2 and 2.3) as the center of rotation, through which, forty, 7-voxel thick, digital radial sagittal slices of the digital 3D reconstruction were serially served at 4.5° intervals for delineation (Fig. 2.3A, B and C).

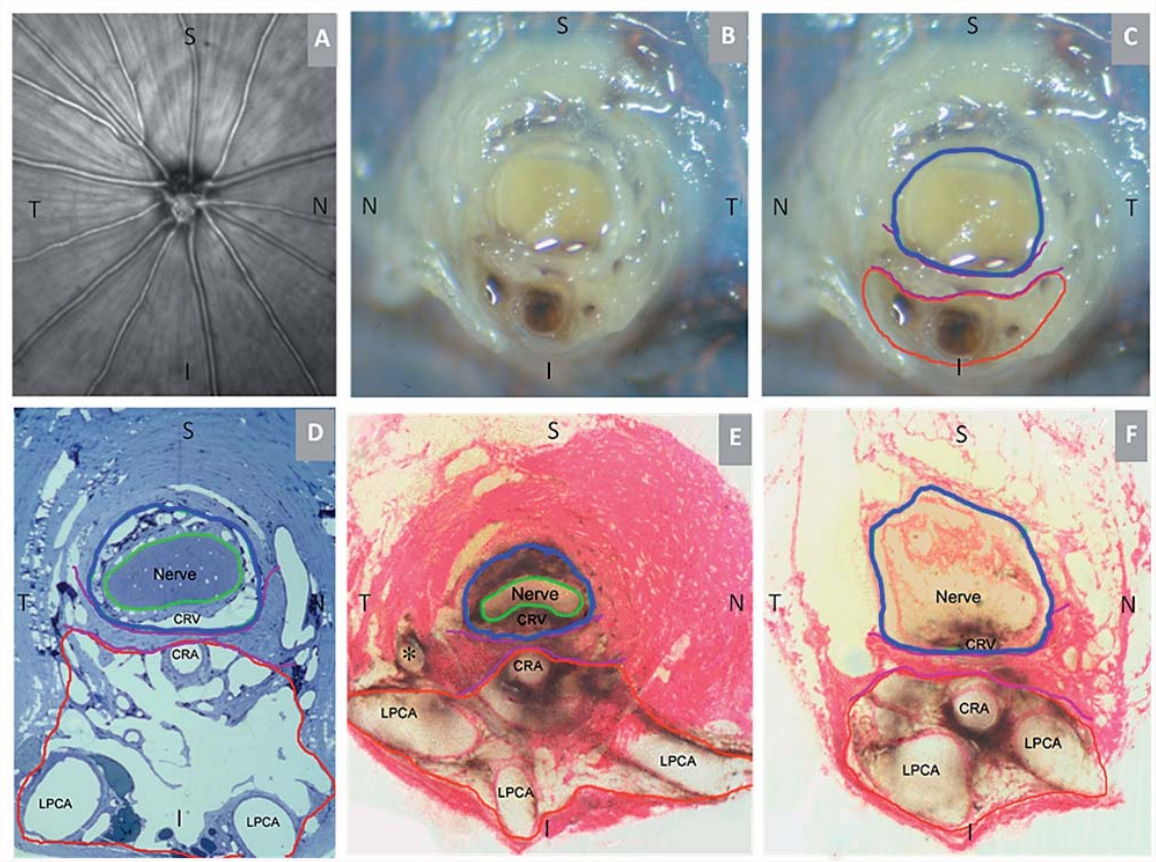

Figure 2.1. Rat Optic Nerve Head Macroscopic and Microscopic Relationships I – Transverse Sections. (A) 30 degree SD-OCT Infrared Reflectance image of the rat optic disc (the vitreal surface of the optic nerve head) (courtesy of Brad Fortune). (B) Macroscopic appearance of the cut surface of the rat optic nerve just posterior to the scleral shell (view from the back of the eye). (C) Principal Macroscopic relationships. The neurovenous bundle (green) and the more-inferior arterial bundle (red) are separated by a sling of scleral tissues (the scleral sling, purple) (view from the back of the eye). (D-E) Principal scleral openings. Unlike the primate, there are two principal openings within the sclera of the rat ONH: 1) the neurovenous canal (blue) and the more-inferior arterial opening (red), which is not a well-defined canal, being irregular due to the choroidal branches of the LPCAs (D and E) and separated from the neurovenous canal by the scleral sling (purple). Unlike the primate, which has on average 15 short posterior ciliary arteries that are evenly distributed around the circumference of the scleral canal, the inferior concentration of the LPCAs and the density of their intrascleral branches to the choroid combined with the actual CRA canal (D – F) suggest an "effective" second opening in the sclera. (D) Transverse histologic section through the scleral portion of the optic nerve head demonstrating the same relationships seen posterior to the globe in panels B and C. Note that the neurovenous bundle consists of the optic nerve surrounded by a vascular tissue within the inferior portion of which runs the CRV. The arterial bundle is made up of the central retinal artery the two main LPCAs and their intrascleral branches to the choroid (vascular spaces in between the principal arteries - not labeled). (E) An acquired, digital transverse section image from a histomorphometric reconstruction demonstrating the same relationships as (D). (F) Digital section image from the same eye just posterior to the globe and close to the view seen macroscopically in (C). The red oblique line in (F) marks the location of a digital radial section image that is not shown. The intrascleral (E) and retrobulbar short posterior ciliary arteries (*) are branches of the LPCAs rather than the Ophthalmic Artery. A preferential superior-temporal course of the optic nerve and neurovenous bundle as they pass through the sclera into the orbit are suggested by comparing the green circle in (F) to (E). CRV- Central retinal vein, LPCAs- Long Posterior Ciliary Arteries. N – Nasal; T – Temporal; I – Inferior; S – Superior

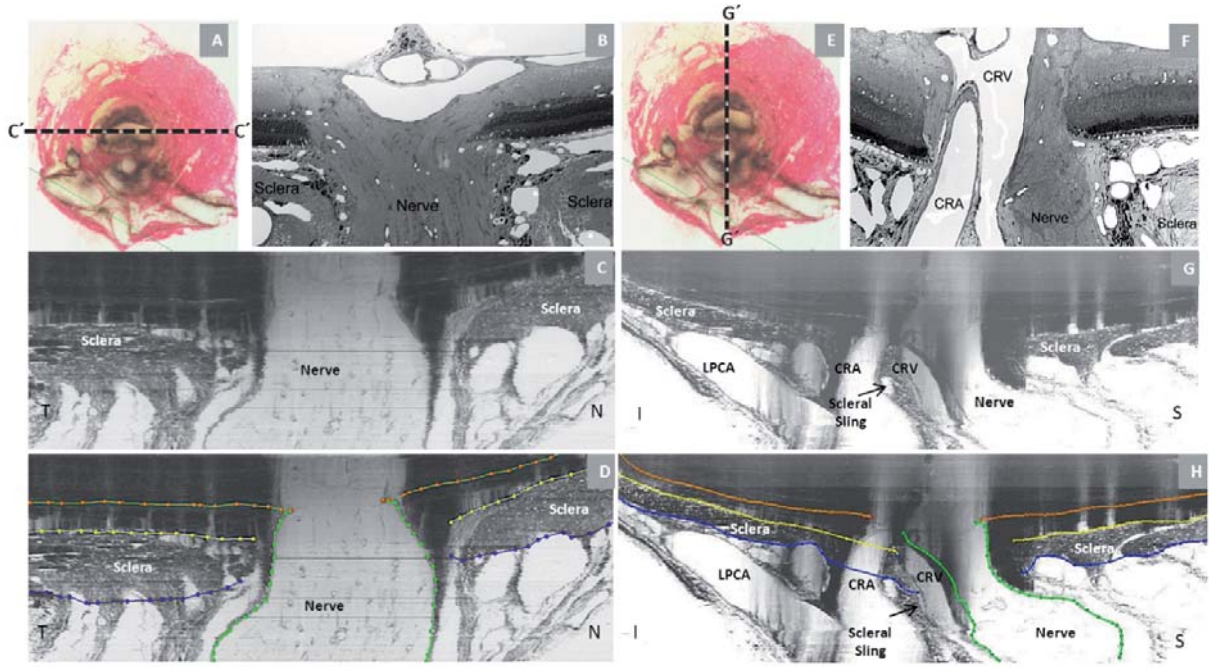

Figure 2.2. Rat Optic Nerve Head Macroscopic and Microscopic Relationships II – Sagittal Sections. Horizontal (upper panels - A, B,C and D) and vertical (lower panels - E, F, G and H) sagittal views of the rat ONH centered upon the scleral portion of the neurovascular canal (A and E). Panels (B, C and D) and (F, G and H) are digital sagittal sections (location relative to the ONH marked as C' and G' in (A) and (E) of the same histomorphometric reconstruction in which acquired transverse section images were shown in Supplemental figure 1 and panels D and H are the same sections showing the delineation of the different structures. The process of creating digital sagittal sections from the histomorphometric volume is explained in Supplemental Figure 3. Panels (B) and (F) are histologic sections of another eye acquired in locations similar to (C) and (G). Most descriptions of the rat ONH show horizontal (C) or vertical (G) sagittal sections of the ONH that are cropped close to the end of the sclera which has the effect of emphasizing the similarities of the neurovenous canal to the scleral canal of the primate. However within the horizontal (C) and vertical (G) digital sagittal sections of the histomorphometric reconstructions, the importance of the venous plexus that surrounds the nerve within the neurovenous canal, the sclera sling and the inferior arterial vessels can be appreciated. Note also the general temporal slant of the nerve in (B) and the superior slant of the nerve in (F). Taken together, these observations within horizontal and vertical sagittal sections confirm the general superior temporal path of the optic nerve tissues suggested within the serial transverse section images of Figure 1 (see Figure legend). Note that within panels (C) and (G) of Figure 2, the dark shadows extending upward from the sclera are a result of the fact that in serial transverse sectioning from the vitreous (top) to the orbital optic nerve (bottom) the dark choroidal pigment can be seen until the sectioning plane passes through it, creating the appearance of a shadow within the retina and vitreous . CRV- Central retinal vein, LPCA- Long Posterior Ciliary Arteries. CRA-Central Retinal Artery; N – Nasal; T – Temporal; I – Inferior; S – Superior. Orange line: Bruch's Membrane, Yellow line: anterior sclera. Blue line: Posterior Sclera. Green line: Nerve boundary.

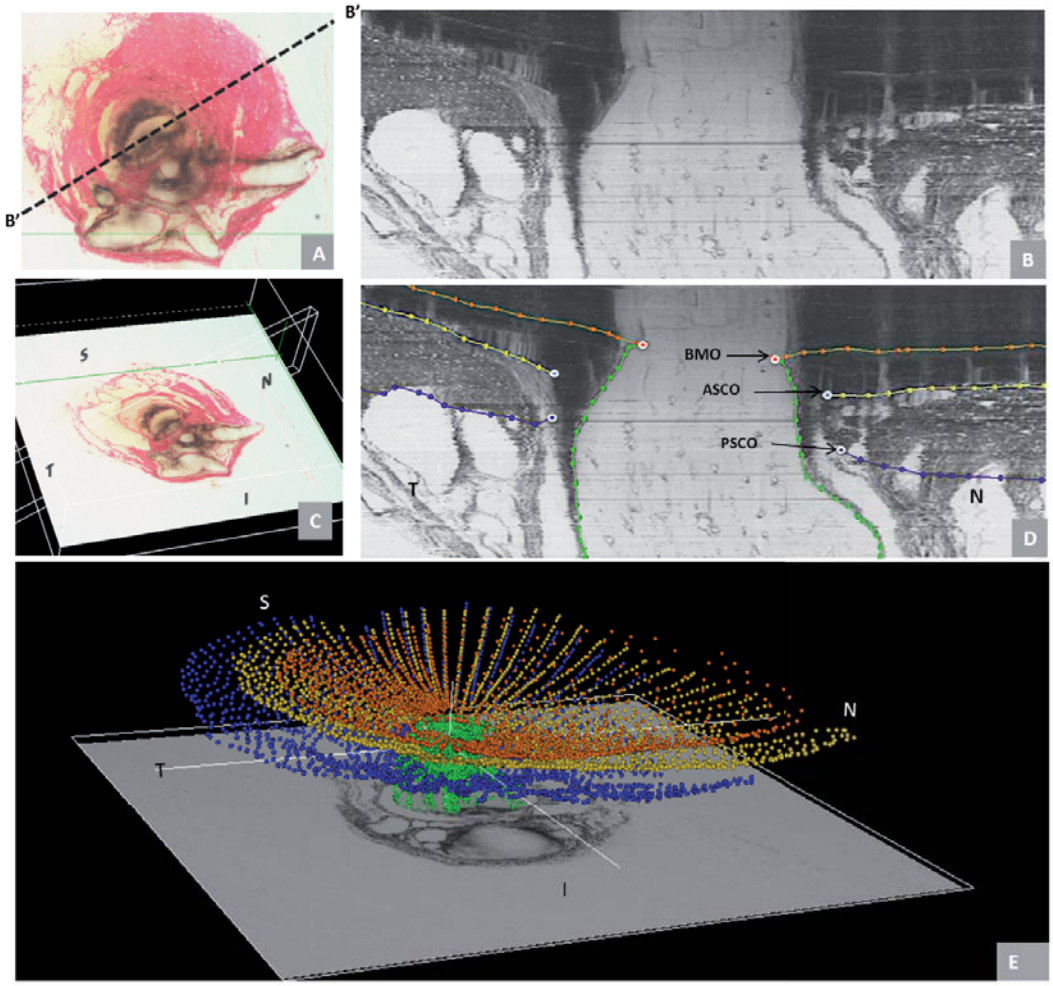

Figure 2.3. Points within 40 Digital Serial Radial Sagittal Section Images of each ONH. The delineator first assigned the center of the scleral portion of the optic nerve (A) to be the center of rotation through which, forty, 7-voxel thick, digital radial sagittal section images (B) of the digital 3-D reconstruction (C) were serially served at 4.5º intervals. The Nasal-Temporal location of (B) is shown here two dimensionally (dotted line marked B-B') within the transverse section image in (A) and three-dimensionally (7 µm thick white-edged rectangle) within the 3-D reconstruction in (C). Within each digital sagittal section image (B) the delineator marked four landmark surfaces and three pairs of neurovenous canal landmarks (one point on each side of the canal). The landmark surfaces were: (1) Bruch's membrane (orange); (2) the anterior (yellow) and (3) posterior (blue) surfaces of peripapillary sclera ; and (4) the optic nerve boundary extending from Bruch's membrane opening, through the scleral canal and along the pia mater to the posterior edge of the reconstruction (green). The landmark points were Bruch's Membrane Opening (BMO – red), the anterior scleral canal opening (ASCO – light blue) and the posterior scleral canal opening (PSCO – purple). A representative point cloud which contains all delineated landmark types for all 40 radial sections of an individual reconstruction is viewed from its superior surface three dimensionally in (D) (temporal is to the left and nasal is to the right). Three dimensional reconstructions of the landmark point clouds (D) of each eye were 3D visualized together and separately (turning each landmark category on and off) so as to qualitatively determine their principal macroscopic relationships. In Panel (E) the superior temporal course of the optic nerve as it passes through the sclera and its sharper bend into the orbit can be appreciated. N – Nasal; T – Temporal; I – Inferior; S – Superior.

Because visualization of Bruch's Membrane (BM), Bruch's Membrane Opening (BMO) and several deep ONH landmarks was most consistent within Green channel as opposed to white light section images, delineation was carried out within green channel digital section images for each study eye. Four landmark surfaces and three pairs of neurovascular ca-

nal landmarks (one point on each side of the canal) were delineated within each digital section image.

The landmark surfaces were: (1) BM; (2) the anterior and (3) posterior surfaces of peripapillary sclera; and (4) the optic nerve boundary extending from BMO, through the neurovascular scleral canal and along the pia mater to the posterior edge of the reconstruction (Fig. 2.3B). The landmark points were BMO, the anterior scleral canal opening (ASCO) and the posterior scleral canal opening (PSCO).

Delineation of these landmarks was "three dimensional" because while marking the digital sagittal section image (Fig. 2.3B), the delineator simultaneously viewed a second window, (that was linked to the first), displaying the cursor's real-time 3D location within the appropriate digital transverse section image (Fig. 2.3A). The 3D Cartesian coordinates and category number for each mark were saved, generating a 3D point cloud representing each of the marked structures (Fig. 2.3D). These point clouds were then surfaced and could themselves be cut and visualized at any angle allowing observations and measurements to be made between the regions of actual delineation.

2.2.3. 3D delineation of the ONH and peripapillary scleral vasculature and scleral sling (Fig. 2.4)

As opposed to the landmark and surface delineations outlined above which were performed within serial digital sagittal section images (Fig. 3), vessel and scleral sling delineation were performed within every fourth digital transverse section image while simultaneously viewing linked windows which displayed vertical or horizontal digital sagittal sections (notice this is not clinical vertical or horizontal sections due to our embedding angles) of the reconstruction through the point being delineated (Fig. 2.4. A-D). The following landmark categories were individually marked and cataloged within each delineated transverse section image: (1) Ophthalmic artery (OA); (2) central retinal artery (CRA); (3) long posterior ciliary arteries (LPCAs); (4) short posterior ciliary arteries (SPCAs); (5) Central retinal vein (CRV); and (6) the vascular or neural boundary of the scleral sling (Figs. 2.1, 2.2 and 2.4). Three dimensional reconstructions of the landmark point clouds (Fig. 2.4 E-H and Fig. 2.5) were then visualized together and separately (turning each landmark category on and off) so as to determine their principal macroscopic relationships.

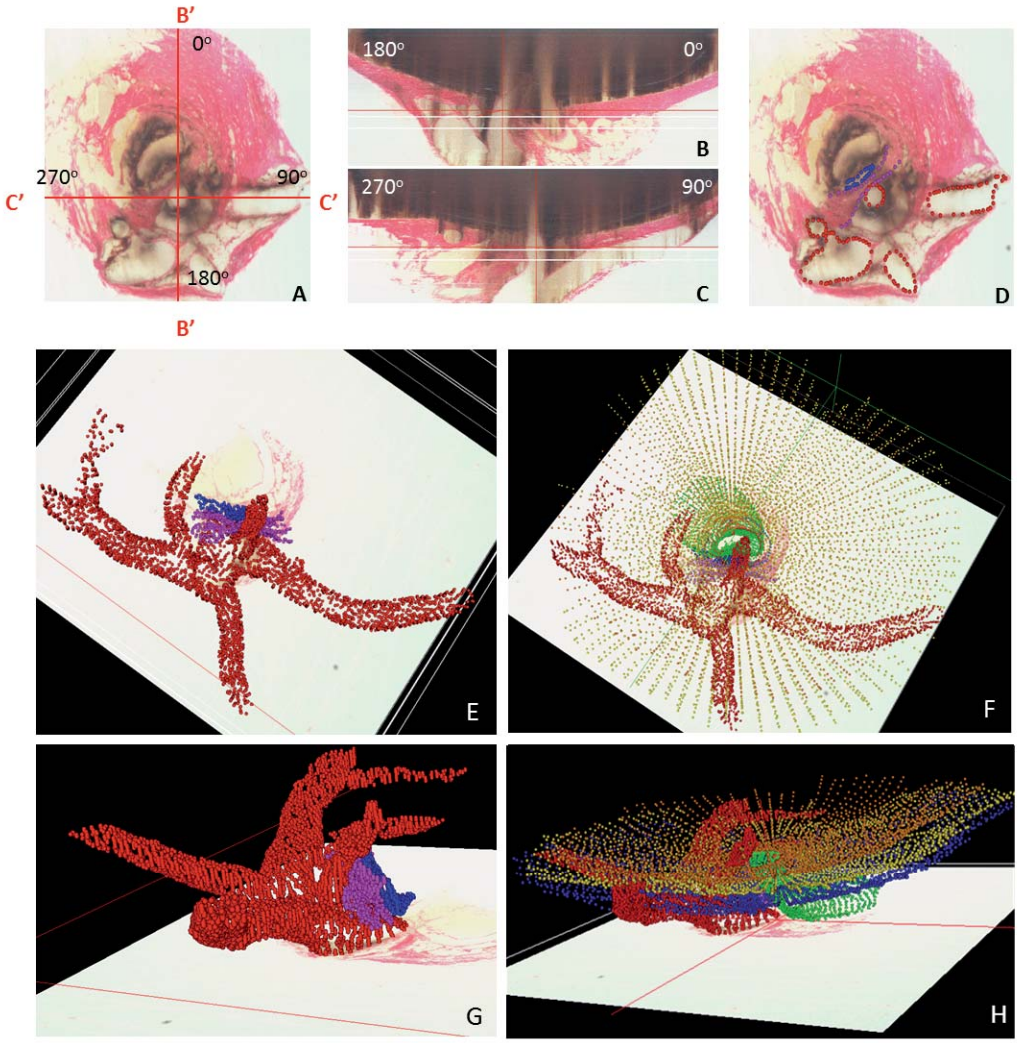

Figure 2.4. 3-D Delineation of the ONH and Peripapillary Scleral Vasculature and Scleral Sling within Digital Transverse Section Images. Vessel and scleral sling delineation were performed within every fourth digital transverse section image (A) while simultaneously viewing one linked window which displayed either embedded vertical (B) or embedded horizontal (C) digital sagittal sections through the point being delineated. The lines marked B'-B' and C'-C' in panel (A) mark the location of the embedded vertical and embedded horizontal digital sagittal section images depicted in panel (B) and (C), respectively. Note that these are vertical and horizontal sections through the 3D reconstruction, but because the tissues are not embedded in perfect clinical orientation, they are not "anatomic" vertical and horizontal sections through the ONH. In Figure 2, this same reconstruction has been turned so that an accurate clinical orientation has been achieved and "anatomic" vertical and horizontal sections are shown. The following landmark categories were individually marked and catalogued within each delineated transverse section image (D): Ophthalmic artery (OA - red); (2) Central retinal artery (CRA - red);(3) Long posterior ciliary arteries (LPCA - red); (4) Short posterior ciliary arteries (SPCA – reds – and branches of the LPCAs in rats); (5) Central retinal vein (CRV - blue); and (6) the vascular or neural boundary of the scleral sling (magenta). Three dimensional reconstructions of the landmark point clouds (panels E - H) were then 3-D visualized together and separately (turning each landmark category on and off) so as to determine their principal macroscopic relationships

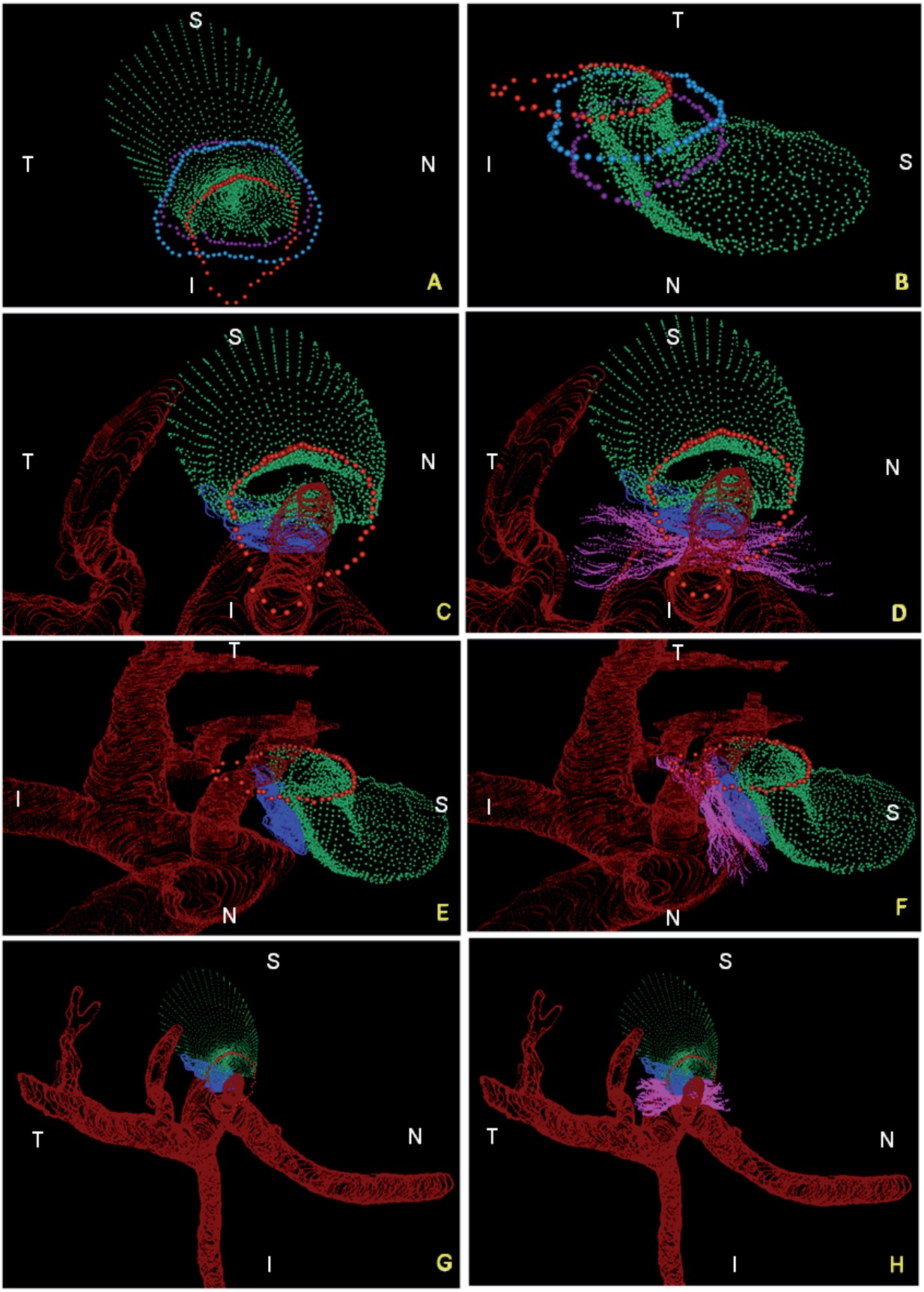
S
T
N
I
A
T
I
S
N
B
S
T
N
I
C
S
T
N
I
D
T
I
S
N
E
T
I
S
N
F
S
T
N
I
G
S
T
N
I
H

(From previous page) **Fig. 2.5. Summary of the 3D relationships between BMO, the ASCO and PSCO, the Optic Nerve, the Central Retinal Vein, the Central Retinal Artery and the Long Posterior Ciliary Arteries (with and without their intrascleral branches) as visualized within the 3D Point Clouds from a Representative Normal Rat Eye.** The relationship of BMO (red),ASCO (light blue) and PSCO (purple) relative to the optic nerve (green) can be seen from a clinical orientation in panel (A) and longitudinally in panel (B). In panels (C)**e**(F) the ASCO and PSCO Point clouds have been turned off and the CRV, CRA and LPCA point clouds have each been turned on. First, notice that BMO is not round (A) but inferiorly elongated to accommodate the passage of the CRA and CRV (blue vessel) to the retina. Notice also, that BMO is shifted inferiorly relative to the ASCO and PSCO. Second, notice the space between the neural tissue and the BMO, ASCO and PSCO in panel (B). At the level of BMO, the nerve abuts BM superiorly and there is space inferior to the nerve (filled by the CRV and CRA) as noted above. Note in Panel B, that because of the shift in BMO relative to the ASCO and PSCO, BM effectively extends beyond the scleral portion of the neural canal. Superiorly this creates an edge or extension of BM against which the neural bundle abuts. Inferiorly, it creates an elongation of BMO to accommodate the inferior vessels. The net effect of this shift is to create a superior-directed, oblique passage of the nerve through the wall of the rat eye that is best appreciated in Panels B, E and F. At the level of its passage through the anterior (ASCO) and posterior (PSCO) sclera the nerve is surrounded by a vascular plexus which we are not able to independently delineate using our current method. Third, there are three long posterior ciliary arteries which branch from the CRA behind the globe and pass together through the sclera (inferior to the neurovascular canal) to achieve the choroid. Their tangential rather than perpendicular passage through the sclera is depicted in (E) and (F) (see also Fig. 2.4F, H). Fourth, short posterior ciliary arteries (defined to be primary branches of the ophthalmic artery that individually pass through the sclera) were not identified. Instead the few arteries that independently pass through the sclera superiorly (G), where identified, appear to be retrobulbar branches of the LPCAs. Fifth, unlike the primate eye in which there are 15 short posterior ciliary arteries that are relatively equidistant from one another around the circumference of the optic nerve, the choroidal blood supply in the rat appears to originate inferiorly from a dense plexus of intrascleral LPCA branches which effectively fill the space between the three LPCA branches (see Fig. 2.1D-F). Some of these vessels extend within the sclera and choroid superiorly, around the neurovascular canal. It is the density of the LPCAs and their intrascleral branches inferiorly that suggests an "effective" second opening in the sclera. Sixth, the CRA and CRV are separated from each other and the nerve proper and supported by a "sling" (magenta) of scleral tissues that forms the inferior border of the neurovascular scleral canal opening and the superior border of the more-inferior arterial opening. N - Nasal; T-Temporal; I -Inferior; S -Superior.

2.2.4. Masked Delineation Strategy.

Both eyes of each rat were delineated by a single delineator who was masked to the treatment status of each eye. Final delineations were checked for accuracy by two experienced observers (HY and CFB) masked as to the treatment condition of each eye.

2.2.5. Delineation Reproducibility Study

Both the Control and EG eyes of each animal were delineated by a single delineator (MP). Upon completion of the initial delineation of each eye, the marks were reviewed by 2 authors (CFB and HY) to expand our understanding of the anatomy and to reach agreement on the anatomic landmarks of greatest interest. Both eyes of three animals were then delineated on two subsequent occasions by the same delineator (MP), at least 2 weeks apart, to assess intra-delineator variability. The intraclass-Correlation Coefficient (ICC) (see statistical analysis, below) for all reported parameters was calculated (Rosner, 2011).

2.3. Parameterization and Quantification

Parameters are italicized to distinguish their behavior from the behavior of the underlying anatomic landmarks (which are not italicized).

2.3.1. Bruch's Membrane Opening (BMO) and the neurovascular scleral canal (Figs. 2.6 and 2.7)

For each ONH reconstruction, individual planes were fit to the 80 BMO points, 80 neurovascular ASCO points and 80 neurovascular PSCO points, (2 points for each landmark within each of 40 digital radial sagittal sections, as outlined above (Appendix Fig. 2.6A) using a least-squares algorithm. The BMO plane became the reference plane for a series of subsequent measurements and the basis for the second peripheral anterior scleral reference plane (Appendix Figs. 2.6A, 2.7 and 2.8). The cross-sectional area of BMO (*BMO Area*) as well as the neurovascular sclera canal at the level of the ASCO and PSCO (*ASCO and PSCO area*) were calculated as the area within the projection of the BMO, ASCO and PSCO points to their respective fitted planes (Appendix Fig.1B). Using the centroid of the projected BMO, ASCO and PSCO points, 80 radius measurements were made within their respective fitted planes at 4.5º intervals (Appendix Fig. 2.6C). To assess their relative shapes, the *Horizontal/ Vertical (H/V) Diameter Ratios* were calculated for ASCO, and PSCO.

2.3.2. Optic nerve cross-sectional area within the scleral canal (Fig. 2.7)

Optic nerve (ON) cross-sectional area, radii and shape (*H/V Diameter Ratios*) were quantified within the ASCO (*ON-ASCO*) and PSCO (*ON-PSCO*) planes using the delineated optic nerve boundary as illustrated in Appendix Fig. 2.7. *Optic Nerve Volume* (the volume defined by the ASCO plane, PSCO plane and optic nerve boundary) was also quantified.

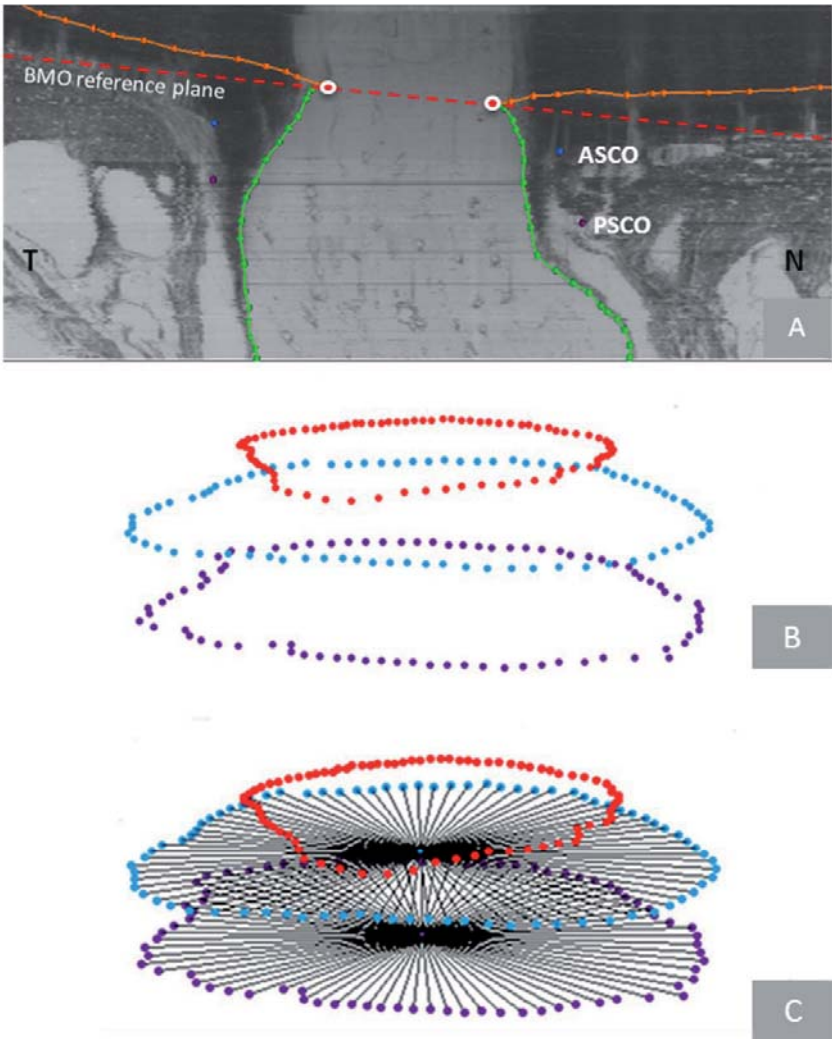

Figure 2.6 Bruch's Membrane Opening (BMO) and Neurovascular Scleral Canal Parameterization. **(**A) Within each ONH reconstruction, individual planes were fit to the 80 BMO points, 80 ASCO points and 80 PSCO points which are illustrated in cross-section within a digital sagittal section image. (**N** – Nasal; **T** – Temporal). **(B)** The crossectional area of all three openings (BMO, ASCO and PSCO) was calculated as the area within the projection of the BMO, ASCO and PSCO points to their respective fitted planes. **(C)** Using the centroid of the projected BMO, ASCO and PSCO points, 80 radius measurements were made within their respective fitted planes at 4.5 degree intervals.

2.3.3 *Anterior scleral sling depth, BMO/ASCO/PSCO depth,* and *Anterior Peripapillary Scleral Surface Depth* relative to a peripheral anterior scleral reference plane (Fig. 2.8)

BMO Depth, ASCO Depth, PSCO Depth (Fig. 2.8 C) were separately measured relative to a peripheral anterior scleral reference plane (Fig. 2.8 A) within each digital sagittal section image as illustrated in Appendix Fig. 2.8 B and C. *Anterior Peripapillary Scleral Depth* was

measured relative to the same reference plane commencing at 350 μm and extending to 700 μm from the projection of the ASCO centroid line (in 50 μm increments) as illustrated in Appendix Fig. 2.8 D. These distances were chosen because this was a region of sclera that was common to all studied eyes (i.e. 350 μm corresponded to the smallest radius and 700 μm the largest radius from the centroid of ASCO that included sclera for all 360º within each of the 16 rat volumes).

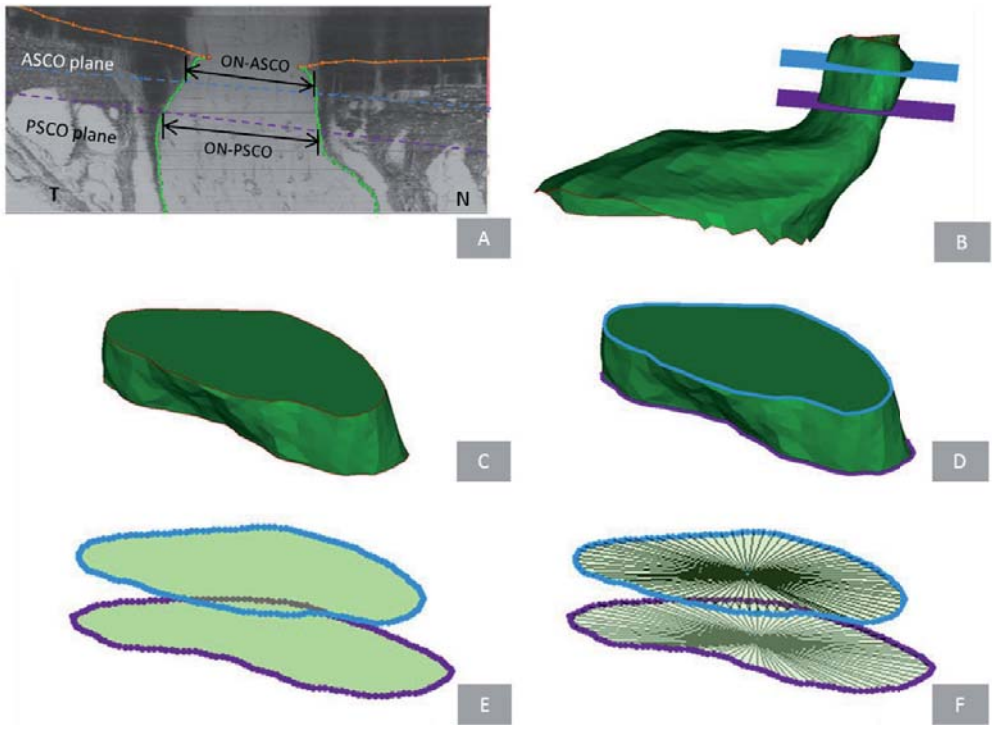

Figure 2.7. Scleral Canal Optic Nerve Area, and Volume Parameterization. Optic nerve crossectional area and radii were quantified within the ASCO (ON-ASCO) and PSCO (ON-PSCO) planes using the delineated optic nerve boundary (green dots) as illustrated within digital sagittal sections in panel (A). ON crossectional area within BMO (ON-BMO) could not be quantified due to obstruction of its boundaries by pigment from the perineural venous plexus. In (B) the optic nerve point cloud (from all 40 delineated sections) has been surfaced (green) and the position of the ASCO (light blue) and PSCO (purple) planes relative to the optic nerve is shown. Please note that while the ASCO and PSCO planes are based on the respective openings within the sclera (Figure 5, above, and panel A of this figure) it is the scleral canal optic nerve volume or the optic nerve volume within the canal (not including the surrounding venous plexus) and between the planes that is isolated within (C). The ON-ASCO (light blue) and ON-PSCO (purple) surfaces of the scleral canal optic nerve volume are highlighted in (D), and their areas and radii are quantified in (E) and (F). The orientation of panels (B) – (F) is approximately that of (A) - Temporal (T) left and Nasal (N) right.

2.3.4. Peripapillary Scleral and Peripapillary Choroidal Thickness (Fig. 2.9)

Peripapillary Scleral and Choroidal Thickness were separately measured within each digital sagittal section image in 50 μm increments radially commencing at 350 μm and extending to 700 μm (*Peripapillary Scleral Thickness*) or 600 μm (*Peripapillary Choroidal Thickness*) from

the projection of the ASCO centroid onto the BMO reference plane as illustrated in Fig. 2.9. Again 350 μm corresponded to the smallest radius outside the major vessels and 600 or 700 μm (depending on the parameter) was the largest radius present in all the specimens.

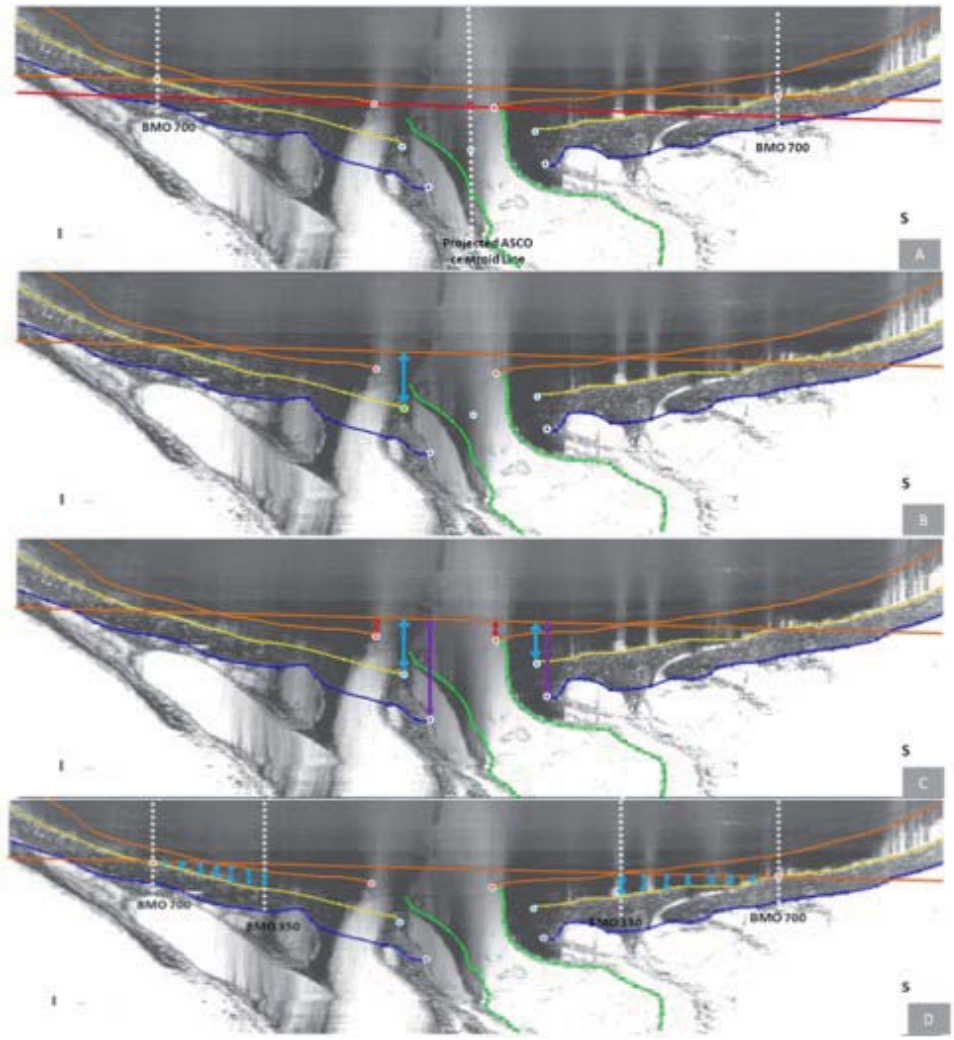

Figure 2.8. *Anterior Scleral Sling Depth*, *BMO Depth* and *Anterior Peripapillary Scleral Depth* relative to a peripheral anterior scleral reference plane. (A) A peripheral anterior scleral reference plane was generated from a ring of points (orange dot with white border) on the anterior scleral surface at a distance 700 microns (BMO 700) from the projected ASCO centroid line. (B) *ASCO Depth (blue arrow)* was measured relative to the peripheral anterior scleral reference plane in each radial section in which the sling surface could be identified (approximately 8 section images per ONH). Circled in yellow you can see the most anterior aspect of the scleral sling. (C) *BMO Depth* was measured for each BMO point relative to the same reference plane within each section. PSCO (purple arrow), ASCO Depth (blue arrow) and BMO depth (red arrow) were calculated relative to this peripheral anterior scleral reference plane as well. (D) *Anterior Peripapillary Scleral Depth* relative to the same reference plane was measured at a distance of BMO 350 to BMO 700 μm (in 50 μm increments) on the fitted anterior scleral surface (yellow line). Red dot with white border – BMO; Blue dot with white border – ASCO; Purple dot with white border – PSCO; Projected ASCO centroid line (A) - perpendicular line to the BMO reference plane (red line) passing through the raw ASCO centroid (blue dot with white border); Blue dot with red border (B) - projected ASCO centroid; *BMO 350/700* - Perpendicular line from the BMO reference plane at a distance of 350/700 μm from the projected ASCO centroid line so as to define BMO 350/700 eccentricity. I – Inferior; S – Superior. . Orange line: Bruch's Membrane, Yellow line: anterior sclera. Blue line: Posterior Sclera. Green line: Nerve boundary.

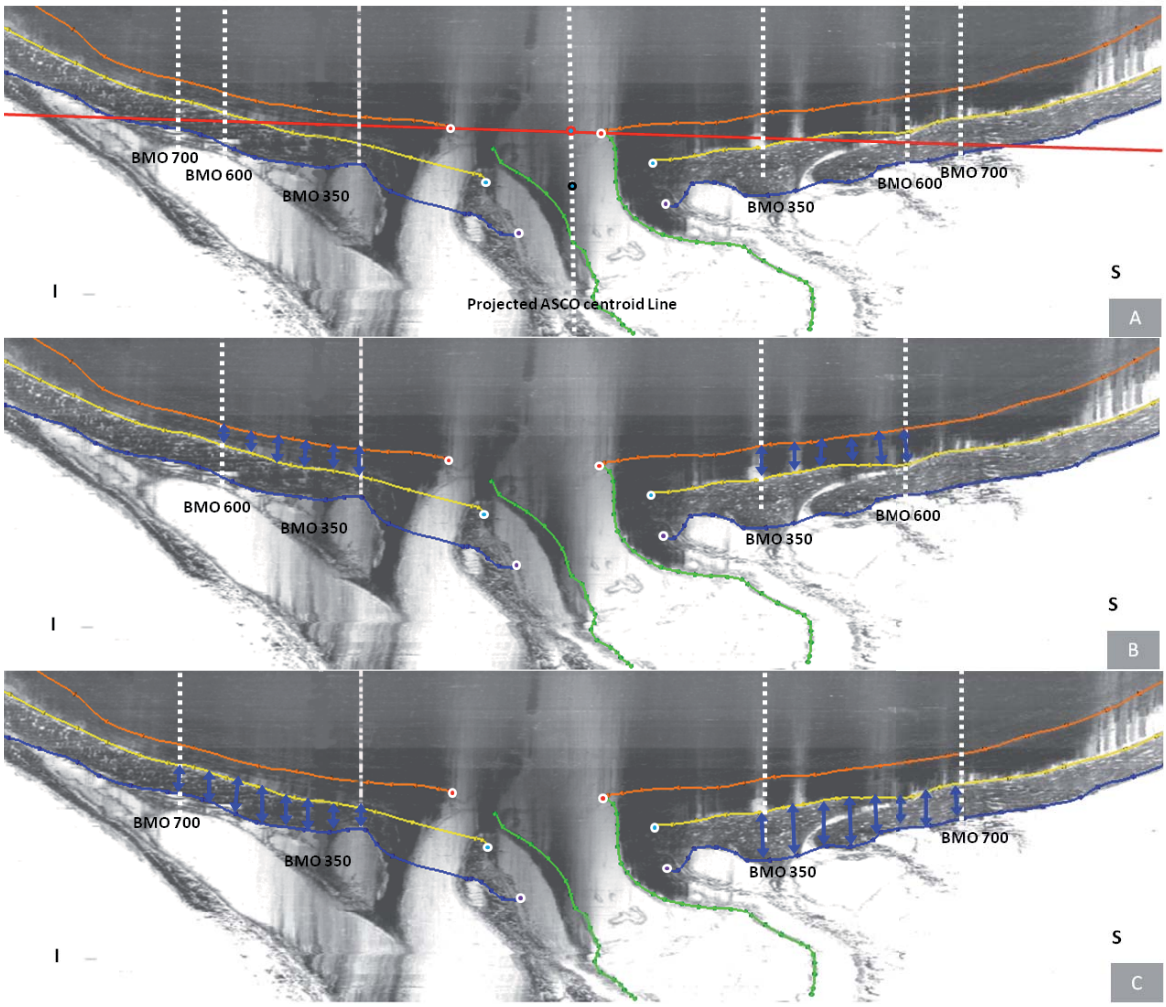

Figure 2.9*. Peripapillary Choroidal* and *Peripapillary Scleral Thickness* Parameterization. (A) Projected ASCO centroid line is a perpendicular line to the BMO reference plane (red line) passing through the raw ASCO centroid (blue dot with black border) and projected ASCO centroid (Blue dot with red border). *BMO 350/600/700*: Perpendicular line from the BMO reference plane at a distance of 350/600/700 ìm from the projected ASCO centroid line so as to define BMO 350/600/700 eccentricity. (B) *Peripapillary Choroidal Thickness (dark blue arrows)* was measured perpendicular to Bruch's Membrane surfaces in 50 ìm increments along the BMO reference plane between the BMO 350 to BMO 600 landmarks. (C) *Peripapillary Scleral Thickness (dark blue arrows)* was measured perpendicular to the anterior scleral surface in 50 ìm increments along the BMO reference plane between the BMO 350 to BMO 700 landmarks Red dots with white border – BMO; Blue dots with white border – ASCO; Purple dot with white border - PSCO. Blue dot with black border (A) – ASCO centroid; I – Inferior; S – Superior. . Orange line: Bruch's Membrane, Yellow line: anterior sclera. Blue line: Posterior Sclera. Green line: Nerve boundary..

2.3.5. The inferior arterial scleral opening

Because its boundaries are not consistently clearly visible we were not able to quantify the inferior opening in the sclera created by the central retinal artery, the LPCAs and the LPCA intrascleral branches using our current techniques.

2.3.6. The Optic Nerve Gap Distance

In addition, to assess preferential displacement of the nerve within the neurovascular canal of the EG eyes, two new parameters measuring the distance between the neurovascular

scleral canal wall and the contained optic nerve (the optic nerve gap distance) were calculated within all 80 radial locations: 1) the ASCO to ON-ASCO distance *(ASCO ON-ASCO Distance);* and 2) the PSCO to ON-PSCO distance (*PSCO ON-PSCO Distance).*

2.4. Statistical Analysis

Mixed effects linear regression models were formed to compare the radial structures (*ASCO radius* vs *PSCO radius*, *ON-ASCO radius* vs *ON-PSCO radius*). Within each normal control rat, anterior and posterior scleral and neural canal sizes were compared using a linear model fitted with generalized least squares (GLS). Mixed effects linear regression models were formed to compare the radial structures (*ASCO radius* vs *PSCO radius*, *ON-ASCO radius* vs *ON-PSCO radius)*. Within each normal control rat, anterior and posterior scleral and neural canal sizes were compared using a linear model fitted with generalized least squares (GLS). Statistical significance was defined to occur at $p < 0.05$ after adjusted to multiple comparisons.

EG versus Control eye global data were compared using a paired, two-sided student T-test with significance defined to occur at $p<0.0022$ to adjust for multiple (n=23) comparisons (Guo and Yuan, 2015). For the subset of parameters with multiple values per eye, overall (experiment-wide) EG eye effects were assessed within each region using a linear mixed effects model, accounting for multiple data points per eye and two eyes per rat (significance defined at $p<0.0125$, to adjust for 4 regional comparisons per parameter). An exponential spatial correlation structure was assumed within each eye, based on the distances between delineated points. EG vs Control eye comparisons for each animal globally (significance defined at $p<0.005$, 13 comparisons per rat) and by each quadrant (significance defined at $p<0.0001$, 13 comparisons per quadrant) were carried out using generalized least squares models assuming exponential spatial correlation structure. Within the reproducibility study, the ICC was calculated from one-way ANOVA. Correlation between the magnitude of global EG eye change in the area and volume optic nerve parameters (*ASCO area*, *PSCO area*, *ON-ASCO area*, *ON-PSCO area* and *ON Volume*) and the orbital optic nerve injury scale was assessed for statistical significance using Pearson's correlation coefficient ($p<0.05$ without adjustment due to the small number of purposeful comparisons).

All the analyses were carried out either in R (the R Foundation for Statistical Computing, Vienna, Austria) or Microsoft Excel (Microsoft, Redmond, WA, USA).

3

Experiments and Supporting Publications

3.1. General Objectives

- To Three-Dimensionally (3D) reconstruct normal control ONH so as to characterize and quantify their macroscopic and microscopic anatomy.
- To provide the first rat 3D histomorphometric description of deep ONH changes in experimental early glaucoma model.

A summary of the most important results of each publication as well as a copy of each of them is provided (compendium of publications)

3.2. First Paper: Rat Optic Nerve Head Anatomy within 3D histomorphometric reconstructions of normal control eyes.

Marta Pazos, Hongli Yang, Stuart K. Gardiner, William O.Cepurna, Elaine C. Johnson, John C. Morrison, Claude F. Burgoyne.

Exp Eye Research 139 (2015) 1-12

3.2.1. Abstract

Purpose: To three-dimensionally (3D) characterize the principal macroscopic and microscopic relationships within the rat ONH and quantify them in normal control eyes.

Methods: Perfusion-fixed, trephinated ONH from 8 normal control eyes of 8 Brown Norway Rats were 3D histomorphometrically reconstructed, visualized, delineated and parametrized.

Results: The rat ONH consists of 2 scleral openings, (a superior neurovascular and inferior arterial) separated by a thin connective tissue strip we have termed the "scleral sling". Within the superior opening, the nerve abuts a prominent extension of Bruch's Membrane (BM) superiorly and is surrounded by a vascular plexus, as it passes through the sclera, that is a continuous from the choroid into and through the dural sheath and contains the central retinal vein (CRV), (inferiorly). The inferior scleral opening contains the central retinal artery and three long posterior ciliary arteries which obliquely pass through the sclera to obtain the choroid. Bruch's Membrane Opening (BMO) is irregular and vertically elongated, enclosing the nerve (superiorly) and CRV and CRA (inferiorly). Overall mean BMO Depth, BMO Area, Choroidal Thickness and peripapillary Scleral Thickness were 29μm, 56.5 x 10^3 μm^2, 57 μm and 104 μm respectively. Mean anterior scleral canal opening (ASCO) and posterior scleral canal opening (PSCO) radii were 201 ± 15 μm and 204 ± 16 μm, respectively. Mean optic nerve area at the ASCO and PSCO were 46.3 x 10^3 ± 4.4 x10^3 μm^2 and 44.1 x10^3 ± 4.5 x 10^3 μm^2 respectively.

Conclusions: The 3D complexity of the rat ONH and the extent to which it differs from the primate have been under-appreciated within previous 2D studies. Properly understood, these anatomic differences may provide new insights into the relative susceptibilities of the rat and primate ONH to elevated intraocular pressure.

3.2.2. Principal Macroscopic and microscopic relationships

The Rat ONH consists of two principal passages through the sclera (Fig.2.1-2.5): a well demarcated superior neurovascular canal that contains the ON and its peri-neural vascular plexus (continuos with and extending from the choroid to the dural sheets veins and containing the CRV, inferiorly) and a less clearly defined, more-inferior arterial opening through which pass the CRA, LPCAs (fig 3.2) and their intrascleral branches to the peripapillary choroid. The connective tissue wall of these two openings and the outer walls of the vessels that pass trough them fuse with a sling of scleral connective tissues to form a separating structure that we have called the *scleral sling* .

At the level of the sclera, also unlike the primate, there is a prominent vascular plexus between the neural tissue and the ASCO and PSCO (fig.3.1). Within the scleral portion of the neurovascular canal there were sporadic organized connective tissue structures within our reconstructions; however no clear evidence of laminar beams were observed using our technique.

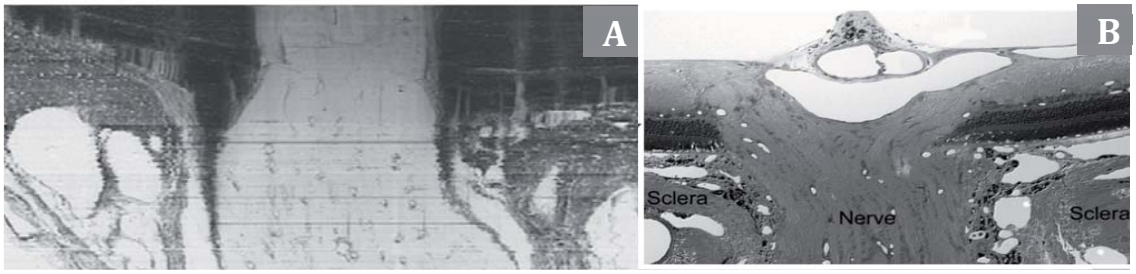

Figure 3.1. Perineural vascular plexus. Panel A is a digital sagittal section image and panel B is a horizontal histologic section of a normal control eye. Please note the continuity of the choroidal and perineural vascular plexus.

3.2.3. Summary of the 3D relationships between BMO, the ASCO and PSCO, the Optic Nerve, the Central Retinal Vein, the Central Retinal Artery and the Long Posterior Ciliary Arteries (with and without their intrascleral branches) as visualized within the 3D Point Clouds in Normal control eyes.

A representative Normal Rat Eye is shown in figure 3.3. The relationship of BMO (red), ASCO (light blue) and PSCO (purple) relative to the optic nerve (green) can be seen from a clinical orientation in panel (A) and longitudinally in panel (B). In panels (C)-(F) the ASCO and PSCO Point clouds have been turned off and the CRV, CRA and LPCA point clouds have each been turned on.

First, notice that BMO is not round (A) but inferiorly elongated to accommodate the passage of the CRA and CRV (blue vessel) to the retina. Notice also, that BMO is shifted inferiorly relative to the ASCO and PSCO.

Second, notice the space between the neural tissue and the BMO, ASCO and PSCO in panel (B). At the level of BMO, the nerve abuts BM superiorly and there is space inferior to the nerve (filled by the CRV and CRA) as noted above. Note in Panel B, that because of the shift in BMO relative to the ASCO and PSCO, BM effectively extends beyond the scleral portion of the neural canal. Superiorly this creates an edge or extension of BM against which the neural bundle abuts. Inferiorly, it creates an elongation of BMO to accommodate the inferior vessels. The net effect of this shift is to create a superior-directed, oblique passage of the nerve through the wall of the rat eye that is best appreciated in Panels B, E and F. At the level of its passage through the anterior (ASCO) and posterior (PSCO) sclera the nerve is surrounded by a vascular plexus which we are not able to independently delineate using our current method.

Third, there are three long posterior ciliary arteries (LPCAs) which branch from the CRA behind the globe and pass together through the sclera (inferior to the neurovascular canal) to achieve the choroid. Their tangential rather than perpendicular passage through the sclera is depicted in (E) and (F) (see also Fig. 2.4F, H and Fig. 3.2).

Fourth, short posterior ciliary arteries (defined to be primary branches of the ophthalmic artery that individually pass through the sclera) were not identified. Instead the few arteries that independently pass through the sclera superiorly (G), where identified, appear to be retrobulbar branches of the LPCAs.

Fifth, unlike the primate eye in which there are 15 short posterior ciliary arteries that are relatively equidistant from one another around the circumference of the optic nerve, the choroidal blood supply in the rat appears to originate inferiorly from a dense plexus of intrascleral LPCA branches which effectively fill the space between the three LPCA branches (see Fig. 2.1D-F). Some of these vessels extend within the sclera and choroid superiorly, around the neurovascular canal. It is the density of the LPCAs and their intrascleral branches inferiorly that suggests an “effective” second opening in the sclera.

Sixth, the CRA and CRV are separated from each other and the nerve proper and supported by a "sling" (magenta) of scleral tissues that forms the inferior border of the neurovascular scleral canal opening and the superior border of the more-inferior arterial opening.

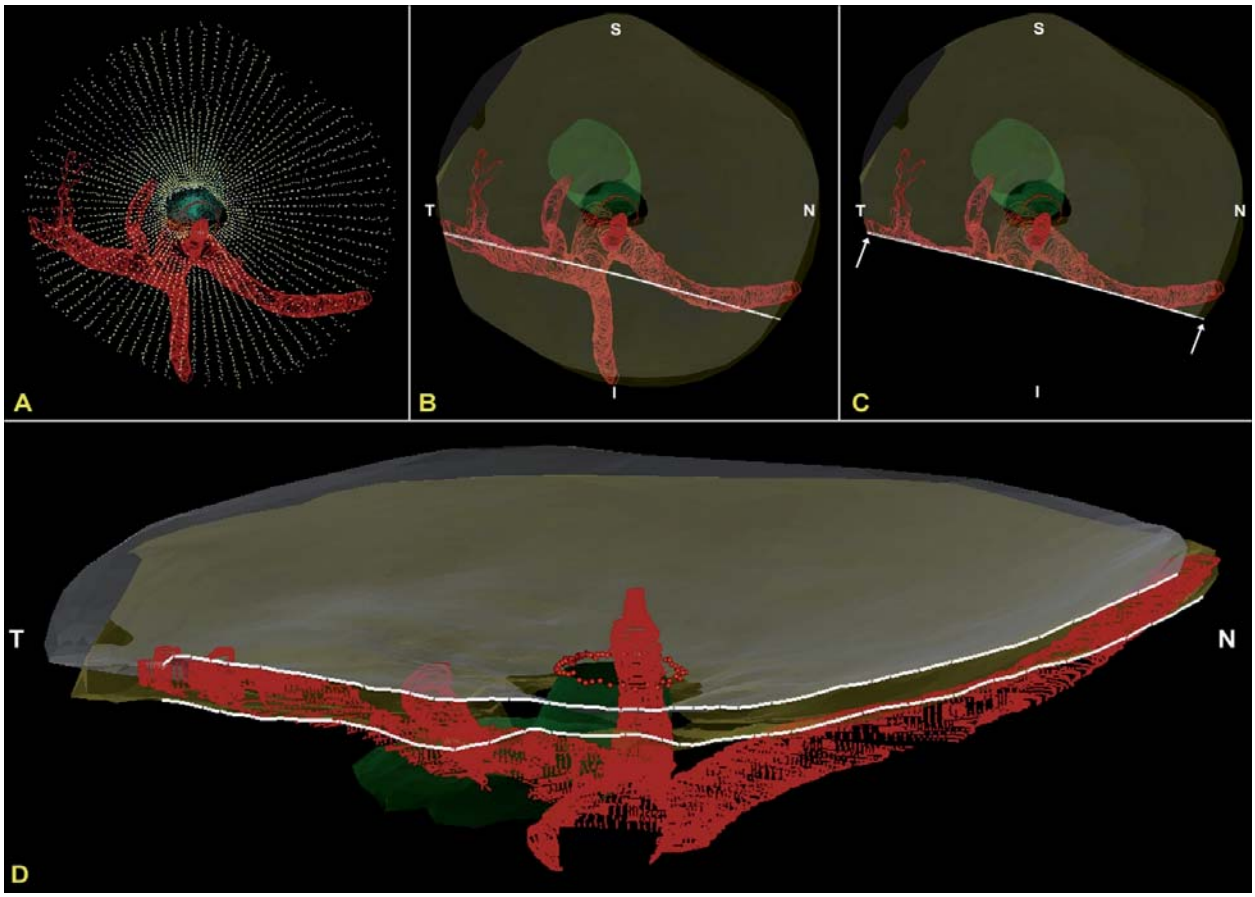

FIg. 3.2. The CRA passes perpendicularly and the LPCAs pass obliquely through the arterial scleral opening (views from the anterior or vitreous surface). (A) Standard Point cloud 3D reconstruction showing the scleral openings, nerve and BMO (B) The anterior and posterior scleral surface point clouds from the ONH in (A) have been transparently surfaced. Dark transparent circles correspond to the scleral openings and the nerve is transparent green, BMO is shown with red dots (C) A digital section through portions of both the nasal and temporal LPCAs has been removed and its cut surface is visualized in (D). Note that the inferior LPCA is, in this eye, a branch of the temporal LPCA (B). The temporal LPCA (left in B and D) enters the sclera near the CRA opening and slowly achieves the choroidal space well away from the ONH. The nasal LPCA (right in Band D) takes an even more gradual course through the sclera. In most eyes, the space between the LPCAs and the CRA contains choroidal branches from the LPCA which can be very dense (Fig. 2.1D-F). Finally, note the general superior and temporal passage of the nerve (transparent green) relative to the dark scleral canal openings and (red) inferior arterial tree (Panels B and C). N-Nasal; T- Temporal; I -Inferior; S - Superior.

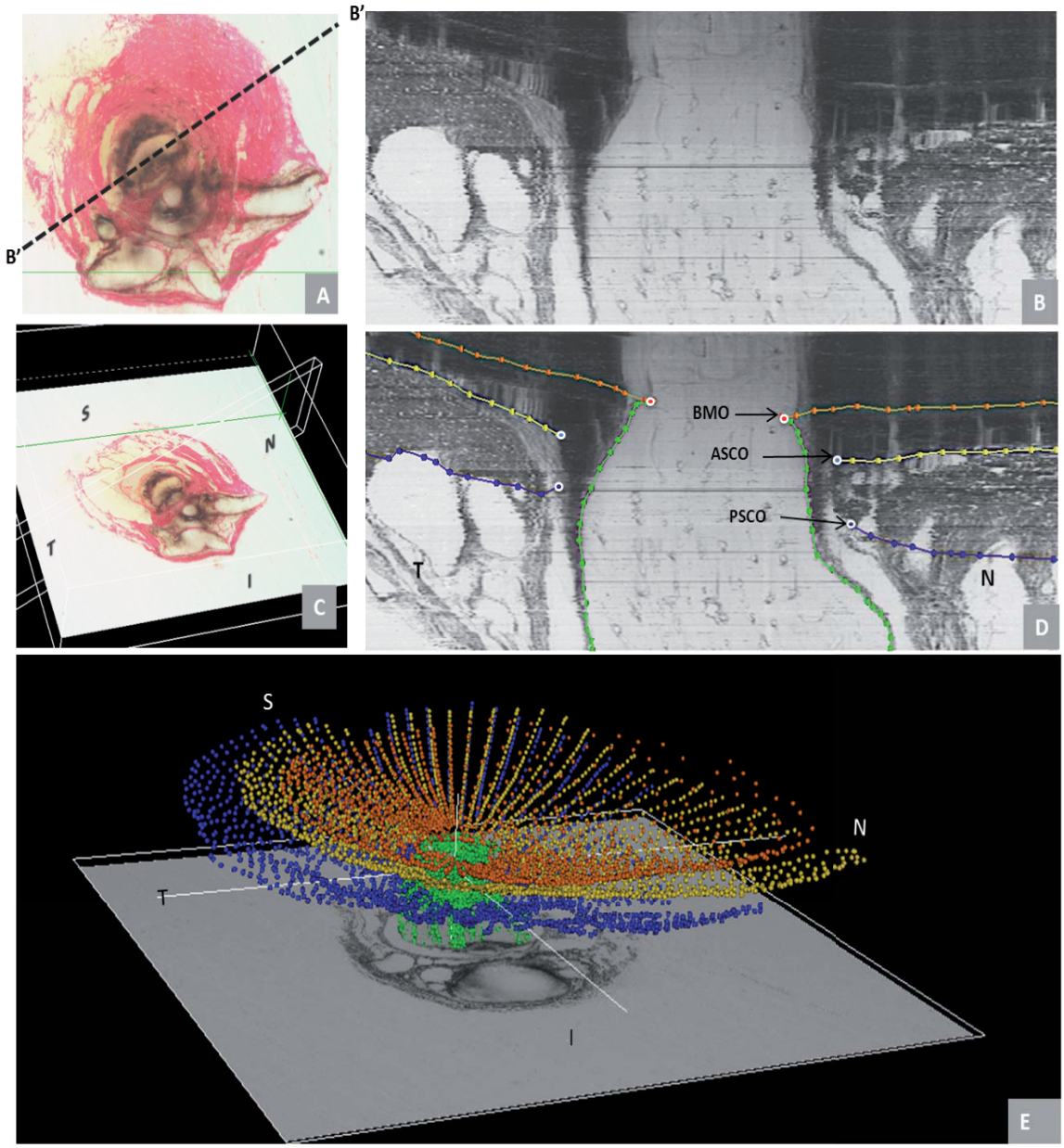

Fig. 3.3. Summary of the 3D relationships between BMO, the ASCO and PSCO, the Optic Nerve, the Central Retinal Vein, the Central Retinal Artery and the Long Posterior Ciliary Arteries (with and without their intrascleral branches) as visualized within the 3D Point Clouds in a representative normal control eye (see text for details)
N e Nasal; T e Temporal; I e Inferior; S e Superior

3.2.4. Principal quantitative results

3.2.4.1. Parameters treated Globally

3.2.4.1.1. BMO size and area

Parame-ters	Rat Number								Mean	SD
	1	2	3	4	5	6	7	8		
BMO Area (μm^2)	$6.15x10^4$	$4.75x10^4$	$5.26x10^4$	$5.71x10^4$	$5.18x10^4$	$6.89x10^4$	$5.40x10^4$	$5.82x10^4$	$5.65x10^4$	$0.50x10^4$
Mean BMO Radii (μm)	139 ± 18	122 ±14	129 ± 9	135 ±6	128 ± 12	148 ±8	131 ±10	136 ±7	133	6

Table 3.1. BMO Size by Study Eye.

3.2.4.1.2. *BMO Depht, ASCO Depth*, *PSCO Depth* and *Anterior Peripapillary Scleral Depth*

Parameters	Rat Number								Mean	SD
	1	2	3	4	5	6	7	8		
BMO Depth (μm)	16 ±11	47 ±9	39 ±4	36 ±9	26±10	37 ±6	-1 ±5	33 ±7	29	12
ASCO Depth (μm)	78 ±22	103 ±20	112 ±18	105 ±16	88±16	106 ±23	73 ±13	94 ±15	95	16
PSCO Depth (μm)	160 ±28	170 ±25	167 ±20	182 ±19	164 ±23	172 ±27	141 ±23	170 ±29	166	15
Scleral Depth (μm)	27±36	39±29	32±24	38±28	38±24	36±26	18±23	33±25	33	7

Table 3.2. *BMO Depth, ASCO depth, PSCO depth* and *Anterior Peripapillary Scleral Depth* relative to a peripheral anterior scleral reference plane.

3.2.4.1.3. Peripapillary Scleral and Choroidal Thickness

Parameters	Rat Number								Mean	SD
	1	2	3	4	5	6	7	8		
Scleral Thick-ness (μm)	109 ±26	105 ±23	107 ±19	105 ±19	105 ±15	109 ±18	97 ±23	103 ±21	105	4
Choroidal Thi-ckness (μm)	56 ±13	45 ±10	54 ±13	55 ±11	60 ±11	70 ±26	61 ±14	54 ±10	57	7

Table 3.3. Peripapillary Scleral and Choroidal Thickness

3.2.4.1.4. The Neurovascular scleral canal and its contained optic nerve

Parameters	Rat Number								Mean	SD
	1	2	3	4	5	6	7	8		
Neurovascular Canal										
ASCO Area (μm^2)	$1.49x10^5$	$1.22x10^5$	$1.23x10^5$	$1.02x10^5$	$1.56x10^5$	$1.12x10^5$	$1.38x10^5$	$1.33x10^5$	$1.29x10^5$	$0.21x10^5$
ASCO Radius (µm)	216 ±31	196 ±21	196 ±29	179 ±16	223 ±16	183 ±18	209 ±16	204 ±25	201	14
ASCO H/V Diameter Ratio	1.24	1.26	1.42	1.26	1.11	1.25	1.17	1.38	1.26	0.11
PSCO Area (μm^2)	$1.58x10^5$	$1.13x10^5$	$1.39x10^5$	$1.13x10^5$	$1.53x10^5$	NA	$1.57x10^5$	$1.09x10^5$	$1.35x10^5$	$0.27x10^5$
PSCO Radius (µm)	223 ±35	189 ±15	209 ±30	189 ±18	220 ±20	NA	223 ±17	185 ±23	204	17
PSCO H/V Diameter Ratio	1.47	1.09	1.39	1.19	1.13	NA	1.36	1.33	1.28	0.12
Optic nerve										
ON-ASCO Area (μm^2)	$4.54x10^4$	$4.25x10^4$	$4.36x10^4$	$4.45x10^4$	$5.36x10^4$	$4.73x10^4$	$4.15x10^4$	$5.20x10^4$	$4.63x10^4$	$0.95x10^4$
ON-ASCO Radius (µm)	117 ±33	112 ±34	114 ±32	115 ±32	127 ±29	119 ±28	112 ±25	126 ±24	118	12
ON-ASCO H/V Diameter Ratio	1.82	2.18	2.18	2.08	1.97	1.87	1.86	1.66	1.95	0.16
ON-PSCO Area (μm^2)	$4.80x10^4$	$4.28x10^4$	$4.36x10^4$	$3.99x10^4$	$5.34x10^4$	NA	$4.24x10^4$	$4.14x10^4$	$4.42x10^4$	$0.97x10^4$
ON-PSCO Radius (µm)	117 ±41	108 ±44	107 ±41	104 ±43	124 ±41	111±42	111 ±33	106 ±43	111	12
ON-PSCO H/V Diameter Ratio	2.40	2.72	2.59	2.97	2.29	NA	1.89	1.81	2.38	0.35
ON Volume (μm^3)	$3.95x10^6$	$2.92x10^6$	$2.29x10^6$	$3.25x10^6$	$4.04x10^6$	$3.20x10^6$	$2.88x10^6$	$3.67x10^6$	$3.27x10^6$	$0.89x10^6$

Table 3.4. The neurovascular scleral canal and its contained optic nerve

3.2.4.2. Parameters treated Regionally

Parameters[1]	Superior Mean±SD	Inferior Mean±SD	Nasal Mean±SD	Temporal Mean±SD
Neurovascular Canal				
BMO Radius	135±10	138±15	132±11	128±16
BMO Depth	27±13	32±17	32±16	26±17
ASCO Radius[2]	187±22	186±22	217±23	214±20*
ASCO Depth	78±22	109±21	91±22	79±19
PSCO Radius[2]	196±25	188±22	213±22	222±23*
PSCO Depth	145±16	189±19	177±24	152±20
Optic Nerve				
ON-ASCO Radius[2]	98±9	90±14	141±19*	142±2*
ON-PSCO Radius[2]	86±10*	68±12	145±31*	146±29*
Sclera/choroid				
Scleral Thickness[2]	99±11*	91±18	113±22*	116±14*
Scleral Depth[2]	30±25*	41±29*	37±27*	22±26
Choroidal Thickness	57±11	56±14	59±23	55±14

[1]Only parameters which include multiple measurements per region were included in this analysis
[2] Regional effects for this parameter are statistically significant within ANOVA using a linear mixed effects model ($p<0.05$, after adjustment for multiple comparisons).
Blue: quadrant with the lowest value. All other quadrants were compared to the quadrant with the lowest value. *this regional value is significantly different from the lowest regional value of this parameter ($p<0.05$, ANOVA after adjustment for multiple comparisons.

Table 3.5. Overall Regional Values for each Parameter

3.2.4.2.1 Eye-specific comparisons of *BMO*, *ASCO* and PSCO in Normal Control Eyes.

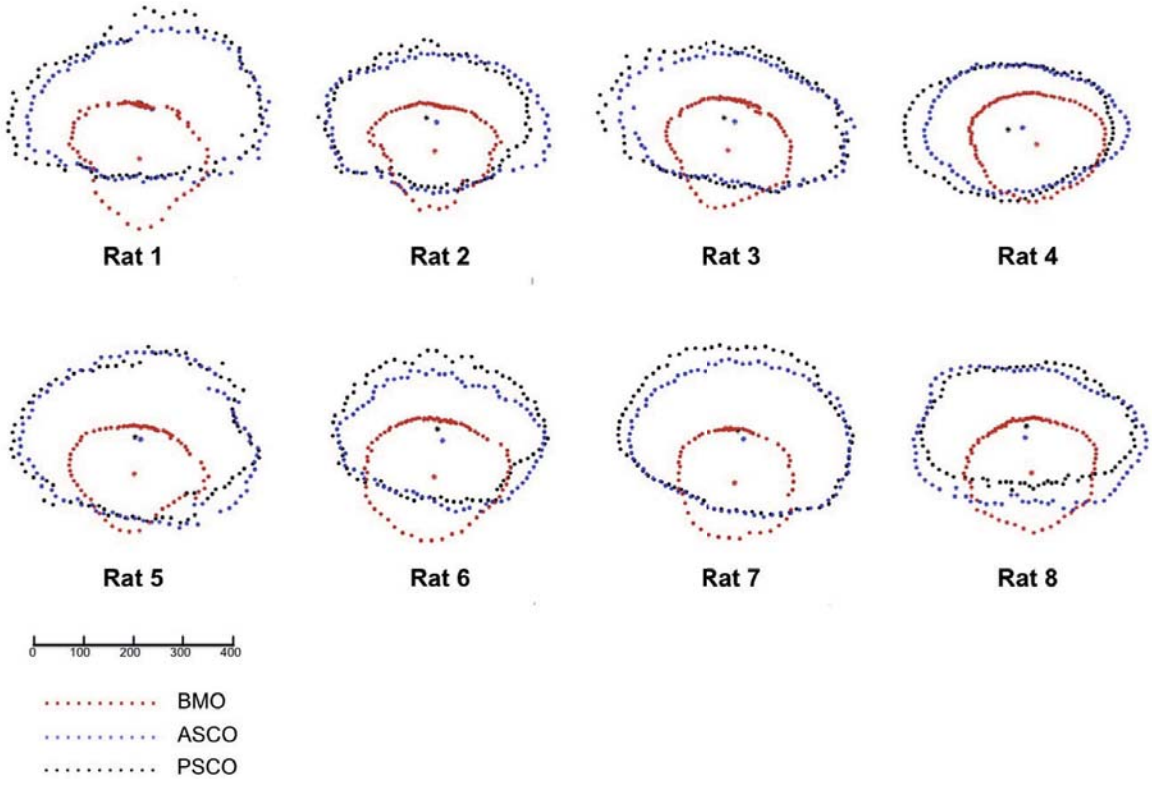

Fig. 3.4.. Eye-specific comparisons of BMO (red), ASCO (blue) and PSCO (black) for the 8 normal control eyes. All data are in right eye configuration. Delineated points for each structure along with their centroid are superimposed by projection to the BMO reference plane for comparison purposes. These data suggest the extent to which BMO is shifted inferiorly relative to the ASCO and PSCO for all 8 study eyes. Combined with the oblique course of the optic nerve bundle visualized in Fig. 3.3. above, these data provide anatomic support for the oblique course of the nerve from BMO through the PSCO, the superior extension of BM (and inferior shift of BMO) relative to the ASCO and PSCO, and the physical abutment of RGC axons against BMO superiorly in the rat ONH. The scale is in micrometers.

3.2.5. COPY OF THE FIRST PAPER

Rat Optic Nerve Head Anatomy within 3D histomorphometric reconstructions of normal control eyes.

Marta Pazos, Hongli Yang, Stuart K. Gardiner, William O.Cepurna, Elaine C. Johnson, John C. Morrison, Claude F. Burgoyne.

Exp Eye Research 139 (2015) 1-12

Experimental Eye Research 139 (2015) 1–12

Contents lists available at ScienceDirect

Experimental Eye Research

journal homepage: www.elsevier.com/locate/yexer

Rat optic nerve head anatomy within 3D histomorphometric reconstructions of normal control eyes☆

Marta Pazos [a, d, 1], Hongli Yang [a, 1], Stuart K. Gardiner [b], William O. Cepurna [c], Elaine C. Johnson [c], John C. Morrison [c], Claude F. Burgoyne [a, *]

[a] Devers Eye Institute, Optic Nerve Head Research Laboratory, Legacy Research Institute, Portland, OR, USA
[b] Devers Eye Institute, Discoveries in Sight Research Laboratories, Legacy Research Institute, Portland, OR, USA
[c] Kenneth C. Swan Ocular Neurobiology Laboratory, Casey Eye Institute, Oregon Health and Science University, Portland, OR, USA
[d] Hospital de l'Esperança, Parc de Salut Mar, Universitat Autònoma de Barcelona, Barcelona, Spain

ARTICLE INFO

Article history:
Received 30 December 2014
Received in revised form
24 April 2015
Accepted in revised form 19 May 2015
Available online 26 May 2015

Keywords:
Glaucoma
Rat
Optic nerve head
Neural canal
Scleral canal
Optic nerve

ABSTRACT

The purpose of this study is to three-dimensionally (3D) characterize the principal macroscopic and microscopic relationships within the rat optic nerve head (ONH) and quantify them in normal control eyes. Perfusion-fixed, trephinated ONH from 8 normal control eyes of 8 Brown Norway Rats were 3D histomorphometrically reconstructed, visualized, delineated and parameterized. The rat ONH consists of 2 scleral openings, (a superior neurovascular and inferior arterial) separated by a thin connective tissue strip we have termed the "scleral sling". Within the superior opening, the nerve abuts a prominent extension of Bruch's Membrane (BM) superiorly and is surrounded by a vascular plexus, as it passes through the sclera, that is a continuous from the choroid into and through the dural sheath and contains the central retinal vein (CRV), (inferiorly). The inferior scleral opening contains the central retinal artery and three long posterior ciliary arteries which obliquely pass through the sclera to obtain the choroid. Bruch's Membrane Opening (BMO) is irregular and vertically elongated, enclosing the nerve (superiorly) and CRV and CRA (inferiorly). Overall mean *BMO Depth*, *BMO Area*, *Choroidal Thickness* and peripapillary *Scleral Thickness* were 29 μm, 56.5 × 10^3 μm^2, 57 μm and 104 μm respectively. Mean anterior scleral canal opening (*ASCO*) and posterior scleral canal opening (*PSCO*) radii were 201 ± 15 μm and 204 ± 16 μm, respectively. Mean optic nerve area at the ASCO and PSCO were 46.3 × 10^3 ± 4.4 × 10^3 μm^2 and 44.1 × 10^3 ± 4.5 × 10^3 μm^2 respectively. In conclusion, the 3D complexity of the rat ONH and the extent to which it differs from the primate have been under-appreciated within previous 2D studies. Properly understood, these anatomic differences may provide new insights into the relative susceptibilities of the rat and primate ONH to elevated intraocular pressure.

1. Introduction

Nonhuman primate (NHP) experimental glaucoma is a well-established animal model for studying human glaucoma in part because the NHP optic nerve head (ONH) shares a close anatomic association with the human ONH. However, these animals are impractical for studies that require large animal numbers and at present cannot easily be genetically manipulated. For these and other reasons, mouse and rat (Dai et al., 2012; Howell et al., 2007; Johnson and Tomarev, 2010; Mabuchi et al., 2003, 2004; May, 2008; Morrison et al., 2011, 2008; Pang and Clark, 2007; Ruiz-Ederra and Verkman, 2006) experimental glaucoma models are increasingly utilized to study the mechanisms of chronic intraocular pressure-induced optic nerve head (ONH) and retinal ganglion cell (RGC) axon injury.

The anatomy of the rodent ONH is widely recognized to differ from the human and non-human primate (Dai et al., 2012; Morrison et al., 2011, 1999; Sugiyama et al., 1999). Post mortem,

☆ Supported in part by NIH grants R01EY011610 (CFB), R01EY10145 (JCM) and R01EY16866 (ECJ)) from the National Eye Institute, National Institutes of Health, Bethesda, Maryland; The Legacy Good Samaritan Foundation, Portland, Oregon; the Sears Trust for Biomedical Research, Mexico, Missouri; the Alcon Research Institute, Fort Worth, Texas; and an unrestricted grant from Research to Prevent Blindness.
* Corresponding author. Devers Eye Institute, Optic Nerve Head Research Laboratory, 1225 NE 2nd Ave, Portland, OR, 97232, USA.
E-mail address: cfburgoyne@deverseye.org (C.F. Burgoyne).
[1] Marta Pazos and Hongli Yang are co-first authors of this work.

http://dx.doi.org/10.1016/j.exer.2015.05.011
0014-4835/

histologic measurements in fixed and processed tissues suggest that the rat eye is approximately 6.29 mm in axial length and 6.41 mm in diameter, with a posterior sclera that is about 5 to 10 times thinner and a circular scleral canal that is about 4 times smaller than the human eye. Normal rat optic nerve axon counts range from 0.11 to 0.14 million axons compared to 1.2 to 2.0 million in the human eye and from 0.9 to 1.4 million in monkeys. Reported differences in normal rat ONH anatomy include a lack of a well-defined collagenous lamina cribrosa, a cellular lamina-like structure formed by sparse connective tissue associated with blood vessels lined with astrocytes (Dai et al., 2012; Li et al., 2015) and composed of extracellular matrix materials which are themselves similar to those within the primate lamina cribrosa (Fujita et al., 2000; Johansson, 1987; Morrison et al., 1995a, 2011), a perineural vascular plexus that surrounds the optic nerve within the scleral canal (Morrison et al., 1999; Sugiyama et al., 1999) and an ophthalmic artery (OA) that splits just posterior to the globe into the central retinal artery (CRA) and three long posterior ciliary arteries (LPCAs) (Morrison et al., 1999; Sugiyama et al., 1999). All previous characterizations of the rat ONH have been based upon traditional histologic sections or 2D photos of 3D vascular casts. These studies have therefore lacked the ability to digitally sample and visualize the same reconstruction from multiple viewpoints at the same time so as to confront, understand and characterize its principal organizing relationships.

The purpose of the present study was to perform high-resolution (1.5 μm × 1.5 μm × 1.5 μm voxel) 3D histomorphometric reconstruction of the ONH and peripapillary scleral trephines of 8 normal control eyes of 8 Brown Norway rats so as to describe and quantify the important macroscopic and microscopic morphologic relationships. Our conceptual framework for organizing the anatomy of the rat ONH is explained in Figs. 1 and 7. These concepts are necessary to understand the logic of our measurement parameters which are explained in Appendix Figs. 1–4. Table 1 is a reference for all abbreviations. In this report we present data on the contralateral "normal" control eyes of 8 rats that were given unilateral experimental glaucoma (EG) in one eye. In a follow-up study, we will use similar techniques to test hypotheses about how these relationships will change in early rat EG.

2. Materials and methods

2.1. Animals and eyes

All animals were treated in accordance with the ARVO Statement for the Use of Animals in Ophthalmic and Vision Research. Eight normal control eyes of 8 male Brown Norway rats, between 9.5 and 10.5 months of age, were studied (Table 2) under constant light conditions for this report. Eye-specific mean IOP (by TonoPen testing (Moore et al., 1995, 1993; Morrison et al., 2009)) for the 8 eyes of this study was within the normal range of our previous reports for animals under constant light (Johnson et al., 2015, 1996; Moore et al., 1996; Morrison, 2005; Morrison et al., 2005; Pang and Clark, 2007). These eyes represent the normal control eyes of 8 rats that had undergone 4 weeks of unilateral chronic IOP elevation following hypertonic saline treatment (Jia et al., 2000; Morrison et al., 1997) to the trabecular meshwork of the contralateral study eye. A follow up report, will describe the changes in the 8 early EG eyes of these same animals, however, a delineation reproducibility study, described below, was performed in both eyes of each animal.

2.2. Rat Euthanasia and fixation

All animals were sacrificed under isoflurane anesthesia by transcardial injection (1 ml/kg) of heparin (1000 U/ml) containing 10 mg/ml sodium nitroprusside followed by 1 L of 5% glutaraldehyde in 0.1 M phosphate buffer (pH 7.2).

2.3. 3D histomorphometric reconstruction of the ONH

The ONH and peripapillary sclera of each eye were trephined (3-mm-diameter), embedded in paraffin, mounted to a microtome (RM2165; Leica, Wetzlar, Germany) and serial sectioned at 1.5 μm thickness from the vitreous surface through the optic nerve head into the orbital optic nerve (Burgoyne et al., 2004). After each section was cut, the block surface was stained with a 1:1 (v/v) mixture of Ponceau S and acid fuchsin stains, then imaged at a resolution of 1.5 × 1.5 μm per pixel using a custom device (Burgoyne et al., 2004). For each ONH 275 to 501 serial digital transverse section images were thus generated, aligned and stacked into a digital 3D reconstruction (Burgoyne et al., 2004; Downs et al., 2007; Yang et al., 2007a, 2007b, 2009b, 2011).

2.4. Initial qualitative 3D visualization of each ONH reconstruction and comparison to existing light and electron microscopy

To gain an initial understanding of the anatomy (Figs. 1 and 2) and to design a landmark and parameterization scheme appropriate to the rat ONH (Appendix Figs. 1–4), 40 radial digital sagittal sections from each ONH reconstruction (Fig. 3A and B) were viewed by the authors (as a group) using our custom Multiview 3D visualization software (based on the Visualization Toolkit [VTK], Clifton Park, NY) (Burgoyne et al., 2004; Downs et al., 2007; Morrison et al., 1999; Yang et al., 2007a, 2007b, 2009b). Where indicated, selected comparisons were made to existing stained histologic sections, electron micrographs and vascular casting photographs from normal rat eyes that had been studied as part of a series of previous reports (Morrison et al., 2011, 1995b, 2005, 1997). With the basic macroscopic and microscopic relationships thus established (Figs. 1 and 2), strategies for delineation (Figs. 3 and 4) and parameterization (Appendix Figs. 1–4) were developed and executed. Final qualitative 3D visualization of the delineated point clouds (Figs. 3–7) were then performed to confirm the anatomic relationships described herein.

2.5. 3D delineation of the ONH and peripapillary scleral landmark points (Fig. 3)

We have previously published our 3D delineation method in detail (Downs et al., 2007; Yang et al., 2007b, 2011). In summary, each 3D ONH reconstruction was loaded into Multiview memory and the delineator assigned the approximate center of the optic nerve (Figs. 2 and 3) as the center of rotation, through which, forty, 7-voxel thick, digital radial sagittal slices of the digital 3D reconstruction were serially served at 4.5° intervals for delineation (Fig. 3A, B and C). Because visualization of Bruch's Membrane (BM), Bruch's Membrane Opening (BMO) and several deep ONH landmarks was most consistent within Green channel as opposed to white light section images, delineation was carried out within green channel digital section images for each study eye. Four landmark surfaces and three pairs of neurovascular canal landmarks (one point on each side of the canal) were delineated within each digital section image. The landmark surfaces were: (1) BM; (2) the anterior and (3) posterior surfaces of peripapillary sclera; and (4) the optic nerve boundary extending from BMO, through the neurovascular scleral canal and along the pia mater to the posterior edge of the reconstruction (Fig. 3B). The landmark points were BMO, the anterior scleral canal opening (ASCO) and the posterior scleral canal opening (PSCO).

Delineation of these landmarks was "three dimensional"

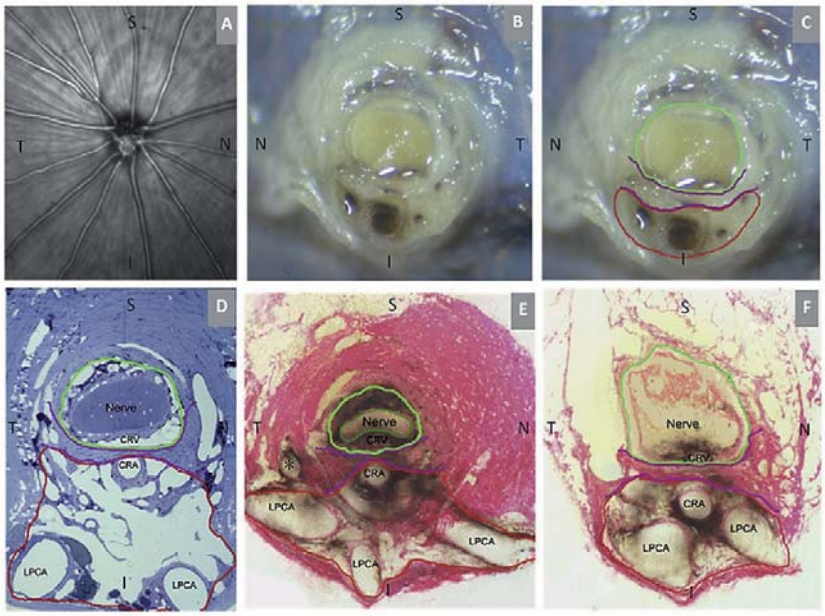

Fig. 1. Rat Optic Nerve Head Macroscopic and Microscopic Relationships I – Transverse Sections. (A) 30° SD-OCT Infrared Reflectance image of the rat optic disc (the vitreous surface of the optic nerve head) (courtesy of Brad Fortune). (B) Macroscopic appearance of the cut surface of the rat optic nerve just posterior to the scleral shell (view from the back of the eye). (C) Principal macroscopic relationships: 1) the **neurovascular bundle (green)**; and the more-inferior **2) arterial bundle (red)**; are separated by a sling of scleral tissues **3) the scleral sling (purple)** (view from the back of the eye). (D–E) Principal scleral openings. Unlike the primate, there are two principal openings within the sclera of the rat ONH: 1) the neurovascular canal (green) and the more-inferior arterial opening (red), which is not a well-defined canal, being irregular due to the choroidal branches of the LPCAs (D and E) and separated from the neurovascular canal by the scleral sling (purple). Unlike the primate, which has on average 15 short posterior ciliary arteries that are evenly distributed around the circumference of the scleral canal, the inferior concentration of the LPCAs and the density of their intrascleral branches to the choroid combined with the actual CRA canal (D–F) suggest an "effective" second opening in the sclera. (D) Transverse histologic section through the scleral portion of the optic nerve head demonstrating the same relationships seen posterior to the globe in panels B and C. Note that the neurovascular bundle consists of the optic nerve surrounded by a vascular plexus within the inferior portion of which runs the CRV. The arterial bundle is made up of the central retinal artery, the two main LPCAs and their intrascleral branches to the choroid (vascular spaces in between the principal arteries – not labeled). (E) A digital transverse section image from a histomorphometric reconstruction demonstrating the same relationships as (D). (F) Digital section image from the same eye just posterior to the globe and close to the view seen macroscopically in (C). The intrascleral (E) and retrobulbar short posterior ciliary arteries (F) are branches of the LPCAs rather than the Ophthalmic Artery. A preferential superior-temporal course of the optic nerve and neurovascular bundle as they pass through the sclera into the orbit are suggested by comparing the green circle in (F) to (E). CRV– Central retinal vein, LPCAs- Long Posterior Ciliary Arteries. N – Nasal; T – Temporal; I – Inferior; S – Superior.

because while marking the digital sagittal section image (Fig. 3B), the delineator simultaneously viewed a second window, (that was linked to the first), displaying the cursor's real-time 3D location within the appropriate digital transverse section image (Fig. 3A). The 3D Cartesian coordinates and category number for each mark were saved, generating a 3D point cloud representing each of the marked structures (Fig. 3D). These point clouds were then surfaced and could themselves be cut and visualized at any angle allowing observations and measurements to be made between the regions of actual delineation.

2.6. 3D delineation of the ONH and peripapillary scleral vasculature and scleral sling (Fig. 4)

As opposed to the landmark and surface delineations outlined above which were performed within serial digital sagittal section images (Fig. 3), vessel and scleral sling delineation were performed within every fourth digital transverse section image while simultaneously viewing linked windows which displayed vertical or horizontal digital sagittal sections (notice this is not clinical vertical or horizontal sections due to our embedding angles) of the reconstruction through the point being delineated (Fig. 4A–D). The following landmark categories were individually marked and cataloged within each delineated transverse section image: (1) Ophthalmic artery (OA); (2) central retinal artery (CRA); (3) long posterior ciliary arteries (LPCAs); (4) short posterior ciliary arteries (SPCAs); (5) Central retinal vein (CRV); and (6) the vascular or neural boundary of the scleral sling (Figs. 1, 2 and 4). Three dimensional reconstructions of the landmark point clouds (Fig. 4E–H and Fig. 5) were then visualized together and separately (turning each landmark category on and off) so as to determine their principal macroscopic relationships.

2.7. Delineation reproducibility study

Both the normal and experimental glaucoma eye of each animal were delineated by a single delineator (MP). Upon completion of the initial delineation of each eye, the marks were reviewed by 2 senior authors (CFB and HY) to expand our understanding of the anatomy and to reach agreement on the anatomic landmarks of greatest interest. Both eyes of three animals were then delineated on two subsequent occasions by the same delineator (MP), at least 2 weeks apart, to assess intra-delineator variability. The Intraclass-Correlation Coefficient (ICC) (see statistical analysis, below) for all

Table 1
Abbreviations and definitions table.

Abbreviation	Meaning
ANOVA	Analysis of Variance
ASCO	Anterior Scleral Canal Opening
BM	Bruch's Membrane
BMO	Bruch's Membrane Opening
CI	Confidence Interval
CRA	Central Retinal Artery
CRV	Central Retinal Vein
Eye-specific results	Parameters related to an individual eye
GLS	Generalized Least Squares
H/V	Horizontal/Vertical Ratio
I	Inferior
ICC	Intraclass Correlation Coefficient
IOP	Intraocular Pressure
LPCA	Long Posterior Ciliary Artery
N	Nasal
NA	Not Available or Not Applicable
OA	Ophthalmic Artery
OD	Right Eye
ON	Optic Nerve
ON-ASCO	Optic Nerve area at the level of ASCO
ON-PSCO	Optic Nerve area at the level of PSCO
ONH	Optic Nerve Head
OS	Left Eye
Overall results	Global parameters (all rats together)
PSCO	Posterior Scleral Canal Opening
S	Superior
SD	Standard Deviation
SPCA	Short Posterior Ciliary Artery
T	Temporal

reported parameters were calculated (Rosner, 2011).

2.8. Parameterization and quantification

Parameters are italicized to distinguish their behavior from the behavior of the underlying anatomic landmarks (which are not italicized).

2.9. Bruch's Membrane Opening (BMO) and the neurovascular scleral canal (Appendix Figs. 1 and 2)

For each ONH reconstruction, individual planes were fit to the 80 BMO points, 80 neurovascular ASCO points and 80 neurovascular PSCO points, (2 points for each landmark within each of 40 digital radial sagittal sections, as outlined above (Appendix Fig. 1A) using a least-squares algorithm. The BMO plane became the reference plane for a series of subsequent measurements and the basis for the second peripheral anterior scleral reference plane (Appendix Figs. 1A, 2 and 3). The cross-sectional area of BMO (*BMO Area*) as well as the neurovascular sclera canal at the level of the ASCO and PSCO (*ASCO* and *PSCO area*) were calculated as the area within the projection of the BMO, ASCO and PSCO points to their respective fitted planes (Appendix Fig. 1B). Using the centroid of the projected BMO, ASCO and PSCO points, 80 radius measurements were made within their respective fitted planes at 4.5° intervals (Appendix Fig. 1C). To assess their relative shapes, the *Horizontal/Vertical (H/V) Diameter Ratios* were calculated for ASCO, and PSCO.

Table 2
Animal and eye data.

No.	ID	Age at sacrifice (months)	Eye	Mean IOP (mmHg)	Number of digital serial section images
1	MR8	9.5	OD	28.5	400
2	MR10	9.5	OS	28.8	313
3	MR1	9.5	OS	28.3	398
4	MR9	9.5	OS	28.4	307
5	MR12	10.5	OS	28.5	275
6	MR11	10.5	OS	28.3	375
7	MR5	9.5	OD	28.8	484
8	MR4	9.5	OD	28.4	501

No. – Rat number for this Study; ID – Laboratory Rat Identification Number; Eye – OD–Right eye, OS-left eye; Mean IOP (mmHg) – Mean IOP of all IOP measurements taken AM and PM for each eye; Number of Digital Serial Section Images-number of digital serial section images required to reconstruct each optic nerve head.

2.10. Optic nerve cross-sectional area within the scleral canal (Appendix Fig. 2)

Optic nerve (ON) cross-sectional area, radii and shape (*H/V Diameter Ratios*) were quantified within the ASCO (*ON-ASCO*) and PSCO (*ON–PSCO*) planes using the delineated optic nerve boundary as illustrated in Appendix Fig. 2. *Optic Nerve Volume* (the volume defined by the ASCO plane, PSCO plane and optic nerve boundary) was also quantified.

2.11. Anterior scleral sling depth, BMO/ASCO/PSCO depth, and Anterior Peripapillary Scleral Surface Depth relative to a peripheral anterior scleral reference plane (Appendix Fig. 3)

BMO Depth, *ASCO Depth*, *PSCO Depth* (Appendix Fig. 3C) were separately measured relative to a peripheral anterior scleral reference plane (Appendix Fig. 3A) within each digital sagittal section image as illustrated in Appendix Fig. 3B and C. *Anterior Peripapillary Scleral Depth* was measured relative to the same reference plane commencing at 350 μm and extending to 700 μm from the projection of the ASCO centroid line (in 50 μm increments) as illustrated in Appendix Fig. 3D. These distances were chosen because this was a region of sclera that was common to all studied eyes (i.e. 350 μm corresponded to the smallest radius and 700 μm the largest radius from the centroid of ASCO that included sclera for all 360° within each of the 8 rat volumes).

2.12. Peripapillary Scleral and Peripapillary Choroidal Thickness (Appendix Fig. 4)

Peripapillary Scleral and *Choroidal Thickness* were separately measured within each digital sagittal section image in 50 μm increments radially commencing at 350 μm and extending to 700 μm (*Peripapillary Scleral Thickness*) or 600 μm (*Peripapillary Choroidal Thickness*) from the projection of the ASCO centroid onto the BMO reference plane as illustrated in Appendix Fig. 4. Again 350 μm corresponded to the smallest radius outside the major vessels and 600 or 700 μm (depending on the parameter) was the largest radius present in all the specimens.

2.13. The inferior arterial scleral opening

Because its boundaries are not consistently clearly visible we were not able to quantify the inferior opening in the sclera created by the central retinal artery, the LPCAs and the LPCA intrascleral branches using our current techniques.

2.14. Statistical analysis

Mixed effects linear regression models were formed to compare the radial structures (*ASCO radius vs PSCO radius*, *ON-ASCO radios vs ON-PSCO radius*). Within each rat, anterior and posterior scleral and neural canal sizes were compared using a linear model fitted with generalized least squares (GLS). To assess consistency or reproducibility of the quantitative measurements made in different days

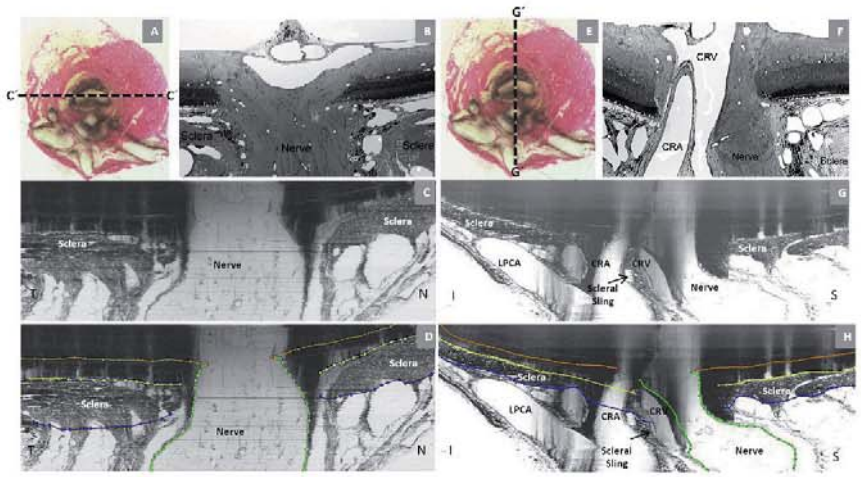

Fig. 2. Rat Optic Nerve Head Macroscopic and Microscopic Relationships II. Horizontal (panels – A, B,C and D) and vertical (panels – E, F, G and H) sagittal views of the rat ONH centered upon the scleral portion of the neurovascular canal (A and E). Panels (C) and (G) are digital horizontal and vertical sagittal sections (location relative to the ONH marked as C′ and G′ in (A) and (E) of the same histomorphometric reconstruction in which acquired transverse section images were shown in Fig. 1. Panels D and H are the same sections showing the delineation of the different structures. The process of creating digital radial sagittal sections from the histomorphometric volume is explained in Fig. 3, below. Panels (B) and (F) are histologic sections of another eye acquired in locations similar to (C) and (G). Note the continuity of the choroidal and perineural vascular plexus within both sections. Most published descriptions of the rat ONH show horizontal (C) or vertical (G) sagittal sections of the ONH that are cropped close to the end of the sclera which has the effect of emphasizing the similarities of the neurovascular canal to the scleral canal of the primate. However within the horizontal (C) and vertical (G) digital sagittal sections of the histomorphometric reconstructions, the importance of the vascular plexus that surrounds the nerve within the neurovascular canal, the sclera sling and the inferior arterial vessels can be appreciated. Note also the general temporal slant of the nerve in (B) and the superior slant of the nerve in (F). Taken together, these observations within horizontal and vertical sagittal sections confirm the general superior temporal path of the optic nerve tissues suggested within the serial transverse section images of Fig. 1 (see Figure legend). Note that within panels (C) and (G) of Fig. 2, the dark shadows extending upward from the sclera are a result of the fact that in serial transverse sectioning from the vitreous (top) to the orbital optic nerve (bottom) the dark choroidal pigment can be seen until the sectioning plane passes through it, creating the appearance of a shadow within the retina and vitreous. CRV– Central retinal vein, LPCA – Long Posterior Ciliary Arteries. CRA-Central Retinal Artery; N – Nasal; T – Temporal; I – Inferior; S – Superior.

measuring the same parameters, the ICC was calculated from one-way ANOVA (Rosner, 2011). When multiple measurements within an eye were not present (*ASCO area*, *PSCO area*) a linear regression was performed. ANOVA using linear mixed effect model was used to determine whether there was an overall regional effect. A secondary analysis was carried out to compare the quadrant with the lowest value to the rest of other three quadrants. Statistical significance was defined to occur at $p < 0.05$ after adjusted to multiple comparisons. Analysis was performed either in R (the R Foundation for Statistical Computing, Vienna, Austria) or Microsoft Excel (Microsoft, Redmond, WA, USA).

3. Results

Animal demographic data are reported in Table 2.

3.1. Principal macroscopic and microscopic relationships

The rat optic nerve head consists of two principal passages through the sclera (Figs. 1–5): a well demarcated superior neurovascular canal that contains the optic nerve and its peri-neural vascular plexus (continuous with and extending from the choroid to the dural sheet veins and containing the CRV, inferiorly) and a less clearly defined, more-inferior arterial opening through which pass the CRA, LPCAs and their intrascleral branches to the peripapillary choroid. The connective tissue wall of these two openings and the outer walls of the vessels that pass through them fuse with a sling of scleral connective tissues to form a separating structure that we have called the *scleral sling*.

Figs. 1 and 2 describe these relationships in 2 dimensions and Figs. 3–7 utilize the 3D point clouds of the delineated landmarks from a representative rat ONH to emphasize the following features. First, at the level of BMO, BM extends prominently beyond the scleral canal opening (Figs. 2, 5 and 6) superiorly to physically abut the RGC axon bundles, (Fig. 5) while both the CRV and CRA physically separate the RGC axons from BMO inferiorly (Fig. 5). The fact that the CRA passes through the sclera inferior to the neurovascular canal (within its own opening) but joins the CRV within the inferior portion of BMO, leaves BMO irregularly shaped with an inferior elongation that is not present in the primate eye (Figs. 5 and 6).

Second, at the level of the sclera, also unlike the primate, there is a prominent vascular plexus between the neural tissue and the ASCO and PSCO in Figs. 2B and 3B. Within the scleral portion of the neurovascular canal there were sporadic organized connective tissue structures within our reconstructions; however no clear evidence of laminar beams were observed using our technique. Also unlike the primate in which the shape of the optic nerve as it passes through the sclera ranges from circular to a vertical ellipse, in the rat eye, the optic nerve passes through the neurovascular scleral canal as a horizontal, kidney bean-like ellipse, with the ratio of horizontal to vertical diameter varying from 1.66 to 2.18 in these 8 normal ONH (see the quantitative results, below).

Third, there are 3 LPCAs which branch from the CRA behind the globe and pass (together with the CRA) through the sclera inferior to the neurovascular canal to achieve the choroid (Figs. 1, 2, 4, 5 and 7). Their tangential rather than perpendicular passage through the sclera is depicted in Fig. 7 in which the anterior and posterior scleral point clouds have been surfaced so as to enhance LPCA and scleral visualization. Fourth, short posterior ciliary arteries (SPCA) - defined to be primary branches of the ophthalmic artery that individually pass through the sclera do not appear to exist in the rat

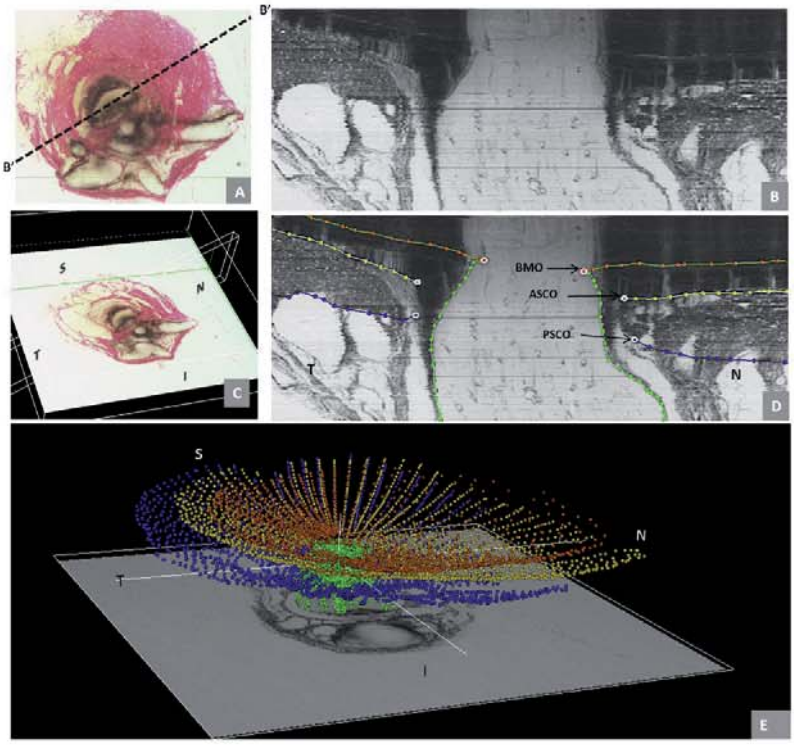

Fig. 3. 3D Delineation of the ONH and Peripapillary Scleral Landmarks. Delineated landmark points within 40 digital radial sagittal section images of a representative ONH. The delineator first assigned the center of the scleral portion of the optic nerve (A) to be the center of rotation through which, forty, 7-voxel thick, digital radial sagittal section images (B) of the digital 3D reconstruction (C) were serially served at 4.5° intervals. The Nasal-Temporal location of (B) is shown here two dimensionally (dotted line marked B'-B') within the transverse section image in (A) and three-dimensionally (7 μm thick white-edged rectangle) within the 3D reconstruction in (C). Within each digital sagittal section image (B) the delineator marked four landmark surfaces and three pairs of neurovascular canal landmarks (one point on each side of the canal). The landmark surfaces were: (1) Bruch's membrane (orange); (2) the anterior (yellow) and (3) posterior (blue) surfaces of peripapillary sclera; and (4) the optic nerve boundary extending from Bruch's membrane opening, through the scleral canal and along the pia mater to the posterior edge of the reconstruction (green). The landmark points were Bruch's Membrane Opening (BMO – red), the anterior scleral canal opening (ASCO – light blue) and the posterior scleral canal opening (PSCO – purple). A representative point cloud which contains all delineated landmark types for all 40 radial sections of an individual reconstruction is viewed from its superior surface three dimensionally in (D) (nasal is to the left and temporal is to the right). Three dimensional reconstructions of the landmark point clouds (D) of each eye were 3D visualized together and separately (turning each landmark category on and off) so as to qualitatively determine their principal macroscopic relationships. In Panel (E) the superior course of the optic nerve (outlined by green dots) as it passes through the sclera and its sharper bend into the orbit can be appreciated. N – Nasal; T – Temporal; I – Inferior; S – Superior.

eye. While there appear to be a few arteries that independently pass through the sclera superiorly (Fig. 5G), where identified, these seem to be retrobulbar branches of the LPCAs. Fifth, unlike the primate eye in which there are approximately 15 SPCAs (Sugiyama et al., 1994) that are relatively equidistant from one another around the circumference of the optic nerve and follow a relatively perpendicular course through the sclera, the choroidal blood supply in the rat appears to originate inferiorly from a dense plexus of tangentially running, intrascleral LPCA branches which effectively fill the space between the three LPCA branches and the CRA. Some of these vessels extend within the sclera and choroid superiorly, around the neurovascular canal. It is the density of the LPCAs and their intrascleral branches inferiorly that does not allow the sclera between them to be discerned. Thus, unlike the neurovascular scleral opening which is regular enough to call a canal, the borders of the inferior arterial opening are highly irregular, preventing quantitative parameterization of this opening by our method.

Sixth, within the sclera, and prior to their intertwining within the inferior notch of BMO, the CRA and CRV are separated by a "sling" of scleral tissues (the scleral sling) which forms the inferior border of the neurovascular scleral canal opening and the superior border of the more-inferior arterial opening (Figs. 1, 2, 4 and 5).

3.2. Principal quantitative results

3.2.1. Reproducibility

Reproducibility was excellent (ICC values greater than 0.75 (Appendix Table 1)) or fair to good (ICC 0.5–0.75) for all parameters (Rosner, 2011).

3.2.2. Parameters treated globally

The eye-specific means and standard deviations (SDs) for our global parameters are reported in Appendix Tables 1–4

3.2.2.1. BMO size (Appendix Table 2). Eye-specific *BMO Area* ranged from 4.76×10^4 to 6.90×10^4 μm^2 with an overall mean of $5.65 \times 10^4 \pm 0.66 \times 10^4$ μm^2. *Eye-specific mean BMO Radii* ranged from 122 ± 14 to 148 ± 8 μm, with an overall mean of 133 ± 8 μm.

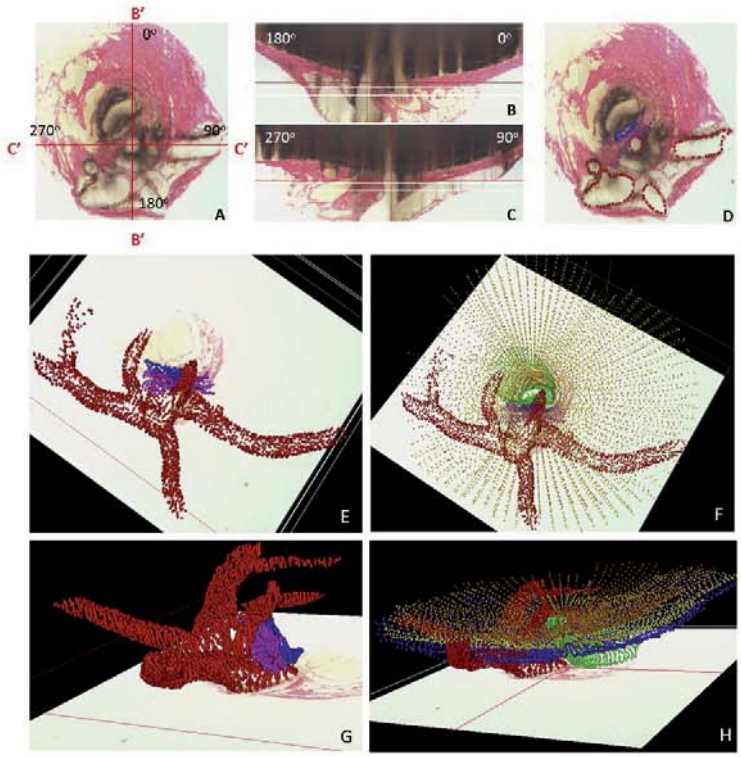

Fig. 4. 3D Delineation of the ONH and Peripapillary Scleral Vasculature and Scleral Sling within Digital Transverse Section Images. Vessel and scleral sling delineation were performed within every fourth digital transverse section image (A) while simultaneously viewing one linked window which displayed either embedded vertical (B) or embedded horizontal (C) digital sagittal sections through the point being delineated. The lines marked B′-B′ and C′-C′ in panel (A) mark the location of the embedded vertical and embedded horizontal digital sagittal section images depicted in panel (B) and (C), respectively. Note that these are vertical and horizontal sections through the 3D reconstruction, but because the tissues are not embedded in perfect clinical orientation, they are not "anatomic" vertical and horizontal sections through the ONH. In Fig. 2, this same reconstruction has been turned so that an accurate clinical orientation has been achieved and "anatomic" vertical and horizontal sections are shown. The following landmark categories were individually marked and cataloged within each delineated transverse section image (D): Ophthalmic artery (OA – red); (2) Central retinal artery (CRA – red); (3) Long posterior ciliary arteries (LPCA – red); (4) Short posterior ciliary arteries (SPCA – reds – and branches of the LPCAs in rats); (5) Central retinal vein (CRV – blue); and (6) the vascular or neural boundary of the scleral sling (magenta). Three dimensional reconstructions of the landmark point clouds (panels E–H) were then 3D visualized together and separately (turning each landmark category on and off) so as to determine their principal macroscopic relationships.

3.2.2.2. The neurovascular scleral canal (Appendix Table 3). *PSCO Area* ($1.33 \times 10^5 \pm 0.21 \times 10^5$ μm^2) was greater than *ASCO Area* ($1.29 \times 10^5 \pm 0.19 \times 10^5$ μm^2) overall but this difference was not significant. Since there is a vascular plexus surrounding the nerve, which includes the CRV inferiorly, *ASCO* and *PSCO Areas* and *Radii* were larger than those of the neural tissues themselves (*ON-ASCO* and *ON-PSCO Areas* and *Radius* values, respectively). Mean *ASCO* and Mean *PSCO Area* were 2.8 and 3.0 times greater than Mean *ON-ASCO* and Mean *ON-PSCO Area*, respectively. PSCO Radius (204 ± 16 μm) was similar to ASCO Radius, (201 ± 15) μm overall, but this difference did not achieve significance. However, eye-specific mean PSCO radius was significantly larger than mean ASCO radius in four animals (Rats 3, 4, 6, and 7, $p < 0.05$, GLS method). Eye-specific *ASCO* and *PSCO H/V Diameter Ratios* ranged from 1.11 to 1.42 (ASCO) and 1.10 to 1.47 (PSCO) respectively confirming the horizontal orientation of the long axis of the ellipse in all 8 eyes.

3.2.2.3. The optic nerve within the neurovascular scleral canal (Appendix Table 4). *ON-ASCO Area* was very similar to *ON-PSCO Area* both overall (means $4.63 \times 10^4 \pm 0.44 \times 10^4$ μm^2 vs $4.41 \times 10^4 \pm 0.45 \times 10^4$ μm^2) and within each animal ($p > 0.05$). Eye-specific *ON-ASCO H/V Diameter Ratios* ranged from 1.66 to 2.18 and *ON-PSCO H/V Diameter Ratios* ranged from 1.81 to 2.97, respectively. Eye-specific *ON Volume* ranged from 2.29×10^6 to 4.04×10^6 μm^3 with an overall mean of $3.28 \times 10^6 \pm 0.59 \times 10^6$ μm^3.

3.2.2.4. BMO depth, ASCO depth, PSCO depth and Anterior Peripapillary Scleral Surface Depth relative to a peripheral anterior scleral reference plane (Appendix Table 4). Eye-specific *BMO Depth* relative to a peripheral anterior scleral reference plane (Fig. 7C) ranged from −1 ± 5 to 47 ± 9 μm (overall mean of 29 ± 15 μm). Eye-specific *Anterior Peripapillary Scleral Surface Depth* relative to the same reference plane (Fig. 7D) ranged from 19 ± 23 to 39 ± 29 μm (overall mean of 33 ± 7 μm).

3.2.2.5. Peripapillary Scleral and Choroidal Thickness (Appendix Table 5). Eye-specific *Peripapillary Scleral Thickness* ranged from 97 ± 23 to 110 ± 18 μm. *Peripapillary Choroidal Thickness* ranged from 45 ± 11 to 70 ± 26 μm.

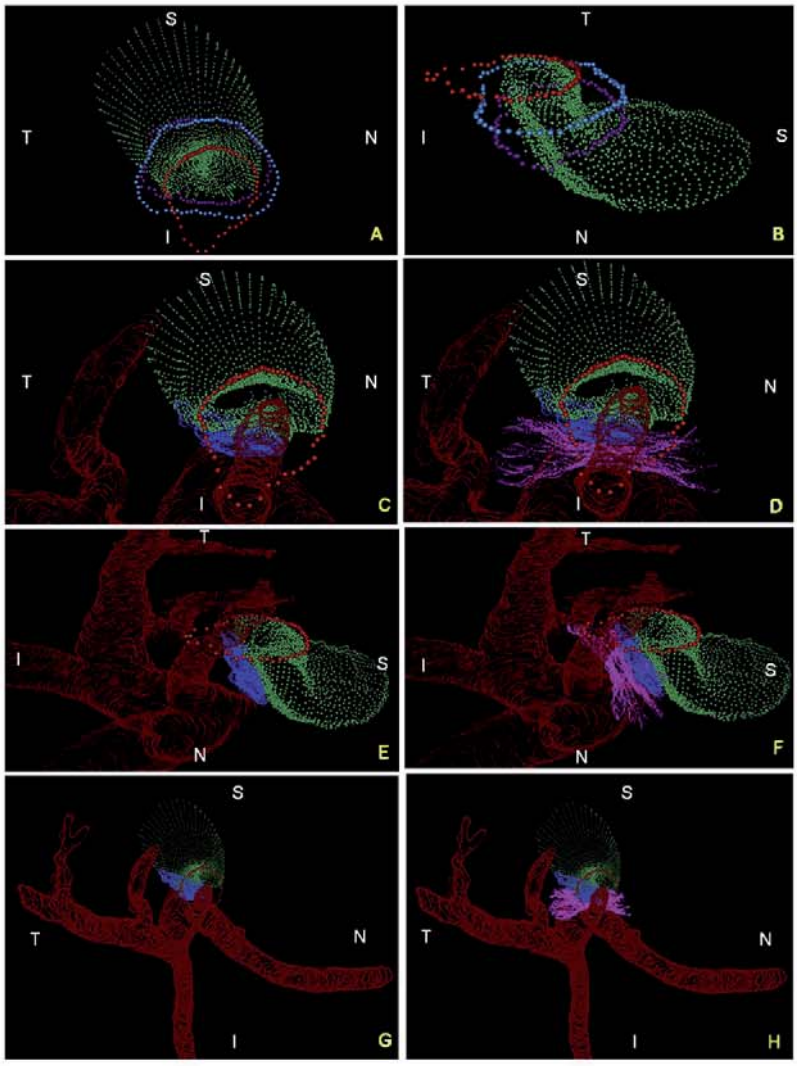

Fig. 5. Summary of the 3D relationships between BMO, the ASCO and PSCO, the Optic Nerve, the Central Retinal Vein, the Central Retinal Artery and the Long Posterior Ciliary Arteries (with and without their intrascleral branches) as visualized within the 3D Point Clouds from a Representative Normal Rat Eye. The relationship of BMO (red), ASCO (light blue) and PSCO (purple) relative to the optic nerve (green) can be seen from a clinical orientation in panel (A) and longitudinally in panel (B). In panels (C)–(F) the ASCO and PSCO Point clouds have been turned off and the CRV, CRA and LPCA point clouds have each been turned on. First, notice that BMO is not round (A) but inferiorly elongated to accommodate the passage of the CRA and CRV (blue vessel) to the retina. Notice also, that BMO is shifted inferiorly relative to the ASCO and PSCO. Second, notice the space between the neural tissue and the BMO, ASCO and PSCO in panel (B). At the level of BMO, the nerve abuts BM superiorly and there is space inferior to the nerve (filled by the CRV and CRA) as noted above. Note in Panel B, that because of the shift in BMO relative to the ASCO and PSCO, BM effectively extends beyond the scleral portion of the neural canal. Superiorly this creates an edge or extension of BM against which the neural bundle abuts. Inferiorly, it creates an elongation of BMO to accommodate the inferior vessels. The net effect of this shift is to create a superior-directed, oblique passage of the nerve through the wall of the rat eye that is best appreciated in Panels B, E and F. At the level of its passage through the anterior (ASCO) and posterior (PSCO) sclera the nerve is surrounded by a vascular plexus which we are not able to independently delineate using our current method. Third, there are three long posterior ciliary arteries which branch from the CRA behind the globe and pass together through the sclera (inferior to the neurovascular canal) to achieve the choroid. Their tangential rather than perpendicular passage through the sclera is depicted in (E) and (F) (see also Fig. 4F, H and Fig. 7). Fourth, short posterior ciliary arteries (defined to be primary branches of the ophthalmic artery that individually pass through the sclera) were not identified. Instead the few arteries that independently pass through the sclera superiorly (G), where identified, appear to be retrobulbar branches of the LPCAs. Fifth, unlike the primate eye in which there are 15 short posterior ciliary arteries that are relatively equidistant from one another around the circumference of the optic nerve, the choroidal blood supply in the rat appears to originate inferiorly from a dense plexus of intrascleral LPCA branches which effectively fill the space between the three LPCA branches (see Fig. 1D–F). Some of these vessels extend within the sclera and choroid superiorly, around the neurovascular canal. It is the density of the LPCAs and their intrascleral branches inferiorly that suggests an "effective" second opening in the sclera. Sixth, the CRA and CRV are separated from each other and the nerve proper and supported by a "sling" (magenta) of scleral tissues that forms the inferior border of the neurovascular scleral canal opening and the superior border of the more-inferior arterial opening. N – Nasal; T – Temporal; I – Inferior; S – Superior.

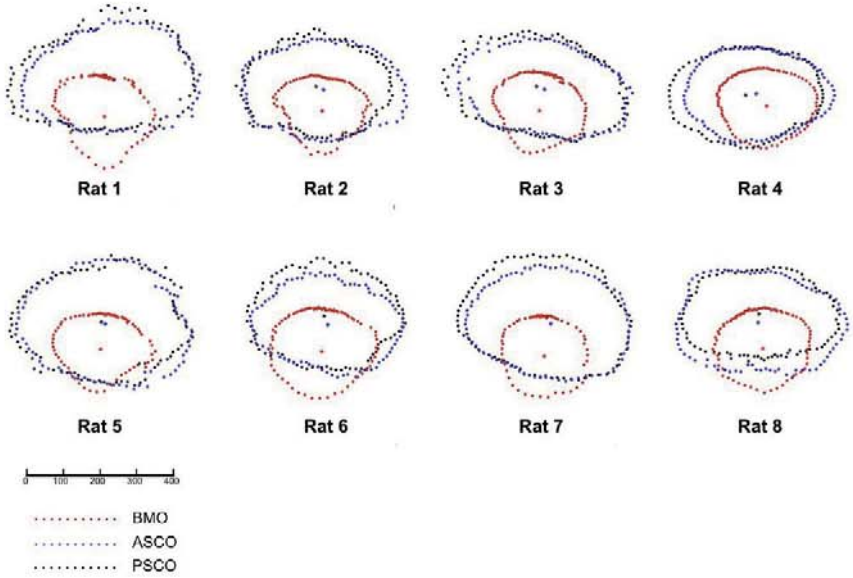

Fig. 6. Eye-specific comparisons of BMO (red), ASCO (blue) and PSCO (black) for the 8 normal control eyes. All data are in right eye configuration. Delineated points for each structure along with their centroid are superimposed by projection to the BMO reference plane for comparison purposes. These data suggest the extent to which BMO is shifted inferiorly relative to the ASCO and PSCO for all 8 study eyes. Combined with the oblique course of the optic nerve bundle visualized in Fig. 5, above, these data provide anatomic support for the oblique course of the nerve from BMO through the PSCO, the superior extension of BM (and inferior shift of BMO) relative to the ASCO and PSCO, and the physical abutment of RGC axons against BMO superiorly in the rat ONH. The scale is in micrometers.

3.2.3. Parameters treated regionally

Appendix Table 6 reports overall regional values for the subset of parameters which include multiple measurements per region. Regional effects were significant ($p < 0.05$ ANOVA) for *ASCO Radius, PSCO Radius, ON-ASCO radius, ON-PSCO radius, Scleral Thickness and Scleral Depth*. Among these parameters, *ON-PSCO radius* was significantly smaller within the inferior quadrant, *scleral thickness* was significantly thinner within the inferior quadrant, and *scleral depth* was significantly shallower in the temporal quadrant compared to all other quadrants. *ASCO Radius, PSCO Radius, ON-ASCO and ON-PSCO radius were smallest within the inferior quadrant.*

4. Discussion

The principal findings of this study are as follows. First, while the rat ONH is built around a well-defined neurovascular scleral canal that contains the retinal ganglion cell axon bundles surrounded by a vascular plexus that includes the CRV, we believe that the density of the more-inferior CRA and LPCA passageways through the sclera effectively constitute a second, arterial scleral opening that is less well defined and separated from the neurovascular scleral opening by a thin connective tissue band we have named the scleral sling. Second, at the level of BMO, BM extends prominently beyond the scleral canal opening superiorly to physically abut the RGC axon bundles, while inferiorly, the CRV and CRA physically separate the RGC axons from BMO. Third, the fact that the CRA passes through the sclera inferior to the neurovascular canal (within its own opening) but joins the CRV within the inferior portion of BMO, leaves BMO irregularly shaped with an inferior elongation that is not present in the primate eye. Fourth, within the neurovascular canal, at the level of the sclera, the retinal ganglion cell axons are bundled into a nerve that is surrounded by a vascular plexus in a manner that leaves its physical attachments to the surrounding sclera impossible to discern by our method (see discussion below). This plexus appears to be a continuation of the choroid that ultimately drains into the retrobulbar pial and dural sheaths. Fifth, the three branches of the LPCAs densely and obliquely penetrate the peripapillary sclera inferior to the neurovascular canal to obtain and run within the peripapillary choroid. Apart from the creation of an effective second opening in the sclera (as mentioned above) these LPCAs along with their dense intrascleral branches that pass to the superior choroid (similar to but less complete than the primate circle of Zinn-Haler) appear to be the principal source of blood supply to the choroid. In fact we found no evidence for SPCAs (defined to be separate branches of the Ophthalmic Artery) in these reconstructions.

This is the first description of the rat ONH that defines it to consist of two separate passage ways through the sclera separated by a thin connective tissue strip (that we have termed the scleral sling). While the biomechanical implications of this anatomy remain to be determined, the large and irregular inferior arterial passageway (containing the CRA, the LPCAs and their intrascleral branches) combined with the lack of SPCAs, are two conditions that do not exist in the primate eye.

While the prominent superior extension of BM has not previously been noted, it is easily visualized within Spectral Domain Optical Coherence Tomographic B-scans (verbal communication, Brad Fortune). The superior location of RGC axon interaction with BMO has previously been described by light microscopy (Morrison et al., 2011, 2008). The fact that the retinal ganglion cell axons are surrounded by a vascular plexus within the neurovascular canal and that this plexus is at least regionally continuous with the peripapillary choroid has been noted by a series of previous

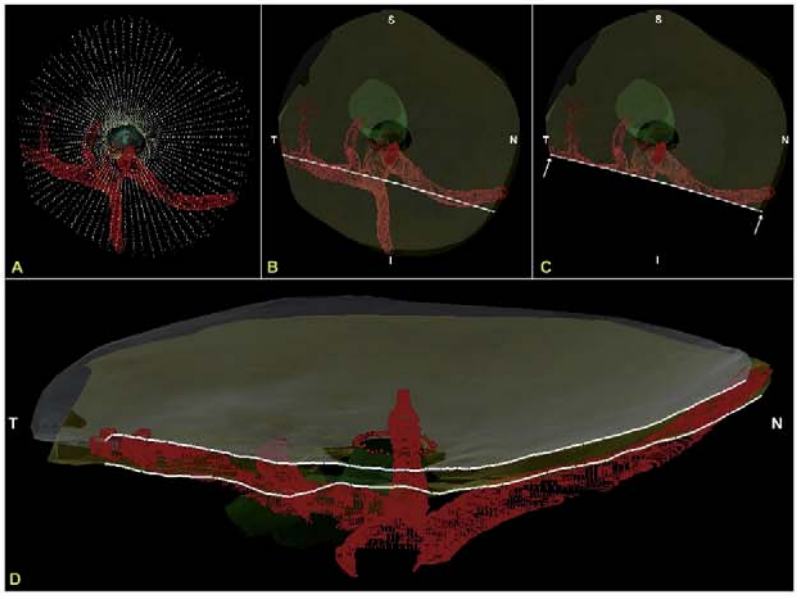

Fig. 7. The CRA passes perpendicularly and the LPCAs pass obliquely through the arterial scleral opening (views from the anterior or vitreous surface). (A) Standard Point cloud 3D reconstruction showing the scleral openings, nerve and BMO (B) The anterior and posterior scleral surface point clouds from the ONH in (A) have been transparently surfaced. Dark transparent circles correspond to the scleral openings and the nerve is transparent green, BMO is shown with red dots (C) A digital section through portions of both the nasal and temporal LPCAs has been removed and its cut surface is visualized in (D). Note that the inferior LPCA is, in this eye, a branch of the temporal LPCA (B). The temporal LPCA (left in B and D) enters the sclera near the CRA opening and slowly achieves the choroidal space well away from the ONH. The nasal LPCA (right in Band D) takes an even more gradual course through the sclera. In most eyes, the space between the LPCAs and the CRA contains choroidal branches from the LPCA which can be very dense (Fig. 1D–F). Finally, note the general superior and temporal passage of the nerve (transparent green) relative to the dark scleral canal openings and (red) inferior arterial tree (Panels B and C). N – Nasal; T – Temporal; I – Inferior; S – Superior.

investigators (Dai et al., 2012; Morrison et al., 1999; Sugiyama et al., 1999). In longitudinal sections from both studies (similar to Fig. 2, panels B and F in this report) clear continuity between the choroid and the peri-neural vascular plexus can be appreciated. This vascular plexus does not exist in the primate and is difficult to examine with our method due to the heavy pigmentation contained therein.

In the primate, the peripapillary sclera and scleral canal wall connective tissues are thought to govern the distribution of IOP-related stress and strain within the lamina cribrosa connective tissues (Burgoyne and Downs, 2008; Sigal et al., 2005). Given the lack of a detectible connective tissue lamina and connective tissue connections between the nerve and the sclera, by our technique, the question of how the sclera transfers load to the retinal ganglion cell axons and the astrocytes that span the nerve within the canal is of substantial biomechanical interest. Two recent papers have described the relationship between the radially arrayed, rat optic nerve head astrocytes, the optic nerve pial sheath (a continuation of the pia that merges with Bruch's Membrane at its opening) and this vascular plexus (Dai et al., 2012; Li et al., 2015). Their description of the plexus suggests that it contains dense connective tissue septa. If these septa directly or indirectly span the plexus to link the sheath and the sclera, then they may be the means by which the sclera transfers IOP-related load to the ONH astrocytic array. The geometry and material properties of these cells, the sheath, and these septal connections to the sclera, thus require further study.

Regarding our quantitative results, previous studies (Downs et al., 2007; Yang et al., 2009a, 2009b, 2011) in a total of 21 normal eyes of 21 monkeys suggest that the mean rat *BMO Area* and mean rat BMO radii we report are 4.7% and 23% (respectively) that of the monkey. In humans, Ren et al. (Ren et al., 2009) used a post-mortem, 2-D technique within histologic sections to report mean BMO diameter that suggest the *BMO Radii* data we report appear to be approximately 17% the size of the human eye. Recently, using Spectral-Domain (SD) OCT in 48 healthy humans, Chauhan and colleagues reported a BMO Area of 1.7 mm^2 (1.4–1.9) which is about 30 times larger than the rat eye (Chauhan et al., 2013).

Like the (single) scleral canal in the primate, the neurovascular scleral canal in the rat expands within the sclera in half of the rat eyes. Interestingly, a study performed using en face Optical Coherence Tomography reported in vivo, OCT-detected ASCO diameter values of approximately 665 μm in 18 normal Dark Agouti rats (Guo et al., 2005). While tissue shrinkage due to fixation, embedding and species difference (estimated to be as high as 30%) (Abramson et al., 2003) may explain these differences, the in vivo study did not clarify the orientation of their measurements (long versus short axis of the horizontal ellipse), nor did it detect the elliptical (rather than circular) shape of this opening as we have herein described. In a post-mortem histologic study of 6 normal human ONHs, (Sigal et al., 2010) ASCO radius was 1.2 times larger than the monkey and 4 times larger than the rat eye.

Finally, because the manner in which mean scleral thickness measurements were made in rats was different from previous measurements made by us in monkeys (Burgoyne et al., 2004; Downs et al., 2007; Yang et al., 2007a, 2007b, 2009b, 2011), and others in humans (Ren et al., 2009; Sigal et al., 2010), direct comparison to the literature is not straightforward. Our data suggest that monkey peripapillary scleral thickness is 2–4 times thicker

than that of the rat when compared at a similar eccentricity to the PSCO. Studies in human eyes (Norman et al., 2010; Ren et al., 2009; Sigal et al., 2010), which are not well matched to the location of measurement in our study, together suggest that human peripapillary sclera is profoundly thicker than that of the rat.

The limitations of our method of 3D reconstruction have been discussed previously (Burgoyne et al., 2004) and include: (1) anterior-to-posterior resolutions limited to 1.5 μm by the fact that the current stain penetrates approximately 1.5 μm into the block; (2) the stain is applied by hand to the block face with a cotton-tipped swab, and the excess is manually removed with lens paper, and thus staining variation between section images can be substantial; (3) there are tissue shrinkage effects (both from fixation and embedding) associated with this technique that may be unique to the rat eye and different within each constituent tissue of the ONH; and (4) the dense pigmentation of the rat vascular plexus surrounding the nerve may lead to an overestimation of ASCO and PSCO especially in the temporal/superior quadrants, due to the bending of the nerve; (5) Comparisons to our nonhuman primate and human cadaver eye data may be similar since post-tissue processing is similar, but comparisons to other post-mortem or in-vivo measurements may be affected by these differences; (6) Delineations were made using the approximate center of the ON as the point of rotation and the radial measurements were made from the centroids based on those delineations. The delineator's estimate of the ON center, and the fact that it was not necessarily the center of other ONH structures, may have influenced the regional sampling of the data.

Finally, it is possible that normal control eyes from unilateral EG animals raised in constant light environments, may not be identical to naive normal control eyes from bilaterally normal animals raised in the usual 12 hour light/dark cycle. However, there are no descriptions of normal control eye alteration in the rat unilateral EG model and none of the 8 normal control eyes in this study were found to have detectible alterations in their optic nerve axons by 2 graders masked to the status of each eye. While we do not believe that the morphologic relationships we describe will be different in naive status of raised in 12 hour light/dark conditions, the generalization of our quantitative findings to naïve normal eyes of all ages, rat strain and lighting conditions must be the subject of future studies.

In summary, we have performed the first 3D characterization of the macroscopic and microscopic ONH anatomy of the rat eye. Our study is the first to describe the rat ONH as consisting of two scleral openings and clarify that the CRA does not accompany the CRV within the neurovascular canal, but passes through a separate, large, irregular opening, inferior to it, accompanied by the LPCAs and their dense intra-scleral branches. Our findings confirm the presence of a vascular plexus that is continuous from the choroid to the optic nerve sheathes and surrounds the optic nerve within the neurovascular canal. We describe an anatomic proximity between the RGC axon bundles and a prominent extension of BM superiorly that is unique to that region. These data suggest that the rat ONH is remarkably different from the primate ONH. We propose that similar studies are now needed in the mouse and that inter-species differences will provide new insights into ONH susceptibility to glaucomatous damage in each species. Finally, we have used the same techniques described herein to study changes in the contralateral early EG eyes of these same 8 animals. The results of this study will be the subject of a future report.

Acknowledgments

The authors gratefully acknowledge the following individuals for their assistance with this study.

Jonathan Grimm and Juan Reynaud for their assistance with software for volumetric and thickness quantification, Brad Fortune, Carla Abbott and Ross Ethier for their careful review of the manuscript and data interpretation, and Galen Williams and Christy Hardin for their performance of the serial section staining and imaging.

Appendix A. Supplementary data

Supplementary data related to this article can be found at http://dx.doi.org/10.1016/j.exer.2015.05.011.

References

Abramson, D.H., et al., 2003. Optic nerve tissue shrinkage during pathologic processing after enucleation for retinoblastoma. Arch. Ophthalmol. 121, 73–75.
Burgoyne, C.F., Downs, J.C., 2008. Premise and prediction-how optic nerve head biomechanics underlies the susceptibility and clinical behavior of the aged optic nerve head. J. Glaucoma 17, 318–328.
Burgoyne, C.F., et al., 2004. Three-dimensional reconstruction of normal and early glaucoma monkey optic nerve head connective tissues. Invest Ophthalmol. Vis. Sci. 45, 4388–4399.
Chauhan, B.C., et al., 2013. Enhanced detection of open-angle glaucoma with an anatomically accurate optical coherence tomography-derived neuroretinal rim parameter. Ophthalmology 120, 535–543.
Dai, C., et al., 2012. Structural basis of glaucoma: the fortified astrocytes of the optic nerve head are the target of raised intraocular pressure. Glia 60, 13–28.
Downs, J.C., et al., 2007. Three-dimensional histomorphometry of the normal and early glaucomatous monkey optic nerve head: neural canal and subarachnoid space architecture. Invest Ophthalmol. Vis. Sci. 48, 3195–3208.
Fujita, Y., et al., 2000. Comparative study of the lamina cribrosa and the pial septa in the vertebrate optic nerve and their relationship to the myelinated axons. Tissue Cell. 32, 293–301.
Guo, L., et al., 2005. En face optical coherence tomography: a new method to analyse structural changes of the optic nerve head in rat glaucoma. Br. J. Ophthalmol. 89, 1210–1216.
Howell, G.R., et al., 2007. Axons of retinal ganglion cells are insulted in the optic nerve early in DBA/2J glaucoma. J. Cell. Biol. 179, 1523–1537.
Jia, L., et al., 2000. Patterns of intraocular pressure elevation after aqueous humor outflow obstruction in rats. Invest Ophthalmol. Vis. Sci. 41, 1380–1385.
Johansson, J.O., 1987. The lamina cribrosa in the eyes of rats, hamsters, gerbils and guinea pigs. Acta Anat. (Basel) 128, 55–62.
Johnson, E.C., et al., 2015. Radiation pretreatment does not protect the rat optic nerve from elevated intraocular pressure-induced injury. Invest Ophthalmol. Vis. Sci. 56, 412–419.
Johnson, E.C., et al., 1996. The effect of chronically elevated intraocular pressure on the rat optic nerve head extracellular matrix. Exp. Eye Res. 62, 663–674.
Johnson, T.V., Tomarev, S.I., 2010. Rodent models of glaucoma. Brain Res. Bull. 81, 349–358.
Li, Y., et al., 2015. An energy theory of glaucoma. Glia. http://dx.doi.org/10.1002/glia.22825. First published on Mar 23, 2015 as.
Mabuchi, F., et al., 2003. Optic nerve damage in experimental mouse ocular hypertension. Invest Ophthalmol. Vis. Sci. 44, 4321–4330.
Mabuchi, F., et al., 2004. Regional optic nerve damage in experimental mouse glaucoma. Invest Ophthalmol. Vis. Sci. 45, 4352–4358.
May, C.A., 2008. Comparative anatomy of the optic nerve head and inner retina in non-primate animal models used for glaucoma research. Open Ophthalmol. J. 2, 94–101.
Moore, C.G., et al., 1995. Long-term non-invasive measurement of intraocular pressure in the rat eye. Curr. Eye Res. 14, 711–717.
Moore, C.G., et al., 1996. Circadian rhythm of intraocular pressure in the rat. Curr. Eye Res. 15, 185–191.
Moore, C.G., et al., 1993. Noninvasive measurement of rat intraocular pressure with the Tono-Pen. Invest Ophthalmol. Vis. Sci. 34, 363–369.
Morrison, J., et al., 1995a. Structure and composition of the rodent lamina cribrosa. Exp. Eye Res. 60, 127–135.
Morrison, J.C., 2005. Elevated intraocular pressure and optic nerve injury models in the rat. J. Glaucoma 14, 315–317.
Morrison, J.C., et al., 2011. Pathophysiology of human glaucomatous optic nerve damage: insights from rodent models of glaucoma. Exp. Eye Res. 93, 156–164.
Morrison, J.C., et al., 1995b. Limbal microvasculature of the rat eye. Invest Ophthalmol. Vis. Sci. 36, 751–756.
Morrison, J.C., et al., 2009. Reliability and sensitivity of the TonoLab rebound tonometer in awake Brown Norway rats. Invest Ophthalmol. Vis. Sci. 50, 2802–2808.
Morrison, J.C., et al., 2008. Rat models for glaucoma research. Prog. Brain Res. 173, 285–301.
Morrison, J.C., et al., 2005. Understanding mechanisms of pressure-induced optic nerve damage. Prog. Retin Eye Res. 24, 217–240.
Morrison, J.C., et al., 1999. Microvasculature of the rat optic nerve head. Invest.

Ophthalmol. Vis. Sci. 40, 1702–1709.
Morrison, J.C., et al., 1997. A rat model of chronic pressure-induced optic nerve damage. Exp. Eye Res. 64, 85–96.
Norman, R.E., et al., 2010. Dimensions of the human sclera: thickness measurement and regional changes with axial length. Exp. Eye Res. 90, 277–284.
Pang, I.H., Clark, A.F., 2007. Rodent models for glaucoma retinopathy and optic neuropathy. J. Glaucoma 16, 483–505.
Ren, R., et al., 2009. Lamina cribrosa and peripapillary sclera histomorphometry in normal and advanced glaucomatous Chinese eyes with various axial length. Invest Ophthalmol. Vis. Sci. 50, 2175–2184.
Rosner, B., 2011. 12.9. The intraclass correlation coefficient. In: Fundamentals of Biostatistics, Seventh ed. Harvard University. Brooks/Cole Cengage Learning, Boston, MA, p. 569.
Ruiz-Ederra, J., Verkman, A.S., 2006. Mouse model of sustained elevation in intraocular pressure produced by episcleral vein occlusion. Exp. Eye Res. 82, 879–884.
Sigal, I.A., et al., 2005. Factors influencing optic nerve head biomechanics. Invest. Ophthalmol. Vis. Sci. 46, 4189–4199.
Sigal, I.A., et al., 2010. 3D morphometry of the human optic nerve head. Exp. Eye Res. 90, 70–80.
Sugiyama, K., et al., 1994. Optic nerve and peripapillary choroidal microvasculature in the primate. J. Glaucoma 3 (Suppl. 1), S45–S54.
Sugiyama, K., et al., 1999. Optic nerve and peripapillary choroidal microvasculature of the rat eye. Invest. Ophthalmol. Vis. Sci. 40, 3084–3090.
Yang, H., et al., 2007a. 3-D histomorphometry of the normal and early glaucomatous monkey optic nerve head: prelaminar neural tissues and cupping. Invest Ophthalmol. Vis. Sci. 48, 5068–5084.
Yang, H., et al., 2009a. Physiologic intereye differences in monkey optic nerve head architecture and their relation to changes in early experimental glaucoma. Invest Ophthalmol. Vis. Sci. 50, 224–234.
Yang, H., et al., 2007b. 3-D histomorphometry of the normal and early glaucomatous monkey optic nerve head: lamina cribrosa and peripapillary scleral position and thickness. Invest Ophthalmol. Vis. Sci. 48, 4597–4607.
Yang, H., et al., 2009b. Deformation of the normal monkey optic nerve head connective tissue after acute IOP elevation within 3-D histomorphometric reconstructions. Invest Ophthalmol. Vis. Sci. 50, 5785–5799.
Yang, H., et al., 2011. Deformation of the early glaucomatous monkey optic nerve head connective tissue after acute IOP elevation in 3-D histomorphometric reconstructions. Invest Ophthalmol. Vis. Sci. 52, 345–363.

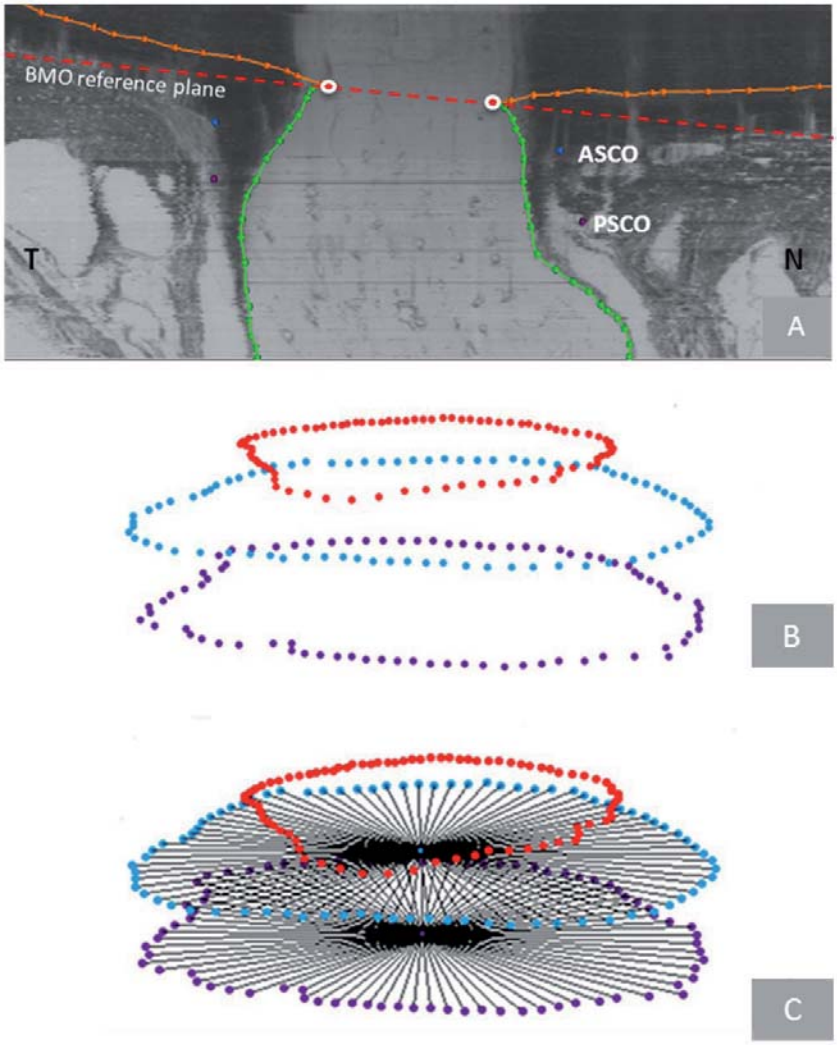

Appendix Figure 1. Bruch's Membrane Opening (BMO) and Neurovascular Scleral Canal Parameterization. Within each ONH reconstruction, individual planes were fit to the 80 BMO points, 80 ASCO points and 80 PSCO points which are illustrated in cross-section within a digital sagittal section image. (A). The cross-sectional area of all three openings (BMO, ASCO and PSCO) was calculated as the area within the projection of the BMO, ASCO and PSCO points to their respective fitted planes (B). Using the centroid of the projected BMO, ASCO and PSCO points, 80 radius measurements were made within their respective fitted planes at 4.5 degree intervals (C). N – Nasal; T – Temporal.

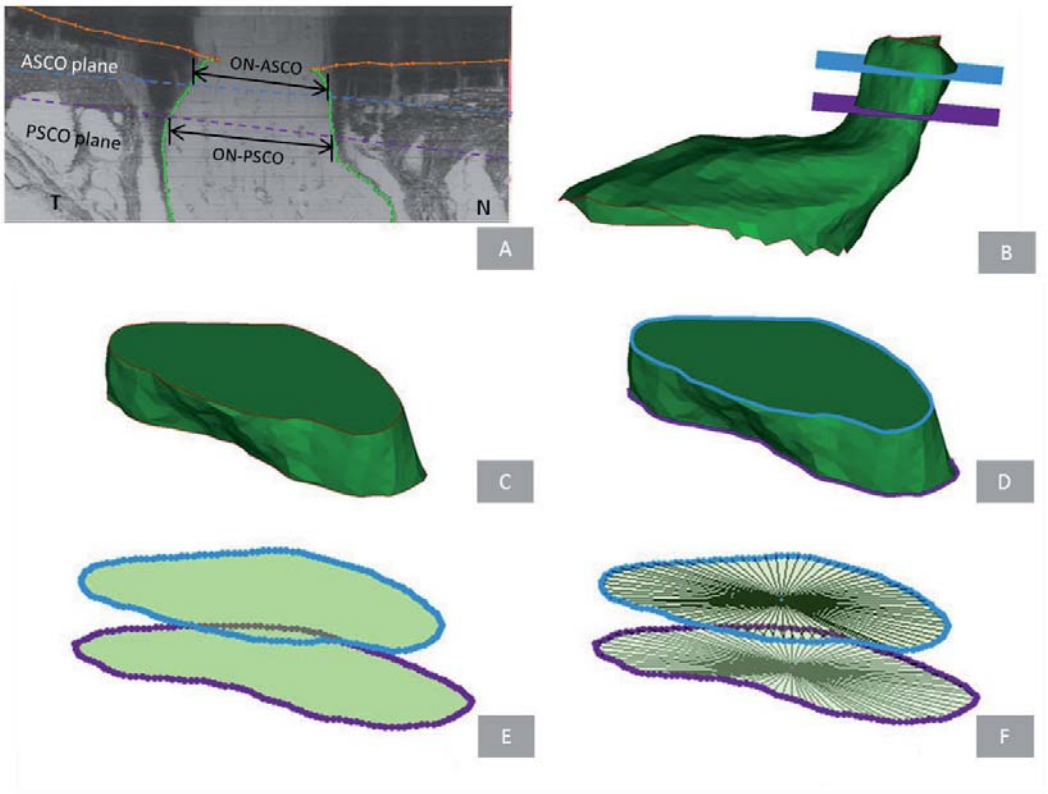

Appendix Figure 2. Scleral Canal Optic Nerve Area, and Volume Parameterization. Optic nerve cross-sectional area and radii were quantified within the ASCO (ON-ASCO) and PSCO (ON-PSCO) planes using the delineated optic nerve boundary (green dots) as illustrated within digital sagittal sections in panel (A). ON cross-sectional area within BMO (ON-BMO) could not be quantified due to obstruction of its boundaries by pigment from the perineural vascular plexus. In (B) the optic nerve point cloud (from all 40 delineated sections) has been surfaced (green) and the position of the ASCO (light blue) and PSCO (purple) planes relative to the optic nerve is shown. Please note that while the ASCO and PSCO planes are based on the respective openings within the sclera (Figure 5, above, and panel A of this figure) it is the scleral canal optic nerve volume or the optic nerve volume within the canal (not including the surrounding vascular plexus) and between the planes that is isolated within (C). The ON-ASCO (light blue) and ON-PSCO (purple) surfaces of the scleral canal optic nerve volume are highlighted in (D), and their areas and radii are quantified in (E) and (F). The orientation of panels (B) – (F) is approximately that of (A) - Temporal (T) left and Nasal (N) right.

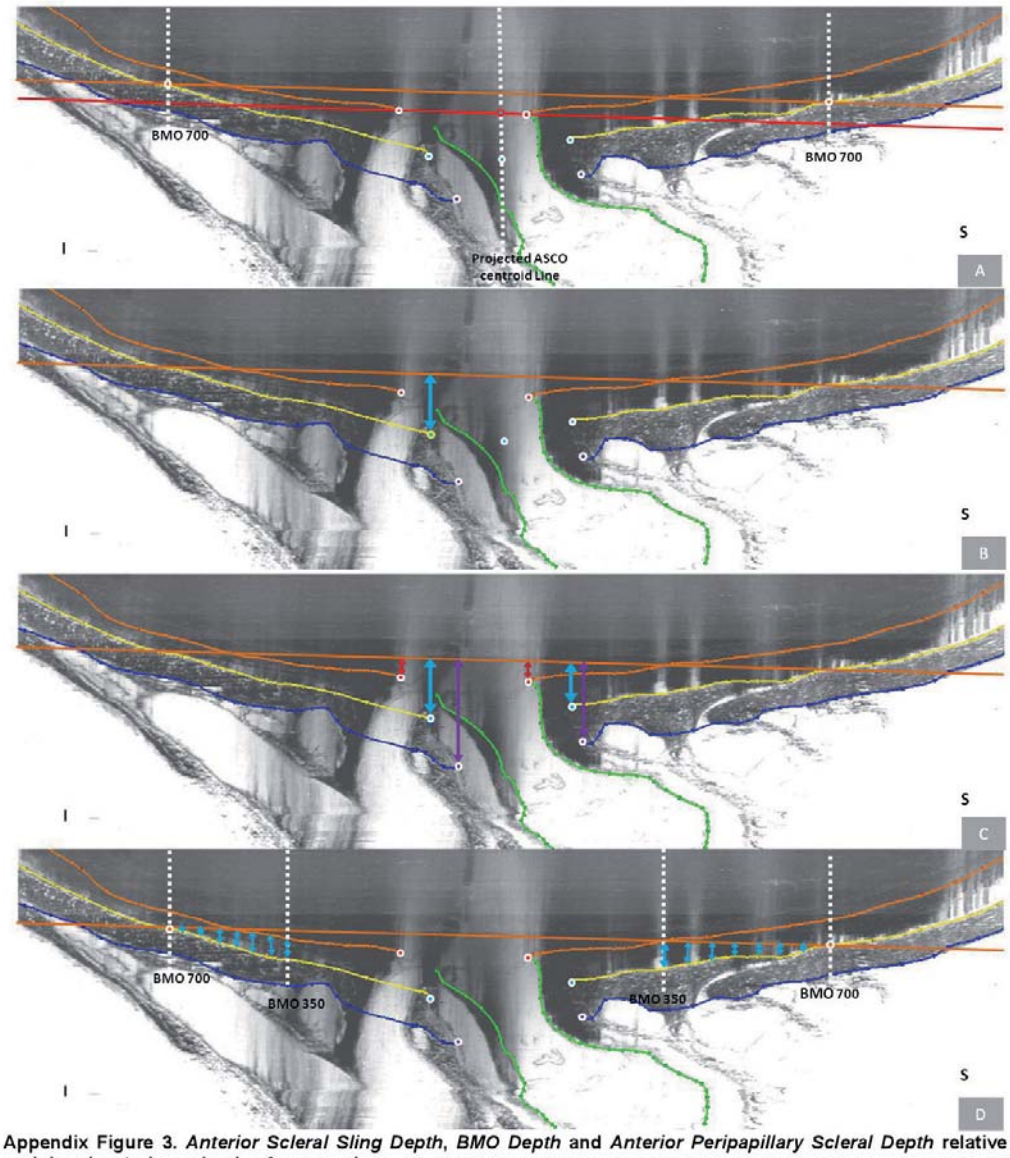

Appendix Figure 3. ***Anterior Scleral Sling Depth*****,** ***BMO Depth*** **and** ***Anterior Peripapillary Scleral Depth*** **relative to a peripheral anterior scleral reference plane.** (A) A peripheral anterior scleral reference plane was generated from a ring of points (orange dot with white border) on the anterior scleral surface at a distance 700 microns (BMO 700) from the projected ASCO centroid line. (B) *Anterior Scleral Sling Depth (blue arrow)* was measured relative to the peripheral anterior scleral reference plane in each radial section in which the sling surface could be identified (approximately 8 section images per ONH). Circled in yellow you can see the most anterior aspect of the scleral sling. (C) *BMO Depth* was measured for each BMO point relative to the same reference plane within each section. PSCO (purple arrow), ASCO Depth (blue arrow) and BMO depth (red arrow) were calculated relative to this peripheral anterior scleral reference plane as well. (D) *Anterior Peripapillary Scleral Depth* relative to the same reference plane was measured at a distance of BMO 350 to BMO 700 ⌈m (in 50 ⌈m increments) on the fitted anterior scleral surface (yellow line). Red dot with white border – BMO; Blue dot with white border – ASCO; Purple dot with white border – PSCO; Projected ASCO centroid line (A) - perpendicular line to the BMO reference plane (red line) passing through the raw ASCO centroid (blue dot with black border); Blue dot with red border (B) - projected ASCO centroid; *BMO 350/700* - Perpendicular line from the BMO reference plane at a distance of 350/700 ⌈m from the projected ASCO centroid line so as to define BMO 350/700 eccentricity. I – Inferior; S – Superior.

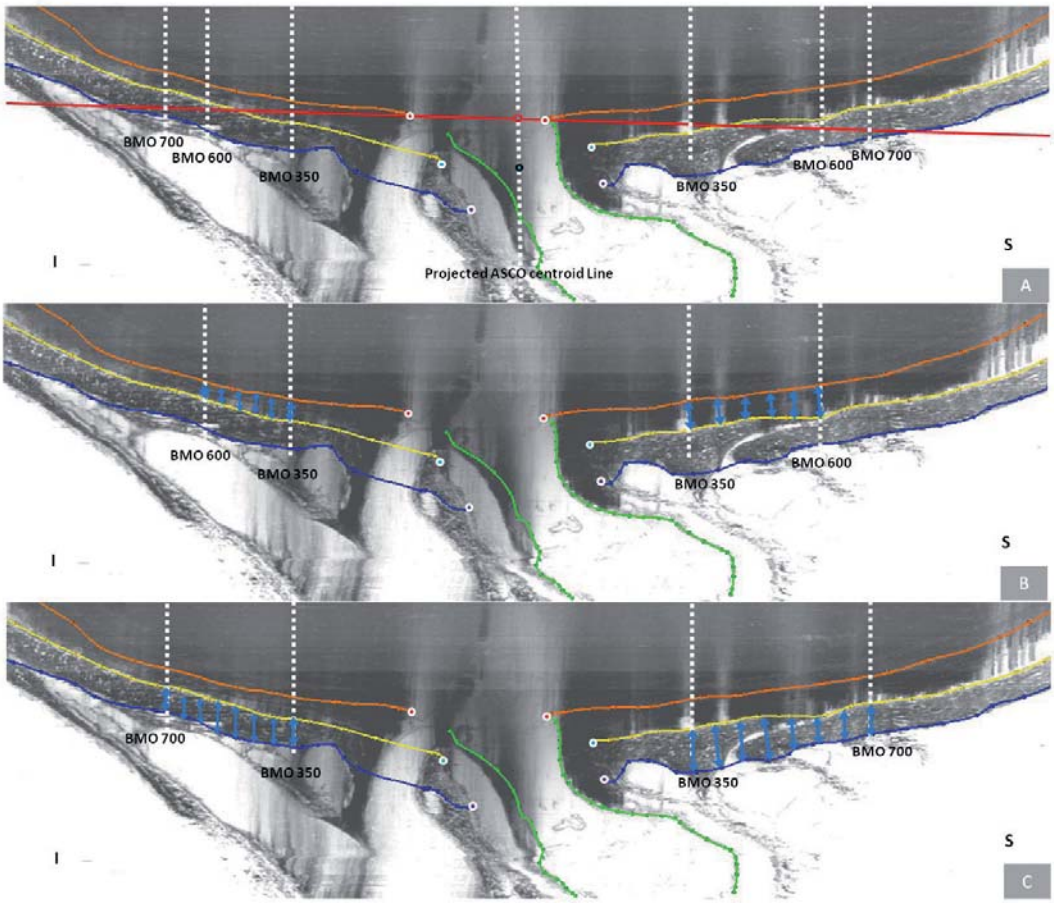

Appendix Figure 4. ***Peripapillary Chroidal*** **and** ***Peripapillary Scleral Thickness*** **Parameterization**. (A) Projected ASCO centroid line is a perpendicular line to the BMO reference plane (red line) passing through the raw ASCO centroid (blue dot with black border) and projected ASCO centroid (Blue dot with red border). *BMO 350/600/700*: Perpendicular line from the BMO reference plane at a distance of 350/600/700 µm from the projected ASCO centroid line so as to define BMO 350/600/700 eccentricity. **(B)** *Peripapillary Choroidal Thickness (cyan arrows)* was measured perpendicular to Bruch's Membrane surfaces in 50 µm increments along the BMO reference plane between the BMO 350 to BMO 600 landmarks. **(C)** *Peripapillary Scleral Thickness (cyan arrows)* was measured perpendicular to the anterior scleral surface in 50 µm increments along the BMO reference plane between the BMO 350 to BMO 700 landmarks Red dots with white border – BMO; Blue dots with white border – ASCO; Purple dot with white border - PSCO. Blue dot with black border (A) – ASCO centroid. I – Inferior; S – Superior.

Parameter Name	ICC (Low 95%CI-High 95%CI)
BMO Area	0.55 (0.06-0.91)
BMO Radius	0.54 (0.05-0.90)
BMO Depth	0.97 (0.87-0.99)
ASCO Area	0.93 (0.77-0.99)
ASCO Radius	0.93 (0.77-0.99)
ASCO Depth	0.81 (0.45-0.96)
ASCO H/V	0.76 (0.36-0.96)
PSCO Area	0.75 (0.34-0.95)
PSCO Radius	0.77 (0.38-0.96)
PSCO Depth	0.58 (0.10-0.91)
PSCO H/V	0.85 (0.54-0.97)
ON-ASCO Area	0.95 (0.84-0.99)
ON-ASCO Radius	0.95 (0.83-0.99)
ON-ASCO H/V	0.85 (0.55-0.97)
ON-PSCO Area	0.98 (0.91-0.99)
ON-PSCO Radius	0.98 (0.91-0.99)
ON-PSCO H/V	0.97 (0.87-0.99)
ON-Volume	0.88 (0.62-0.98)
Scleral thickness	0.71 (0.28-0.95)
Scleral Depth	0.95 (0.82-0.99)
Choroidal Thickness	0.55 (0.06-0.91)

ICC-Intraclass Correlation Coefficient characterizes the proportion of the total variance (sum of within-subject and between-subject) within our data that is explained by the variance between-subject. Data for both the control and experimental glaucoma eyes of 3 rats on 3 different days are shown here. In most cases the value of the ICC ranges from 0 to 1. As the ICC approaches a value of 1.0 there is perfect agreement between readings within same subject. As ICC approaches a value of 0.0 there is no agreement between readings within same subject. ICC grading: <0.4 - Poor Reproducibility; 0.4-0.75-Fair to Good Reproducibility; >0.75-Excellent Reproducibility. Only parameters with ICC > .5 were included in this report.

CI- Confidence Interval

Appendix Table 1. Reproducibility Study Data

Parameters	Rat Number								Mean	SD
	1	2	3	4	5	6	7	8		
BMO Area (μm^2)	$6.15x10^4$	$4.75x10^4$	$5.26x10^4$	$5.71x10^4$	$5.18x10^4$	$6.89x10^4$	$5.40x10^4$	$5.82x10^4$	$5.65x10^4$	$0.50x10^4$
Mean BMO Radii (μm)	139 ± 18	122 ±14	129 ± 9	135 ±6	128 ± 12	148 ±8	131 ±10	136 ±7	133	6

Appendix Table 2. BMO Size by Study Eye.

Parameters	Rat Number								Mean	SD
	1	2	3	4	5	6	7	8		
Neural/Venous Canal										
ASCO Area (μm^2)	$1.49x10^5$	$1.22x10^5$	$1.23x10^5$	$1.02x10^5$	$1.56x10^5$	$1.12x10^5$	$1.38x10^5$	$1.33x10^5$	$1.29x10^5$	$0.21x10^5$
ASCO Radius (µm)	216 ±31	196 ±21	196 ±29	179 ±16	223 ±16	183 ±18	209 ±16	204 ±25	201	14
ASCO H/V Diameter Ratio	1.24	1.26	1.42	1.26	1.11	1.25	1.17	1.38	1.26	0.11
PSCO Area (μm^2)	$1.58x10^5$	$1.13x10^5$	$1.39x10^5$	$1.13x10^5$	$1.53x10^5$	NA	$1.57x10^5$	$1.09x10^5$	$1.35x10^5$	$0.27x10^5$
PSCO Radius (µm)	223 ±35	189 ±15	209 ±30	189 ±18	220 ±20	NA	223 ±17	185 ±23	204	17
PSCO H/V Diameter Ratio	1.47	1.09	1.39	1.19	1.13	NA	1.36	1.33	1.28	0.12
Optic nerve										
ON-ASCO Area (μm^2)	$4.54x10^4$	$4.25x10^4$	$4.36x10^4$	$4.45x10^4$	$5.36x10^4$	$4.73x10^4$	$4.15x10^4$	$5.20x10^4$	$4.63x10^4$	$0.95x10^4$
ON-ASCO Radius (µm)	117 ±33	112 ±34	114 ±32	115 ±32	127 ±29	119 ±28	112 ±25	126 ±24	118	12
ON-ASCO H/V Diameter Ratio	1.82	2.18	2.18	2.08	1.97	1.87	1.86	1.66	1.95	0.16
ON-PSCO Area (μm^2)	$4.80x10^4$	$4.28x10^4$	$4.36x10^4$	$3.99x10^4$	$5.34x10^4$	NA	$4.24x10^4$	$4.14x10^4$	$4.42x10^4$	$0.97x10^4$
ON-PSCO Radius (µm)	117 ±41	108 ±44	107 ±41	104 ±43	124 ±41	111±42	111 ±33	106 ±43	111	12
ON-PSCO H/V Diameter Ratio	2.40	2.72	2.59	2.97	2.29	NA	1.89	1.81	2.38	0.35
ON Volume (μm^3)	$3.95x10^6$	$2.92x10^6$	$2.29x10^6$	$3.25x10^6$	$4.04x10^6$	$3.20x10^6$	$2.88x10^6$	$3.67x10^6$	$3.27x10^6$	$0.89x10^6$

* See Appendix Figures 1 and 2 for an explanation of each parameter.

Appendix Table 3. The neurovascular scleral canal and its contained optic nerve (Figures 5 and 6)*

Parameters	Rat Number								Mean	SD
	1	2	3	4	5	6	7	8		
BMO Depth (µm)	16 ±11	47 ±9	39 ±4	36 ±9	26±10	37 ±6	-1 ±5	33 ±7	29	12
ASCO Depth (µm)	78 ±22	103 ±20	112 ±18	105 ±16	88±16	106 ±23	73 ±13	94 ±15	95	16
PSCO Depth (µm)	160 ±28	170 ±25	167 ±20	182 ±19	164 ±23	172 ±27	141 ±23	170 ±29	166	15
Scleral Depth (µm)	27±36	39±29	32±24	38±28	38±24	36±26	18±23	33±25	33	7

* See Appendix Figure 3 for an explanation of each parameter.

Appendix Table 4. *BMO Depth, ASCO depth, PSCO depth* and *Anterior Peripapillary Scleral Depth* relative to a peripheral anterior scleral reference plane (Figure 7)*.

Parameters	Rat Number								Mean	SD
	1	2	3	4	5	6	7	8		
Scleral Thickness (µm)	109 ±26	105 ±23	107 ±19	105 ±19	105 ±15	109 ±18	97 ±23	103 ±21	105	4
Choroidal Thickness (µm)	56 ±13	45 ±10	54 ±13	55 ±11	60 ±11	70 ±26	61 ±14	54 ±10	57	7

* See Appendix Figure 4 for an explanation of each parameter.

Appendix Table 5. Peripapillary Scleral and Choroidal Thickness (Figure 8)*

Parameters[1]	Superior Mean±SD	Inferior Mean±SD	Nasal Mean±SD	Temporal Mean±SD
Neural/Venous Canal				
BMO Radius	135±10	138±15	132±11	128±16
BMO Depth	27±13	32±17	32±16	26±17
ASCO Radius[2]	187±22	186±22	217±23	214±20*
ASCO Depth	78±22	109±21	91±22	79±19
PSCO Radius[2]	196±25	188±22	213±22	222±23*
PSCO Depth	145±16	189±19	177±24	152±20
Optic Nerve				
ON-ASCO Radius[2]	98±9	90±14	141±19*	142±2*
ON-PSCO Radius[2]	86±10*	68±12	145±31*	146±29*
Sclera/choroid				
Scleral Thickness[2]	99±11*	91±18	113±22*	116±14*
Scleral Depth[2]	30±25*	41±29*	37±27*	22±26
Choroidal Thickness	57±11	56±14	59±23	55±14

[1] Only parameters which include multiple measurements per region were included in this analysis
[2] Regional effects for this parameter are statistically significant within ANOVA using a linear mixed effects model ($p<0.05$, after adjustment for multiple comparisons).
Blue: quadrant with the lowest value. All other quadrants were compared to the quadrant with the lowest value.
*this regional value is significantly different from the lowest regional value of this parameter ($p<0.05$, ANOVA after adjustment for multiple comparisons.

Appendix Table 6. Overall Regional Values for each Parameter

3.3. Second Paper: Expansions of the neurovascular scleral canal and contained optic nerve occur early in the hypertonic saline rat experimental glaucoma model

Marta Pazos, Hongli Yang, Stuart K. Gardiner, William O.Cepurna, Elaine C. Johnson, John C. Morrison, Claude F. Burgoyne.

Exp Eye Res. 2015 Oct 21. pii: S0014-4835(15)30052-X. doi: 10.1016/j.exer.2015.10.014. [Epub ahead of print]

3.3.1. Abstract

Purpose. To characterize early optic nerve head (ONH) structural change in rat experimental glaucoma (EG).

Methods. Unilateral intraocular pressure (IOP) elevation was induced in Brown Norway rats by hypertonic saline injection into the episcleral veins and animals were sacrificed 4 weeks later by perfusion fixation. Optic nerve cross-sections were graded from 1 (normal) to 5 (extensive injury) by 5 masked observers. ONH's with peripapillary retina and sclera were embedded, serial sectioned, 3-D reconstructed, delineated, and quantified. Overall and animal-specific EG versus Control eye ONH parameter differences were assessed globally and regionally by linear mixed effect models with significance criteria adjusted for multiple comparisons.

Results. Expansions of the optic nerve and surrounding anterior scleral canal opening achieved statistical significance overall ($p<.0022$), and in 7 of 8 EG eyes ($p<.005$). In at least 5 EG eyes, significant expansions ($p<.005$) in Bruch's membrane opening (range 3-10%), the anterior and posterior scleral canal openings (8-21% and 5-21%, respectively), and the optic nerve at the anterior and posterior scleral canal openings (11-30% and 8-41%, respectively) were detected. Optic nerve expansion was greatest within the superior and inferior quadrants. Optic nerve expansion at the posterior scleral canal opening was significantly correlated to optic nerve damage ($R= 0.768$, $P=.042$).

Conclusion: In the rat ONH, the optic nerve and surrounding Bruch's membrane opening and neurovascular scleral canal expand early in their response to chronic experimental IOP elevation. These findings provide phenotypic landmarks and imaging targets for detecting the development of experimental glaucomatous optic neuropathy in the rat eye.

3.3.2. Descriptive Results

3.3.2.1. Animal and Eye Data

Rat Number	ID	Age at sacrifice *(months)*	Eye	Status	Mean IOP *(mmHg)*	Mean IOP difference *(mmHg)*	EG Eye Peak IOP *(mmHg)*	Optic Nerve Damage Grade	Number of Serial Section Images
1	MR8	9.5	OD	C	28.5	5		1	400
			OS	EG	33.5		42.3	1.22	383
2	MR10	9.5	OD	EG	29.2	0.4	45	1.6	465
			OS	C	28.8			1	313
3	MR1	9.5	OD	EG	33.3	5	39.1	2	696
			OS	C	28.3			1	398
4	MR9	9.5	OD	EG	35	6.6	45.8	2.36	430
			OS	C	28.4			1	307
5	MR12	10.5	OD	EG	29.6	1.1	36	2.47	500
			OS	C	28.5			1	275
6	MR11	10.5	OD	EG	32.1	3.8	41	2.9	230
			OS	C	28.3			1	375
7	MR5	9.5	OD	C	28.8	3.7		1	484
			OS	EG	32.5		40.9	3	480
8	MR4	9.5	OD	C	28.4	6.2		1	501
			OS	EG	34.6		42.3	3.28	455

ID – Laboratory Rat Identification Number; **Age**- in months; **Eye** - OD-Right eye, OS-left eye**; Status**- C- Control, EG-Experimental Glaucoma; **Mean IOP** (mmHg)- Mean IOP of all IOP measurements taken AM and PM for each eye**; Mean IOP difference**- Mean IOP of the EG eye minus Mean IOP of the Contol eye (mmHg). **EG Eye Peak IOP** - Maximum IOP in mmHg obtained in the EG eye; **Optic Nerve Damage Grade:** average score of orbital optic nerve cross section grading performed by 5 masked observers using a previously published scale (Morrison *Exp.Eye Res*.1997). **Number of Digital Serial Section Images**- number of serial digital section images required to reconstruct each optic nerve head.

Table 3.6. Animal and Eye Data

Both the EG and the Control eyes of eight brown male Norway rats (aged from 9.5 to 10.5 months) were studied. A detailed description of the 8 Control eyes is contained within our previous report (Pazos et al. 2015). Eye-specific mean IOP in the Control eyes ranged from 28.3 to 28.5 mmHg. Eye-specific mean IOP in the EG eyes ranged from 28.3 to 34.6 mmHg, with *Mean IOP Differences* ranging from 0.4 to 6.6 mmHg and *Peak IOPs* ranging from 36 to 45.8 mmHg. The *mean optic nerve damage grade* for all 8 Control eyes was 1.0 (no detectable damage) and ranged from 1.22 (Rat 1) to 3.28 (Rat 8) in the EG eyes. For this and the previous normal Control eye report (Pazos et al. 2015) study animals were numbered 1-8 based on the magnitude of each animal's EG eye *optic nerve damage grade*. Several parameters could not be calculated for the EG eye of Animal 6 due to poor visualization of the outer scleral canal and peripapillary sclera.

3.3.2.2. Delineation Reproducibility

Parameter Name	ICC (Low 95%CI-High 95%CI)
BMO Area	0.55 (0.06-0.91)
BMO Radius	0.54 (0.05-0.90)
BMO Depth	0.97 (0.87-0.99)
ASCO Area	0.93 (0.77-0.99)
ASCO Radius	0.93 (0.77-0.99)
ASCO Depth	0.81 (0.45-0.96)
ASCO H/V	0.76 (0.36-0.96)
PSCO Area	0.75 (0.34-0.95)
PSCO Radius	0.77 (0.38-0.96)
PSCO Depth	0.58 (0.10-0.91)
PSCO H/V	0.85 (0.54-0.97)
ON-ASCO Area	0.95 (0.84-0.99)
ON-ASCO Radius	0.95 (0.83-0.99)
ON-ASCO H/V	0.85 (0.55-0.97)
ON-PSCO Area	0.98 (0.91-0.99)
ON-PSCO Radius	0.98 (0.91-0.99)
ON-PSCO H/V	0.97 (0.87-0.99)
ON-Volume	0.88 (0.62-0.98)
ASCO-ON-ASCO distance	0.93 (0.75 -0.99)
PSCO-ON-PSCO distance	0.49 (0 - 0.89)
Scleral thickness	0.71 (0.28-0.95)
Scleral Depth	0.95 (0.82-0.99)
Choroidal Thickness	0.55 (0.06-0.91)

ICC - Intraclass Correlation Coefficient , **CI**- Confidence Interval
ICC grading: <0.4 - Poor Reproducibility; 0.4-0.75-Fair to Good Reproducibility; 0.75-Excellent Reproducibility. Only parameters with Fair to Good or excellent reproducibility were included in this report.

Table 3.7. - Reproducibility Data

3.3.3. Quantitative Results

3.3.3.1. Overall and Animal Specific Global and Regional Parameter Change

Overall global values for each parameter by treatment group are reported in Table 3. 8. Animal-specific, global parameter change frequency (among the 8 EG eyes) and direction are summarized for each parameter in Table 3.9. Overall regional values for each parameter by treatment group are reported in Table 3.10. The frequency of animal-specific, EG eye regional change is summarized for each parameter in Table 3.11.

Parameters	Control Eyes (Mean±SD)	EG Eyes (Mean±SD)	P-Value
Neurovascular Canal			
BMO Area (μm^2)	$5.65\pm0.66\times10^4$	$6.13\pm0.51\times10^4$	0.0375
BMO Radius (µm)	133±8	139±6	0.0358
BMO Depth (µm)	29±15	35±12	0.3448
ASCO Area (μm^2)	$1.29\times10^5\pm0.19\times10^5$	$1.60\times10^5\pm0.21\times10^5$	**0.0016***
ASCO Radius (µm)	201±15	224±14	**0.0016***
ASCO H/V Diameter Ratio	1.26±0.10	1.24±0.11	0.6974
ASCO Depth (µm)	95±14	92±16	0.5450
PSCO Area (μm^2)[1]	$1.35\times10^5\pm0.23\times10^5$	$1.67\times10^5\pm0.27\times10^5$	0.0118
PSCO radius (µm)[1]	206±17	229±17	0.0104
PSCO H/V Diameter Ratio[1]	1.28±0.14	1.22±0.12	0.4276
PSCO Depth (µm)[1]	165±13	162±15	0.6787
Optic Nerve			
ON-ASCO Area (μm^2)	$4.63\times10^4\pm0.44\times10^4$	$6.13\times10^4\pm0.94\times10^4$	**0.0021***
ON-ASCO Radius (µm)	118±6	137±12	**0.0012***
ON-ASCO H/V Diameter Ratio	1.96±0.19	1.60±0.16	**<0.001***
ON-PSCO Area (μm^2)[1]	$4.42\times10^4\pm0.48\times10^4$	$6.07\times10^4\pm0.98\times10^4$	0.0089
ON-PSCO Radius (µm)[1]	111±7	134±12	0.0066
ON-PSCO H/V Diameter Ratio[1]	2.38±0.43	2.21±0.35	0.4971
ON Volume (μm^3)[1]	$3.29\times10^6\pm0.64\times10^6$	$4.59\times10^6\pm0.90\times10^6$	0.0175
Optic Nerve/Scleral Canal Gap Distance			
ASCO-ON-ASCO Distance (µm)	81±13	85±13	0.4080
PSCO-ON-PSCO Distance (µm)[1]	93±13	94±15	0.8342
Sclera/Choroid			
Scleral Thickness (µm)[1]	104±4	104±4	0.8265
Scleral Depth (µm)	33±7	35±7	0.5296
Choroidal Thickness (µm)	57±7	52±11	0.3142

Statistical significance was defined to occur at the *p<0.0022 (Paired T-Test) due to multiple comparisons;
[1]These parameters calculations were obtained without rat 6 data
EG - Experimental Glaucoma

Table 3.8. Overall Global Values for each Parameter by Treatment Group

Parameter[1]	Number of Rats Demonstrating EG Eye Change[2]		Range of significant EG Eye Change (%)[3]	
	+	-	+	-
Neurovascular Canal				
BMO Radius (µm)	5	0	5 ~ 13 (3 ~ 10)	0 (0)
BMO Depth (µm)[4]	5	2	2 ~ 28	-21 ~ -12
ASCO Radius (µm)	7	0	16~ 38 *(8 ~ 21)*	0 (0)
ASCO Depth (µm)	1	2	16	-30 ~ -18
PSCO Radius (µm)[4]	6	0	10 ~ 43 *(5 ~ 21)*	0 (0)
PSCO Depth (µm)[5]	3	4	11 ~ 18	-28 ~ -7
Optic Nerve				
ON-ASCO Radius (µm)	7	0	14 ~ 34 *(11 ~ 30)*	0 (0)
ON-PSCO Radius (µm)	6	0	9 ~ 43 (8 ~ 41)	0 (0)
Optic Nerve to Scleral Canal Gap Distance				
ASCO-ON-ASCO Distance (µm)	4	1	14 ~ 17 (18 ~ 26)	-12 (-13)
PSCO-ON-PSCO Distance (µm)[4]	2	2	14 ~ 28 (18 ~ 29)	-17~ -10 (-16 ~ -10)
Sclera/Choroid				
Scleral Thickness (µm)[4]	3	2	4 ~ 6 *(4 ~ 5)*	-9 ~ -7 *(-8 ~ -7)*
Scleral Depth (µm)	4	1	6 ~ 10	-10
Choroidal Thickness (µm)	2	6	4 ~ 19 *(8 ~ 32)*	-20 ~ -5 *(-29 ~ -7)*

[1]Only parameters in which multiple measurements per eye were possible were included in this analysis

[2] Between eye comparison (EG versus control) was carried out for each parameter for each animal using generalized least squares model (gls**).** Statistically significant between-eye differences were established at $p<0.005$ due to multiple comparisons. Positive sign (+) means increased, negative sign (-) means reduction.

[3]The range of statistically significant EG eye change in micrometers. Percentage is in parentheses *(expressed as the percent of the contralateral control Eye).* Positive sign (+) means increased, negative sign (-) means reduction.

[4]This parameter could only be measured in 7 of the 8 animals

Table 3.9. Frequency of Animal-Specific EG Eye Global Change for each Parameter

Parameters	Superior		Inferior		Nasal		Temporal	
	C (Mean±SD)	EG (Mean±SD)	C (Mean±SD)	EG (Mean±SD)	C (Mean±SD)	EG (Mean±SD)	C (Mean±SD)	EG (Mean±SD)
Neurovascular Canal								
BMO Radius	135±10	141±10	138±15	143±18	132±11	137±11	128±16	136±17
BMO Depth	27±13	31±14	32±17	39±13	32±16	39±14	26±18	32±14
ASCO Radius	187±22	**208±18***	186±21	205±19	217±22	244±24	214±19	**240±22***
ASCO Depth	83±15	78±15	113±20	111±18	101±17	93±20	84±22	85±22
PSCO Radius	196±25	214±21	188±22	203±20	213±22	246±29	222±23	252±32
PSCO Depth	145±16	135±14	189±19	191±20	177±24	171±28	152±20	151±22
Optic Nerve								
ON-ASCO Radius	98±9	**121±13***	90±14	116±17	141±20	156±18	142±22	156±19
N-PSCO Radius	86±10	**111±15***	68±12	94±20	145±31	165±26	146±29	164±29
Optic Nerve to Scleral Canal Gap Distance								
ASCO-ON-ASCO Distance (μm)	107±32	117±27	75±21	57±18	72±28	86±30	72±26	82±26
PSCO-ON-PSCO Distance (μm)	115±32	113±27	112±22	97±15	60±35	73±30	82±31	95±35
Sclera/choroid								
Scleral Thickness	99±14	98±15	91±20	91±19	113±19	113±16	116±23	112±21
Scleral Depth	30±25	29±22	41±31	46±32	37±27	37±30	22±26	28±28
Choroidal Thickness	57±11	49±16	56±14	51±18	59±22	51±15	55±15	58±25

* Statistically significant EG versus Control Eye difference established at $p<0.0125$ due to multiple comparisons (linear mixed effects model)
All values are in micrometers.

Table 3.10. Overall Regional Values for each Parameter by Treatment Group

Parameters	Superior				Inferior				Nasal				Temporal			
	# of Animals[1]		Range of EG Eye Change (%)[2]		# of Animals[1]		Range of EG Eye Change (%)[2]		# of Animals[1]		Range of EG Eye Change (%)[2]		# of Animals[1]		Range of EG Eye Change (%)	
	+	-	+	-	+	-	+	-	+	-	+	-	+	-	+	-
Neurovascular Canal																
BMO Radius	3	0	13 ~ 18 (*9 ~15*)	0(0)	2	0	15 ~ 19 (*11*~ 15)	0 (0)	2	0	11 ~19 (*9 ~15*)	0 (0)	2	0	10 ~ 17 (7 ~ 14)	0 (0)
BMO Depth	3	2	18 ~ 20	-16 ~ -13	4	2	6 ~ 36	-22 ~-16	4	3	14 ~37	-18 ~-8	4	2	4 ~ 30	-26 ~-10
ASCO Radius	7	1	14 ~44 *(7 ~ 26)*	-21 *(-10)*	5	0	22 ~36 (*13 ~ 20)*	0 *(0)*	5	0	23~63 (*11 ~28*)	0 (0)	5	0	15 ~48 (7 ~ 23)	0 (0)
ASCO Depth	2	2	11 ~14	-36 ~-22	1	2	28	-31 ~-15	1	4	31	-30 ~ -14	2	2	15 ~ 25	-25 ~-21
PSCO Radius	5	0	25 ~ 37 (12 ~22)	0 (0)	3	0	26 ~42 (15 ~ 27)	0 (0)	5	0	18 ~71 (8~ 32)	0 (0)	5	0	15 ~ 57 (6 ~24)	0 (0)
PSCO Depth	0	3	0 (0)	-25 ~-15	2	1	17 ~ 33	-26	1	3	33	-36 ~-23	2	2	21 ~ 37	-28 ~-24
Optic Nerve																
ON-ASCO Radius	8	0	5~ 35 *(5 ~ 37)*	0 (0)	8	0	9 ~ 39 (*11 - 44)*	0 (0)	4	0	14 ~32 (*10 ~ 24*)	0 (0)	4	0	13 ~ 30 (9 ~*23*)	0 (0)
ON-PSCO Radius	6	0	13~46 *(16 ~ 57)*	0 (0)	5	0	25 ~ 48 (*36-79*)	0 (0)	3	0	31~ 40 (*23 ~ 28*)	0 (0)	3	0	29 ~ 39 (21~ 27)	0 (0)
Optic Nerve to Scleral Canal Gap Distance																
ASCO-ON-ASCO Distance	5	1	18~49 (16~78)	-66(-43)	0	5	0 (0)	-41~ -19 (-47~ -24)	4	0	17~52 (26 ~ 77)	0 (0)	3	1	13 ~34 (20 ~ 54)	-30 (-32)
PSCO-ON-PSCO Distance	3	3	19~47(20~55)	-61~-13(-39~-14)	1	2	25 (28)	-52 ~-23 (-37 ~-18)	2	1	26~68 (64~140)	-58 (-50)	2	1	52~ 56 (60 ~ 83)	-27 (-24)
Sclera/choroid																
Scleral Thickness	2	2	9 ~ 10 *(11 ~ 12)*	-22 ~-6 (-20 ~-6)	2	1	9 ~ 15 (10 ~ 18)	-10 (-11)	1	0	7 (*7*)	0 (0)	0	2	0	-20 ~-18 *(-15*
Scleral depth	1	2	14	-21 ~-9	1	0	23	0	0	0	0	0	3	1	14 ~23	-13
Choroidal Thickness	1	6	19 (31)	-21~-4 (-35 ~-7)	1	5	19 (33)	-21~-7 (-36 ~-12)	2	4	8 ~ 10 (16 ~25)	-44~-10(-47~-19)	3	4	5 ~ 21 (11 ~36)	-22 ~-7 (-37 ~-1

Statistical significance for regional parameter change within each animal was required to achieve p<0.0001 due to multiple comparisons (linear model using generalized least squares) Values are in microns or *(percent in parentheses)*

[1]number of animals achieving statistically significant change in this parameter within this region. Positive sign (+): increase. Negative sign (-): reduction.

[2]range of the statistically significant EG eye change in micrometers and percentage % *(reported as the percent of the contralateral normal eye)* Positive sign (+): increase. Negative sign (-): reduction.

Table 3.11. Frequency of Animal-Specific EG Eye Regional Change for each Parameter

Parameter[1]	Rat Number															
	Rat 1		Rat 2		Rat 3		Rat 4		Rat 5		Rat 6[2]		Rat 7		Rat 8	
	C	EG	C	EG	C	EG	C	EG	C	EG	C	EG	C	EG	C	EG
NeurovascularCanal																
BMO Area (μm^2)	$6.15x10^4$	$5.88 x10^4$	$4.76 x10^4$	$5.69 x10^4$	$5.26x10^4$	$5.45 x10^4$	$5.71 x10^4$	$6.11 x10^4$	$5.18 x10^4$	$5.86 x10^4$	$6.90 x10^4$	$6.72 x10^4$	$5.40 x10^4$	$6.50x10^4$	$5.83x10^4$	$6.84x10^4$
BMO Radius (μm)	139±18	135±19	122±14	**133±22***	129±11	131±9	135±6	**139±10***	128±12	**136±13***	148±8	146±8	131±10	**144±9***	136±7	**147±10***
BMO Depth	16±11	**38±11***	47 ±9	**26±7***	39±5	**51±10***	36±9	34±6	26±10	**28±9***	37±6	**56±6***	-1±5	**27±9***	33±8	**22±6***
ASCO Area (μm^2)	$1.49x10^5$	$1.45 x10^5$	$1.22x10^5$	$1.45 x10^5$	$1.23x10^5$	$1.60 x10^5$	$1.02 x10^5$	$1.50 x10^5$	$1.57 x10^5$	$2.09 x10^5$	$1.06 x10^5$	$150 x10^5$	$1.38 x10^5$	$1.69 x10^5$	$1.33 x10^5$	$1.55 x10^5$
ASCO Radius (μm)	216±25	213±31	196±21	**215±10***	196±29	**225±21***	180±16	**217±21***	223±16	**256±33***	183±18	**217±22***	209±16	**231±26***	205±25	**221±24***
ASCO H/V Ratio	1.24	1.37	1.26	1.01	1.42	1.28	1.26	1.19	1.11	1.24	1.25	1.26	1.17	1.31	1.38	1.27
ASCO Depth	78±22	78 ±18	104±20	**74±19***	112 ±18	117±17	105 ±16	**87±22***	88 ±17	**104±20***	106±23	106±12	73±13	77±15	94±15	91±9
PSCO Area (μm^2)	$1.59x10^5$	$1.52 x10^5$	$1.13 x10^5$	$1.45 x10^5$	$1.40x10^5$	$1.72 x10^5$	$1.13 x10^5$	$1.47 x10^5$	$1.54x10^5$	$2.23 x10^5$	$1.22 x10^5$	NA	$1.58 x10^5$	$1.74 x10^5$	$1.09 x10^5$	$1.60 x10^5$
PSCO Radius (μm)	223 ±30	218±35	189 ±15	**214±16***	209 ±30	**233±21***	189 ±18	**215±26***	220±20	**263±42***	197±13	NA	223 ±17	**233±29***	185 ±23	**224±25***
PSCO H/V Ratio	1.47	1.15	1.10	1.06	1.40	1.21	1.20	1.23	1.13	1.38	1.21	NA	1.36	1.13	1.33	1.37
PSCO Depth	160±28	**153±22***	170±25	**142±27***	167±20	**181±25***	182 ±19	**163±27***	164 ±23	**182±36***	172±27	NA	141±23	**152±26***	171±29	**163±24***
Optic Nerve (ON)																
ON-ASCO Area (μm^2)	$4.54x10^4$	$5.66x10^4$	$4.26x10^4$	$4.13x10^4$	$4.36x10^4$	$6.88x10^4$	$4.46x10^4$	$5.90x10^4$	$5.37x10^4$	$6.45x10^4$	$4.73 x10^4$	$6.14 x10^4$	$4.16 x10^4$	$6.85 x10^4$	$5.20 x10^4$	$7.02 x10^6$
ON-ASCO Radius (μm)	117 ±27	**133±19***	112 ±33	112±26	114±32	**145±29***	115 ±32	**135±25***	128 ±29	**142±22***	120 ±28	**139±20***	112 ±25	**146±20***	127 ±24	**148±22***
ON-ASCO H/V Ratio	1.82	1.52	2.18	1.90	2.18	1.74	2.08	1.66	1.97	1.57	1.88	1.42	1.86	1.44	1.66	1.51
ON-PSCO Area (μm^2)	$4.81x10^4$	$4.99x10^4$	$4.28x10^4$	$4.78x10^4$	$4.14x10^4$	$6.79x10^4$	$3.99x10^4$	$5.61x10^4$	$5.34x10^4$	$6.39 x10^4$	$4.37 x10^4$	NA	$4.25 x10^4$	$6.52 x10^4$	$4.14 x10^4$	$7.44 x10^6$
ON-PSCO Radius (μm)	117 ±41	119±42	108±44	**117±39***	107±41	**142±39***	105±43	**128±40***	124±41	**139±31***	111±42	NA	112±33	**140±33***	106±43	**150±37***
ON-PSCO H/V Ratio	2.41	2.43	2.72	2.34	2.60	2.04	2.97	2.10	2.29	1.64	2.55	NA	1.89	2.18	1.81	2.75
ON Volume (μm^3)	$3.95x10^6$	$3.78x10^6$	$2.92x10^6$	$3.08x10^4$	$2.29x10^6$	$4.61x10^6$	$3.25x10^6$	$4.69x10^6$	$4.04x10^6$	$4.95 x10^6$	$3.20 x10^6$	NA	$2.88 x10^6$	$5.54 x10^6$	$3.67 x10^6$	$5.50 x10^6$
Optic Nerve to Scleral Canal Gap Distance																
ASCO-ON-ASCO Distance (μm)	91±48	80±24	84±20	**101±37***	82±19	78±26	64±22	**81±29***	94±31	**111±46***	63±20	**77±32***	95±26	**83±28***	76±28	73±19
PSCO-ON-PSCO Distance (μm)	104±41	98±20	81±34	**95±41***	101±31	**91±32***	83±42	87±22	96±38	**123±23***	86±35	NA	110±38	**92±29***	78±27	74±19
Sclera/Choroid																
Scleral Thickness (μm)	109±26	**101±17***	105±23	103±18	107±19	106±21	105±19	**110±18***	105±15	**98±24***	110±18	N/A	101±25	**106±19***	97±23	**101±22***
Scleral Depth	27±36	**32±27***	39±29	**29±23***	38±28	37±32	32±27	33±28	38±24	**47±35***	37±26	**45±30***	19±23	**27±26***	33±25	31±26
Choroidal Thickness	56 ±13	**46±13***	45±11	**48±11***	54±14	**44±17***	55±11	**48±15***	60±11	**80±20***	70±26	**50±12***	61±14	**56±19***	54±10	**49±15***

EG eye value is significantly different from the contralateral normal eye (Generalized least squares model, $p < 0.005$ due to adjustment for multiple comparisons)*[1]Included parameters are those with multiple measurements per eye which are required to assess animal-specific EG eye versus Control eye differences [2]Outer scleral canal and peripapillary scleral parameters are missing for the EG eye of Rat 6 due to poor visualization within its 3D histomorphometric reconstruction.

Table 3.12. Animal Specific Global Values for each Parameter

3.3.3.2. Representation of the delineated points for the different parameters studied and its comparison in Normal Controls vs EG Eyes

3.3.3.2.1. Neurovascular Canal Parameters: BMO, ASCO, PSCO

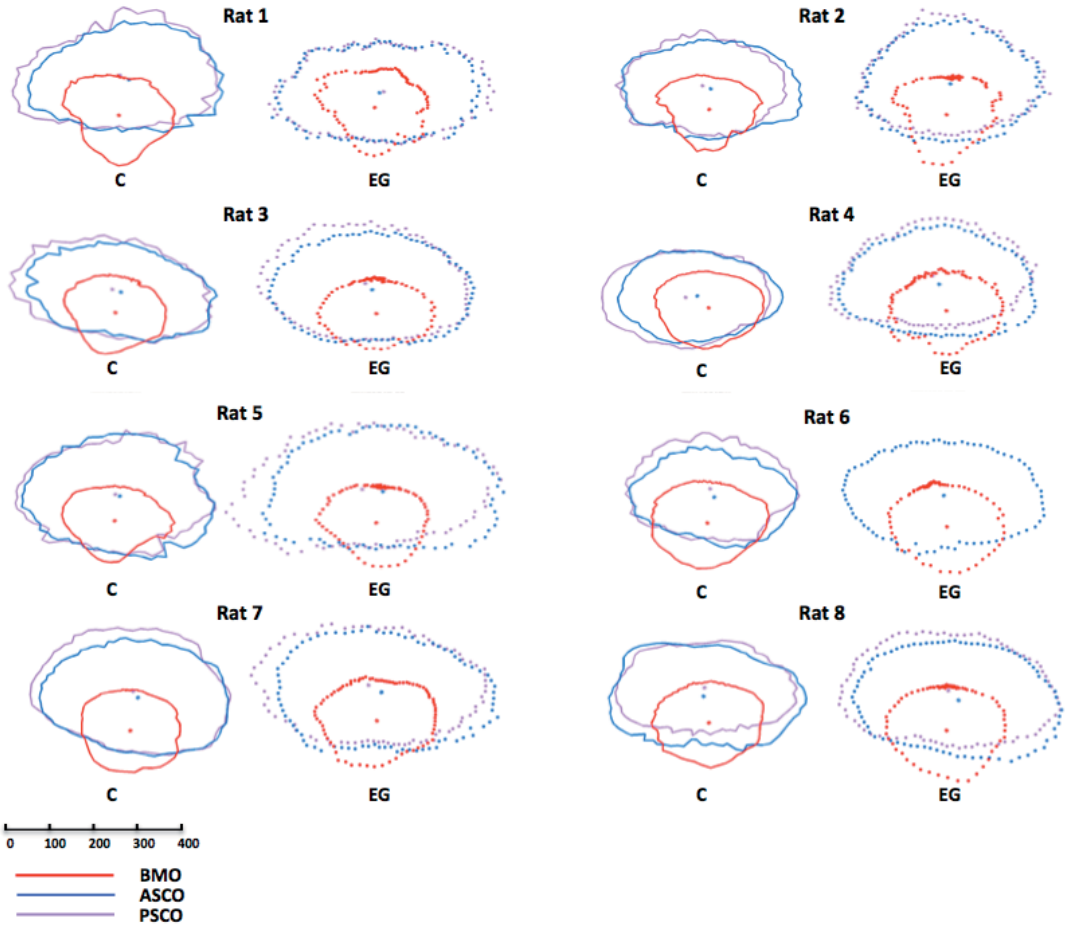

Figure 3.5. Within and between-eye comparisons of BMO (red), ASCO (blue) and PSCO (purple) for the Control (solid lines) and EG (dotted lines) eye of each animal. Delineated points for each structure along with their centroid are shown in right eye orientation projected onto the BMO reference plane (x axis horizontal and y axis vertical) for comparison purposes. The BMO centroid for each eye has been used to horizontally align the data for the two eyes of each animal. Note that the ASCO and PSCO centroids tend to be vertically separated and further away from the BMO centroid in the EG eyes with the greatest damage (Rats 4, 5, 7 and 8). These data suggest that apart from the EG eye expansion of these individual openings (demonstrated most clearly Figures 3.6, 3.7 and 3.8), glaucomatous alteration of the rat neurovascular scleral canal includes a vertical shift of the PSCO relative to the ASCO and BMO which becomes more pronounced as ON damage progresses. The scale is in micrometers. PSCO data is not available for the EG eye of Rat 6.

.

The following pictures represent separately the BMO, ASCO and PSCO delineation points overlay comparisons of the Normal vs EG eye in each studied rat and show the rats in which this comparison was statistically significant.

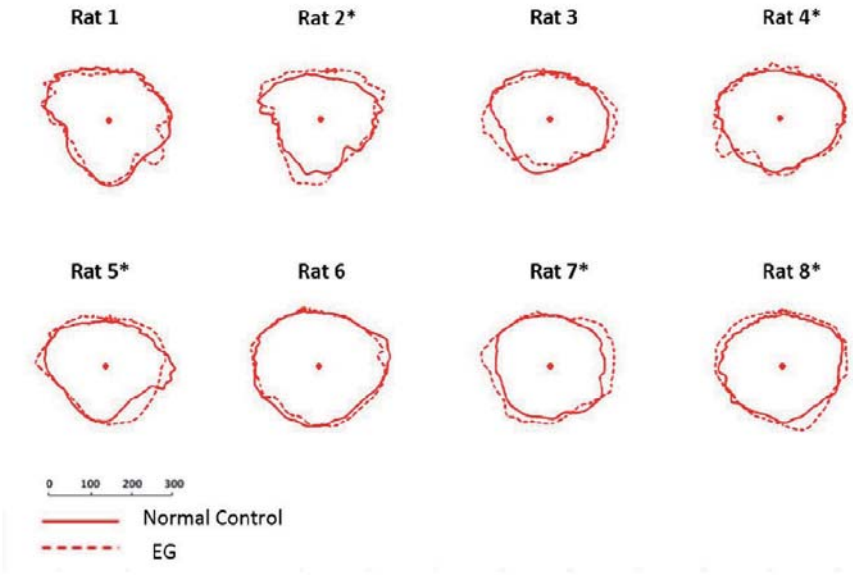

Figure 3.6. EG (dotted line) versus Control (solid line) eye Bruch's Membrane Opening (BMO) comparison for each animal. BMO data points for the Control and EG eye of each rat are schematically overlaid using the BMO centroid of each eye. All data are in right eye orientation. The scale is in micrometers. **(*)** denotes animals in which Global EG versus Control Eye *BMO radius* differences achieved significance (Table 3.12)

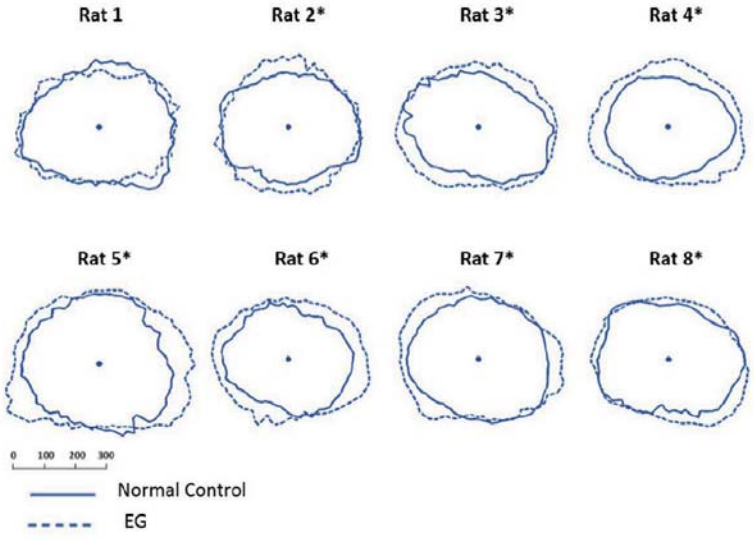

Figure 3.7. EG (dotted line) versus Control (solid line) eye Anterior Scleral Canal Opening (ASCO) comparison for each animal. ASCO data points for the Control and EG eye of each rat are schematically overlaid using the ASCO centroid of each eye. All data are in right eye orientation. The scale is in micrometers. **(*)** denotes animals in which Global EG versus Control Eye *ASCO radius* differences achieved significance (Table 3.12).

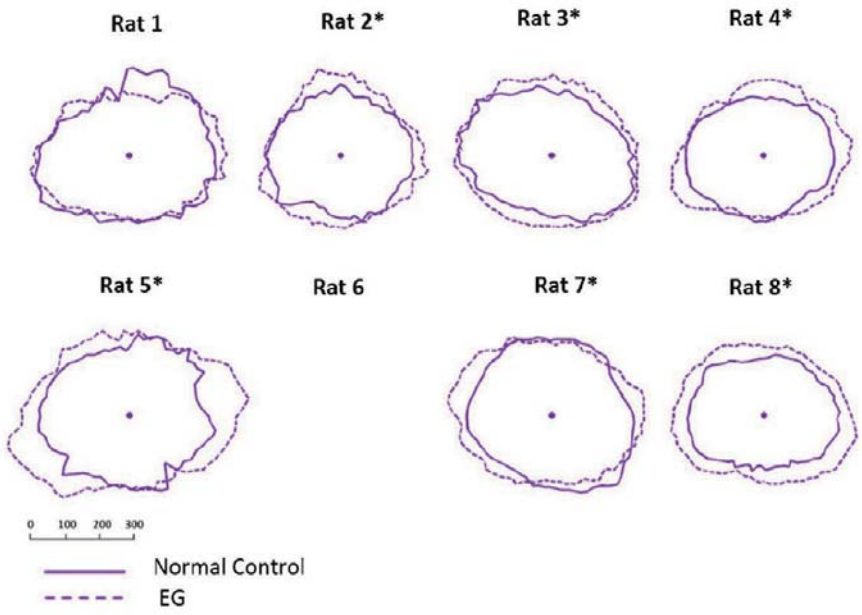

Figure 3.8. EG (dotted line) versus Control (solid line) eye Posterior Scleral Canal Opening (PSCO) comparison for each animal. PSCO data points for the Control and EG eye of each rat are schematically overlaid using the PSCO centroid of each eye. All data are in right eye orientation. The scale is in micrometers. (*) denotes animals in which Global EG versus Control Eye PS*CO radius* differences achieved significance (Table 3.12). PSCO data for the EG eye of Rat 6 were not available.

3.3.3.2.2. The Optic Nerve

Among all statistically significant EG versus Control Eye differences, optic nerve size differences were greatest in magnitude and occurred most consistently among the 8 EG eyes. Overall mean *ON-ASCO Area* was 32% larger and mean *ON-ASCO radius* was 16% larger in the EG compared to the Control eyes ($p<.0021$ and $p<.0012$, respectively). Overall mean *ON-ASCO H/V Diameter Ratio* was 22.5% smaller in the EG compared to the Control eyes, ($p<0.001$) suggesting that EG eye optic nerve expansion was greater within the vertical compared to the horizontal axis.

Animal-specific EG eye values were significantly larger than Control eye values for: *ON-ASCO Radius* within 7 animals (ranging from 11 to 30%, $p<0.005$, Figures 3.9 and 3.11 and *ON-PSCO Radius* in 6 out of the 7 animals in which it could be measured (ranging from 8 to 41%, $p<0.005$, Figure 3.10 and Figure 3.12). Within the overall regional analysis, (Table 5), *ON-ASCO Radius* and *ON-PSCO Radius* demonstrated significantly larger EG versus Control eye values within the superior region. EG eye values were significantly larger than Control eyes for *ON-ASCO Radius* in all 8 animals within the superior and inferior quadrants (Table 3.8). EG eye values were significantly larger than Control eye values for *ON-PSCO Radius* in 6 animals within the superior and 5 animals within the inferior quadrant (Table 3.11).

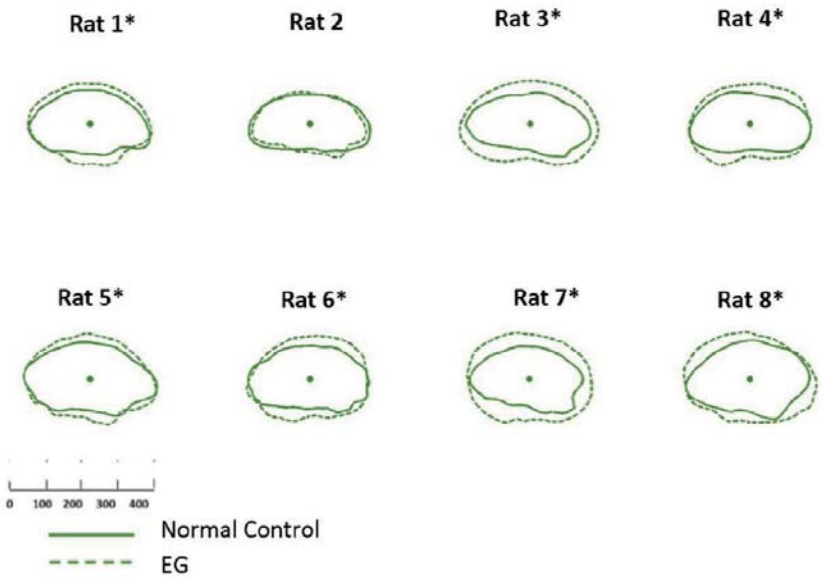

Figure 3.9. EG (dotted line) versus Control (solid line) eye *Optic Nerve within the Anterior Scleral Canal Opening* (*ON-ASCO)* comparison for each study animal. ON-ASCO data points for the Control and EG eye of each rat are schematically overlaid using the ON-ASCO centroid of each eye. All data are in right eye orientation. The scale is in micrometers. **(*)** denotes animals in which Global EG versus Control Eye *ON-ASCO radius* differences achieved significance (Table 3.12).

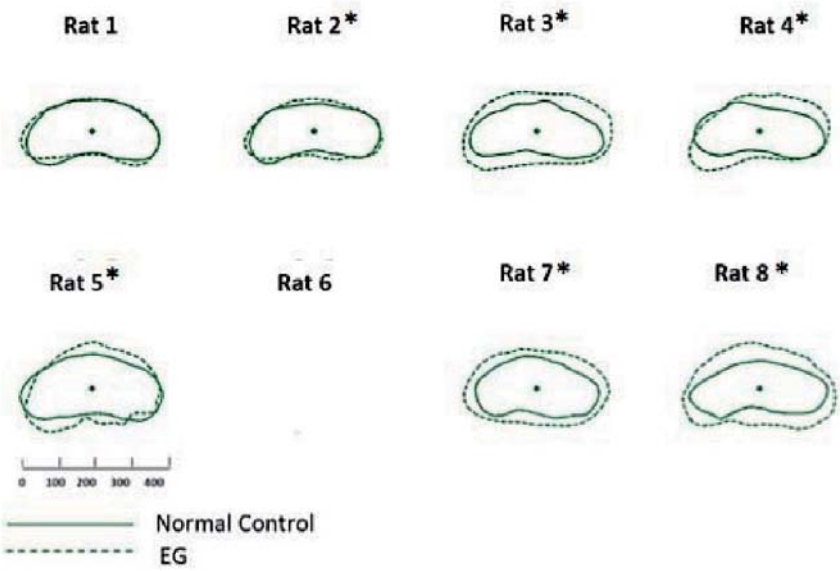

Figure 3.10. EG (dotted line) versus Control (solid line) eye *Optic Nerve within the Posterior Scleral Canal Opening* (*ON-PSCO)* comparison for each study animal. ON-PSCO data points for the Control and EG eye of each rat are schematically overlaid using the ON-PSCO centroid of each eye. All data are in right eye orientation. The scale is in micrometers. **(*)** denotes animals in which Global EG versus Control Eye *ON-PSCO radius* differences achieved significance (Table 3.12). ON-PSCO data for EG eye of Rat 6 were not available.

3.3.3.2.3. The Optic Nerve Inside this Neurovascular Canal

The following two figures represent the ON gap distance at the level of the ASCO and PSCO respectively.

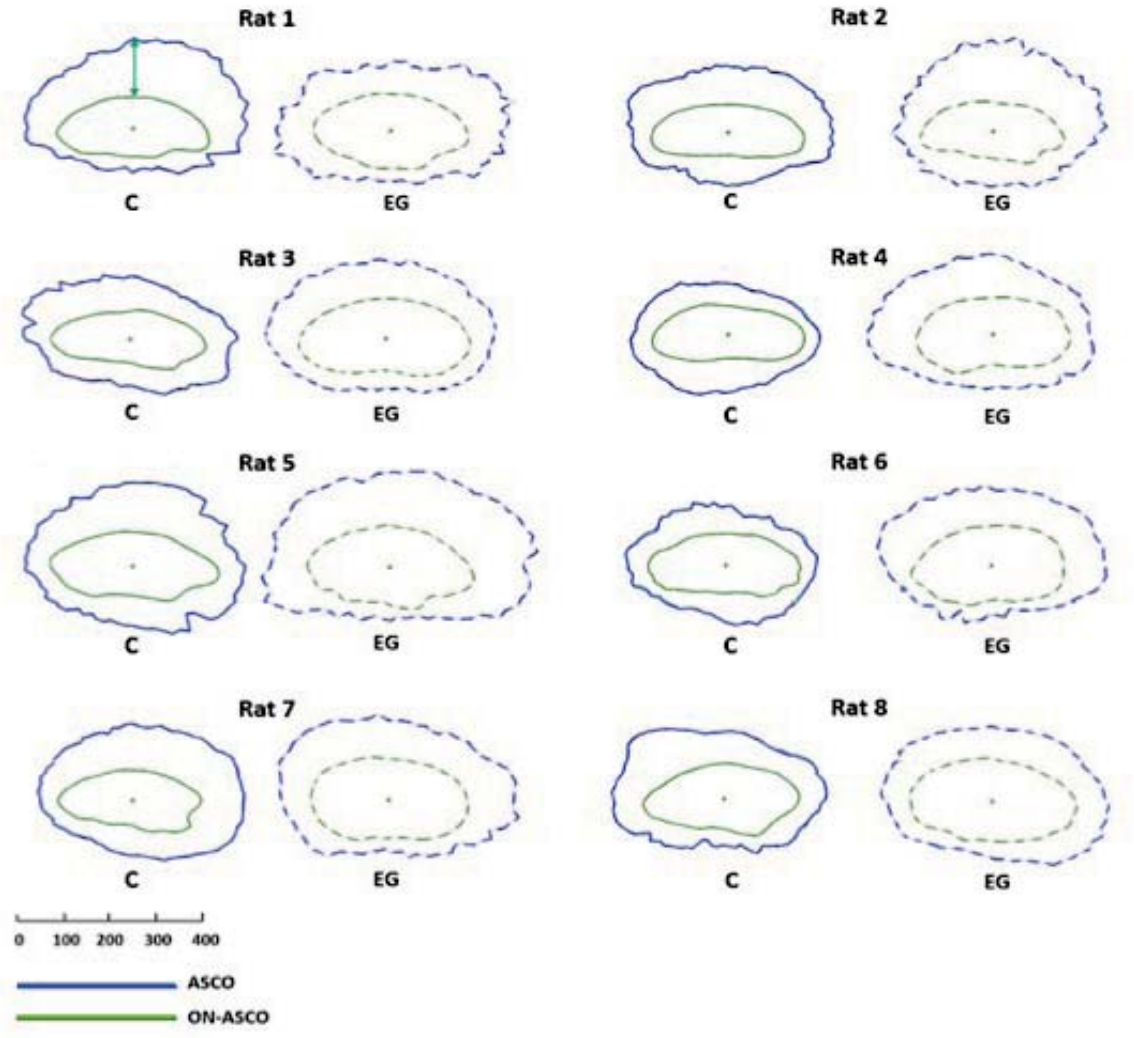

Figure 3.11. Animal-specific, EG (dotted line) versus Control Eye (solid line) comparisons of Anterior Scleral Canal Opening (ASCO - blue) and Optic Nerve – ASCO (ON-ASCO - green) and the ASCO-to- Optic Nerve ASCO Gap Distance (ASCO-ON-ASCO) (green arrow upper left). ASCO fitted spline and ON-ASCO fitted spline were projected onto the ASCO reference plane for comparison purposes. The ON-ASCO centroid for each eye has been used to horizontally align the data from each eye. The green arrow (Control eye of Rat 1, upper left) schematically depicts the *ASCO-ON-ASCO Gap Distance* measurement (here showing 1 of a total of 80 radial measurements – see methods). Animal- specific EG vs Control eye overlays of ASCO and ON-ASCO data can be seen in Supplemental Figures 9 and 11, respectively. Global EG eye increases in *ASCO radius* were present within Animals 2-8. Global EG eye increases in *ON-ASCO radius* were present within Animals 1 and 3–8. Global EG eye *ASCO-ON-ASCO Distance* was significantly increased within Animals 2, 4, 5, 6 and 7. The scale is in micrometers.

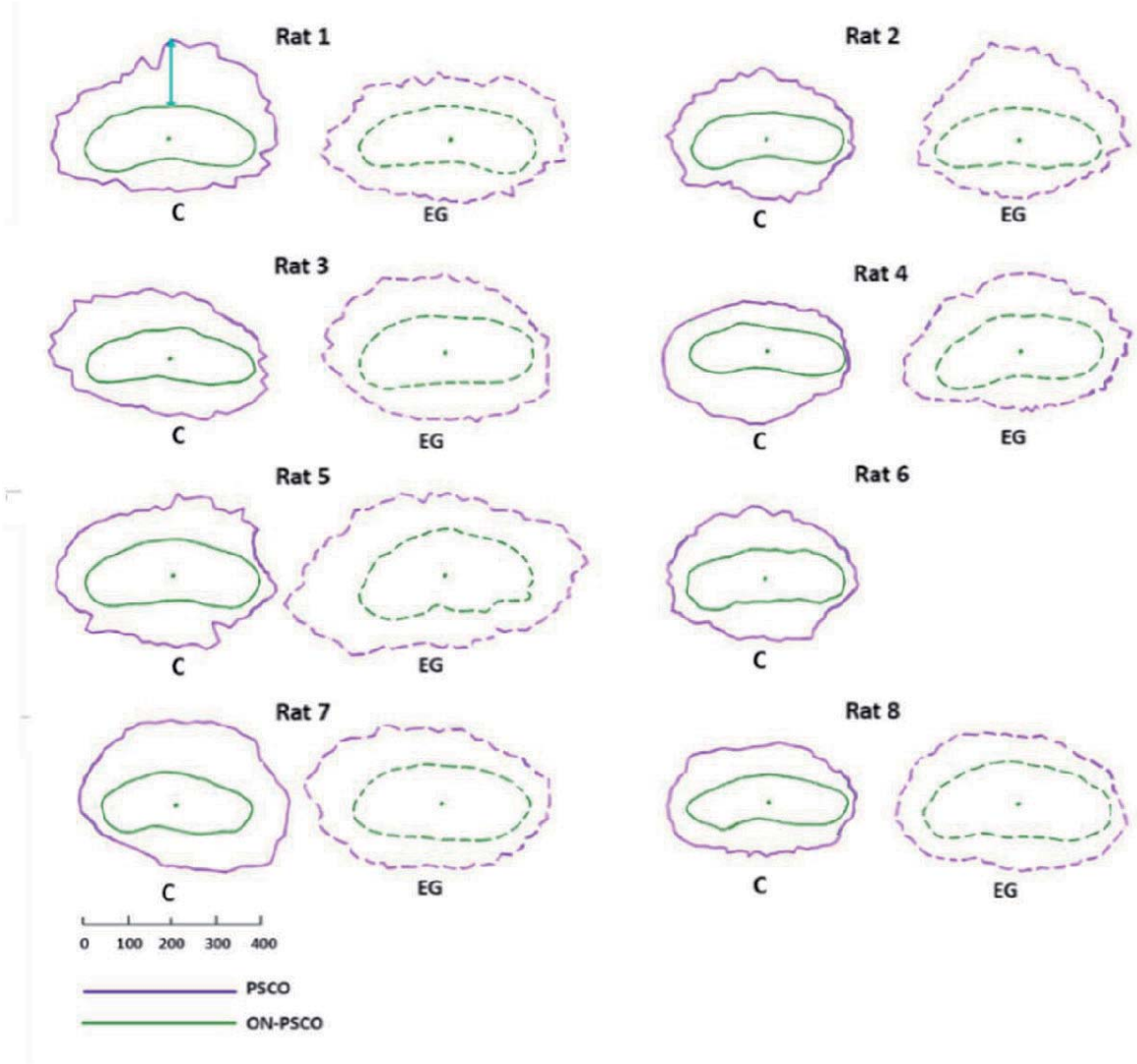

Figure 3.12. Animal-specific, EG (dotted line) versus Control Eye (solid line) comparisons of Posterior Scleral Canal Opening (PSCO – Purple) and Optic Nerve–PSCO (ON-PSCO - green). PSCO fitted spline and ON-PSCO fitted spline are projected onto the PSCO reference plane for comparison purposes. The ON-PSCO centroid for each eye has been used to horizontally align the data from each eye. The green arrow (Control eye of Rat 1, upper left) schematically depicts the *PSCO-ON-PSCO Distance* measurement (here showing 1 of a total of 80 radial measurements – see methods). Animal-specific EG vs Control eye overlays of PSCO and ON-PSCO data can be seen in Supplemental Figures 10 and 12, respectively. Global EG eye *PSCO-ON-PSCO Distance* was significantly increased within Animals 2, 3, 5, and 7. The scale is in micrometers

3.3.3.3. Correlation with orbital axon nerve degeneration

ON-PSCO Area expansion was significantly correlated to EG eye *optic nerve injury grade* (R=0.768; p=0.042) among the 7 EG eyes for which there was ON-PSCO data (Figure 3.13).

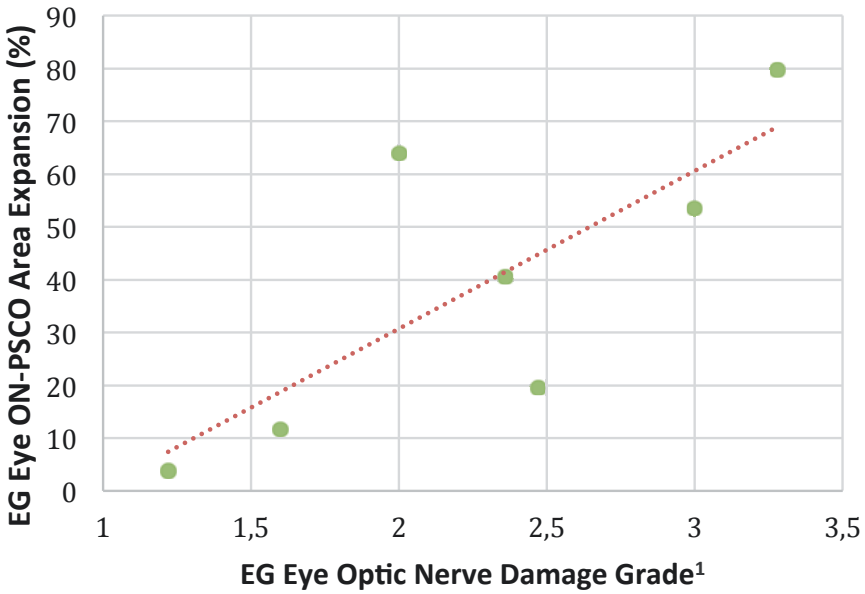

Figure 3.13. Correlation between EG Eye *ON-PSCO Area* Expansion and EG eye *Optic Nerve Damage Grade* (Table 3.6). EG vs Control eye *ON-PSCO Area* expansion was significantly correlated to EG eye *Optic Nerve Damage Grade* (R= 0.768, P=0.042).[1] Optic nerve qualitative damage nerve grading adapted from Morrison et al 1997.

3.3.4.COPY OF THE SECOND PAPER

Expansions of the neurovascular scleral canal and contained optic nerve occur early in the hypertonic saline rat experimental glaucoma model

.

Marta Pazos, Hongli Yang, Stuart K. Gardiner, William O.Cepurna, Elaine C. Johnson, John C. Morrison, Claude F. Burgoyne.

Exp Eye Res. 2015 Oct 21. pii: S0014-4835(15)30052-X. doi: 10.1016/j.exer.2015.10.014.

[Epub ahead of print]

Expansions of the Neurovascular Scleral Canal and Contained Optic Nerve Occur Early in the Hypertonic Saline Rat Experimental Glaucoma Model.

Marta Pazos[d], Hongli Yang[a], Stuart K. Gardiner[b], *W.O. Cepurna[c], E.C. Johnson[c], J.C. Morrison[c],* Claude F. Burgoyne[a]

From the [a]Devers Eye Institute, Optic Nerve Head Research Laboratory, Legacy Research Institute, Portland, Oregon, and the [b]Devers Eye Institute, Discoveries in Sight Research Laboratories, Legacy Research Institute, Portland, Oregon, and the [c]Kenneth C. Swan Ocular Neurobiology Laboratory, Casey Eye Institute, Oregon Health and Science University, Portland, Oregon, and [d]Hospital de l'Esperança. Parc de Salut Mar. Universitat Autònoma de Barcelona, Barcelona, Spain.

Marta Pazos and Hongli Yang are co-first authors of this work.

Supported in part by NIH grants R01EY011610 (CFB), R01EY10145 (JCM) and R01EY16866 (ECJ)) from the National Eye Institute, National Institutes of Health, Bethesda, Maryland; The Legacy Good Samaritan Foundation, Portland, Oregon; the Sears Trust for Biomedical Research, Mexico, Missouri; the Alcon Research Institute, Fort Worth, Texas; and an unrestricted grant from Research to Prevent Blindness.

Word count (text only):	5553
Tables:	6
Figures:	6
Supplemental Tables:	2
Supplemental Figures:	11
Section code:	GL

Keywords: Glaucoma, Rat, Optic Nerve Head, Neural Canal, scleral canal, Optic Nerve,
Proprietary Interest Category: N

Corresponding Author:
Claude F. Burgoyne, MD,
Devers Eye Institute, Optic Nerve Head Research Laboratory,
1225 NE 2nd Ave, Portland OR 97232.
Email: cfburgoyne@deverseye.org.
Tel: +1-503-413-5441
Fax: +1-503-413-5179

Abstract

Purpose. To characterize early optic nerve head (ONH) structural change in rat experimental glaucoma (EG).

Methods. Unilateral intraocular pressure (IOP) elevation was induced in Brown Norway rats by hypertonic saline injection into the episcleral veins and animals were sacrificed 4 weeks later by perfusion fixation. Optic nerve cross-sections were graded from 1 (normal) to 5 (extensive injury) by 5 masked observers. ONH's with peripapillary retina and sclera were embedded, serial sectioned, 3-D reconstructed, delineated, and quantified. Overall and animal-specific EG versus Control eye ONH parameter differences were assessed globally and regionally by linear mixed effect models with significance criteria adjusted for multiple comparisons.

Results. Expansions of the optic nerve and surrounding anterior scleral canal opening achieved statistical significance overall ($p<.0022$), and in 7 of 8 EG eyes ($p<.005$). In at least 5 EG eyes, significant expansions ($p<.005$) in Bruch's membrane opening (range 3-10%), the anterior and posterior scleral canal openings (8-21% and 5-21%, respectively), and the optic nerve at the anterior and posterior scleral canal openings (11-30% and 8-41%, respectively) were detected. Optic nerve expansion was greatest within the superior and inferior quadrants. Optic nerve expansion at the posterior scleral canal opening was significantly correlated to optic nerve damage ($R= 0.768$, $P=.042$).

Conclusion: In the rat ONH, the optic nerve and surrounding Bruch's membrane opening and neurovascular scleral canal expand early in their response to chronic experimental IOP elevation. These findings provide phenotypic landmarks and imaging targets for detecting the development of experimental glaucomatous optic neuropathy in the rat eye.

Introduction

Mouse and rat experimental glaucoma models are increasingly utilized to study the mechanisms of chronic intraocular pressure-induced optic nerve injury. While the nonhuman primate experimental glaucoma model (Burgoyne, 2015b) benefits from optic nerve head (ONH) anatomy and physiology that is similar to the human ONH, the model is impractical for studies that require large sample sizes. By contrast, rodent models (Crowston et al., 2015; Fernandes et al., 2015; Morgan and Tribble, 2015; Morrison et al., 2015; Overby and Clark, 2015; Pang et al., 2015) display pathophysiologic changes that are comparable to human glaucoma, despite substantial differences in ONH anatomy.

The suitability of rodent models is based upon several lines of reasoning. First, a series of previous reports have determined that early (if not the earliest) damage to the retinal ganglion cell axons occurs within the ONH tissues in all induced and spontaneous forms of rodent (Morrison, 2005; Morrison et al., 2011; Morrison et al., 2008; Morrison et al., 1997; Morrison et al., 1998; Schlamp et al., 2006) and primate (Burgoyne et al., 2004; Downs et al., 2007; Yang et al., 2007a; Yang et al., 2007b) chronic IOP elevation. Second, to a certain degree, the rodent ONH demonstrates characteristics that are analogues to the primate ONH (Morrison et al., 2011). These include similar ultrastructural relationships between astrocytes and axons (Morrison et al., 1995; Morrison et al., 1997) as well as similar cellular changes (Hernandez et al., 1990; Johnson et al., 1996; Morrison et al., 1990), neural canal expansion (Chauhan et al., 2002; Guo et al., 2005) and posterior deformation of the ONH surface in response to chronic IOP elevation (Chauhan et al., 2002). Likewise, chronic models of IOP elevation in rats have also demonstrated a predilection for early superior optic nerve injury (Dai et al., 2012; Huang and Knighton, 2009; Li et al., 2015; Morrison, 2005; Morrison et al., 1997; WoldeMussie et al., 2001) (Morrison JC, et al. *IOVS* 2002; ARVO E-Abstract 2885). Understanding the basis for this regional susceptibility in rats may provide insight into mechanisms of regional susceptibility in humans.

Third, the anatomy of the rodent ONH is also very different from the human and non-human primate (Morrison et al., 2011). Understanding these differences and recognizing how they contribute to species-related differences in age-related retinal ganglion cell axon loss (Cepurna et al., 2005) and age-related differences in the susceptibility of axon transport to acute (Kong et al.,

2009) and chronic IOP elevation (Morrison et al., 1997) (Morrison JC et al. *IOVS* 2007; 48: ARVO E-Abstract 3662; Johnson EC et al. *IOVS* 2008; 49: ARVO E-Abstract 4059) should provide important knowledge about these same phenomena in human eyes.

We recently performed high-resolution (1.5 cubic micron voxel) 3D histomorphometric reconstruction of the optic nerve head (ONH) and peripapillary sclera from both the normal control (Control) and experimental glaucoma (EG) eyes of eight brown Norway rats that had undergone 4 weeks of unilateral chronic IOP elevation. In an initial publication (Pazos et al., 2015), we described the 3D histomorphometric anatomy of the 8 Control rat ONHs and characterized the differences between the normal control rat and primate ONH (Figures 1 - 7 of our previous report) (Pazos et al., 2015). That study was the first to describe the rat ONH as consisting of two scleral openings (a neurovascular and arterial) and clarify that the central retinal artery (CRA) does not accompany the central retinal vein (CRV) within the neurovascular canal, but passes through a separate, large, irregular opening, inferior to it, accompanied by the long posterior ciliary arteries (LCPAs) and their dense intra-scleral branches. Our study confirmed the presence of a previously described (Dai et al., 2012; Morrison et al., 1999; Sugiyama et al., 1999) vascular plexus that is continuous from the choroid to the optic nerve sheathes and surrounds the optic nerve within the neurovascular scleral canal. It additionally confirmed the anatomic proximity of the retinal ganglion cell (RGC) axon bundles and a prominent extension of Bruch's Membrane (BM) superiorly that is unique to that region.

The purpose of the present report is to 3-D characterize overall and animal specific, global and regional EG versus Control eye differences within the 8 rats of our previous report (Pazos et al., 2015).

Materials and Methods

Table 1 defines all abbreviations. Supplemental Figures 1-3 (corresponding to figures 1-3 of our previous publication (Pazos et al., 2015)) review the macroscopic and microscopic relationships of the rat ONH. See our previous report (Pazos et al., 2015) for more detailed illustration of the 3D relationships among the neural, vascular and connective components of the rat ONH. Throughout the present report, all right and left eye data are presented in right eye

orientation and all *parameters* are italicized to distinguish the behavior of *measured parameters* from the behavior of the underlying anatomy they characterize (not italicized).

Animals and eyes. All animals were treated in accordance with the ARVO Statement for the Use of Animals in Ophthalmic and Vision Research. Both the Control and EG eyes of 8 adult male brown Norway rats, between 9.5 and 10.5 months of age, were studied (Table 2).

Induction of chronic unilateral experimental IOP elevation and its measurement in rats. Animals were housed initially in standard lighting conditions, with lights automatically turned on at 6 AM and off at 6 PM. One week before the hypertonic episcleral vein injection in one eye (the treated eye), each animal was placed in constant light conditions (24 hours exposure to 40-90 lux) (Morrison et al., 2005; Pang et al., 2005). Following injection, each animal was followed for 4 weeks, and then sacrificed (see below). IOP readings in both the Control and EG eyes of each animal were made while awake (using 0.5% proparacaine hydrochloride as topical anesthesia to avoid the effects of general anesthetics) using a hand-held TonoPen tonometer. IOP was measured at least every other day, with a minimum of 14 IOP readings over the 4 weeks post saline injection. Mean IOP for both eyes of each animal was calculated as the area under the curve of an IOP vs days plot divided by the number of days. The Mean IOP Difference for each animal was defined to be the difference between the mean IOP of the EG versus the Control eye. The Peak IOP for each animal was defined to be the highest IOP in the EG eye.

Rat Euthanasia, Fixation and Injury Grade analysis. All animals were sacrificed 4 weeks post-initial saline injection to the treated eye under isoflurane anesthesia by transcardial injection of heparin (1 ml/kg) containing 10 mg ml sodium nitroprusside followed by 1 liter of 5% glutaraldehyde in 0.1 M phosphate buffer (pH 7.2). Optic nerves were dissected, washed, dehydrated and embedded in Spurr's resin as previously described (Morrison et al., 1998). Using light microscopy, 5 masked observers graded the orbital optic nerve cross-section from each eye using a previously published scale from 1 (no injury) to 5 (active degeneration involving the whole nerve area) (Jia et al., 2000) and their grades were averaged to obtain the final injury grade for each nerve.

3-D Histomorphometric Reconstruction of the ONH. The ONH and peripapillary sclera of each eye were trephined (3-mm-diameter), embedded in paraffin, mounted to a microtome (RM2165; Leica, Wetzlar, Germany) and serial sectioned at 1.5 μm thickness from the vitreous surface through the optic nerve head into the orbital optic nerve (Burgoyne et al., 2004). After each section was cut, the block surface was stained with a 1:1 (v/v) mixture of Ponceau S and acid fuchsin stains, then imaged at a resolution of 1.5 x 1.5 μm per pixel using a custom device (Burgoyne et al., 2004) . For each ONH 275 to 501 serial digital transverse section images were thus generated, aligned and stacked into a digital 3-D reconstruction (Burgoyne et al., 2004; Downs et al., 2007; Yang et al., 2007a; Yang et al., 2009a; Yang et al., 2007b; Yang et al., 2011a).

3-D Delineation of the Rat ONH and Peripapillary Scleral Landmark Points. Each 3-D ONH reconstruction was loaded into our custom Multiview 3-D visualization and delineation software (based on the Visualization Toolkit [VTK], Clifton Park, NY) (Burgoyne et al., 2004; Downs et al., 2007; Morrison et al., 1999; Yang et al., 2007a; Yang et al., 2009a; Yang et al., 2007b). A delineator assigned the approximate center of the optic nerve (Supplemental Figure 3) as the center of rotation, through which, forty, 7-voxel thick, digital radial sagittal slices of the digital 3-D reconstruction were serially served at 4.5° intervals for delineation. Because visualization of Bruch's Membrane (BM), Bruch's Membrane Opening (BMO) and several deep ONH landmarks was most consistent within Green channel as opposed to white light section images, delineation was carried out within green channel digital section images for each study eye. Four landmark surfaces and three pairs of neurovascular canal landmark points (one point on each side of the canal) were delineated within each digital section image (Supplemental Figure 3). The landmark surfaces were: (1) BM; (2) the anterior and (3) posterior surfaces of peripapillary sclera; and (4) the outer optic nerve boundaries extending on both sides of the nerve from BMO, through the neurovascular scleral canal and along the pia mater to the posterior edge of the reconstruction. The landmark points were BMO, the anterior scleral canal opening (ASCO) and the posterior scleral canal opening (PSCO).

Masked Delineation Strategy. Both eyes of each rat were delineated by a single delineator who was masked to the treatment status of each eye. Final delineations were checked for accuracy by two experienced observers (HY and CFB) masked as to the treatment condition of each eye.

Delineation Reproducibility Study. Both the Control and EG eye of each animal were delineated by a single delineator (MP). Upon completion of the initial delineation of each eye, the marks were reviewed by 2 authors (CFB and HY) to expand our understanding of the anatomy and to reach agreement on the anatomic landmarks of greatest interest. Both eyes of three animals were then delineated on two subsequent occasions by the same delineator (MP), at least 2 weeks apart, to assess intra-delineator variability. The intraclass-Correlation Coefficient (ICC) (see statistical analysis, below) for all reported parameters were calculated (Rosner, 2011).

Parameterization and Quantification. For each 3-D ONH reconstruction, a plane satisfying a least-squares error restraint was fit to the 80 BMO points (Pazos et al., 2015), creating a BMO reference plane which served as the reference plane for a series of subsequent measurements (Supplemental Figure 4) and the base for the second peripheral anterior scleral reference plane (Supplemental Figure 6). The following parameters have been previously described (Pazos et al., 2015) and are illustrated in Supplemental Figures 4-7: BMO and the neurovascular canal parameters: *ASCO and PSCO Areas, Radii and Depths,* Horizontal/Vertical (H/V) Diameter Ratios for BMO, ASCO and PSCO; Optic Nerve cross-sectional parameters: Optic Nerve cross sectional area, radii and shape (H/V diameter ratios) at the level of ASCO (*ON-ASCO*) and PSCO (*ON-PSCO*) as well as the *Optic Nerve Volume*; Scleral and Choroidal Parameters: *Scleral Sling Depth, Scleral Depth, Scleral Thickness and Choroidal Thickness*. In addition, to assess preferential displacement of the nerve within the neurovascular canal of the EG eyes, two new parameters measuring the distance between the neurovascular scleral canal wall and the contained optic nerve (the optic nerve gap distance) were calculated within all 80 radial locations: 1) the ASCO to ON-ASCO distance *(ASCO ON-ASCO Distance);* and 2) the PSCO to ON-PSCO distance (*PSCO ON-PSCO Distance)* (See Figure 2 and Supplemental Figure 11, (respectively) for diagrams.

Statistical Analysis. EG versus Control eye global data were compared using a paired, two-sided student T-test with significance defined to occur at $p<0.0022$ to adjust for multiple (n=23) comparisons (Guo and Yuan, 2015). For the subset of parameters with multiple values per eye, overall (experiment-wide) EG eye effects were assessed within each region using a linear mixed effects model, accounting for multiple data points per eye and two eyes per rat (significance defined at $p<0.0125$, to adjust for 4 regional comparisons per parameter). An exponential spatial correlation structure was assumed within each eye, based on the distances between delineated points. EG vs Control eye comparisons for each animal globally (significance defined at $p<0.005$,13 comparisons per rat) and by each quadrant (significance defined at $p<0.0001$, 13 comparisons per quadrant) were carried out using generalized least squares models assuming exponential spatial correlation structure. Within the reproducibility study, the ICC was calculated from one-way ANOVA. Correlation between the magnitude of global EG eye change in the area and volume optic nerve parameters (ASCO area, PSCO area, ON-ASCO area, ON-PSCO area and ON Volume) and the orbital optic nerve injury scale was assessed for statistical significance using Pearson's correlation coefficient ($p<0.05$ without adjustment due to the small number of purposeful comparisons). Analysis was carried out either in R (the R Foundation for Statistical Computing, Vienna, Austria) or Microsoft Excel (Microsoft, Redmond, WA, USA).

Results

Animal and Eye Data (Table 2). Both the EG and the Control eyes of eight brown male Norway rats (aged from 9.5 to 10.5 months) were studied. A detailed description of the 8 Control eyes is contained within our previous report (Pazos et al., 2015). Eye-specific mean IOP in the Control eyes ranged from 28.3 to 28.5 mmHg. Eye-specific mean IOP in the EG eyes ranged from 28.3 to 34.6 mmHg, with *Mean IOP Differences* ranging from 0.4 to 6.6 mmHg and *Peak IOPs* ranging from 36 to 45.8 mmHg. The *mean optic nerve damage grade* for all 8 Control eyes was 1.0 (no detectable damage) and ranged from 1.22 (Rat 1) to 3.28 (Rat 8) in the EG eyes. For this and the previous normal Control eye report (Pazos et al., 2015) study animals were numbered 1-8 based on the magnitude of each animal's EG eye *optic nerve damage grade*. Several parameters could not be calculated for the EG eye of Animal 6 due to poor visualization of the outer scleral canal and peripapillary sclera.

Delineation Reproducibility. Reproducibility was excellent (ICC values greater than 0.75) or fair to good (ICC 0.49-0.75) for all parameters included in this study (Supplemental Table 1).

Overall and Animal Specific Global and Regional Parameter Change

Overall global values for each parameter by treatment group are reported in Table 3. Animal-specific, global parameter change is reported in Supplemental Table 2 and its frequency (among the 8 EG eyes) and direction are summarized for each parameter in Table 4. Overall regional values for each parameter by treatment group are reported in Table 5. The frequency of animal-specific, EG eye regional change is summarized for each parameter in Table 6.

Neurovascular Canal. EG versus Control eye plots of BMO, ASCO and PSCO are shown for each animal in Figure 1 and Supplemental Figures 8-10. Overall mean *ASCO Area* was 24% larger ($p<.0016$) and mean *ASCO radius* was 11% larger ($p<.0016$) in the EG compared to the Control eyes (Table 3). Animal-specific EG eye values were significantly larger than Control eyes for *BMO Radius* in 5 animals (ranging from 3 to 10%) (Figure 1 and Table 4), *ASCO Radius* in 7 animals (ranging from 8 to 21% (Figures 1-2, and Table 4), and *PSCO Radius in* 6 of the 7 EG eyes with *PSCO Radius* measurements (ranging from 5 to 21%).

Within the overall regional analysis (Table 5), *ASCO Radius* demonstrated significantly larger EG vs Control eye values within the superior and temporal quadrants ($p<0.0125$). Animal-specific EG vs Control eye values for *ASCO Radius* were larger within 7 animals and smaller in the 8th within the superior quadrant, and larger in 5 animals temporally, nasally and inferiorly. EG versus Control eye values for *PSCO Radius* were larger in 5 animals within the superior, nasal and temporal quadrants.

Optic Nerve. Among all statistically significant EG versus Control Eye differences, optic nerve size differences were greatest in magnitude and occurred most consistently among the 8 EG eyes. EG versus Control eye plots of ON-ASCO relative to ASCO (Figure 2), ON-ASCO alone (Figure 3) and ON-PSCO alone (Figure 4) demonstrate larger EG eye optic nerves at both openings. Overall mean *ON-ASCO Area* was 32% larger and mean *ON-ASCO radius* was 16% larger in the EG compared to the Control eyes ($p<.0021$ and $p<.0012$, respectively). Overall mean *ON-ASCO H/V Diameter Ratio* was 22.5% smaller in the EG compared to the Control eyes, ($p<0.001$) suggesting that EG eye optic nerve expansion was greater within the vertical compared to the horizontal axis.

Animal-specific EG eye values were significantly larger than Control eye values for: *ON-ASCO Radius* within 7 animals (ranging from 11 to 30%, $p<0.005$, Figures 2 and 3) and *ON-PSCO Radius* in 6 out of the 7 animals in which it could be measured (ranging from 8 to 41%, $p<0.005$, Figure 4 and Supplemental Figure 11). Within the overall regional analysis, (Table 5), *ON-ASCO Radius* and *ON-PSCO Radius* demonstrated significantly larger EG versus Control eye values within the superior region. EG eye values were significantly larger than Control eyes for *ON-ASCO Radius* in all 8 animals within the superior and inferior quadrants (Table 6). EG eye values were significantly larger than Control eye values for *ON-PSCO Radius* in 6 animals within the superior and 5 animals within the inferior quadrant (Table 6).

Optic Nerve to Scleral Canal Gap Distance (Figure 2). Animal-specific EG eye values were significantly larger than Control eye values for *ASCO-ON-ASCO in 4 animals* ranging from 18 to 26% and significantly smaller (by 13%) in a fifth animal (Table 4). EG eye values were

significantly larger than Control eye values for *ASCO-ON-ASCO* in 5 animals superiorly, significantly smaller in 5 animals inferiorly and significantly larger in 4 animals nasally (Table 6).

Peripapillary Sclera and Choroid. Animal-specific EG eye values for *Scleral Depth* were significantly larger than Control eyes in 4 animals and smaller than the Control eye in a 5th animal (Table 4). All 8 animals demonstrated significant EG versus Control eye differences in *Choroidal Thickness* with 6 animals demonstrating smaller EG eye values (ranging from -29 to -7%) and 2 animals demonstrating larger EG eye values (ranging from 8-32%). *Choroidal Thickness* demonstrated the most frequent animal-specific, regional EG versus control eye differences with EG eye values smaller than Control eyes in 6 animals superiorly, 5 animals inferiorly, and 4 animals nasally and temporally.

Correlation with orbital optic nerve axon degeneration.

ON-PSCO Area expansion was significantly correlated to EG eye *optic nerve injury grade* (R=0.768; p=0.042) among the 7 EG eyes for which there was ON-PSCO data (Figure 5).

Discussion

This study 3D histomorphometrically characterizes early ONH neural and connective tissue change in the hypertonic rat model of unilateral EG. Our principle findings are as follows. First, the connective tissue openings that define the neurovascular canal of the rat ONH, (BMO, ASCO and PSCO), each expand early in EG. Second, among all forms of EG eye change, optic nerve expansion within the scleral canal was greatest in magnitude, occurred most frequently among the 8 EG eyes, and was preferential to the superior and inferior quadrants. Third, the magnitude of optic nerve expansion correlated to the post-mortem optic nerve axon injury grade.

EG eye expansions of the neurovascular canal and contained optic nerve (Figure 6) were present in all 8 animals. Five of 8 EG eyes demonstrated *BMO radius* expansion, 7 of 8 EG eyes demonstrated *ASCO radius* expansion and *PSCO radius* expansion was detected in 6 of the 7 EG eyes in which it could be measured. Chauhan et al (Chauhan et al., 2002), using the hypertonic saline model, was the first to document sequential and progressive ONH surface "cupping" as well as probable BMO and scleral canal expansion by in vivo confocal scanning laser tomography

(CSLT) in the rat EG model. However, CSLT alterations in the ONH neural canal opening were only detected after significant elevations of IOP and in association with loss of over 55% of the axons. In that study, it is not clear if BMO or the ASCO was being measured within the CSLT data sets because the nature of what is seen as the "disc margin" in clinical photographs and CSLT images of rat eyes has not yet been determined(Reis et al., 2012a; Reis et al., 2012b; Strouthidis et al., 2010; Strouthidis et al., 2009). Guo et al, (Guo et al., 2005) using en-face in-vivo Optical Coherence Tomography (OCT), reported progressive expansion of the optic disc area and a progressive ASCO expansion in 18 Dark Agouti EG rats. However, in their study, OCT visualization of BM, BMO, the anterior scleral surface and the ASCO were not clearly documented relative to one another.

Our post-mortem data clarify these findings by detecting neurovascular canal expansion at the level of BMO and the sclera (ASCO and PSCO) early in the optic neuropathy of chronic IOP elevation in the rat eye. We observed significant changes in ASCO in EG eyes with optic nerve injury grades of 2 through 3.28 which equate to estimated axonal loss from 15 to 34%- using the Morrison conversion scale (Jia et al., 2000; Morrison et al., 2005).

Our data further suggest radial optic nerve expansion within the neurovascular scleral canal and suggest the magnitude of expansion correlates to orbital optic nerve injury. These findings are important because the detection of longitudinal change in the diameter of the optic nerve within the neurovascular scleral canal may become an achievable OCT imaging target as this technology is applied to the rodent eye (Fortune et al., 2011; Guo and Yuan, 2015; Nagata et al., 2009; Zhang et al., 2011). EG eyes also demonstrated significantly larger increases in *ON-ASCO* and *ON-PSCO Radius* in the superior and inferior regions, significant *ON-ASCO H/V diameter ratio* reduction and animal-specific changes in the *ASCO-ON*-ASCO gap distance that most frequently occurred in the superior and inferior quadrants. Taken together these findings suggest preferential optic nerve expansion within the vertical compared to the horizontal axes. These findings may be manifestations of, or contribute, to the mechanisms which underlie, previously reported, preferential superior susceptibility to ONH axonal damage in the rat eye (Dai et al., 2012; Huang and Knighton, 2009; Li et al., 2015; Morrison, 2005; Morrison et al., 1997; WoldeMussie et al., 2001) ,

EG eye optic nerve expansion may be a manifestation of edema, cell proliferation, remodeling and/or synthesis of "laminar-like" connective tissue (Johnson et al., 1996). In a separate study of rat early EG eyes, swollen axons have been noted within the ONH, filled with vesicular material consistent with both axon transport obstruction and axonal degeneration (Morrison et al., 1997). More recently, genomic studies have demonstrated mRNA alterations compatible with cell proliferation pathways at the same stage of damage (Howell et al., 2011; Johnson et al., 2011; Johnson et al., 2007). We have previously reported thickening of the lamina cribrosa and profound connective tissue remodeling at a similar early stage of monkey EG (Burgoyne, 2015b; Burgoyne et al., 2014; Yang et al., 2007b; Yang et al., 2011b) (Stowell C, et al. *IOVS* 2014;55:ARVO E-Abstract 5034).

In the primate, the peripapillary sclera and scleral canal wall connective tissues are thought to govern the distribution of IOP-related stress within the lamina cribrosa connective tissues (Burgoyne and Downs, 2008; Sigal, 2009; Sigal et al., 2009a, b). The question of how the sclera transfers load to the rodent retinal ganglion cell axons and the astrocytes that span the nerve within the canal is of substantial biomechanical interest. Two recent papers have described the relationship between the radially arrayed, rat optic nerve head astrocytes, the optic nerve sheath (a continuation of the pia that merges with Bruch's Membrane at its opening – see Supplemental Figures 2-4) and the vascular plexus that surrounds the nerve within the neurovascular canal, effectively isolating it from the sclera (Dai et al., 2012; Li et al., 2015).

In the first of these articles (Dai et al., 2012), Dai and colleagues described a radial array of "fortified" astrocytes in the normal rat ONH, and early disinsertion of the superior astrocyte footplates from the pial sheath with subsequent loss of the astrocytes and eventual axon loss following 1 week of chronic IOP elevation. Their description of the vascular plexus that surrounds the optic nerve, (which is poorly visualized within our reconstructions due to its heavy pigmentation) suggests that it contains dense connective tissue septa. We suggest that if these septa directly or indirectly span the plexus to link the sheath and the sclera, they may be the means by which the sclera transfers IOP-related load to the radial ONH astrocytic array. It is possible that the inferior shift of the nerve within the canal demonstrated in 5 of the 8 EG eyes in this report, reflects damage to the superior vascular plexus connective tissue septa that both

explains this shift and either contributes to or results from the processes that damage the underlying astrocyte footplates.

Previous studies in the monkey unilateral EG model (Burgoyne et al., 2004; Downs et al., 2007; Yang et al., 2007a; Yang et al., 2007b) have reported only small *BMO area* increases and only in a small subset of early EG eyes (Burgoyne et al., 2004; Downs et al., 2007; Yang et al., 2007a; Yang et al., 2007b). In the present study, global *BMO radius* expansion was present in 5 of the 8 animals and regional expansion was present in a subset of eyes. While the *cumulative IOP insults* to the rat and monkey BMO connective tissues should not be directly compared, the frequency of BMO expansion in early rat EG suggests that the rat BM connective tissues immediately adjacent to BMO may demonstrate less structural stiffness than those of the monkey either due to being less thick or more compliant or both.

The choroid was thinner in the EG (compared to the Control) eyes of 6 animals and thicker in 2 animals. Between-eye differences in choroidal thickness in our study eyes should be interpreted carefully because the study was not designed to test hypotheses about choroidal thickness and IOP was not manometrically controlled at the same level in the Control and EG eyes at the time of perfusion. The peripapillary choroid likely plays an important role in the rat ONH blood supply since it is continuous with the vascular plexus surrounding the optic nerve within the neurovascular scleral canal. In vivo, longitudinal choroidal thickness measurements at manometrically controlled pressures by OCT(Pierru et al., 2014; Wang and Zhang, 2014; Yiu et al., 2014) are required to detect longitudinal choroidal thickness changes in the rat EG models. Separate from thickness, choroidal blood flow measurements within these vessels may be soon within the reach of a variety of OCT angiographic techniques(Baumann et al., 2011; Zhi et al., 2011; Zhi et al., 2012; Zotter et al., 2011).

Outward bowing of the peripapillary sclera was indirectly assessed in this study using two parameters - *Scleral Depth* and *BMO Depth* (Supplemental Figure 3) both of which measured relative to a peripheral scleral reference plane. Outward bowing of the peripapillary sclera relative to this more peripheral reference plane would be expected to manifest as an increase in both parameters if no other effects were present. *Scleral Depth* was increased in 4 and decreased in 1 EG eye, respectively. *BMO Depth* was significantly increased in 5 and decreased in 2 EG eyes.

Direct longitudinal detection of posterior bowing of the peripapillary sclera by in-vivo SDOCT or MRI imaging in eyes carried to more advanced stages of IOP insult is required to confirm the significance of these findings (He et al., 2014; Heickell et al., 2001; Strouthidis et al., 2011a).

The limitations of our method of 3-D reconstruction have been previously discussed (Burgoyne et al., 2004; Pazos et al., 2015) and include: (1) anterior-to-posterior resolution limited to 1.5 μm; (2) hand application of the stain to the block face using a cotton-tipped swab providing the potential for substantial staining variation between section images; (3) tissue shrinkage effects (both from fixation and embedding) which may be unique to the rat eye. While comparisons to our nonhuman primate (Burgoyne et al., 2004; Downs et al., 2007; Yang et al., 2007a; Yang et al., 2007b; Yang et al., 2009b) publications may be similar (since fixation and post-tissue processing is similar), comparisons to other post-mortem or in-vivo measurements may be profoundly affected by these differences.

We intended to study rats with early damage which is why all animals were sacrificed after 4 weeks of IOP elevation. The statistical significance of many of the changes is likely dependent on this choice. While the ONH are "early" in terms of time (4 weeks since injection), the percent axon loss in the EG eyes of this study, (as estimated by the correlation between axon counts to axon damage injury grade correlations) (Morrison et al., 2005), were *<5%, ≈10%, ≈18%, <20%, <22%, <35%, <35%, and ≈35%, respectively*. These data suggest that the majority of EG eyes in this study were at an early to moderate stage of axon loss. Determination of the earliest ONH alterations in the rat EG model will be the subject of future reports. Characterization of maximum physiologic between eye differences (Yang et al., 2009a) (using bilateral normal animals) is ultimately required to be certain that the early EG eye differences we report exceed between eye-differences within bilaterally normal animals. Generalization of our findings to naïve normal eyes of all ages, strain and lighting conditions should not be assumed.

The animals in this study were sacrificed using sodium nitroprusside which is a potent vasodilator that is commonly given to improve the removal of blood from the ONH vasculature during perfusion fixation. While it is unlikely that our finding of EG eye scleral canal expansion was influenced by vasodilation, it is conceivable that the optic nerve blood vessels in the EG eyes

were preferentially influenced by the nitroprusside and a portion or all of the optic nerve expansion was on this basis. Certainly, as deep optic nerve head imaging improves in the rat experimental glaucoma models, longitudinal detection of scleral canal expansion as well as optic nerve expansion within the scleral canal should be confirmed using these techniques. However, we do not believe that preferential optic nerve swelling in the EG eye is the most likely explanation for our optic nerve findings for the following reasons. First, we would expect that the peri-neural vascular plexus would dilate more than the smaller vessels in the optic nerve and this would have the net effect of compressing rather than expanding the nerve within the scleral canal. Second, the genomic studies mentioned above, have demonstrated significant increases in DNA content and mRNA alterations compatible with cell proliferation pathways and inflammation at the same stage of damage (Howell et al., 2011; Johnson et al., 2011; Johnson et al., 2007). We believe that these processes, alone, likely underlie optic nerve enlargement in the EG eye.

Finally, to date, there have been no rigorous descriptions of what constitutes a "*glaucomatous*" optic neuropathy in the rodent eye. In the monkey, we have argued that ONH surface "cupping" that does not include ONH connective tissue deformation and remodeling is a non-specific feature of all forms of RGC axonal injury and is not specific to chronic IOP elevation (Burgoyne, 2015a). From our findings in monkeys (Burgoyne, 2015b; He et al., 2014; Strouthidis et al., 2011b) we have argued that the same features of the neuropathy should be present in human eyes and we are currently using OCT ONH imaging to describe these phenomena in glaucoma patients (Ren et al., 2014).

We propose that the rat ONH neural and connective tissue alterations described herein are core components of the neuropathy that occurs 4 weeks after the onset of chronic moderate experimental IOP elevation in the rat eye. Their presence should be sought and confirmed in all experimental models of "glaucomatous" optic neuropathy in the rat eye whether due to spontaneous (Goldblum and Mittag, 2002) or experimental chronic IOP elevation (Chauhan et al., 2002; Morrison et al., 2008; Morrison et al., 1997), ischemia (Naskar et al., 2002), endothelin (Chauhan et al., 2004; Murphy et al., 2010; Prasanna et al., 2011), or immune system manipulation (Joachim et al., 2013; Tezel and Wax, 2004; Wax et al., 2008).

Because there are, at present, no experimental models for the induction of a glaucomatous optic neuropathy in any species that do not depend upon chronic IOP elevation, such a model remains an important experimental target for glaucoma research. We propose that our findings should serve as phenotypic benchmarks for all future rat models of glaucomatous ONH injury that do (Chauhan et al., 2002; Goldblum and Mittag, 2002; Morrison, 2005; Morrison et al., 2008; Morrison et al., 1997; WoldeMussie et al., 2001) and do not (Chauhan et al., 2004; Naskar et al., 2002; Prasanna et al., 2011; Tezel and Wax, 2004; Tseng et al., 2015; Votruba et al., 2003; Wax et al., 2008; WoldeMussie et al., 2001) involve spontaneous or experimental IOP elevation.

In summary, we have performed the first 3D histomorphometric study of early alterations to the rat ONH following chronic experimental IOP elevation. Our findings suggest that radial expansion of the ONH connective tissue openings in Bruch's Membrane and the sclera, as suggested by previous studies (Chauhan et al., 2002; Guo et al., 2005), accompanied by preferential superior and inferior radial expansion of the optic nerve within the scleral canal are early components of the optic neuropathy of chronic experimental IOP elevation in the rat eye.

Acknowledgments

The authors gratefully acknowledge the following individuals for their assistance with this study. Juan Reynaud for his assistance with improving the visibility of the rat ONH anatomy within the green channel and providing software for volumetric and thickness quantification. Galen Williams for his assistance with serial sectioning the tissues. Joanne Couchman for her assistance with manuscript preparation.

TABLES

Abbreviation/Term	Meaning/Definition
Animal-specific results	Animal-specific EG vs Control eye Difference
ANOVA	Analysis of Variance
ASCO	Anterior Scleral Canal Opening
ASCO-ON-ASCO	Gap distance measured radially between the ASCO and the ON-ASCO
BMO	Bruch's Membrane Opening
CI	Confidence Interval
CRA	Central Retinal Artery
CRV	Central Retinal Vein
Eye-specific results	Parameters related to an individual eye
Global Results	Non-regionalized ONH or scleral data
GLS	Generalized Least Squares
H/V	Horizontal/Vertical Ratio
I	Inferior
ICC	Intraclass Correlation Coefficient
IOP	Intraocular Pressure
LPCA	Long Posterior Ciliary Artery
N	Nasal
NA	Not Available or Not Applicable
OA	Ophthalmic Artery
OD	Right Eye
OS	Left Eye
ON-ASCO	Optic Nerve area at the level of ASCO
ON-PSCO	Optic Nerve area at the level of PSCO
ONH	Optic Nerve Head
Overall results	Data from all rats considered together
PSCO	Posterior Scleral Canal Opening
PSCO-ON-PSCO	Gap distance measured radially between the PSCO and the ON-ASCO
S	Superior
SD	Standard Deviation
SPCA	Short Posterior Ciliary Artery
T	Temporal

Table 1. Abbreviations, Terms and Definitions

Rat Number	ID	Age at sacrifice *(months)*	Eye	Status	Mean IOP *(mmHg)*	Mean IOP difference *(mmHg)*	EG Eye Peak IOP *(mmHg)*	Optic Nerve Damage Grade	Number of Serial Section Images
1	MR8	9.5	OD	C	28.5	5		1	400
			OS	EG	33.5		42.3	1.22	383
2	MR10	9.5	OD	EG	29.2	0.4	45	1.6	465
			OS	C	28.8			1	313
3	MR1	9.5	OD	EG	33.3	5	39.1	2	696
			OS	C	28.3			1	398
4	MR9	9.5	OD	EG	35	6.6	45.8	2.36	430
			OS	C	28.4			1	307
5	MR12	10.5	OD	EG	29.6	1.1	36	2.47	500
			OS	C	28.5			1	275
6	MR11	10.5	OD	EG	32.1	3.8	41	2.9	230
			OS	C	28.3			1	375
7	MR5	9.5	OD	C	28.8	3.7		1	484
			OS	EG	32.5		40.9	3	480
8	MR4	9.5	OD	C	28.4	6.2		1	501
			OS	EG	34.6		42.3	3.28	455

ID – Laboratory Rat Identification Number; **Age**- in months; **Eye** - OD-Right eye, OS-left eye**; Status**- C- Control, EG-Experimental Glaucoma; **Mean IOP** (mmHg)- Mean IOP of all IOP measurements taken AM and PM for each eye**; Mean IOP difference-** Mean IOP of the EG eye minus Mean IOP of the Contol eye (mmHg). **EG Eye Peak IOP -** Maximum IOP in mmHg obtained in the EG eye; **Optic Nerve Damage Grade:** average score of orbital optic nerve cross section grading performed by 5 masked observers using a previously published scale (Morrison *Exp.Eye Res.*1997). **Number of Digital Serial Section Images**- number of serial digital section images required to reconstruct each optic nerve head.

Table 2. Animal and Eye Data.

Parameters	Control Eyes (Mean±SD)	EG Eyes (Mean±SD)	P-Value
Neurovascular Canal			
BMO Area (μm^2)	$5.65\pm0.66\times10^4$	$6.13\pm0.51\times10^4$	0.0375
BMO Radius (µm)	133±8	139±6	0.0358
BMO Depth (µm)	29±15	35±12	0.3448
ASCO Area (μm^2)	$1.29\times10^5\pm0.19\times10^5$	$1.60\times10^5\pm0.21\times10^5$	**0.0016***
ASCO Radius (µm)	201±15	224±14	**0.0016***
ASCO H/V Diameter Ratio	1.26±0.10	1.24±0.11	0.6974
ASCO Depth (µm)	95±14	92±16	0.5450
PSCO Area (μm^2)[1]	$1.35\times10^5\pm0.23\times10^5$	$1.67\times10^5\pm0.27\times10^5$	0.0118
PSCO radius (µm)[1]	206±17	229±17	0.0104
PSCO H/V Diameter Ratio[1]	1.28±0.14	1.22±0.12	0.4276
PSCO Depth (µm)[1]	165±13	162±15	0.6787
Optic Nerve			
ON-ASCO Area (μm^2)	$4.63\times10^4\pm0.44\times10^4$	$6.13\times10^4\pm0.94\times10^4$	**0.0021***
ON-ASCO Radius (µm)	118±6	137±12	**0.0012***
ON-ASCO H/V Diameter Ratio	1.96±0.19	1.60±0.16	**<0.001***
ON-PSCO Area (μm^2)[1]	$4.42\times10^4\pm0.48\times10^4$	$6.07\times10^4\pm0.98\times10^4$	0.0089
ON-PSCO Radius (µm)[1]	111±7	134±12	0.0066
ON-PSCO H/V Diameter Ratio[1]	2.38±0.43	2.21±0.35	0.4971
ON Volume (μm^3)[1]	$3.29\times10^6\pm0.64\times10^6$	$4.59\times10^6\pm0.90\times10^6$	0.0175
Optic Nerve/Scleral Canal Gap Distance			
ASCO-ON-ASCO Distance (µm)	81±13	85±13	0.4080
PSCO-ON-PSCO Distance (µm)[1]	93±13	94±15	0.8342
Sclera/Choroid			
Scleral Thickness (µm)[1]	104±4	104±4	0.8265
Scleral Depth (µm)	33±7	35±7	0.5296
Choroidal Thickness (µm)	57±7	52±11	0.3142

Statistical significance was defined to occur at the *p<0.0022 (Paired T-Test) due to multiple comparisons;
[1]These parameters calculations were obtained without rat 6 data
EG - Experimental Glaucoma

Table 3. Overall Global Values for each Parameter by Treatment Group

Parameter[1]	Number of Rats Demonstrating EG Eye Change[2]		Range of significant EG Eye Change (%)[3]	
	+	-	+	-
Neurovascular Canal				
BMO Radius (µm)	5	0	5 ~ 13 (3 ~ 10)	0 (0)
BMO Depth (µm)[4]	5	2	2 ~ 28	-21 ~ -12
ASCO Radius (µm)	7	0	16~ 38 *(8 ~ 21)*	0 (0)
ASCO Depth (µm)	1	2	16	-30 ~ -18
PSCO Radius (µm)[4]	6	0	10 ~ 43 *(5 ~ 21)*	0 (0)
PSCO Depth (µm)[5]	3	4	11 ~ 18	-28 ~ -7
Optic Nerve				
ON-ASCO Radius (µm)	7	0	14 ~ 34 *(11 ~ 30)*	0 (0)
ON-PSCO Radius (µm)	6	0	9 ~ 43 (8 ~ 41)	0 (0)
Optic Nerve to Scleral Canal Gap Distance				
ASCO-ON-ASCO Distance (µm)	4	1	14 ~ 17 (18 ~ 26)	-12 (-13)
PSCO-ON-PSCO Distance (µm)[4]	2	2	14 ~ 28 (18 ~ 29)	-17~ -10 (-16 ~ -10)
Sclera/Choroid				
Scleral Thickness (µm)[4]	3	2	4 ~ 6 *(4 ~ 5)*	-9 ~ -7 *(-8 ~ -7)*
Scleral Depth (µm)	4	1	6 ~ 10	-10
Choroidal Thickness (µm)	2	6	4 ~ 19 *(8 ~ 32)*	-20 ~ -5 *(-29 ~ -7)*

[1]Only parameters in which multiple measurements per eye were possible were included in this analysis

[2] Between eye comparison (EG versus control) was carried out for each parameter for each animal using generalized least squares model (GLS). Statistically significant between-eye differences were established at $p<0.005$ due to multiple comparisons. Positive sign (+) means increased, negative sign (-) means reduction.

[3]The range of statistically significant EG eye change in micrometers. Percentage is in parentheses *(expressed as the percent of the contralateral control Eye)*. Positive sign (+) means increased, negative sign (-) means reduction.

[4]This parameter could only be measured in 7 of the 8 animals

Table 4. Frequency of Animal-Specific EG Eye Global Change for each Parameter

Parameters	Superior		Inferior		Nasal		Temporal	
	C (Mean±SD)	EG (Mean±SD)	C (Mean±SD)	EG (Mean±SD)	C (Mean±SD)	EG (Mean±SD)	C (Mean±SD)	EG (Mean±SD)
Neurovascular Canal								
BMO Radius	135±10	141±10	138±15	143±18	132±11	137±11	128±16	136±17
BMO Depth	27±13	31±14	32±17	39±13	32±16	39±14	26±18	32±14
ASCO Radius	187±22	**208±18***	186±21	205±19	217±22	244±24	214±19	**240±22***
ASCO Depth	83±15	78±15	113±20	111±18	101±17	93±20	84±22	85±22
PSCO Radius	196±25	214±21	188±22	203±20	213±22	246±29	222±23	252±32
PSCO Depth	145±16	135±14	189±19	191±20	177±24	171±28	152±20	151±22
Optic Nerve								
ON-ASCO Radius	98±9	**121±13***	90±14	116±17	141±20	156±18	142±22	156±19
N-PSCO Radius	86±10	**111±15***	68±12	94±20	145±31	165±26	146±29	164±29
Optic Nerve to Scleral Canal Gap Distance								
ASCO-ON-ASCO Distance (µm)	107±32	117±27	75±21	57±18	72±28	86±30	72±26	82±26
PSCO-ON-PSCO Distance (µm)	115±32	113±27	112±22	97±15	60±35	73±30	82±31	95±35
Sclera/choroid								
Scleral Thickness	99±14	98±15	91±20	91±19	113±19	113±16	116±23	112±21
Scleral Depth	30±25	29±22	41±31	46±32	37±27	37±30	22±26	28±28
Choroidal Thickness	57±11	49±16	56±14	51±18	59±22	51±15	55±15	58±25

* Statistically significant EG versus Control Eye difference established at p<0.0125 due to multiple comparisons (linear mixed effects model)
All values are in micrometers.

Table 5. Overall Regional Values for each Parameter by Treatment Group

Superior				Inferior				Nasal				Temporal			
# of Animals[1]		Range of EG Eye Change (%)[2]		# of Animals[1]		Range of EG Eye Change (%)[2]		# of Animals[1]		Range of EG Eye Change (%)[2]		# of Animals[1]		Range of EG Eye Change (%)[2]	
+	-	+	-	+	-	+	-	+	-	+	-	+	-	+	-
3	0	13 ~ 18 (*9 ~15*)	0(0)	2	0	15 ~ 19 (*11~ 15*)	0 (0)	2	0	11 ~19 (*9 ~15*)	0 (0)	2	0	10 ~ 17 (7 ~ 14)	0 (0)
3	2	18 ~ 20	-16 ~ -13	4	2	6 ~ 36	-22 ~-16	4	3	14 ~37	-18 ~-8	4	2	4 ~ 30	-26 ~-10
7	1	14 ~44 *(7 ~ 26)*	-21 *(-10)*	5	0	22 ~36 (*13 ~ 20*)	0 *(0)*	5	0	23~63 (*11 ~28*)	0 (0)	5	0	15 ~48 (7 ~ 23)	0 (0)
2	2	11 ~14	-36 ~-22	1	2	28	-31 ~-15	1	4	31	-30 ~ -14	2	2	15 ~ 25	-25 ~-21
5	0	25 ~ 37 (12 ~22)	0 (0)	3	0	26 ~42 (15 ~ 27)	0 (0)	5	0	18 ~71 (8~ 32)	0 (0)	5	0	15 ~ 57 (6 ~24)	0 (0)
0	3	0 (0)	-25 ~-15	2	1	17 ~ 33	-26	1	3	33	-36 ~-23	2	2	21 ~ 37	-28 ~-24
8	0	5~ 35 *(5 ~ 37)*	0 (0)	8	0	9 ~ 39 (*11 - 44)*	0 (0)	4	0	14 ~32 (*10 ~ 24*)	0 (0)	4	0	13 ~ 30 (9 ~*23*)	0 (0)
6	0	13~46 *(16 ~ 57)*	0 (0)	5	0	25 ~ 48 (*36-79*)	0 (0)	3	0	31~ 40 (*23 ~ 28*)	0 (0)	3	0	29 ~ 39 (21~ 27)	0 (0)
5	1	18~49 (16~78)	-66(-43)	0	5	0 (0)	-41~ -19 (-47~ -24)	4	0	17~52 (26 ~ 77)	0 (0)	3	1	13 ~34 (20 ~ 54)	-30 (-32)
3	3	19~47(20~55)	-61~-13(-39~-14)	1	2	25 (28)	-52 ~-23 (-37 ~-18)	2	1	26~68 (64~140)	-58 (-50)	2	1	52~ 56 (60 ~ 83)	-27 (-24)
2	2	9 ~ 10 *(11 ~ 12)*	-22 ~-6 (-20 ~-6)	2	1	9 ~ 15 (10 ~ 18)	-10 (-11)	1	0	7 (*7*)	0 (0)	0	2	0	-20 ~-18 *(-15*)
1	2	14	-21 ~-9	1	0	23	0	0	0	0	0	3	1	14 ~23	-13
1	6	19 (31)	-21~-4 (-35 ~-7)	1	5	19 (33)	-21~-7 (-36 ~-12)	2	4	8 ~ 10 (16 ~25)	-44~-10(-47~-19)	3	4	5 ~ 21 (11 ~36)	-22 ~-7 (-37 ~-11)

gnificance for regional parameter change within each animal was required to achieve p<0.0001 due to multiple comparisons (linear model using generalized least squares) Values are in microns *in parentheses)*

animals achieving statistically significant change in this parameter within this region. Positive sign (+): increase. Negative sign (-): reduction.

e statistically significant EG eye change in micrometers and percentage % *(reported as the percent of the contralateral normal eye)* Positive sign (+): increase. Negative sign (-): reduction.

Frequency of Animal-Specific EG Eye Regional Change for each Parameter.

Parameter Name	ICC (Low 95%CI-High 95%CI)
BMO Area	0.55 (0.06-0.91)
BMO Radius	0.54 (0.05-0.90)
BMO Depth	0.97 (0.87-0.99)
ASCO Area	0.93 (0.77-0.99)
ASCO Radius	0.93 (0.77-0.99)
ASCO Depth	0.81 (0.45-0.96)
ASCO H/V	0.76 (0.36-0.96)
PSCO Area	0.75 (0.34-0.95)
PSCO Radius	0.77 (0.38-0.96)
PSCO Depth	0.58 (0.10-0.91)
PSCO H/V	0.85 (0.54-0.97)
ON-ASCO Area	0.95 (0.84-0.99)
ON-ASCO Radius	0.95 (0.83-0.99)
ON-ASCO H/V	0.85 (0.55-0.97)
ON-PSCO Area	0.98 (0.91-0.99)
ON-PSCO Radius	0.98 (0.91-0.99)
ON-PSCO H/V	0.97 (0.87-0.99)
ON-Volume	0.88 (0.62-0.98)
ASCO-ON-ASCO distance	0.93 (0.75 -0.99)
PSCO-ON-PSCO distance	0.49 (0 - 0.89)
Scleral thickness	0.71 (0.28-0.95)
Scleral Depth	0.95 (0.82-0.99)
Choroidal Thickness	0.55 (0.06-0.91)

ICC - Intraclass Correlation Coefficient , **CI**- Confidence Interval
ICC grading: <0.4 - Poor Reproducibility; 0.4-0.75-Fair to Good Reproducibility; >0.75-Excellent Reproducibility. Only parameters with Fair to Good or excellent reproducibility were included in this report.

Supplemental Table 1 - Reproducibility Data

	Rat Number															
rameter[1]	Rat 1		Rat 2		Rat 3		Rat 4		Rat 5		Rat 6[2]		Rat 7		Rat 8	
	C	EG	C	EG	C	EG	C	EG	C	EG	C	EG	C	EG	C	EG
ascularCanal																
Area (μm^2)	$6.15x10^4$	$5.88 x10^4$	$4.76 x10^4$	$5.69 x10^4$	$5.26x10^4$	$5.45 x10^4$	$5.71 x10^4$	$6.11 x10^4$	$5.18 x10^4$	$5.86 x10^4$	$6.90 x10^4$	$6.72 x10^4$	$5.40 x10^4$	$6.50x10^4$	$5.83x10^4$	$6.84x10^4$
Radius (µm)	139±18	135±19	122±14	**133±22***	129±11	131±9	135±6	**139±10***	128±12	**136±13***	148±8	146±8	131±10	**144±9***	136±7	**147±10***
/O Depth	16±11	**38±11***	47 ±9	**26±7***	39±5	**51±10***	36±9	34±6	26±10	**28±9***	37±6	**56±6***	-1±5	**27±9***	33±8	**22±6***
) Area (μm^2)	$1.49x10^5$	$1.45 x10^5$	$1.22x10^5$	$1.45 x10^5$	$1.23x10^5$	$1.60 x10^5$	$1.02 x10^5$	$1.50 x10^5$	$1.57 x10^5$	$2.09 x10^5$	$1.06 x10^5$	$150 x10^5$	$1.38 x10^5$	$1.69 x10^5$	$1.33 x10^5$	$1.55 x10^5$
Radius (µm)	216±25	213±31	196±21	**215±10***	196±29	**225±21***	180±16	**217±21***	223±16	**256±33***	183±18	**217±22***	209±16	**231±26***	205±25	**221±24***
O H/V Ratio	1.24	1.37	1.26	1.01	1.42	1.28	1.26	1.19	1.11	1.24	1.25	1.26	1.17	1.31	1.38	1.27
CO Depth	78±22	78 ±18	104±20	**74±19***	112 ±18	117±17	105 ±16	**87±22***	88 ±17	**104±20***	106±23	106±12	73±13	77±15	94±15	91±9
) Area (μm^2)	$1.59x10^5$	$1.52 x10^5$	$1.13 x10^5$	$1.45 x10^5$	$1.40x10^5$	$1.72 x10^5$	$1.13 x10^5$	$1.47 x10^5$	$1.54x10^5$	$2.23 x10^5$	$1.22 x10^5$	NA	$1.58 x10^5$	$1.74 x10^5$	$1.09 x10^5$	$1.60 x10^5$
Radius (µm)	223 ±30	218±35	189 ±15	**214±16***	209 ±30	**233±21***	189 ±18	**215±26***	220±20	**263±42***	197±13	NA	223 ±17	**233±29***	185 ±23	**224±25***
O H/V Ratio	1.47	1.15	1.10	1.06	1.40	1.21	1.20	1.23	1.13	1.38	1.21	NA	1.36	1.13	1.33	1.37
CO Depth	160±28	**153±22***	170±25	**142±27***	167±20	**181±25***	182 ±19	**163±27***	164 ±23	**182±36***	172±27	NA	141±23	**152±26***	171±29	**163±24***
Nerve (ON)																
CO Area (μm^2)	$4.54x10^4$	$5.66x10^4$	$4.26x10^4$	$4.13x10^4$	$4.36x10^4$	$6.88x10^4$	$4.46x10^4$	$5.90x10^4$	$5.37x10^4$	$6.45x10^4$	$4.73 x10^4$	$6.14 x10^4$	$4.16 x10^4$	$6.85 x10^4$	$5.20 x10^4$	$7.02 x10^6$
CO Radius (µm)	117 ±27	**133±19***	112 ±33	112±26	114±32	**145±29***	115 ±32	**135±25***	128 ±29	**142±22***	120 ±28	**139±20***	112 ±25	**146±20***	127 ±24	**148±22***
CO H/V Ratio	1.82	1.52	2.18	1.90	2.18	1.74	2.08	1.66	1.97	1.57	1.88	1.42	1.86	1.44	1.66	1.51
CO Area (μm^2)	$4.81x10^4$	$4.99x10^4$	$4.28x10^4$	$4.78x10^4$	$4.14x10^4$	$6.79x10^4$	$3.99x10^4$	$5.61x10^4$	$5.34x10^4$	$6.39 x10^4$	$4.37 x10^4$	NA	$4.25 x10^4$	$6.52 x10^4$	$4.14 x10^4$	$7.44 x10^6$
O Radius (µm)	117 ±41	119±42	108±44	**117±39***	107±41	**142±39***	105±43	**128±40***	124±41	**139±31***	111±42	NA	112±33	**140±33***	106±43	**150±37***
CO H/V Ratio	2.41	2.43	2.72	2.34	2.60	2.04	2.97	2.10	2.29	1.64	2.55	NA	1.89	2.18	1.81	2.75
olume (μm^3)	$3.95x10^6$	$3.78x10^6$	$2.92x10^6$	$3.08x10^4$	$2.29x10^6$	$4.61x10^6$	$3.25x10^6$	$4.69x10^6$	$4.04x10^6$	$4.95 x10^6$	$3.20 x10^6$	NA	$2.88 x10^6$	$5.54 x10^6$	$3.67 x10^6$	$5.50 x10^6$
e to Scleral Canal o Distance																
SCO Distance (µm)	91±48	80±24	84±20	**101±37***	82±19	78±26	64±22	**81±29***	94±31	**111±46***	63±20	**77±32***	95±26	**83±28***	76±28	73±19
SCO Distance (µm)	104±41	98±20	81±34	**95±41***	101±31	**91±32***	83±42	87±22	96±38	**123±23***	86±35	NA	110±38	**92±29***	78±27	74±19
ra/Choroid																
Thickness (µm)	109±26	**101±17***	105±23	103±18	107±19	106±21	105±19	**110±18***	105±15	**98±24***	110±18	N/A	101±25	**106±19***	97±23	**101±22***
eral Depth	27±36	**32±27***	39±29	**29±23***	38±28	37±32	32±27	33±28	38±24	**47±35***	37±26	**45±30***	19±23	**27±26***	33±25	31±26
dal Thickness	56 ±13	**46±13***	45±11	**48±11***	54±14	**44±17***	55±11	**48±15***	60±11	**80±20***	70±26	**50±12***	61±14	**56±19***	54±10	**49±15***

is significantly different from the contralateral normal eye (Generalized least squares model, $p < 0.005$ due to adjustment for multiple comparisons)*
ameters are those with multiple measurements per eye which are required to assess animal-specific EG eye versus Control eye differences
canal and peripapillary scleral parameters are missing for the EG eye of Rat 6 due to poor visualization within its 3D histomorphometric reconstruction.

ental Table 2. Animal Specific Global Values for each Parameter.

FIGURES

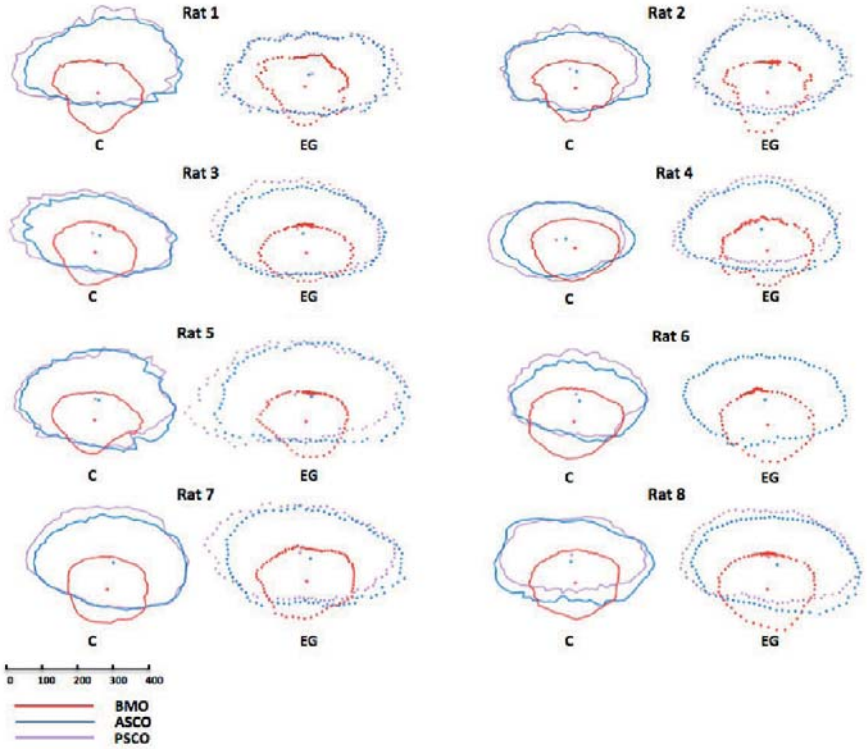

Figure 1. Within and between-eye comparisons of BMO (red), ASCO (blue) and PSCO (purple) for the Control (solid lines) and EG (dotted lines) eye of each animal. Delineated points for each structure along with their centroid are shown in right eye orientation projected onto the BMO reference plane (x axis horizontal and y axis vertical) for comparison purposes. The BMO centroid for each eye has been used to horizontally align the data for the two eyes of each animal. Note that the ASCO and PSCO centroids tend to be vertically separated and further away from the BMO centroid in the EG eyes with the greatest damage (Rats 4, 5, 7 and 8). These data suggest that apart from the EG eye expansion of these individual openings (demonstrated most clearly in Supplemental Figures 8, 9 and 10), glaucomatous alteration of the rat neurovascular scleral canal includes a vertical shift of the PSCO relative to the ASCO and BMO which becomes more pronounced as ON damage progresses. The scale is in micrometers. PSCO data is not available for the EG eye of Rat 6. Animal specific EG vs Control Eye overlays for each individual parameter can be seen in Supplemental Figures 8-10.

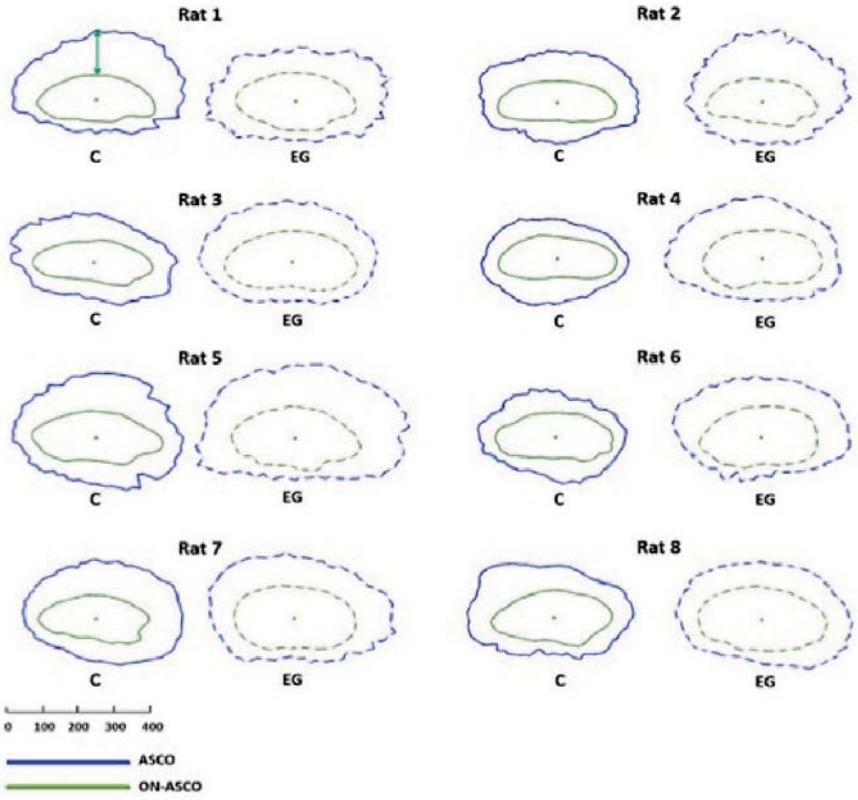

Figure 2. Animal-specific, EG (dotted line) versus Control Eye (solid line) comparisons of Anterior Scleral Canal Opening (ASCO - blue) and Optic Nerve – ASCO (ON-ASCO - green) and the ASCO-to-Optic Nerve ASCO Gap Distance (ASCO-ON-ASCO) (green arrow upper left). ASCO fitted spline and ON-ASCO fitted spline were projected onto the ASCO reference plane for comparison purposes. The ON-ASCO centroid for each eye has been used to horizontally align the data from each eye. The green arrow (Control eye of Rat 1, upper left) schematically depicts the *ASCO-ON-ASCO Gap Distance* measurement (here showing 1 of a total of 80 radial measurements – see methods). Animal- specific EG vs Control eye overlays of ASCO and ON-ASCO data can be seen in Supplemental Figures 9 and 11, respectively. Global EG eye increases in *ASCO radius* were present within Animals 2-8. Global EG eye increases in *ON-ASCO radius* were present within Animals 1 and 3–8. Global EG eye *ASCO-ON-ASCO Distance* was significantly increased within Animals 2, 4, 5, 6 and 7. The scale is in micrometers. See Supplemental Figure 11 for a similar plot of PSCO and ON-PSCO data.

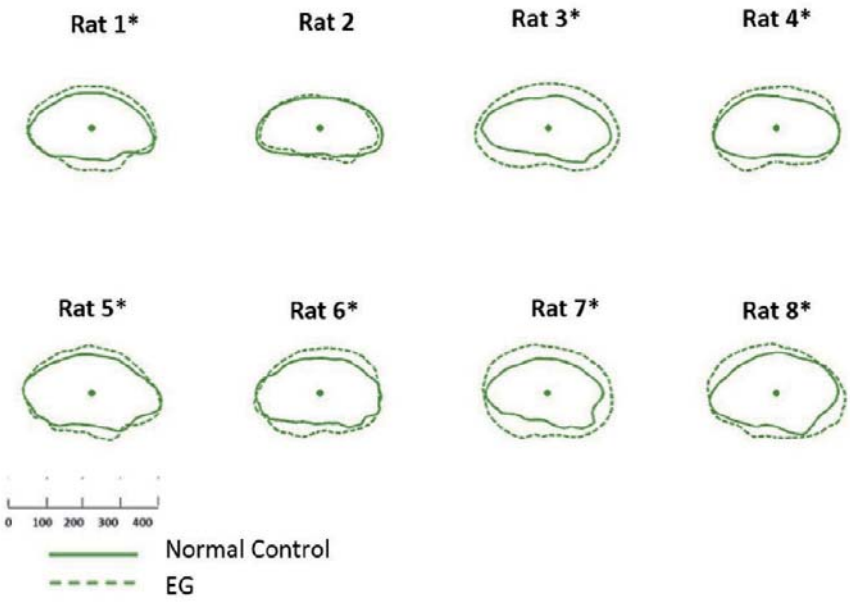

Figure 3. EG (dotted line) versus Control (solid line) eye *Optic Nerve within the Anterior Scleral Canal Opening* (*ON-ASCO*) comparison for each study animal. ON-ASCO data points for the Control and EG eye of each rat are schematically overlaid using the ON-ASCO centroid of each eye. All data are in right eye orientation. The scale is in micrometers. **(*)** denotes animals in which Global EG versus Control Eye *ON-ASCO radius* differences achieved significance (Supplemental Table 2).

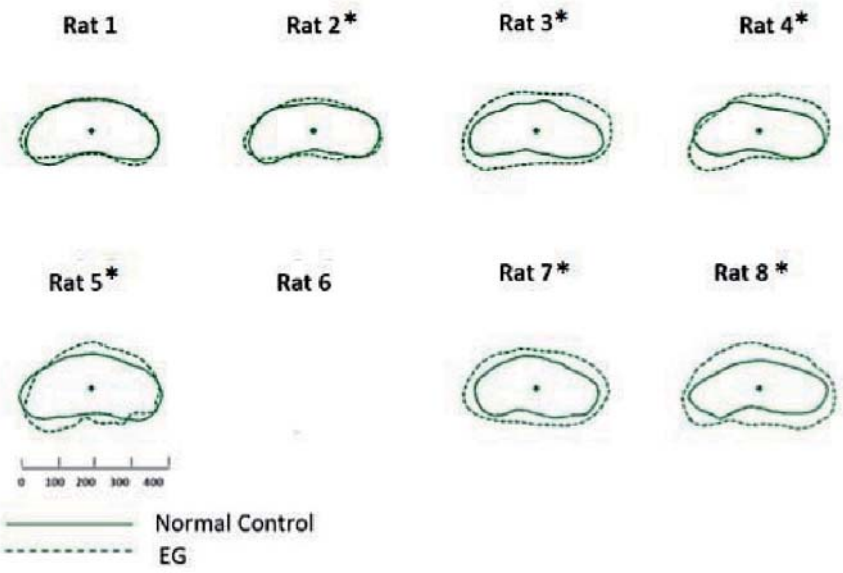

Figure 4. EG (dotted line) versus Control (solid line) eye *Optic Nerve within the Posterior Scleral Canal Opening* (*ON-PSCO*) comparison for each study animal. ON-PSCO data points for the Control and EG eye of each rat are schematically overlaid using the ON-PSCO centroid of each eye. All data are in right eye orientation. The scale is in micrometers. (*) denotes animals in which Global EG versus Control Eye *ON-PSCO radius* differences achieved significance (Supplemental Table 2). ON-PSCO data for EG eye of Rat 6 were not available.

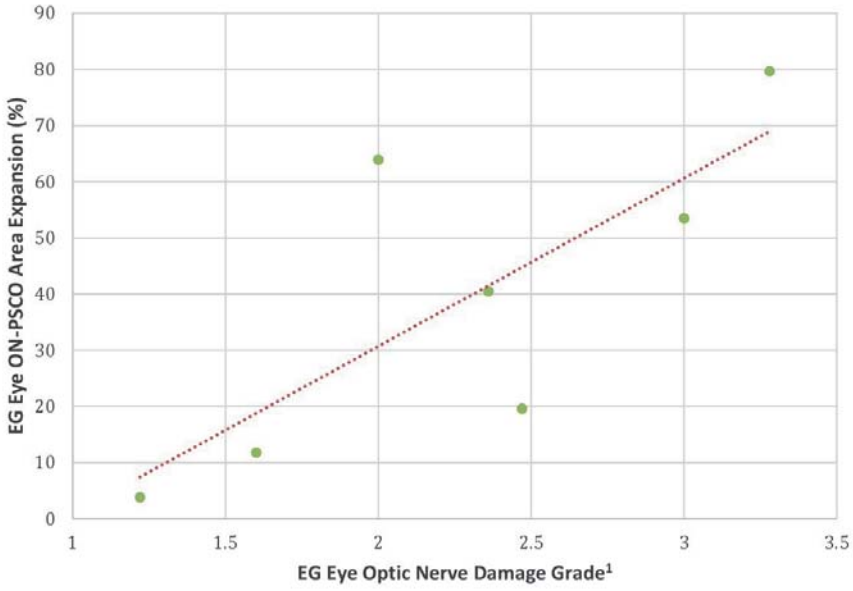

Figure 5. Correlation between EG Eye *ON-PSCO Area* Expansion and EG eye *Optic Nerve Damage Grade* (Table 1). EG vs Control eye *ON-PSCO Area* expansion was significantly correlated to EG eye *Optic Nerve Damage Grade* (R= 0.768, P=0.042). [1]Optic nerve qualitative damage grading adapted from (Morrison et al., 1997).

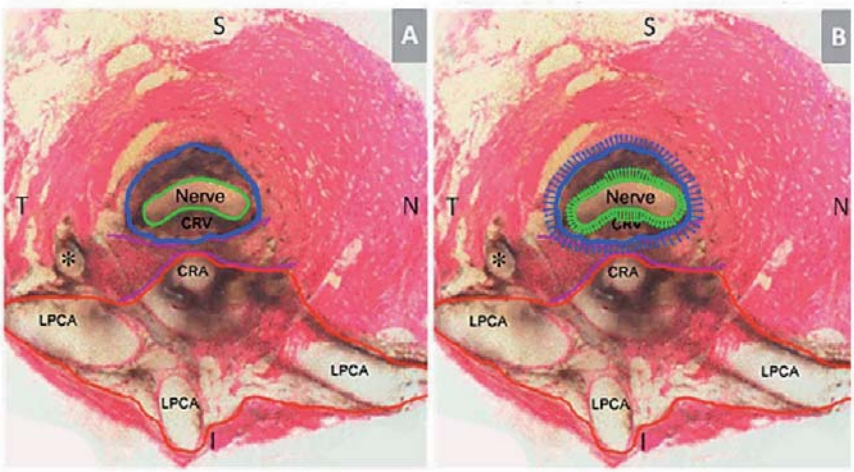

Figure 6. Principal Scleral Openings in the Normal Control Rat Eye (A) and a Schematic Overlay of Optic Nerve and Surrounding Neurovascular Scleral Canal Expansion in Early Experimental Glaucoma (EG) (B). (A) Unlike the primate, there are two principal openings within the sclera of the rat ONH: 1) the superior neurovascular canal (outlined in blue) which contains the optic nerve (green) and the central retinal vein **(CRV)** which both pass within a vascular plexus (brown pigment) that is continuous with the choroid (not shown); and 2) the more inferior arterial opening (outlined in red), which is irregular and contains the central retinal artery (CRA) and the densely packed choroidal branches of the Long Posterior Ciliary Arteries (LPCAs). The two canals are separated by the scleral sling (purple). For a more extensive description of this anatomy see Supplemental Figures 1 and 2. **(B)** Rat optic nerve expansion (green arrows) occurs early in the rat ONH response to chronic experimental IOP elevation and is accompanied by expansion of the surrounding neurovascular scleral canal (blue arrows) that is both more frequent and of greater magnitude within the superior and inferior quadrants. Each arrow represents the magnitude of quadrant change magnified 3 times. S-superior, I – Inferior, N – Nasal, T – Temporal. (*) Identifies a branch of a LPCA.

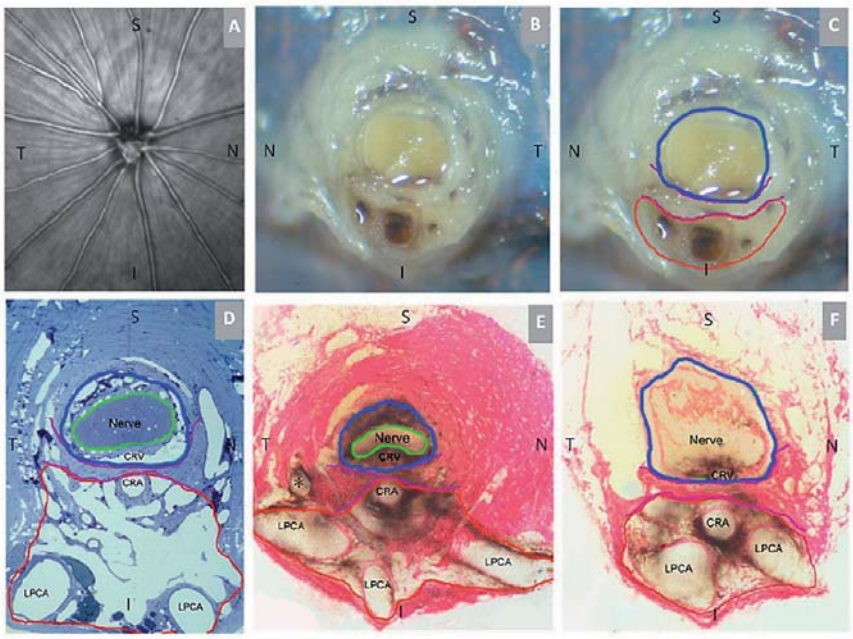

Supplemental Figure 1. Rat Optic Nerve Head Macroscopic and Microscopic Relationships I – Transverse Sections. (A) 30 degree SD-OCT Infrared Reflectance image of the rat optic disc (the vitreal surface of the optic nerve head) (courtesy of Brad Fortune). (B) Macroscopic appearance of the cut surface of the rat optic nerve just posterior to the scleral shell (view from the back of the eye). (C) Principal Macroscopic relationships. The neurovenous bundle (green) and the more-inferior arterial bundle (red) are separated by a sling of scleral tissues (the scleral sling, purple) (view from the back of the eye). (D-E) Principal scleral openings. Unlike the primate, there are two principal openings within the sclera of the rat ONH: 1) the neurovenous canal (blue) and the more-inferior arterial opening (red), which is not a well-defined canal, being irregular due to the choroidal branches of the LPCAs (D and E) and separated from the neurovenous canal by the scleral sling (purple). Unlike the primate, which has on average 15 short posterior ciliary arteries that are evenly distributed around the circumference of the scleral canal, the inferior concentration of the LPCAs and the density of their intrascleral branches to the choroid combined with the actual CRA canal (D – F) suggest an "effective" second opening in the sclera. (D) Transverse histologic section through the scleral portion of the optic nerve head demonstrating the same relationships seen posterior to the globe in panels B and C. Note that the neurovenous bundle consists of the optic nerve surrounded by a vascular tissue within the inferior portion of which runs the CRV. The arterial bundle is made up of the central retinal artery the two main LPCAs and their intrascleral branches to the choroid (vascular spaces in between the principal arteries - not labeled). (E) An acquired, digital transverse section image from a histomorphometric reconstruction demonstrating the same relationships as (D). (F) Digital section image from the same eye just posterior to the globe and close to the view seen macroscopically in (C). The red oblique line in (F) marks the location of a digital radial section image that is not shown. The intrascleral (E) and retrobulbar short posterior ciliary arteries (*) are branches of the LPCAs rather than the Ophthalmic Artery. A preferential superior-temporal course of the optic nerve and neurovenous bundle as they pass through the sclera into the orbit are suggested by comparing the green circle in (F) to (E). CRV- Central retinal vein, LPCAs- Long Posterior Ciliary Arteries. N – Nasal; T – Temporal; I – Inferior; S – Superior. Reproduced with minor alterations and permission from our previous publication (Pazos et al., 2015).

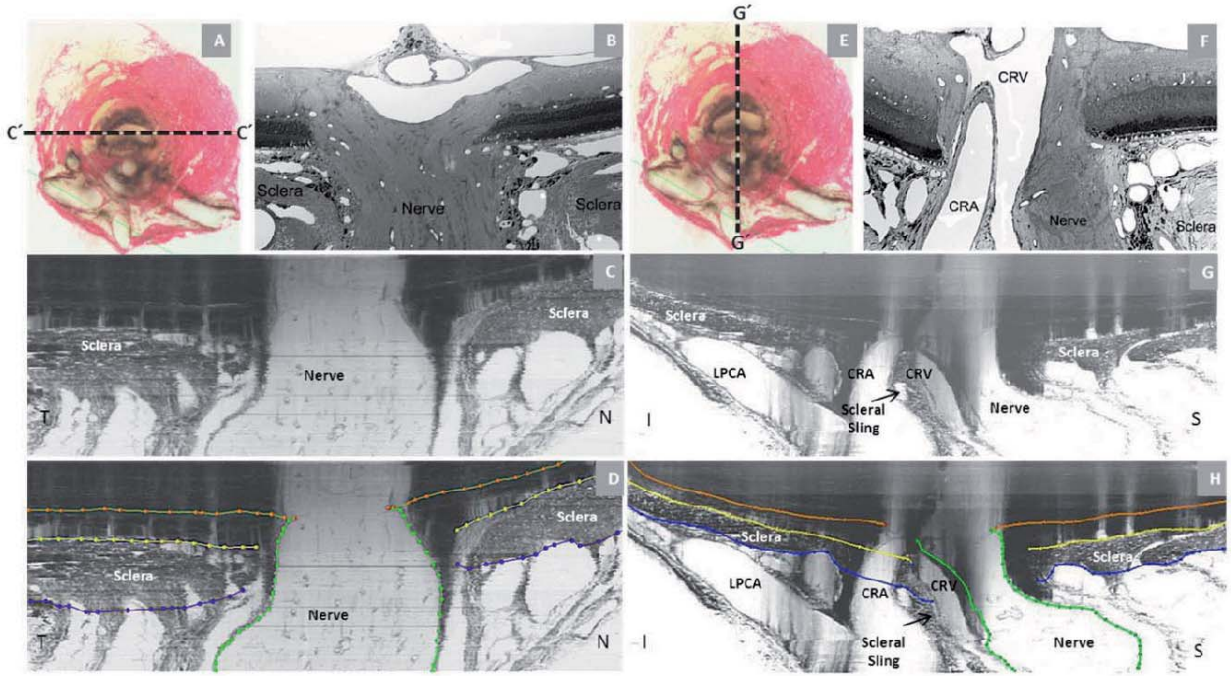

l Figure 2. Rat Optic Nerve Head Macroscopic and Microscopic Relationships II – Sagittal Sections. Horizontal (upper panels - A, B,C and D) and anels - E, F, G and H) sagittal views of the rat ONH centered upon the scleral portion of the neurovascular canal (A and E). Panels (B, C and D) and (F, G and H) are ections (location relative to the ONH marked as C' and G' in (A) and (E) of the same histomorphometric reconstruction in which acquired transverse section images were emental figure 1 and panels D and H are the same sections showing the delineation of the different structures. The process of creating digital sagittal sections from the tric volume is explained in Supplemental Figure 3. Panels (B) and (F) are histologic sections of another eye acquired in locations similar to (C) and (G). Most descriptions show horizontal (C) or vertical (G) sagittal sections of the ONH that are cropped close to the end of the sclera which has the effect of emphasizing the similarities of the anal to the scleral canal of the primate. However within the horizontal (C) and vertical (G) digital sagittal sections of the histomorphometric reconstructions, the he venous plexus that surrounds the nerve within the neurovenous canal, the sclera sling and the inferior arterial vessels can be appreciated. Note also the general of the nerve in (B) and the superior slant of the nerve in (F). Taken together, these observations within horizontal and vertical sagittal sections confirm the general al path of the optic nerve tissues suggested within the serial transverse section images of Figure 1 (see Figure legend). Note that within panels (C) and (G) of Figure 2, vs extending upward from the sclera are a result of the fact that in serial transverse sectioning from the vitreous (top) to the orbital optic nerve (bottom) the dark choroidal seen until the sectioning plane passes through it, creating the appearance of a shadow within the retina and vitreous . CRV- Central retinal vein, LPCA- Long Posterior CRA-Central Retinal Artery; N – Nasal; T – Temporal; I – Inferior; S – Superior. Orange line: Bruch's Membrane, Yellow line: anterior sclera. Blue line: Posterior Sclera. ve boundary. Reproduced with permission from our previous publication (Pazos et al., 2015).

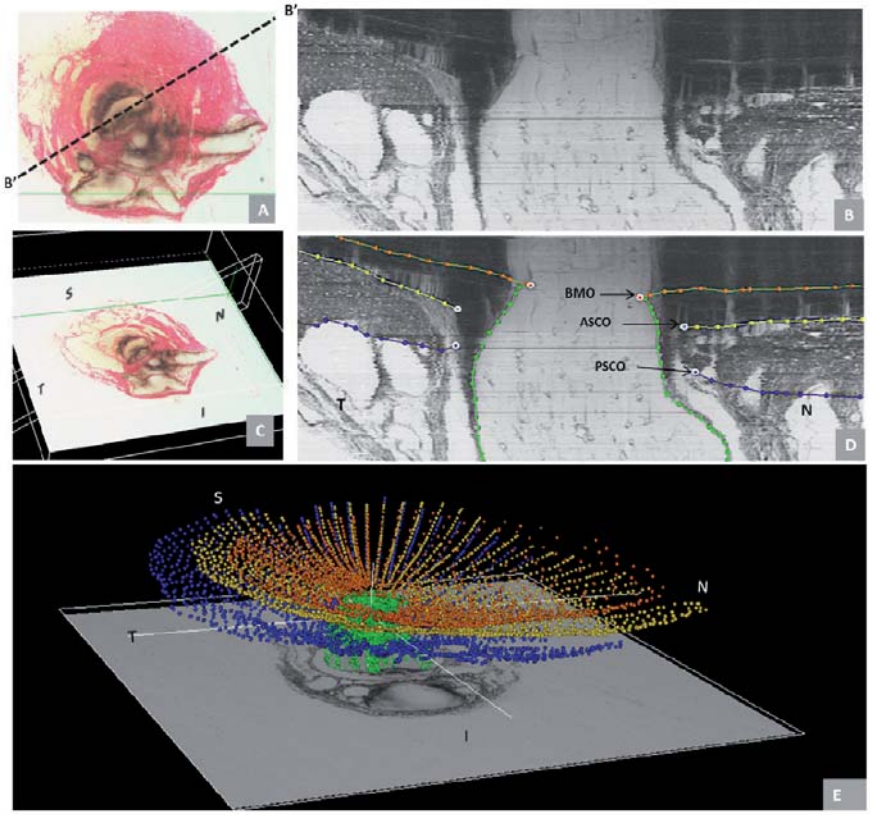

Supplemental Figure 3. Points within 40 Digital Serial Radial Sagittal Section Images of each ONH. The delineator first assigned the center of the scleral portion of the optic nerve (A) to be the center of rotation through which, forty, 7-voxel thick, digital radial sagittal section images (B) of the digital 3-D reconstruction (C) were serially served at 4.5° intervals. The Nasal-Temporal location of (B) is shown here two dimensionally (dotted line marked B-B') within the transverse section image in (A) and three-dimensionally (7 µm thick white-edged rectangle) within the 3-D reconstruction in (C). Within each digital sagittal section image (B) the delineator marked four landmark surfaces and three pairs of neurovenous canal landmarks (one point on each side of the canal). The landmark surfaces were: (1) Bruch's membrane (orange); (2) the anterior (yellow) and (3) posterior (blue) surfaces of peripapillary sclera ; and (4) the optic nerve boundary extending from Bruch's membrane opening, through the scleral canal and along the pia mater to the posterior edge of the reconstruction (green). The landmark points were Bruch's Membrane Opening (BMO – red), the anterior scleral canal opening (ASCO – light blue) and the posterior scleral canal opening (PSCO – purple). A representative point cloud which contains all delineated landmark types for all 40 radial sections of an individual reconstruction is viewed from its superior surface three dimensionally in (D) (temporal is to the left and nasal is to the right). Three dimensional reconstructions of the landmark point clouds (D) of each eye were 3D visualized together and separately (turning each landmark category on and off) so as to qualitatively determine their principal macroscopic relationships. In Panel (E) the superior temporal course of the optic nerve as it passes through the sclera and its sharper bend into the orbit can be appreciated. N – Nasal; T – Temporal; I – Inferior; S – Superior. Reproduced with permission from our previous publication (Pazos et al., 2015).

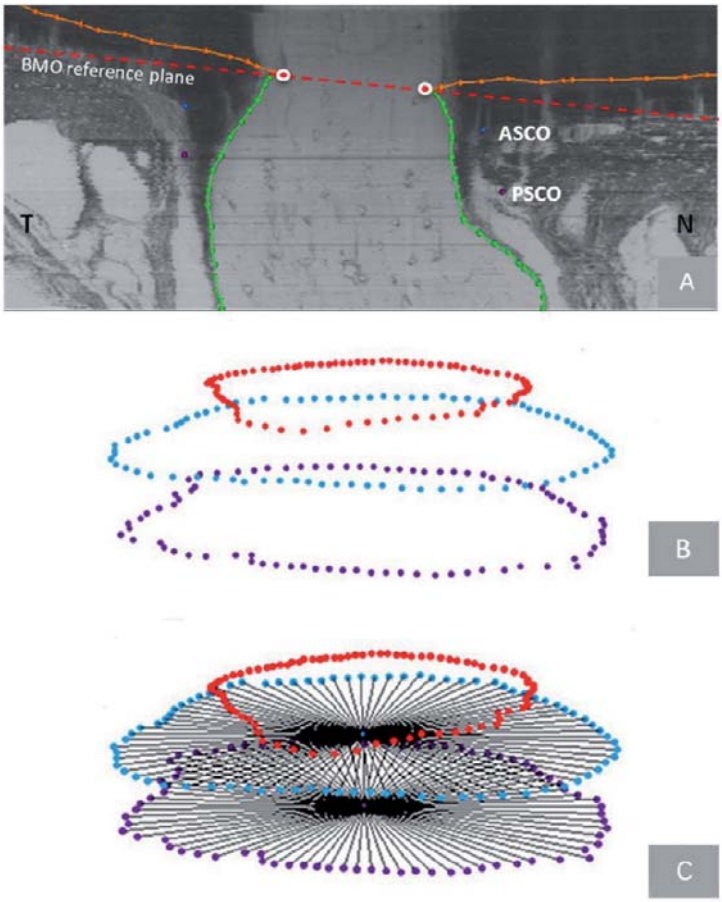

Supplemental Figure 4. Bruch's Membrane Opening (BMO) and Neurovascular Scleral Canal Parameterization. **(A)** Within each ONH reconstruction, individual planes were fit to the 80 BMO points, 80 ASCO points and 80 PSCO points which are illustrated in cross-section within a digital sagittal section image. (**N** – Nasal; **T** – Temporal). **(B)** The cross-sectional area of all three openings (BMO, ASCO and PSCO) was calculated as the area within the projection of the BMO, ASCO and PSCO points to their respective fitted planes. **(C)** Using the centroid of the projected BMO, ASCO and PSCO points, 80 radius measurements were made within their respective fitted planes at 4.5 degree intervals. Reproduced with permission, from Appendix Figure 1 of our previous publication (Pazos et al., 2015).

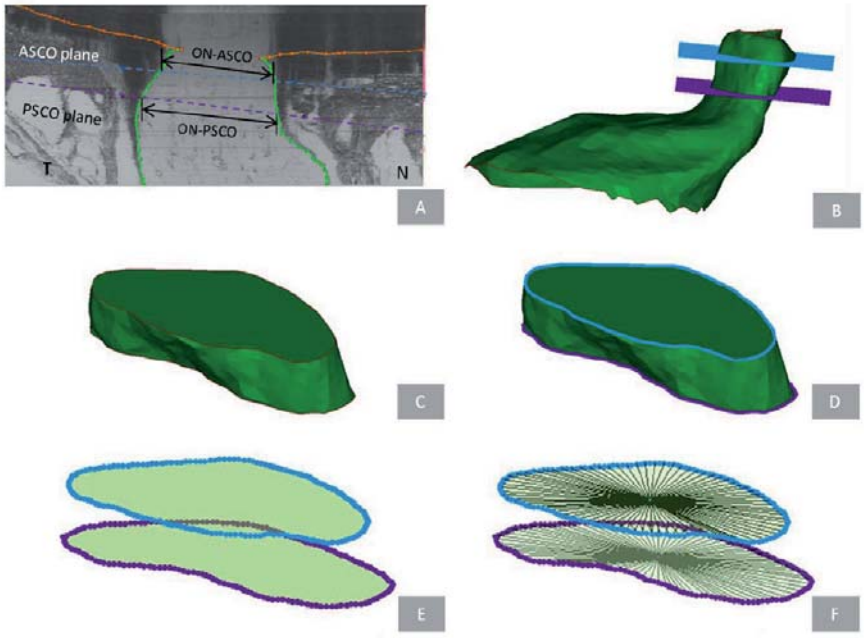

Supplemental Figure 5. Scleral Canal Optic Nerve Area and Volume Parameterization. Optic nerve cross-sectional area and radii were quantified within the ASCO (ON-ASCO) and PSCO (ON-PSCO) planes using the delineated optic nerve boundary (green dots) as illustrated within digital sagittal sections in panel (A). ON cross-sectional area within BMO (ON-BMO) could not be quantified due to obstruction of its boundaries by pigment from the perineural venous plexus. In (B) the optic nerve point cloud (from all 40 delineated sections) has been surfaced (green) and the position of the ASCO (light blue) and PSCO (purple) planes relative to the optic nerve is shown. Please note that while the ASCO and PSCO planes are based on the respective openings within the sclera (Figure 5, above, and panel A of this figure) it is the scleral canal optic nerve volume or the optic nerve volume within the canal (not including the surrounding venous plexus) and between the planes that is isolated within (C). The ON-ASCO (light blue) and ON-PSCO (purple) surfaces of the scleral canal optic nerve volume are highlighted in (D), and their areas and radii are quantified in (E) and (F). The orientation of panels (B) – (F) is approximately that of (A) - Temporal (T) left and Nasal (N) right. Reproduced with permission, from Appendix Figure 2 of our previous publication (Pazos et al., 2015).

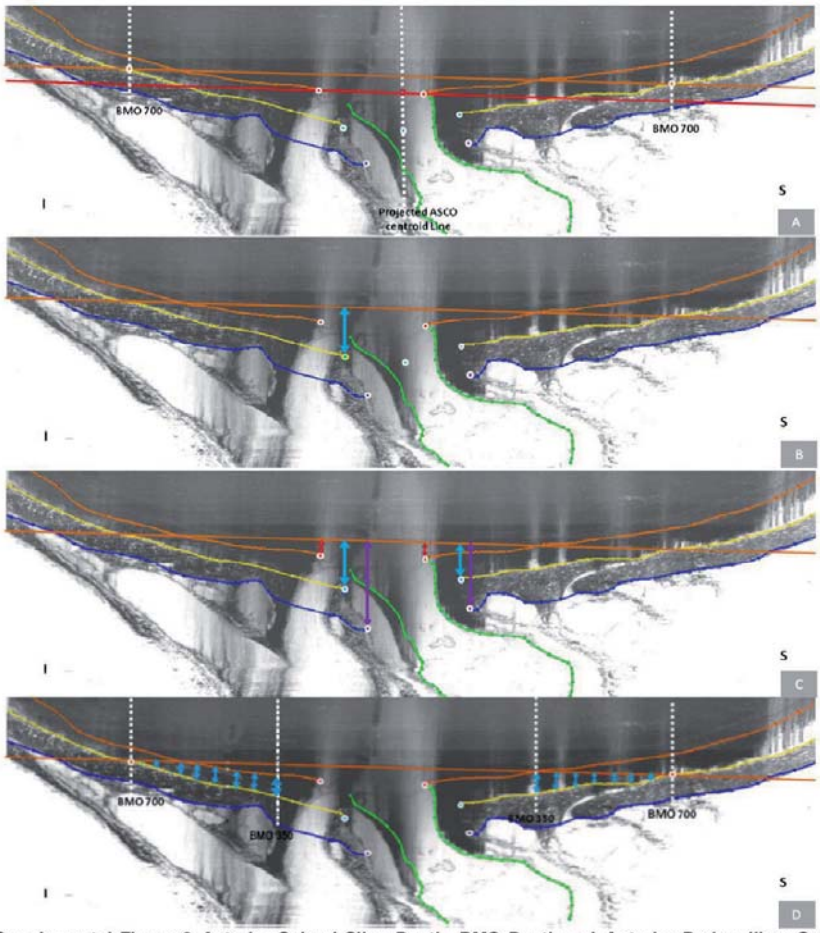

Supplemental Figure 6 *Anterior Scleral Sling Depth*, *BMO Depth* and *Anterior Peripapillary Scleral Depth* relative to a peripheral anterior scleral reference plane. (A) A peripheral anterior scleral reference plane was generated from a ring of points (orange dot with white border) on the anterior scleral surface at a distance 700 microns (BMO 700) from the projected ASCO centroid line. (B) *ASCO Depth (blue arrow)* was measured relative to the peripheral anterior scleral reference plane in each radial section in which the sling surface could be identified (approximately 8 section images per ONH). Circled in yellow you can see the most anterior aspect of the scleral sling. (C) *BMO Depth* was measured for each BMO point relative to the same reference plane within each section. PSCO (purple arrow), ASCO Depth (blue arrow) and BMO depth (red arrow) were calculated relative to this peripheral anterior scleral reference plane as well. (D) *Anterior Peripapillary Scleral Depth* relative to the same reference plane was measured at a distance of BMO 350 to BMO 700 µm (in 50 µm increments) on the fitted anterior scleral surface (yellow line). Red dot with white border – BMO; Blue dot with white border – ASCO; Purple dot with white border – PSCO; Projected ASCO centroid line (A) - perpendicular line to the BMO reference plane (red line) passing through the raw ASCO centroid (blue dot with white border); Blue dot with red border (B) - projected ASCO centroid; *BMO 350/700* - Perpendicular line from the BMO reference plane at a distance of 350/700 µm from the projected ASCO centroid line so as to define BMO 350/700 eccentricity. I – Inferior; S – Superior. . Orange line: Bruch's Membrane, Yellow line: anterior sclera. Blue line: Posterior Sclera. Green line: Nerve boundary. Reproduced with permission, from Appendix Figure 3 of our previous publication (Pazos et al., 2015).

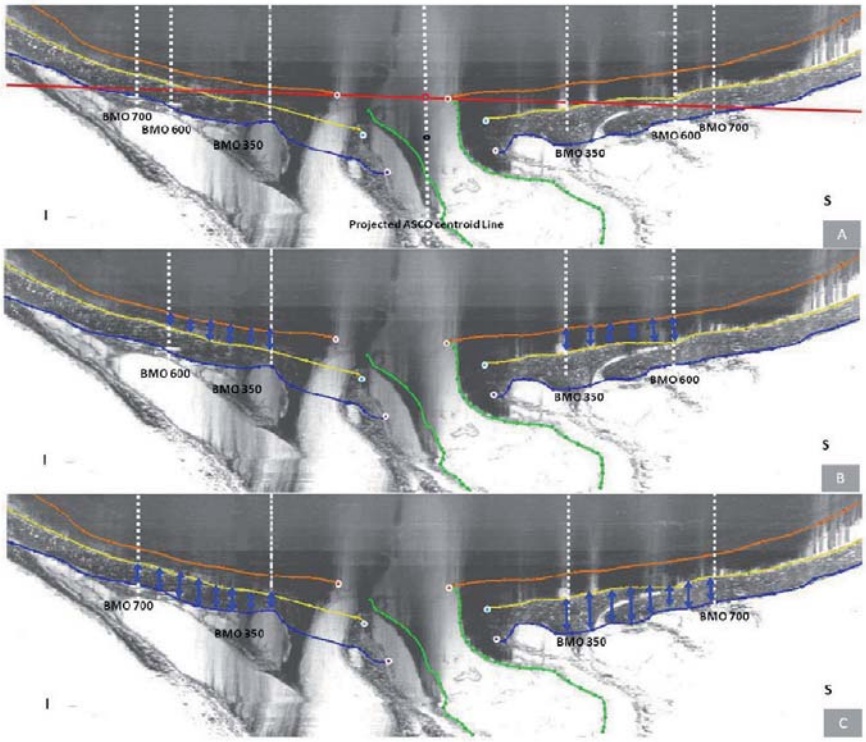

Supplemental Figure 7. *Peripapillary Choroidal* and *Peripapillary Scleral Thickness* Parameterization. (A) Projected ASCO centroid line is a perpendicular line to the BMO reference plane (red line) passing through the raw ASCO centroid (blue dot with black border) and projected ASCO centroid (Blue dot with red border). *BMO 350/600/700*: Perpendicular line from the BMO reference plane at a distance of 350/600/700 m from the projected ASCO centroid line so as to define BMO 350/600/700 eccentricity. (B) *Peripapillary Choroidal Thickness (dark blue arrows)* was measured perpendicular to Bruch's Membrane surfaces in 50 m increments along the BMO reference plane between the BMO 350 to BMO 600 landmarks. (C) *Peripapillary Scleral Thickness (dark blue arrows)* was measured perpendicular to the anterior scleral surface in 50 m increments along the BMO reference plane between the BMO 350 to BMO 700 landmarks Red dots with white border – BMO; Blue dots with white border – ASCO; Purple dot with white border - PSCO. Blue dot with black border (A) – ASCO centroid; I – Inferior; S – Superior. Orange line: Bruch's Membrane, Yellow line: Anterior sclera. Blue line: Posterior Sclera. Green line: Nerve boundary. Reproduced with permission from Appendix Figure 4 of our previous publication (Pazos et al., 2015).

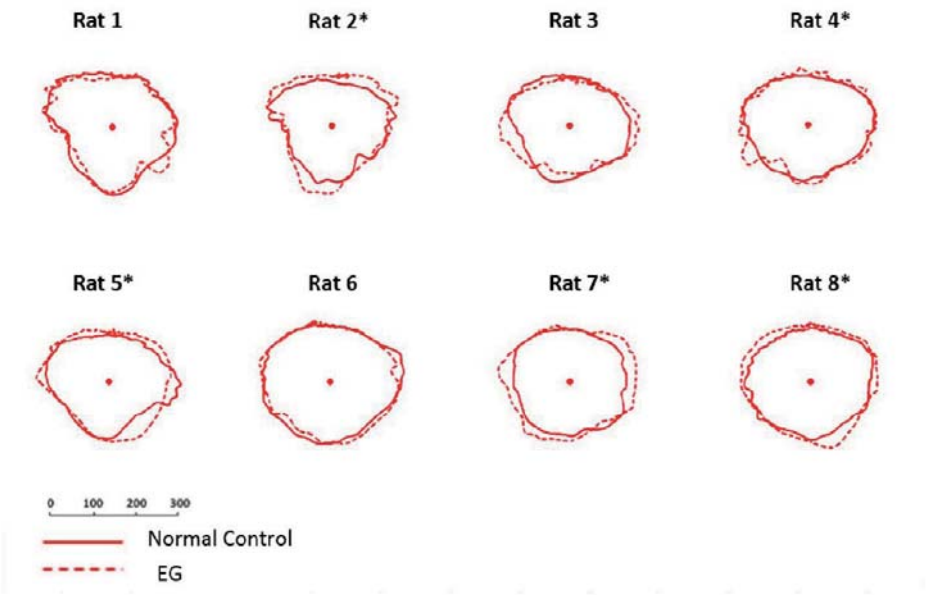

Supplemental Figure 8. EG (dotted line) versus Control (solid line) eye Bruch's Membrane Opening (BMO) comparison for each animal. BMO data points for the Control and EG eye of each rat are schematically overlaid using the BMO centroid of each eye. All data are in right eye orientation. The scale is in micrometers. **(*)** denotes animals in which Global EG versus Control Eye *BMO radius* differences achieved significance (Table 4).

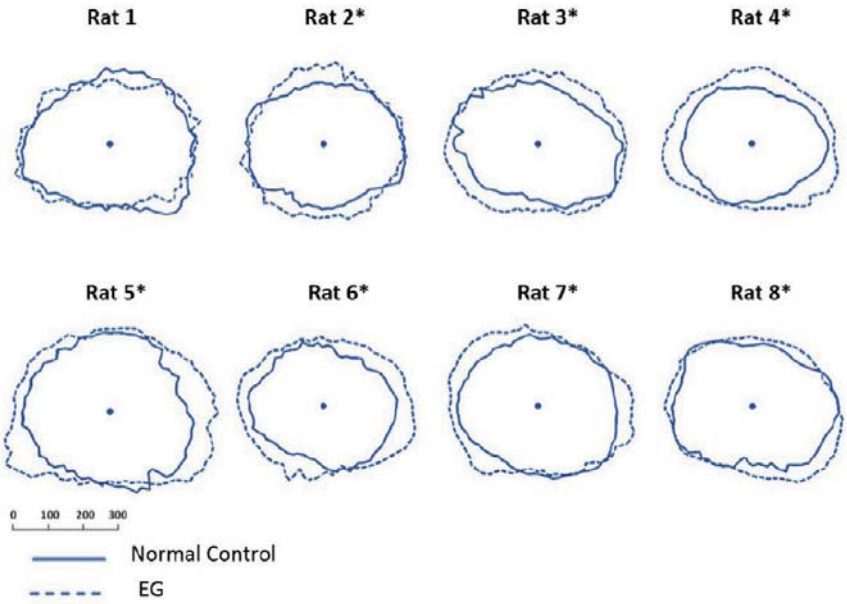

Supplemental Figure 9. EG (dotted line) versus Control (solid line) eye Anterior Scleral Canal Opening (ASCO) comparison for each animal. ASCO data points for the Control and EG eye of each rat are schematically overlaid using the ASCO centroid of each eye. All data are in right eye orientation. The scale is in micrometers. **(*)** denotes animals in which Global EG versus Control Eye *ASCO radius* differences achieved significance (Table 4).

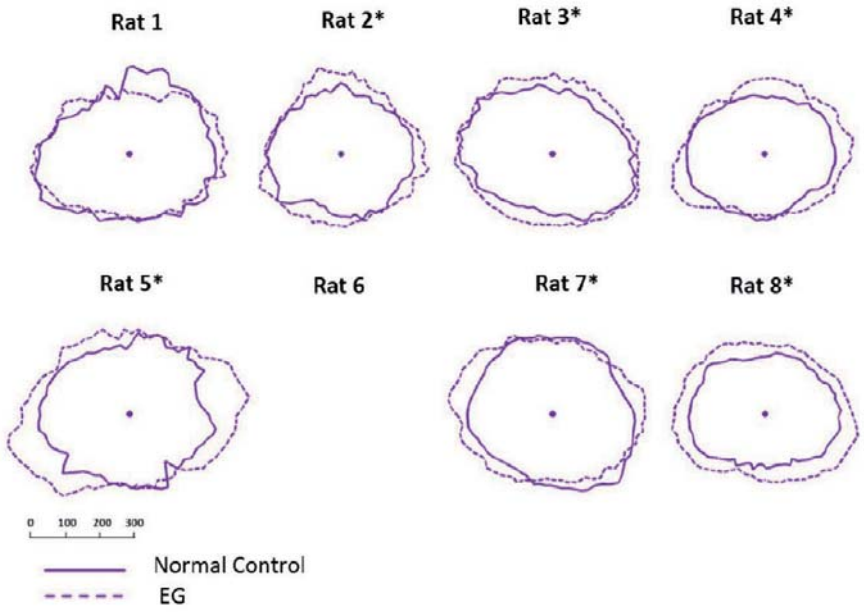

Supplemental Figure 10. EG (dotted line) versus Control (solid line) eye Posterior Scleral Canal Opening (PSCO) comparison for each animal. PSCO data points for the Control and EG eye of each rat are schematically overlaid using the PSCO centroid of each eye. All data are in right eye orientation. The scale is in micrometers. **(*)** denotes animals in which Global EG versus Control Eye PSCO *radius* differences achieved significance (Table 4). PSCO data for the EG eye of Rat 6 were not available.

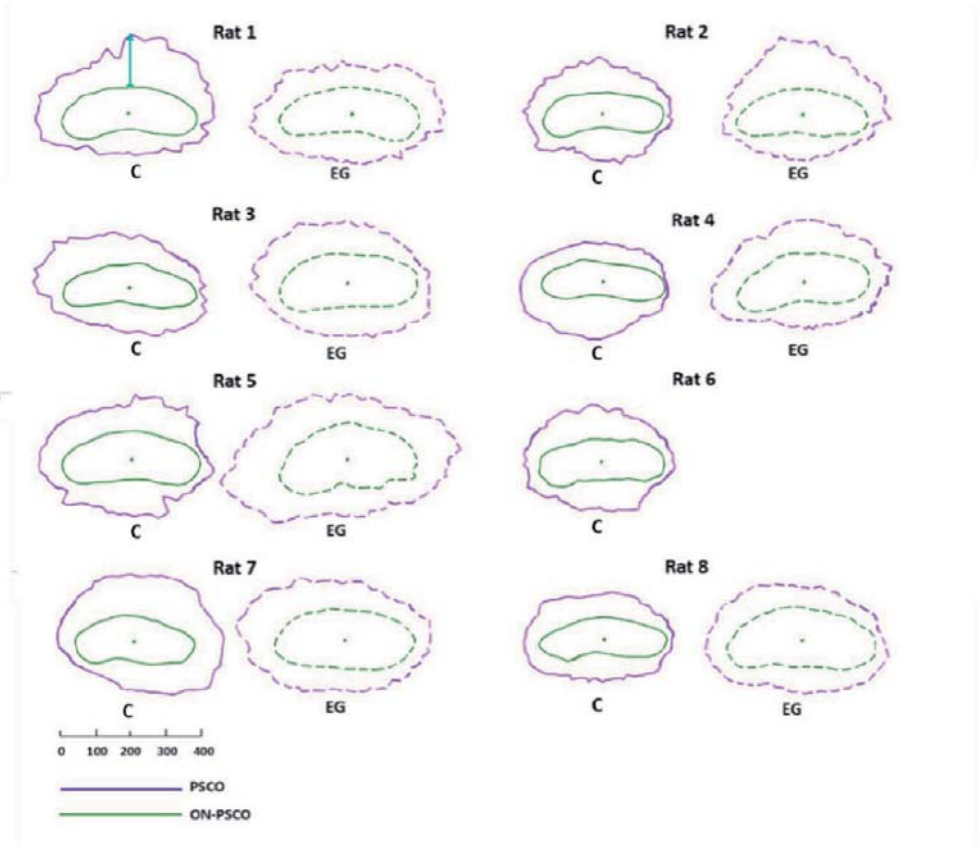

Supplemental Figure 11. Animal-specific, EG (dotted line) versus Control Eye (solid line) comparisons of Posterior Scleral Canal Opening (PSCO – Purple) and Optic Nerve–PSCO (ON-PSCO - green). PSCO fitted spline and ON-PSCO fitted spline are projected onto the PSCO reference plane for comparison purposes. The ON-PSCO centroid for each eye has been used to horizontally align the data from each eye. The green arrow (Control eye of Rat 1, upper left) schematically depicts the *PSCO-ON-PSCO Distance* measurement (here showing 1 of a total of 80 radial measurements – see methods). Animal-specific EG vs Control eye overlays of PSCO and ON-PSCO data can be seen in Supplemental Figures 10 and 12, respectively. Global EG eye *PSCO-ON-PSCO Distance* was significantly increased within Animals 2, 3, 5, and 7. The scale is in micrometers.

References

Baumann, B., et al., 2011. Total retinal blood flow measurement with ultrahigh speed swept source/Fourier domain OCT. Biomed Opt Express. 2, 1539-1552.

Burgoyne, C., 2015a. The Morphological Difference Between Glaucoma and Other Optic Neuropathies. J Neuroophthalmol. 35 Suppl 1, S8-S21.

Burgoyne, C.F., 2015b. The non-human primate experimental glaucoma model. Exp Eye Res. First published on Jun 9, 2015b as doi:10.1016/j.exer.2015.06.005

Burgoyne, C.F., Downs, J.C., 2008. Premise and prediction-how optic nerve head biomechanics underlies the susceptibility and clinical behavior of the aged optic nerve head. J Glaucoma. 17, 318-328.

Burgoyne, C.F., et al., 2004. Three-dimensional reconstruction of normal and early glaucoma monkey optic nerve head connective tissues. Invest Ophthalmol Vis Sci. 45, 4388-4399.

Burgoyne, C.F., et al., 2014. Non-Human Primate (NHP) Optic Nerve Head (ONH) Proteomic Change In Early Experimental Glaucoma (EEG). . ARVO Meeting Abstracts. 55, ARVO Abstract# 4555.

Cepurna, W.O., et al., 2005. Age related optic nerve axonal loss in adult Brown Norway rats. Exp Eye Res. 80, 877-884.

Chauhan, B.C., et al., 2004. Model of endothelin-1-induced chronic optic neuropathy in rat. Invest Ophthalmol Vis Sci. 45, 144-152.

Chauhan, B.C., et al., 2002. Effect of intraocular pressure on optic disc topography, electroretinography, and axonal loss in a chronic pressure-induced rat model of optic nerve damage. Invest. Ophthalmol. Vis. Sci. 43, 2969-2976.

Crowston, J.G., et al., 2015. An acute intraocular pressure challenge to assess retinal ganglion cell injury and recovery in the mouse. Exp Eye Res. First published on Mar 7, 2015 as doi:10.1016/j.exer.2015.03.006

Dai, C., et al., 2012. Structural basis of glaucoma: the fortified astrocytes of the optic nerve head are the target of raised intraocular pressure. Glia. 60, 13-28.

Downs, J.C., et al., 2007. Three-dimensional histomorphometry of the normal and early glaucomatous monkey optic nerve head: neural canal and subarachnoid space architecture. Invest Ophthalmol Vis Sci. 48, 3195-3208.

Fernandes, K.A., et al., 2015. Using genetic mouse models to gain insight into glaucoma: Past results and future possibilities. Exp Eye Res. First published on Jun 24, 2015 as doi:10.1016/j.exer.2015.06.019

Fortune, B., et al., 2011. Deformation of the rodent optic nerve head and peripapillary structures during acute intraocular pressure elevation. Invest Ophthalmol Vis Sci. 52, 6651-6661.

Goldblum, D., Mittag, T., 2002. Prospects for relevant glaucoma models with retinal ganglion cell damage in the rodent eye. Vision Res. 42, 471-478.

Guo, B., Yuan, Y., 2015. A comparative review of methods for comparing means using partially paired data. Stat Methods Med Res. First published on Apr 1, 2015 as doi:10.1177/0962280215577111

Guo, L., et al., 2005. En face optical coherence tomography: a new method to analyse structural changes of the optic nerve head in rat glaucoma. Br J Ophthalmol. 89, 1210-1216.

He, L., et al., 2014. Longitudinal detection of optic nerve head changes by spectral domain optical coherence tomography in early experimental glaucoma. Invest Ophthalmol Vis Sci. 55, 574-586.

Heickell, A.G., et al., 2001. Optic disc surface compliance testing using confocal scanning laser tomography in the normal monkey eye. J Glaucoma. 10, 369-382.

Hernandez, M.R., et al., 1990. Changes in the extracellular matrix of the human optic nerve head in primary open-angle glaucoma. Am J Ophthalmol. 109, 180-188.

Howell, G.R., et al., 2011. Molecular clustering identifies complement and endothelin induction as early events in a mouse model of glaucoma. J Clin Invest. 121, 1429-1444.

Huang, X.R., Knighton, R.W., 2009. Altered F-actin distribution in retinal nerve fiber layer of a rat model of glaucoma. Exp Eye Res. 88, 1107-1114.

Jia, L., et al., 2000. Patterns of intraocular pressure elevation after aqueous humor outflow obstruction in rats. Invest Ophthalmol Vis Sci. 41, 1380-1385.

Joachim, S.C., et al., 2013. Immune response against ocular tissues after immunization with optic nerve antigens in a model of autoimmune glaucoma. Mol Vis. 19, 1804-1814.

Johnson, E.C., et al., 2011. Cell proliferation and interleukin-6-type cytokine signaling are implicated by gene expression responses in early optic nerve head injury in rat glaucoma. Invest Ophthalmol Vis Sci. 52, 504-518.

Johnson, E.C., et al., 2007. Global Changes in Optic Nerve Head Gene Expression after Exposure to Elevated Intraocular Pressure in a Rat Glaucoma Model. Invest. Ophthalmol. Vis. Sci. 48, 3161-3177.

Johnson, E.C., et al., 1996. The effect of chronically elevated intraocular pressure on the rat optic nerve head extracellular matrix. Exp Eye Res. 62, 663-674.

Kong, Y.X., et al., 2009. Functional changes in the retina during and after acute intraocular pressure elevation in mice. Invest Ophthalmol Vis Sci. 50, 5732-5740.

Li, Y., et al., 2015. An energy theory of glaucoma. Glia. 63, 1537-1552.

Morgan, J.E., Tribble, J.R., 2015. Microbead models in glaucoma. Exp Eye Res. First published on Jun 24, 2015 as doi:10.1016/j.exer.2015.06.020

Morrison, J., et al., 1995. Structure and composition of the rodent lamina cribrosa. Exp Eye Res. 60, 127-135.

Morrison, J.C., 2005. Elevated intraocular pressure and optic nerve injury models in the rat. J Glaucoma. 14, 315-317.

Morrison, J.C., et al., 2015. Modeling glaucoma in rats by sclerosing aqueous outflow pathways to elevate intraocular pressure. Exp Eye Res. First published on May 21, 2015 as doi:10.1016/j.exer.2015.05.012

Morrison, J.C., et al., 2011. Pathophysiology of human glaucomatous optic nerve damage: insights from rodent models of glaucoma. Exp Eye Res. 93, 156-164.

Morrison, J.C., et al., 1990. Optic nerve head extracellular matrix in primary optic atrophy and experimental glaucoma. Arch Ophthalmol. 108, 1020-1024.

Morrison, J.C., et al., 2008. Rat models for glaucoma research. Prog Brain Res. 173, 285-301.

Morrison, J.C., et al., 2005. Understanding mechanisms of pressure-induced optic nerve damage. Prog Retin Eye Res. 24, 217-240.

Morrison, J.C., et al., 1999. Microvasculature of the rat optic nerve head. Invest. Ophthalmol. Vis. Sci. 40, 1702-1709.

Morrison, J.C., et al., 1997. A rat model of chronic pressure-induced optic nerve damage. Exp Eye Res. 64, 85-96.

Morrison, J.C., et al., 1998. Glaucoma drops control intraocular pressure and protect optic nerves in a rat model of glaucoma. Invest Ophthalmol Vis Sci. 39, 526-531.

Murphy, J.A., et al., 2010. The role of endothelin-1 and its receptors in optic nerve head astrocyte proliferation. Br J Ophthalmol. 94, 1233-1238.

Nagata, A., et al., 2009. In vivo quantitative evaluation of the rat retinal nerve fiber layer with optical coherence tomography. Invest Ophthalmol Vis Sci. 50, 2809-2815.

Naskar, R., et al., 2002. Detection of early neuron degeneration and accompanying microglial responses in the retina of a rat model of glaucoma. Invest Ophthalmol Vis Sci. 43, 2962-2968.

Overby, D.R., Clark, A.F., 2015. Animal models of glucocorticoid-induced glaucoma. Exp Eye Res. First published on Jun 4, 2015 as doi:10.1016/j.exer.2015.06.002

Pang, I.H., et al., 2015. Elevation of intraocular pressure in rodents using viral vectors targeting the trabecular meshwork. Exp Eye Res. First published on May 26, 2015 as doi:10.1016/j.exer.2015.04.003

Pang, I.H., et al., 2005. Acute effects of glaucoma medications on rat intraocular pressure. Exp Eye Res. 80, 207-214.

Pazos, M., et al., 2015. Rat optic nerve head anatomy within 3D histomorphometric reconstructions of normal control eyes. Exp Eye Res. 139, 1-12.

Pierru, A., et al., 2014. Measurement of subfoveal choroidal thickness after cataract surgery in enhanced depth imaging optical coherence tomography. Invest Ophthalmol Vis Sci. 55, 4967-4974.

Prasanna, G., et al., 2011. Endothelin, astrocytes and glaucoma. Exp Eye Res. 93, 170-177.

Reis, A.S., et al., 2012a. Influence of clinically invisible, but optical coherence tomography detected, optic disc margin anatomy on neuroretinal rim evaluation. Invest Ophthalmol Vis Sci. 53, 1852-1860.

Reis, A.S., et al., 2012b. Optic disc margin anatomy in patients with glaucoma and normal controls with spectral domain optical coherence tomography. Ophthalmology. 119, 738-747.

Ren, R., et al., 2014. Anterior lamina cribrosa surface depth, age, and visual field sensitivity in the Portland Progression Project. Invest Ophthalmol Vis Sci. 55, 1531-1539.

Rosner, B., 2011. 12.9. The Intraclass Correlation Coefficient, Fundamentals of Biostatistics, Seventh Edition ed. Harvard University. Brooks/Cole Cengage Learning, Boston, MA, p. 569.

Schlamp, C.L., et al., 2006. Progressive ganglion cell loss and optic nerve degeneration in DBA/2J mice is variable and asymmetric. BMC Neurosci. 7, 66.

Sigal, I.A., 2009. Interactions between geometry and mechanical properties on the optic nerve head. Invest Ophthalmol Vis Sci. 50, 2785-2795.

Sigal, I.A., et al., 2009a. Modeling individual-specific human optic nerve head biomechanics. Part I: IOP-induced deformations and influence of geometry. Biomech Model Mechanobiol. 8, 85-98.

Sigal, I.A., et al., 2009b. Modeling individual-specific human optic nerve head biomechanics. Part II: influence of material properties. Biomech Model Mechanobiol. 8, 99-109.

Strouthidis, N.G., et al., 2011a. Effect of acute intraocular pressure elevation on the monkey optic nerve head as detected by spectral domain optical coherence tomography. Invest Ophthalmol Vis Sci. 52, 9431-9437.

Strouthidis, N.G., et al., 2011b. Longitudinal change detected by spectral domain optical coherence tomography in the optic nerve head and peripapillary retina in experimental glaucoma. Invest Ophthalmol Vis Sci. 52, 1206-1219.

Strouthidis, N.G., et al., 2010. A comparison of optic nerve head morphology viewed by spectral domain optical coherence tomography and by serial histology. Invest Ophthalmol Vis Sci. 51, 1464-1474.

Strouthidis, N.G., et al., 2009. Comparison of clinical and spectral domain optical coherence tomography optic disc margin anatomy. Invest Ophthalmol Vis Sci. 50, 4709-4718.

Sugiyama, K., et al., 1999. Optic nerve and peripapillary choroidal microvasculature of the rat eye. Invest. Ophthalmol. Vis. Sci. 40, 3084-3090.

Tezel, G., Wax, M.B., 2004. The immune system and glaucoma. Curr Opin Ophthalmol. 15, 80-84.

Tseng, H.C., et al., 2015. Visual impairment in an optineurin mouse model of primary open-angle glaucoma. Neurobiol Aging. 36, 2201-2212.

Votruba, M., et al., 2003. Optic disc morphology of patients with OPA1 autosomal dominant optic atrophy. Br J Ophthalmol. 87, 48-53.

Wang, W., Zhang, X., 2014. Choroidal thickness and primary open-angle glaucoma: a cross-sectional study and meta-analysis. Invest Ophthalmol Vis Sci. 55, 6007-6014.

Wax, M.B., et al., 2008. Induced autoimmunity to heat shock proteins elicits glaucomatous loss of retinal ganglion cell neurons via activated T-cell-derived fas-ligand. J Neurosci. 28, 12085-12096.

WoldeMussie, E., et al., 2001. Neuroprotection of retinal ganglion cells by brimonidine in rats with laser-induced chronic ocular hypertension. Invest Ophthalmol Vis Sci. 42, 2849-2855.

Yang, H., et al., 2007a. 3-D histomorphometry of the normal and early glaucomatous monkey optic nerve head: prelaminar neural tissues and cupping. Invest Ophthalmol Vis Sci. 48, 5068-5084.

Yang, H., et al., 2009a. Physiologic intereye differences in monkey optic nerve head architecture and their relation to changes in early experimental glaucoma. Invest Ophthalmol Vis Sci. 50, 224-234.

Yang, H., et al., 2007b. 3-D histomorphometry of the normal and early glaucomatous monkey optic nerve head: lamina cribrosa and peripapillary scleral position and thickness. Invest Ophthalmol Vis Sci. 48, 4597-4607.

Yang, H., et al., 2009b. Deformation of the normal monkey optic nerve head connective tissue after acute IOP elevation within 3-D histomorphometric reconstructions. Invest Ophthalmol Vis Sci. 50, 5785-5799.

Yang, H., et al., 2011a. Deformation of the early glaucomatous monkey optic nerve head connective tissue after acute IOP elevation in 3-D histomorphometric reconstructions. Invest Ophthalmol Vis Sci. 52, 345-363.

Yang, H., et al., 2011b. Posterior (outward) migration of the lamina cribrosa and early cupping in monkey experimental glaucoma. Invest Ophthalmol Vis Sci. 52, 7109-7121.

Yiu, G., et al., 2014. Characterization of the choroid-scleral junction and suprachoroidal layer in healthy individuals on enhanced-depth imaging optical coherence tomography. JAMA Ophthalmol. 132, 174-181.

Zhang, X., et al., 2011. Dual-band spectral-domain optical coherence tomography for in vivo imaging the spectral contrasts of the retinal nerve fiber layer. Opt Express. 19, 19653-19659.

Zhi, Z., et al., 2011. Volumetric and quantitative imaging of retinal blood flow in rats with optical microangiography. Biomed Opt Express. 2, 579-591.

Zhi, Z., et al., 2012. Impact of intraocular pressure on changes of blood flow in the retina, choroid, and optic nerve head in rats investigated by optical microangiography. Biomed Opt Express. 3, 2220-2233.

Zotter, S., et al., 2011. Visualization of microvasculature by dual-beam phase-resolved Doppler optical coherence tomography. Opt Express. 19, 1217-1227.

4

Discussion

4.1. Rat Optic Nerve Head Anatomy within 3D histomorphometric reconstructions of normal control eyes

4.1.1. Principal Findings

- First, while the rat ONH is built around a well-defined neurovascular scleral canal that contains the retinal ganglion cell axon bundles surrounded by a vascular plexus that includes the CRV, we believe that the density of the more-inferior CRA and LPCA passageways through the sclera effectively constitute a second, arterial scleral opening that is less well defined and separated from the neurovascular scleral opening by a thin connective tissue band we have named the scleral sling.
- Second, at the level of BMO, BM extends prominently beyond the scleral canal opening superiorly to physically abut the RGC axon bundles, while inferiorly, the CRV and CRA physically separate the RGC axons from BMO.

- Third, the fact that the CRA passes through the sclera inferior to the neurovascular canal (within its own opening) but joins the CRVwithin the inferior portion of BMO, leaves BMO irregularly shaped with an inferior elongation that is not present in the primate eye.
- Fourth, within the neurovascular canal, at the level of the sclera, the retinal ganglion cell axons are bundled into a nerve that is surrounded by a vascular plexus in a manner that leaves its physical attachments to the surrounding sclera impossible to discern by ourmethod (see discussion below). This plexus appears to be a continuation of the choroid that ultimately drains into the retrobulbar pial and dural sheaths.
- Fifth, the three branches of the LPCAs densely and obliquely penetrate the peripapillary sclera inferior to the neurovascular canal to obtain and run within the peripapillary choroid. Apart from the creation of an effective second opening in the sclera (as mentioned above) these LPCAs along with their dense intrascleral branches that pass to the superior choroid (similar to but less complete than the primate circle of Zinn-Haler) appear to be the principal source of blood supply to the choroid. In fact we found no evidence for SPCAs (defined to be separate branches of the Ophthalmic Artery) in these reconstructions.

This is the first description of the rat ONH that defines it to consist of two separate passage ways through the sclera separated by a thin connective tissue strip (that we have termed the scleral sling). While the biomechanical implications of this anatomy remain to be determined, the large and irregular inferior arterial passageway (containing the CRA, the LPCAs and their intrascleral branches) combined with the lack of SPCAs, are two conditions that do not exist in the primate eye. While the prominent superior extension of BM has not previously been noted, it is easily visualized within Spectral Domain Optical Coherence Tomographic B-scans (verbal communication, Brad Fortune). The superior location of RGC axon interaction with BMO has previously been described by light microscopy (Morrison et al., 2011, 2008). The fact that the RGC axons are surrounded by a vascular plexus within the neurovascular canal and that this plexus is at least regionally continuous with the peripapillary choroid has been noted by a series of previous investigators (Dai et al., 2012; Morrison et al., 1999; Sugiyama et al., 1999). In longitudinal sections from both studies clear continuity between the choroid and the peri-neural vascular plexus can be appreciated. This

vascular plexus does not exist in the primate and is difficult to examine with our method due to the heavy pigmentation contained therein.

In the primate, the peripapillary sclera and scleral canal Wall connective tissues are thought to govern the distribution of IOP-related stress and strain within the lamina cribrosa connective tissues (Burgoyne and Downs, 2008; Sigal et al., 2005). Given the lack of a detectible connective tissue lamina and connective tissue connections between the nerve and the sclera, by our technique, the question of how the sclera transfers load to the RGC axons and the astrocytes that span the nerve within the canal is of substantial biomechanical interest. Two recent papers have described the relationship between the radially arrayed, rat optic nerve head astrocytes, the optic nerve pial sheath (a continuation of the pia that merges with BM at its opening) and this vascular plexus (Dai et al., 2012; Li et al., 2015). Their description of the plexus suggests that it contains dense connective tissue septa. If these septa directly or indirectly span the plexus to link the sheath and the sclera, then they may be the means by which the sclera transfers IOP-related load to the ONH astrocytic array. The geometry and material properties of these cells, the sheath, and these septal connections to the sclera, thus require further study.

Regarding our quantitative results, previous studies (Downs et al., 2007; Yang et al., 2009a, 2009b, 2011) in a total of 21 normal eyes of 21 monkeys suggest that the mean rat BMO Area and mean rat BMO radii we report are 4.7% and 23% (respectively) that of the monkey. In humans, Ren et al. (Ren et al., 2009) used a postmortem, 2-D technique within histologic sections to report mean BMO diameter that suggest the BMO Radii data we report appear to be approximately 17% the size of the human eye. Recently, using Spectral-Domain (SD) OCT in 48 healthy humans, Chauhan and colleagues reported a BMO Area of 1.7 μm2 (1.4-1.9) which is about 30 times larger than the rat eye (Chauhan et al., 2013).

Like the (single) scleral canal in the primate, the neurovascular scleral canal in the rat expands within the sclera in half of the rat eyes. Interestingly, a study performed using en face Optical Coherence Tomography reported in vivo, OCT-detected ASCO diameter values of approximately 665 mmin 18 normal Dark Agouti rats (Guo et al., 2005). While tissue shrinkage due to fixation, embedding and species difference (estimated to be as high as 30%) (Abramson et al., 2003) may explain these differences, the in vivo study did not clarify the

orientation of their measurements (long versus short axis of the horizontal ellipse), nor did it detect the elliptical (rather than circular) shape of this opening as we have herein described. In a post-mortem histologic study of 6 normal human ONHs, (Sigal et al., 2010) ASCO radius was 1.2 times larger than the monkey and 4 times larger than the rat eye.

Finally, because the manner in which mean scleral thickness measurements were made in rats was different from previous measurements made by us in monkeys (Burgoyne et al., 2004; Downs et al., 2007; Yang et al., 2007a, 2007b, 2009b, 2011), and others in humans (Ren et al., 2009; Sigal et al., 2010), direct comparison to the literature is not straightforward. Our data suggest that monkey peripapillary scleral thickness is 2-4 times thicker than that of the rat when compared at a similar eccentricity to the PSCO. Studies in human eyes (Norman et al., 2010; Ren et al., 2009; Sigal et al., 2010), which are not well matched to the location of measurement in our study, together suggest that human peripapillary sclera is profoundly thicker than that of the rat.

4.1.2 Limitations

The limitations of our method of 3D reconstruction have been discussed previously (Burgoyne et al., 2004) and include:

1. Anterior-to-posterior resolutions limited to 1.5 mm by the fact that the current stain penetrates approximately 1.5 mm into the block
2. The stain is applied by hand to the block face with a cottontipped swab, and the excess is manually removed with lens paper, and thus staining variation between section images can be substantial
3. There are tissue shrinkage effects (both from fixation and embedding) associated with this technique that may be unique to the rat eye and different within each constituent tissue of the ONH
4. The dense pigmentation of the rat vascular plexus surrounding the nerve may lead to an overestimation of ASCO and PSCO especially in the temporal/superior quadrants, due to the bending of the nerve
5. Comparisons to our nonhuman primate and human cadaver eye data may be similar since post-tissue processing is similar, but comparisons to other post-mortem or in-vivo measurements may be affected by these differences

6. Delineations were made using the approximate center of the ON as the point of rotation and the radial measurements were made from the centroids based on those delineations. The delineator's estimate of the ON center, and the fact that it was not necessarily the center of other ONH structures, may have influenced the regional sampling of the data.

Finally, it is possible that normal control eyes from unilateral EG animals raised in constant light environments, may not be identical to naive normal control eyes from bilaterally normal animals raised in the usual 12 hour light/dark cycle. However, there are no descriptions of normal control eye alteration in the rat unilateral EG model and none of the 8 normal control eyes in this study were found to have detectible alterations in their optic nerve axons by 2 graders masked to the status of each eye. While we do not believe
that the morphologic relationships we describe will be different in naive status of raised in 12 hour light/dark conditions, the generalization of our quantitative findings to naïve normal eyes of all ages, rat strain and lighting conditions must be the subject of future studies.

4.2. Expansions of the neurovascular scleral canal and contained optic nerve occur early in the hypertonic saline rat experimental glaucoma model

4.2.1. Principal Findings

This study 3D histomorphometrically characterizes early ONH neural and connective tissue change in the hypertonic rat model of unilateral EG. Our principle findings are as follows:

- First, the connective tissue openings that define the neurovascular canal of the rat ONH, (BMO, ASCO and PSCO), each expand early in EG.
- Second, among all forms of EG eye change, optic nerve expansion within the scleral canal was greatest in magnitude, occurred most frequently among the 8 EG eyes, and was preferential to the superior and inferior quadrants.
- Third, the magnitude of optic nerve expansion correlated to the post-mortem optic nerve axon injury grade.

EG eye expansions of the neurovascular canal and contained optic nerve (Figure 4.1.) were present in all 8 animals. Five of 8 EG eyes demonstrated BMO radius expansion, 7 of 8 EG eyes demonstrated ASCO radius expansion and PSCO radius expansion was detected in 6 of the 7 EG eyes in which it could be measured. Chauhan et al (Chauhan et al., 2002), using the hypertonic saline model, was the first to document sequential and progressive ONH surface "cupping" as well as probable BMO and scleral canal expansion by in vivo confocal scanning laser tomography 12 (CSLT) in the rat EG model. However, CSLT alterations in the ONH neural canal opening were only detected after significant elevations of IOP and in association with loss of over 55% of the axons. In that study, it is not clear if BMO or the ASCO was being measured within the CSLT data sets because the nature of what is seen as the "disc margin" in clinical photographs and CSLT images of rat eyes has not yet been determined (Reis et al., 2012a; Reis et al., 2012b; Strouthidis et al., 2010; Strouthidis et al., 2009). Guo et al, (Guo et al., 2005) using en-face in-vivo Optical Coherence Tomography (OCT), reported progressive expansion of the optic disc area and a progressive ASCO expansion in 18 Dark Agouti EG rats. However, in their study, OCT visualization of BM, BMO, the anterior scleral surface and the ASCO were not clearly documented relative to one another.

Our post-mortem data clarify these findings by detecting neurovascular canal expansion at the level of BMO and the sclera (ASCO and PSCO) early in the optic neuropathy of chronic IOP elevation in the rat eye. We observed significant changes in ASCO in EG eyes with optic nerve injury grades of 2 through 3.28 which equate to estimated axonal loss from 15 to 34%- using the Morrison conversion scale (Jia et al., 2000; Morrison et al., 2005).

Our data further suggest radial optic nerve expansion within the neurovascular scleral canal and suggest the magnitude of expansion correlates to orbital optic nerve injury. These findings are important because the detection of longitudinal change in the diameter of the optic nerve within the neurovascular scleral canal may become an achievable OCT imaging target as this technology is applied to the rodent eye (Fortune et al., 2011; Guo L. et al., 2005; Nagata et al., 2009; Zhang et al., 2011). EG eyes also demonstrated significantly larger increases in ONASCO and ON-PSCO Radius in the superior and inferior regions, significant ON-ASCO H/V diameter ratio reduction and animal-specific changes in the ASCO-ON-ASCO gap distance that most frequently occurred in the superior and inferior quadrants. Taken to-

gether these findings suggest preferential optic nerve expansion within the vertical compared to the horizontal axes. These findings may be manifestations of, or contribute, to the mechanisms which underlie, previously reported, preferential superior susceptibility to ONH axonal damage in the rat eye (Dai et al., 2012; Huang and Knighton, 2009; Li et al., 2015; Morrison, 2005; Morrison et al., 1997; WoldeMussie et al., 2001).

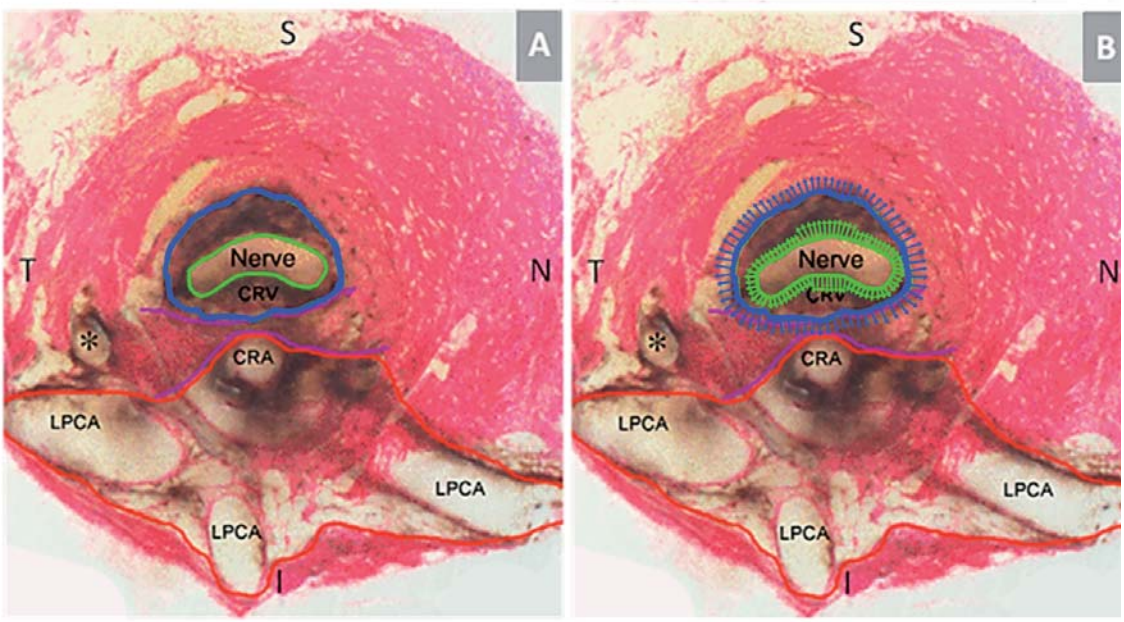

Fig. 4.1. Principal Scleral Openings in the Normal Control Rat Eye (A) and a Schematic Overlay of Optic Nerve and Surrounding Neurovascular Scleral Canal Expansion in Early Experimental Glaucoma (EG). (A) Unlike the primate, there are two principal openings within the sclera of the rat ONH: 1) the superior neurovascular canal (outlined in blue) which contains the optic nerve (green) and the central retinal vein (CRV) which both pass within a vascular plexus (brown pigment) that is continuous with the choroid (not shown); and 2) the more inferior arterial opening (outlined in red), which is irregular and contains the central retinal artery (CRA) and the densely packed choroidal branches of the Long Posterior Ciliary Arteries (LPCAs). The two canals are separated by the scleral sling (purple).. (B) Rat optic nerve expansion (green arrows) occurs early in the rat ONH response to chronic experimental IOP elevation and is accompanied by expansion of the surrounding neurovascular scleral canal (blue arrows) that is both more frequent and of greater magnitude within the superior and inferior quadrants. Each arrow represents the magnitude of quadrant change magnified 3 times. S-superior, I – Inferior, N – Nasal, T – Temporal. (*) Identifies a branch of a LPCA.

EG eye optic nerve expansion may be a manifestation of edema, cell proliferation, remodeling and/or synthesis of "laminar-like" connective tissue (Johnson et al., 1996). In a separate study of rat early EG eyes, swollen axons have been noted within the ONH, filled with vesicular material consistent with both axon transport obstruction and axonal degeneration (Morrison et al., 1997). More recently, genomic studies have demonstrated mRNA alterations compatible with cell proliferation pathways at the same stage of damage (Howell et al., 2011;

Johnson et al., 2011; Johnson et al., 2007). We have previously reported thickening of the lamina cribrosa and profound connective tissue remodeling at a similar early stage of monkey EG (Burgoyne, 2015b; Burgoyne et al., 2014; Yang et al., 2007b; Yang et al., 2011b) (Stowell C, et al. IOVS 2014;55:ARVO E-Abstract 5034).

In the primate, the peripapillary sclera and scleral canal wall connective tissues are thought to govern the distribution of IOP-related stress within the lamina cribrosa connective tissues (Burgoyne and Downs, 2008; Sigal, 2009; Sigal et al., 2009a, b). Thequestion of how the sclera transfers load to the rodent retinal ganglion cell axons and the astrocytes that span the nerve within the canal is of substantial biomechanical interest. Two recent papers have described the relationship between the radially arrayed, rat optic nerve head astrocytes, the optic nerve sheath (a continuation of the pia that merges with Bruch's Membrane at its opening and the vascular plexus that surrounds the nerve within the neurovascular canal, effectively isolating it from the sclera (Dai et al., 2012; Li et al., 2015). In the first of these articles (Dai et al., 2012), Dai and colleagues described a radial array of "fortified" astrocytes in the normal rat ONH, and early disinsertion of the superior astrocyte footplates from the pial sheath with subsequent loss of the astrocytes and eventual axon loss following 1 week of chronic IOP elevation. Their description of the vascular plexus that surrounds the optic nerve, (which is poorly visualized within our reconstructions due to its heavy pigmentation) suggests that it contains dense connective tissue septa. We suggest that if these septa directly or indirectly span the plexus to link the sheath and the sclera, they may be the means by which the sclera transfers IOP-related load to the radial ONH astrocytic array. It is possible that the inferior shift of the nerve within the canal demonstrated in 5 of the 8 EG eyes in this report, reflects damage to the superior vascular plexus connective tissue septa that both explains this shift and either contributes to or results from the processes that damage the underlying astrocyte footplates.

Previous studies in the monkey unilateral EG model (Burgoyne et al., 2004; Downs et al., 2007; Yang et al., 2007a; Yang et al., 2007b) have reported only small BMO area increases and only in a small subset of early EG eyes (Burgoyne et al., 2004; Downs et al., 2007; Yang et al., 2007a; Yang et al., 2007b). In the present study, global BMO radius expansion was present in 5 of the 8 animals and regional expansion was present in a subset of eyes. While the cumulative IOP insults to the rat and monkey BMO connective tissues should not be directly compared, the frequency of BMO expansion in early rat EG suggests that the rat BM connec-

tive tissues immediately adjacent to BMO may demonstrate less structural stiffness than those of the monkey either due to being less thick or more compliant or both.

The choroid was thinner in the EG (compared to the Control) eyes of 6 animals and thickerin 2 animals. Between-eye differences in choroidal thickness in our study eyes should be interpreted carefully because the study was not designed to test hypotheses about choroidal thickness and IOP was not manometrically controlled at the same level in the Control and EG eyes at the time of perfusion. The peripapillary choroid likely plays an important role in the rat ONH blood supply since it is continuous with the vascular plexus surrounding the optic nerve within the neurovascular scleral canal. In vivo, longitudinal choroidal thickness measurements at manometrically controlled pressures by OCT (Pierru et al., 2014; Wang and Zhang, 2014; Yiu et al., 2014) are required to detect longitudinal choroidal thickness changes in the rat EG models. Separate from thickness, choroidal blood flow measurements within these vessels may be son within the reach of a variety of OCT angiographic techniques (Baumann et al., 2011; Zhi et al., 2011; Zhi et al., 2012; Zotter et al., 2011).

Outward bowing of the peripapillary sclera was indirectly assessed in this study using two parameters - Scleral Depth and BMO Depth both of which measured relative to a peripheral scleral reference plane. Outward bowing of the peripapillary sclera relative to this more peripheral reference plane would be expected to manifest as an increase in both parameters if no other effects were present. Scleral Depth was increased in 4 and decreased in 1 EG eye, respectively. BMO Depth was significantly increased in 5 and decreased in 2 EG eyes. Direct longitudinal detection of posterior bowing of the peripapillary sclera by in-vivo SD-OCT or magnetic resonance (MRI) imaging in eyes carried to more advanced stages of IOP insult is required to confirm the significance of these findings (He et al., 2014; Heickell et al., 2001; Strouthidis et al., 2011a).

Finally, to date, there have been no rigorous descriptions of what constitutes a "glaucomatous" optic neuropathy in the rodent eye. In the monkey, we have argued that ONH surface "cupping" that does not include ONH connective tissue deformation and remodeling is a non-specific feature of all forms of RGC axonal injury and is not specific to chronic IOP elevation (Burgoyne, 2015a). From our findings in monkeys (Burgoyne, 2015b;

He et al., 2014; Strouthidis et al., 2011b) we have argued that the same features of the neuropathy should be present in human eyes and we are currently using OCT ONH imaging to describe these phenomena in glaucoma patients (Ren et al., 2014).

We propose that the rat ONH neural and connective tissue alterations described herein are core components of the neuropathy that occurs 4 weeks after the onset of chronic moderate experimental IOP elevation in the rat eye. Their presence should be sought and confirmed in all experimental models of "glaucomatous" optic neuropathy in the rat eye whether due to spontaneous (Goldblum and Mittag, 2002) or experimental chronic IOP elevation (Chauhan et al., 2002; Morrison et al., 2008; Morrison et al., 1997), ischemia (Naskar et al., 2002), endothelin (Chauhan et al., 2004; Murphy et al., 2010; Prasanna et al., 2011), or immune system manipulation (Joachim et al., 2013; Tezel and Wax, 2004; Wax et al., 2008).

Because there are, at present, no experimental models for the induction of a glaucomatous optic neuropathy in any species that do not depend upon chronic IOP elevation, such a model remains an important experimental target for glaucoma research. We propose that our findings should serve as phenotypic benchmarks for all future rat models of glaucomatous ONH injury that do (Chauhan et al., 2002; Goldblum and Mittag, 2002; Morrison, 2005; Morrisonvet al., 2008; Morrison et al., 1997; WoldeMussie et al., 2001) and do not (Chauhan et al., 2004;vNaskar et al., 2002; Prasanna et al., 2011; Tezel and Wax, 2004; Tseng et al., 2015; Votruba etval., 2003; Wax et al., 2008; WoldeMussie et al., 2001) involve spontaneous or experimental IOPelevation.

4.2.2. Limitations

The limitations of our method of 3-D reconstruction have been previously discussed (Burgoyne et al., 2004; Pazos et al., 2015) and include:

1. Anterior-to-posterior resolution limited to 1.5 mm
2. Hand application of the stain to the block face using a cotton-tipped swab providing the potential for substantial staining variation between section images;
3. Tissue shrinkage effects (both from fixation and embedding) which may be unique to the rat eye. While comparisons to our nonhuman primate (Burgoy-

ne et al., 2004; Downs et al., 2007; Yang et al., 2007a; Yang et al., 2007b; Yang et al., 2009b) publications may be similar (since fixation and post-tissue processing is similar), comparisons to other post-mortem or in-vivo measurements may be profoundly affected by these differences.

We intended to study rats with early damage which is why all animals were sacrificed after 4 weeks of IOP elevation. The statistical significance of many of the changes is likely dependent on this choice. While the ONH are "early" in terms of time (4 weeks since injection), the percent axon loss in the EG eyes of this study, (as estimated by the correlation between axon counts to axon damage injury grade correlations) (Morrison et al., 2005), were <5%, ≈10%, ≈18%, <20%, <22%, <35%, <35%, and ≈35%, respectively. These data suggest that the majority of EG eyes in this study were at an early to moderate stage of axon loss. Determination of the earliest ONH alterations in the rat EG model will be the subject of future reports. Characterization of maximum physiologic between eye differences (Yang et al., 2009a) (using bilateral normal animals) is ultimately required to be certain that the early EG eye differences we report exceed between eye-differences within bilaterally normal animals. Generalization of our findings to naïve normal eyes of all ages, strain and lighting conditions should not be assumed.

The animals in this study were sacrificed using sodium nitroprusside which is a potent vasodilator that is commonly given to improve the removal of blood from the ONH vasculature during perfusion fixation. While it is unlikely that our finding of EG eye scleral canal expansión was influenced by vasodilation, it is conceivable that the optic nerve blood vessels in the EG eyes were preferentially influenced by the nitroprusside and a portion or all of the optic nerve

expansion was on this basis. Certainly, as deep optic nerve head imaging improves in the rat experimental glaucoma models, longitudinal detection of scleral canal expansion as well as optic nerve expansion within the scleral canal should be confirmed using these techniques. However, we do not believe that preferential optic nerve swelling in the EG eye is the most likely explanation for our optic nerve findings for the following reasons. First, we would expect that the peri-neural vascular plexus would di-

late more than the smaller vessels in the optic nerve and this would have the net effect of compressing rather than expanding the nerve within the scleral canal. Second, the genomic studies mentioned above, have demonstrated significant increases in DNA content and mRNA alterations compatible with cell proliferation pathways and inflammation at the same stage of damage (Howell et al., 2011; Johnson et al., 2011; Johnson et al., 2007). We believe thathese processes, alone, likely underlie optic nerve enlargement in the EG eye.

4.3.Future work

As we have seen in the ONH biomechanics section of this dissertation, finite element modeling requires accurate geometry (architecture) and material properties of the tissue being modeled as well as in vivo or ex vivo information about its performance under various forms of loading.

The output of these finite element models will be eye-specific engineering stress and strain at the full spectrum physiologic and pathophysiologic IOP. Models of rat eyes will eventually inform 3D Cell cultures of rat ONH astrocytes and scleral fibroblasts to characterize their genomic and proteomic response to model-predicted alterations in their biomechanical environment.

It will be the engineering levels of stress and strain at given levels of IOP, which will provide the first level of comparison between the mouse, rat, monkey and human eye. Then the genomic and proteomic responses in Young and old eyes will be compared. Separately performed acute IOP elevations experiments (which are underway in mice and rats in several laboratories) will be used to assess and compare axonal susceptibility and recobery in young and old animals.

The strategies for digitally reconstructing, visualizing and quantifying the ONH tissues presented herein are the first steps of the process. These papers are intended to lay the foundation for all the work that will follow.

5

Conclusions

5.1. Rat Optic Nerve Head Anatomy within 3D histomorphometric reconstructions of normal control eyes

In summary, we have performed the first 3D characterization of the macroscopic and microscopic ONH anatomy of the rat eye:

1. Our study is the first to describe the rat ONH as consisting of two scleral openings and clarify that the CRA does not accompany the CRV within the neurovascular canal, but passes through a separate, large, irregular opening, inferior to it, accompanied by the LPCAs and their dense intra-scleral branches.

2. Our findings confirm the presence of a vascular plexus that is continuous from the choroid to the optic nerve sheathes and surrounds the optic nerve within the neurovascular canal.

3. We describe an anatomic proximity between the RGC axon bundles and a prominent extension of BM superiorly that is unique to that region.

These data suggest that the rat ONH is remarkably different from the primate ONH. We propose that similar studies are now needed in the mouse and that inter-species differences will provide new insights into ONH susceptibility to glaucomatous damage in each species.

5.2. Expansions of the neurovascular scleral canal and contained optic nerve occur early in the hypertonic saline rat experimental glaucoma model

In summary, we have performed the first 3D histomorphometric study of early alterations to the rat ONH following chronic experimental IOP elevation. Our findings suggest that radial expansion of the ONH connective tissue openings in Bruch's Membrane and the sclera, as suggested by previous studies (Chauhan et al., 2002; Guo et al., 2005), accompanied by preferential superior and inferior radial expansion of the optic nerve within the scleral canal are early components of the optic neuropathy of chronic experimental IOP elevation in the rat eye.

6

References

- Abramson, D.H., et al. Optic nerve tissue shrinkage during pathologic processing after enucleation for retinoblastoma. Arch. Ophthalmol. 2003. 121, 73-75.

- Ahmed, F., Brown, K.M., Stephan, D.A., Morrison, J.C., Johnson, E.C. and Tomarev, S.I. Microarray analysis of changes in mRNA levels in the rat retina after experimental elevation of intraocular pressure. Invest. Ophthalmol. Vis. Sci., 2004. 45(4): 1247–1258.

- AGIS investigators. The Advanced Glaucoma Intervention Study (AGIS): 7. The relationship between control of intraocular pressure and visual field deterioration. Am J Ophthalmol 200; 130(4):429-440.

- Ahn J. K., Park K. H. Morphometric change analysis of the optic nerve head in unilateral disk hemorrhage cases. Am J Ophthalmol, 2002. 134, 920-922.

- Airaksinen P. J., Tuulonen A., Alanko H. I. Rate and pattern of neuroretinal rim area decrease in ocular hypertension and glaucoma. Arch Ophthalmol, 1992. 110, 206-210.

- Airaksinen P. J., Tuulonen. Early glaucoma changes in patients with and without an optic disc haemorrhage. Acta Ophthalmol (Copenh), 1984. 62, 197-202.

- Alamouti B, Funk J. Retinal thickness decreases with age: an OCT study. Br J Opthahlmol 2003;87:899.

- Albon J., Karwatowski W. S., Avery N., Easty D. L., Duance V. C. Changes in the collagenous matrix of the aging human lamina cribrosa. Br J Ophthalmol, 1995. 79, 368-375.

- Albon J, et al. Connective tissue structure of the tree shrew optic nerve and associated ageing ghanges. Invest Ophthalmol Vis Sci, 2007; 48:2134-2144.

- Anderson DR, Hendrickson A. Effect of intraocular pressure on rapid axoplasmic transport in monkey optic nerve. Invest Ophthalmol. 1974; 13:771–83. [PubMed: 4137635]

- Anderson DR, Hoyt WF, Hogan MJ. The fine structure of the astroglia in the human optic nerve and optic nerve head. Trans Am Opthalmol Soc 1967; 65:275.

- Anderson DR. Ultrastructure of the optic nerve head. Arch Ophthalmol 1970; 83:63.

- Anderson DR, Hoyt WF. Ultrastructure of intraorbital portion of human and monkey optic nerve. Arch Ophthalmol 1969a; 82:506.

- Anderson DR. Ultrastructure of the human and monkey lamina cribrosa and optic nerve head. Arch Ophthalmol 1969b; 82:800.

- Anton A., et al. Prevalence of primary open-angle glaucoma in a Spanish population: the Segovia study. J Glaucoma, 2004. 13, 371-376.

- Armaly M. F. On the Distribution of Applanation Pressure. I. Statistical Features and the Effect of Age, Sex, and Family History of Glaucoma. Arch Opthalmol, 1965. 73, 11-18.

- Asai T, Katsumori N, Mizokami K. Retinal ganglion cell damage in human glaucoma. 2. Studies on damage pattern. Nippon Ganka Gakkai Zasshi 1987;91:1204–1213. [PubMed: 3448905]

- Bakalash S., Shlomo G. B., Aloni E., Shaked I., Wheeler L., Ofri R., Schwartz M. T-cell based vaccination for morphological and functional neuroprotection in a

rat model of chronically elevated intraocular pressure. J Mol Med (Berl), 2005. 83, 904-916.

- Barkan O. Glaucoma: classification, causes, and surgical control. Results of microgonioscopic research. Am J Ophthalmol, 1938; 2:1099-114.

- Baumann B et al. Total retinal blood flow measurement with ultrahigh speed swept source/Fourier domain OCT. Biomed Opt Express 2011. 2, 1359-1552.

- Bellezza A. J., Rintalan C. J., Thompson H. W., Downs J. C., Hart R. T., Burgoyne C. F. Deformation of the lamina cribrosa and anterior scleral canal wall in early experimental glaucoma. Invest Ophthalmol Vis Sci, 2003. 44, 623-637.

- Bellezza A. J., Hart R. T., Burgoyne C. F. The optic nerve head as a biomechanical structure: initial finite element modeling. Invest Ophthalmol Vis Sci, 2000. 41, 2991-3000.

- Bengtsson BO. Incidence of manifest glaucoma. Br J Ophthalmol, 1989. 73(7):483-7.

- Bonomi L., Marchini G., Marraffa M., et al. Prevalence of glaucoma and intraocular pressure distribution in a defined population. The Egna-Neumarkt Study. Ophthalmology, 1998. 105, 209-215.

- Brandt JD, Beiser JA, Kass MA, Gordon MO and the OHTS Group. Central Corneal Thickness in the Ocular Hypertension Treatment Study (OHTS). Ophthalmology 2001; 108:1779-1788.

- Brandt J. D. Central corneal thickness--tonometry artifact, or something more? Ophthalmology, 114, 2007. 1963-1964.

- Bron AJ, Tripathi RC, Tripathi BJ. Wolff's anatomy of the eye and orbit. Eight ed. 1997. London: Chapman and Hall Medical.

- Buckingham B. P. et al. Progressive ganglion cell degeneration precedes neuronal loss in a mouse model of glaucoma. J Neurosci, 2008. 28, 2735-2744.

- Burgoyne C. F., Downs J. C., Bellezza A. J., Suh J. K., Hart R. T.. The optic nerve head as a biomechanical structure: a new paradigm for understanding the role of IOP-related stress and strain in the pathophysiology of glaucomatous optic nerve head damage. Prog Retin Eye Res, 2005, 24,39-73.

- Burgoyne CF, et al. Three-dimensional reconstruction of normal and early glaucoma monkey optic nerve head connective tissues. Invest Ophthalmol Vis Sci. 45: 2004, 4388-4399.

- Burgoyne, C.F., Downs, J.C.Premise and prediction-how optic nerve head biomechanics underlies the susceptibility and clinical behavior of the aged optic nerve head. J. Glaucoma 2008. 17, 318-328.

- Burgoyne CF. The morphological difference between glaucoma and other optic neuropathies. J. Neuroophthalmol. 35 (Suppl.1), 2015, S8-S21.

- Burgoyne CF. The non-human- primate experimental glaucoma model, Exp Eye Res. 141, 2015, 57-73.

- Burgoyne CF et al. Non-Human primate Optic Nerve Head Proteomic Change in Early Experimental Glucoma. ARVO Meeting Abstracts 2014. 55, ARVO Abstract #4555.

- Burgoyne CF, Morrison JC: The anatomy and pathophysiology of the optic nerve head in glaucoma. J Glaucoma 2001, 10:S16-S18

- Burgoyne CF. A Biomechanical Paradigm for Axonal Insult Within the Optic Nerve Head. Exp Eye Res. 2011 Aug; 93(2): 120–132.

- Caprioli J., Spaeth G. L. Comparison of the optic nerve head in high- and low-tension glaucoma. Arch Ophthalmol, 1985. 103, 1145-1149.

- Cartwright M. J., Anderson D. R. Correlation of asymmetric damage with asymmetric intraocular pressure in normal-tension glaucoma (low-tension glaucoma). Arch Ophthalmol, 1988. 106, 898-900.

- Casson RJ, Childow G, Wood J et al. Definition of glaucoma: clinical and experimental concepts. Clin& Exp Opthalmol, 2012. 40(5):341-349.

- Chauhan BC and Burgoyne CF. From Clinical Examination of the Optic Disc to Clinical Assessment of the Optic Nerve Head: A Paradigm Change. Am J Ophthalmol. 2013 August; 156 (2):218-227.

- Chauhan, B.C., et al., 2013. Enhanced detection of open-angle glaucoma with an anatomically accurate optical coherence tomography-derived neuroretinal rim parameter. Ophthalmology 120, 535-543.

- Chauhan B.C., et al., Effect of intraocular pressure on optic disc topography, electroretinography, and axonal loss in a chronic pressure-induced rat model of optic nerve damage, *Investig. Ophthalmol. Vis. Sci.* 43, 2002, 2969–2976.

- Chihara E et al. Severe myopia as a risk factor for progressive visual field loss in primary open-angle glaucoma. Opthhalmologica 1997; 211:66.

- CNTGS. Comparison of glaucomatous progression between untreated patients with normal-tension glaucoma and patients with therapeutically reduced intraocular pressures. Collaborative Normal-Tension Glaucoma Study Group. Am J Ophthalmol, 1998; 126, 487-497.

- Coffey M., Reidy A., Wormald R. P. L., Wu J. X., Wright L. A., Courtney P. Prevalence of glaucoma in the west of Ireland (1993) . Br J Ophthalmol, 77, 17-21.

- Congdon N. G., Broman A. T., Bandeen-Roche K., Grover D., Quigley H. A. Central corneal thickness and corneal hysteresis associated with glaucoma damage. Am J Ophthalmol, 2006. 141, 868-875.

- Crichton A., Drance S. M., Douglas G. R., Schulzer M. Unequal intraocular pressure and its relation to asymmetric visual field defects in low-tension glaucoma. Ophthalmology, 1989. 96, 1312-1314.

- Dai, C., et al., 2012. Structural basis of glaucoma: the fortified astrocytes of the optic nerve head are the target of raised intraocular pressure. Glia 60, 13-28.

- Daubs JG, Crick RP. Effect of refractive error on the risk of ocular hypertension and open-angle glaucoma. Trans Opthalmol Soc UK 1921; 101:121.

- De Moraes C. G., et al. Risk factors for visual field progression in treated glaucoma. Arch Ophthalmol, 2011. 129, 562-568.

- Dielemans I., Vingerling J. R., Wolfs R. C., et al. The prevalence of primary open-angle glaucoma in a population-based study in The Netherlands. The Rotterdam Study. Ophthalmology, 1994. 101, 1851-1855.

- Dolman CL, McCormick, Drance SM. Aging of the optic nerve. Arch Ophthalmol 1980;98:2053.

- Douglas G. R., Drance S. M., Schulzer M. The visual field and nerve head in angle-closureglaucoma. A comparison of the effects of acute and chronic angle closure. Arch Ophthalmol, 1975. 93,409-411.

- Downs JC et al. Three-dimensional histomorphometry of the normal and early glaucomatous monkey optic nerve head: neural canal and subarachnoid space architecture. Invest Ophthalmol Vis Sci. 48, 2007, 3195-3208.

- Downs JC, Roberts MD and Sigal IA. Glaucomatous cupping of the lamina cribrosa. A review of the evidence for active progressive remodeling as a mechanism. Exp Eye Res. 2011; 93(2):133-150.

- Downs J. C., Roberts M. D., Burgoyne C. F. Mechanical environment of the optic nerve head in glaucoma. Optom Vis Sci, 2008. 85, 425-435.

- Downs J. C., Blidner R. A., Bellezza A. J., Thompson H. W., Hart R. T., Burgoyne C. F. Peripapillary scleral thickness in perfusion-fixed normal monkey eyes. Invest Ophthalmol Vis Sci, 2002. 43, 2229-2235.

- Downs J. C., Ensor M. E., Bellezza A. J., Thompson H. W., Hart R. T., Burgoyne C. F. Posterior Scleral Thickness in Perfusion-Fixed Normal and Early-Glaucoma Monkey Eyes. Invest Ophthalmol Vis Sci, 2001. 42, 3202-3208.

- Drance S, Anderson DR, Schulzer M. Risk factors for progression of visual field abnormalities in normal-tension glaucoma. Am J Ophthalmol 2001;131:699.

- Drance SM et al. The importance of disc hemorrhage in the prognosis of chronic open-angle glaucoma 1977;95:226.

- Ehlers N. On corneal thickness and intraocular pressure. II. A clinical study on the thickness of the corneal stroma in glaucomatous eyes. Acta Ophthalmol (Copenh), 1970. 48, 1107-1112.

- Elkington A. The structure of the lamina cribrosa in normal and glaucomatous human eyes. Trans Am Acad Ophthalmol otolaryngol 1974, 78, OP290-97.

- Emery JM, Landis D, Paton D, Boniuk M, Craig JM. The lamina cribrosa in normal and glaucomatous human eyes. Trans Am Acad Ophthalmol otolaryngol. 1974, 78, OP290-97.

- Flammer J., Pache M., Resink T. Vasospasm, its role in the pathogenesis of diseases with particular reference to the eye. Prog Retin Eye Res,2001. 20, 319-349.

- Fong DS, Epstein DL, Allingham RR. Glaucoma and myopia: are they related? Int Ophthalmol Clin 1990; 30:215.

- Fontana L., Poinoosawmy D., Bunce C. V., O'Brien C., Hitchings R. A. Pulsatile ocular blood flow investigation in asymmetric normal tension glaucoma and normal subjects. Br J Ophthalmol, 1998. 82, 731-736.

- Fortune B, et al. Deformation of the rodent optic nerve head and peripapillary structures during acute intraocular pressure elevation. Invest Ophthalmol Vis Sci. 2011. 52, 6651-6661.

- Fortune, B., Bui, B.V., Morrison, J.C., Johnson, E.C., Dong, J., Cepurna, W.O., Jia, L., Barber, S. and Cioffi, G.A. Selective ganglion cell functional loss in rats with experimental glaucoma. Invest. Ophthalmol. Vis. Sci., 2004. 45(6):1854–1862.

- Fujita, Y., et al. Comparative study of the lamina cribrosa and the pial septa in the vertebrate optic nerve and their relationship to the myelinated axons. Tissue Cell. . 2000. 32, 293-301

- Gaasterland D., Tanishima T., Kuwabara T. Axoplasmic flow during chronic experimental glaucoma. 1. Light and electron microscopic studies of the monkey optic nerve head during development of glaucomatous cupping. Invest Ophthalmol Vis Sci, 1978. 17, 838-846.

- Garcia-Valenzuela E, Shareef S, Walsh J, et al. Programmed cell death of retinal ganglion cells during experimental glaucoma. Exp Eye Res 1995;61:33–44. [PubMed: 7556468]

- Geijssen H. C., Greve E. L. (1987) The spectrum of primary open angle glaucoma. I: Senile sclerotic glaucoma versus high tension glaucoma. Ophthalmic Surg, 1987. 18, 207-213.

- Goldblum D and Mittag T. Prospects for relevant glaucoma models with retinal ganglion cell damage in the rodent eye. Vis. Res. 2002. 42, 471-478.

- Gordon MO et al. The Ocular Hypertension Treatment Study: baseline factors that predict the onset of primary open angle glaucoma. Arch Ophthalmol, 2002. 120: 714.

- Gordon M. O. et al. Validated prediction model for the development of primary open-angle glaucoma in individuals with ocular hypertension. Ophthalmology, 2007. 114, 10-19.

- Graham S. L., Drance S. M. Nocturnal hypotension: role in glaucoma progression. Surv Ophthalmol, 1999. 43 Suppl 1, S10-16.

- Graham S. L., et al. Ambulatory blood pressure monitoring in glaucoma. The nocturnal dip. Ophthalmology, 1995. 102, 61-69.

- Grodum K., Heijl A., Bengtsson B. Risk of glaucoma in ocular hypertension with and without pseudoexfoliation. Ophthalmology, 2005. 112, 386-390.

- Guo B and Yuan Y. A comparative review of methods comparing means using partially paired data. Stat Methods Med Res, 2015.

- Guo, L., et al.. En face optical coherence tomography: a new method to analyse structural changes of the optic nerve head in rat glaucoma. Br. J. Ophthalmol, 2005. 89, 1210-1216.

- Hare W., et al. Electrophysiological and histological measures of retinal injury in chronic ocular hypertensive monkeys. Eur J Ophthalmol, 2001; 9 Suppl 1, S30-33.

- Hayreh SS. The blood supply of the opric nerve head and the evaluation of it-myth and reality. Prog Retin Eye Res 2001; 20:563.

- Hayreh SS. Anatomy and physiology of the optic nerve head. Trans am Acad Ophthalmol Otorinolaryngol 1974; 78: OP240

- Hayreh S. S., Zimmerman M. B., Podhajsky P., Alward W. L. Nocturnal arterial hypotension and its role in optic nerve head and ocular ischemic disorders. Am J Ophthalmol, 1994. 117, 603-624.

- He L et al. Longitudinal detection of optic nerve head changes by spectral domain optical coherence tomography in early experimental glaucoma. Invest Ophthalmol Vis Sci, 2014. 55, 574-586.

- Heickell AG et al. Optic disc surface compliance testing using confocal scanning laser tomography in the normal monkey eye. J.Glaucoma, 2001. 10, 369-382.

- Heijl A., Leske M. C., Bengtsson B., et al. Reduction of intraocular pressure and glaucoma progression: results from the Early Manifest Glaucoma Trial. Arch Ophthalmol, 2002. 120, 1268-1279.

- Hendricx KH et al. Cumulative incidence of patients with disc hemorrhages in glaucoma and the effect of therapy. Opthhalmology 1994;101:1165.

- Hernandez MR. The optic nerve head in glaucoma: role of astrocytes in tissue remodeling. Prog Retin Eye Res 2000; 19:297.

- Hernandez MR, Luo XX, Andrzejewska W, et al. Age-related changes in the extracellular matrix of the human optic nerve head. Am J Ophthalmol 1989;107:476.

- Hernandez MR. Ultrastructural immunocytochemical analysis of elastin in the human lamina cribrosa: changes in elastic fibers in primary open-angle glaucoma. Invest Opthhalmol Vis Sci 1992; 33:2891.

- Hernandez, M.R., Andrzejewska, W.M. and Neufeld, A.H. Changes in the extracellular matrix of the human optic nerve head in primary open-angle glaucoma. Am. J. Ophthalmol., 1990. 109(2): 180–188.

- Herndon L. W., Weizer J. S., Stinnett S. S. Central corneal thickness as a risk factor for advanced glaucoma damage. Arch Ophthalmol, 2004. 122, 17-21.

- Herschler J and Osher RH. Baring of the circumlinear vessel an early sign of optic nerve damage. Arch Ophthalmol 1980; 98:865.

- Hirata A, Kitaoka T, Ishigooka H, et al. Cytochemical studies of transitional area between retina and optic nerve. Acta Opthalmol (Copenh) 1991; 69-71.

- Hitchings R. A., Spaeth G. L. The optic disc in glaucoma. I: Classification. Br J Ophthalmol, 1976. 60, 778-785.

- Hitchings R. A., Spaeth G. L. Fluorescein angiography in chronic simple and low-tension glaucoma. Br J Ophthalmol, 1977. 61, 126-132.

- Hogan MJ, Alvarado JA, Weldell JE. Histology of the Human Eye. Philadelphia: Saunders; 1971. P.523-606.

- Hong S., Kim C. Y., Seong G. J., Hong Y. J. Central corneal thickness and visual field progression in patients with chronic primary angle-closure glaucoma with low intraocular pressure. Am J Ophthalmol, 2007. 143, 362-363.

- Howell GR et al. Molecular clustering identifies complement and endothelin induction as early events in a mouse model of glaucoma, J. Clin. Investig. 121, 2011, 1429-1444.

- Howell, G.R., et al., Axons of retinal ganglion cells are insulted in the optic nerve early in DBA/2J glaucoma. J. Cell. Biol. 2007. 179, 1523e1537.

- Huang XR and Knighton RW. Altered F-actin distribution in retinal nerve fiber layer of a rat model of glaucoma. 2009. Exp Eye Res. 88, 1107-1114.

- Hu Z, Abramoff MD, Kwon YH, Lee K, Garvin MK. Automated segmentation of neural canal opening and optic cup in 3D spectral optical coherence tomography volumes of the optic nerve head. Invest Ophthalmol Vis Sci. 2010; 51(11):5708–5717. [PubMed: 20554616]

- Ishida K., Yamamoto T., Sugiyama K., Kitazawa Y. Disk hemorrhage is a significantly negative prognostic factor in normal-tension glaucoma. Am J Ophthalmol, 2000. 129, 707-714.

- Iwase A, Suzuki Y, Araie M et al. The prevalence of primary open-angle glaucoma in Japanese: the Tajimi Study. Ophthalmology, 2004:1641-1648.

- Jaffe G. J., Caprioli J. Optical coherence tomography to detect and manage retinal disease and glaucoma. Am J Ophthalmol, 2004. 137, 156-169.

- Janssen P, Naskar R, Moore S, et al. Evidence for glaucoma-induced horizontal cell alterations in the human retina. Ger J Ophthalmol 1996;5:378–385. [PubMed: 9479522]

- Jay J. L., Murdoch J. R. The rate of visual field loss in untreated primary open angle glaucoma. Br J Ophthalmol, 1993. 77, 176-178.

- Jia L et al. Ptterns of intraocular pressure elevation after aqueous humor outflow obstruction in rats. Invest Ophthalmol Vis Sci, 2000, 1380-1385.

- Joachim SC et al. Immune response against ocular tissues after immunization with optic nerve antigens in a model of autoimmune glaucoma. Mol Vis, 2013. 19, 1804-1814.

- Johansson, J.O.. The lamina cribrosa in the eyes of rats, hamsters, gerbils and guinea pigs. Acta Anat. (Basel), 1987. 128, 55-62.

- John SW, Smith RS, Savinova OV, Hawes NL, Chang B, Turnbull D, Davisson M, Roderick TH, Heckenlively JR. Essential iris atrophy, pigment dispersion, and glaucoma in DBA/2J mice. Invest Ophthalmol Vis Sci. 1998; 39(6):951–62. [PubMed: 9579474]

- Johnson, E.C., et al. The effect of chronically elevated intraocular pressure on the rat optic nerve head extracellular matrix. Exp Eye Res. 1996. 62, 663-674.

- Johnson EC et al. Cell proliferation and interleukin-6-type cytokine signaling are implicated by gene expression responses in early optic nerve head injury in rat glaucoma. Invest Ophthalmol Vis Sci, 52, 2011, 504-518.

- Johnson, T.V., Tomarev, S.I., 2010. Rodent models of glaucoma. Brain Res. Bull. 81,349-358.

- Johnson EC et al. Global changes in optic nerve head gene expression after exposure to elevated intraocular pressure in a rat glaucoma mode. Invest Ophthalmol Vis Sci. 48, 2007, 3161-3177.

- Jonas J, Gusek G, Naumann G. Optic disc, cup and neuroretinal rim size, configuration and correlations in normal eyes. Invest Ophthalmol Vis Sci 1988; 29:1151-1158

- Jonas J, Schmidt A, muller-Berght J, Schlotzer-Schrehardt U, Nauman G. Human optic nerve fiber count and optic disc size. Invest Ophthalmol Vis Sci 1992; 33:2012-2018.

- Jonas J. B., Stroux A., Velten I., Juenemann A., Martus P., Budde W. M. Central corneal thickness correlated with glaucoma damage and rate of progression. Invest Ophthalmol Vis Sci, 2005. 46, 1269-1274.

- Jonas JB, Schmidt AM, Muller-Bergh JA, et al. Optic nerve fiber count and diameter of the retrobulbar optic nerve in normal and glaucomatous eyes. Graefes Arch Clin Exp Ophthalmol 1995; 233:421.

- Jonas J. B., Fernandez M. C., Sturmer J. Pattern of glaucomatous neuroretinal rim loss. Ophthalmology, 1993. 100, 63-68.

- Jonas J. B., et al. Predictive factors of the optic nerve head for development or progression of glaucomatous visual field loss. Invest Ophthalmol Vis Sci, 2004. 45, 2613-2618.

- Jonas JB and Xu L. Optic disk hemorrhages in glaucoma. Am J Ophthalmol 1994ab;118:1.

- Jonas JB, Schiro D. Localised wedge shaped defects of the retinal nerve fiber layer in glaucoma. Br J Ophthalmol 1994; 78:285.

- Kahn H. A., Leibowitz H. M., Ganley J. P., Kini M. M., Colton T., Nickerson R. S., Dawber T. R.. The Framingham Eye Study. I. Outline and major prevalence findings. Am J Epidemiol,1977: 106, 17-32.

- Kass MA, Heuer DK, Higginbotham EJ et al. The Ocular Hypertension Treatment Study: a randomized trial determines that ocular hypotensive medication delays or prevents the onset of primary open-angle glaucoma. Arch Opthalmol, 2002. 120(6):701-713.

- Kendell KR, Quigley HA, Kerrigan LA, et al. Primary open-angle glaucoma is not associated with photoreceptor loss. Invest Ophthalmol Vis Sci 1995;36:200–205. [PubMed: 7822147]

- Kerr J., Nelson P., O'Brien C. Pulsatile ocular blood flow in primary open-angle glaucoma and ocular hypertension. Am J Ophthalmol, 2003. 136, 1106-1113.

- Kerrigan LA et al. TUNEL-positive ganglion cells in human primary open-angle glaucoma. Arch Ophthalmol 1997, 115:1031.

- Kim GY et al. Analysis of peripapillary atrophy according to the optic disc shape using spectral- domain OCT. J Korean Ophthalmol Soc 2013; 54(11)Ñ1748-1756.

- Klein B. E., Klein R., Linton K. L. Intraocular pressure in an American community. The Beaver Dam Eye Study. Invest Ophthalmol Vis Sci, 1992: 33, 2224-2228.

- Klein B. E., Klein R., Lee K. E., Hoyer C. J. Does the intraocular pressure effect on optic disc cupping differ by age? Trans Am Ophthalmol Soc, 2006. 104, 143-148.

- Ko MK, Kim DS, Ahn YK. Morphological variations of the peripapillary circle of Zinn-Haller by flat section. Br J Opthhalmol 1999; 83:562.

- Ko M. L., Hu D. N., Ritch R., Sharma S. C. (2000) The combined effect of brain-derived neurotrophic factor and a free radical scavenger in experimental glaucoma. Invest Ophthalmol Vis Sci, 2000. 41, 2967-2971.

- Kong, Y.X., et al. Functional changes in the retina during and after acute intraocular pressure elevation in mice. Invest Ophthalmol Vis Sci, 2009. 50, 5732-5740.

- Le A, et al. Risk factors associated with the incidence of open-angle glaucoma: the visual impairment project. Invest Ophthalmol Vis Sci 2003;44:3783.

- Levkovitch-Verbin H, Quigley HA, Martin KR, Valenta D, Baumrind LA, Pease ME. Translimbal laser photocoagulation to the trabecular meshwork as a model of glaucoma in rats. Invest Ophthalmol Vis Sci. 2002; 43(2):402–10. [PubMed: 11818384]

- Lesk M. R., Hafez A. S., Descovich D. Relationship between central corneal thickness andchanges of optic nerve head topography and blood flow after intraocular pressure reduction in open-angle glaucoma and ocular hypertension. Arch Ophthalmol, 2006. 124, 1568-1572.

- Leske M. C., Heijl A., Hyman L., Bengtsson B., Dong L., Yang Z. Predictors of long-term progression in the early manifest glaucoma trial. Ophthalmology, 2007. 114, 1965-1972.

- Leske MC et al. Patterns of open-angle glaucoma in the Barbados Family Study. Ophthalmology, 2001. 108(6):1015-22.

- Leske MC et al. Factors for glaucoma progression and the effect of treatment: the Early Manifest Glaucoma Trial. Arch Opthalmol 2003; 121:48.

- Li J., Herndon L. W., Asrani S. G., Stinnett S., Allingham R. R. Clinical comparison of the Proview eye pressure monitor with the Goldmann applanation tonometer and the Tonopen. Arch Ophthalmol, 2004. 122, 1117-1121.

- Li Y., et al., An energy theory of glaucoma. *Glia* , 2015. 63, 1537–155

- Lieberman MF, Maumenee AE, Green WR. Histologic studies of the vasculature of the anterior optic nerve. Am J Opthalmol 1976; 82:405

- Mabuchi, F., et al., Optic nerve damage in experimental mouse ocular hypertension. Invest Ophthalmol. Vis. Sci. 2003. 44, 4321e4330.
- Mabuchi, F., et al., 2004. Regional optic nerve damage in experimental mouse glaucoma. Invest Ophthalmol. Vis. Sci. 45, 4352e4358.

- Magoon EH, Robb RM. Development of myelin in human optic nerve and tract: a light and electron microscopic study. Arch Ophthalmol 1981;99:655.

- May, C.A., 2008. Comparative anatomy of the optic nerve head and inner retina in non-primate animal models used for glaucoma research. Open Ophthalmol. J. 2, 94-101.

- Michelson G., Langhans M. J., Groh M. J. Perfusion of the juxtapapillary retina and the neuroretinal rim area in primary open angle glaucoma. J Glaucoma, 1996. 5, 91-98.

- Miglior S., et al. Predictive factors for open-angle glaucoma among patients with ocular hypertension in the European Glaucoma Prevention Study. Ophthalmology, 2007. 114, 3-9.

- Mikelberg FS, Drance SM, Shulzer M, et al. The normal human optic nerve: axon count and axon diameter distribution. Opthhalmology 1989;96:1325.

- Mikelberg FS, Yidegiline HM, White VA et al. Relation between optic nerve axon number and axon diameter to scleral canal area. Ophthalmology 1991;98:60.

- Minckler DS, McLean IW, Tso MO. Distribution of axonal and glial elements in the Rhesus optic nerve head studied by electron microscopy. Am J Ophthalmol 1976; 82:179.

- Minckler D. S., Bunt A. H., Johanson G. W. Orthograde and retrograde axoplasmic transport during acute ocular hypertension in the monkey. Invest Ophthalmol Vis Sci, 16, 1977. 426-441.

- Mitchell P, Wang JJ, Hourihan F. The relationship between glaucoma and pseudoexfoliation: the Blue Mountains Eye Study. Arch Ohthalmol 1999a; 117: 1319.

- Mitchell P et al. The relationship between glaucoma and myopia: the Blue Mountains Eye Study. Opthalmology 1999b, 106:2010.

- Mitchell P et al. Bias in self-reported family history and relationship to glaucoma: the Blue Mountains Eye Study. Ophthalmic Epidemiol 2002;9:333.

- Moore, C.G., Epley, D., Milne, S.T. and Morrison, J.C. Long-term non-invasive measurement of intraocular pressure in the rat eye. Curr. Eye Res.,1995. 14(8): 711–717.

- Moore, C.G., Johnson, E.C. and Morrison, J.C. Circadian rhythm of intraocular pressure in the rat. Curr. Eye Res., 1996. 15(2): 185–191.

- Moore, C.G., Milne, S.T. and Morrison, J.C. Noninvasive measurement of rat intraocular pressure with the Tono-Pen. Invest. Ophthalmol. Vis. Sci., 1993. 34(2): 363–369.

- Morgan WH, Yu DY, Alder VA, Cringle SJ, Cooper RL, House PH, Constable IJ: The correlation between cerebrospinal fluid pressure and retrolaminar tissue pressure. Invest Ophthalmol Vis Sci, 1998; 1419-1428.

- Morgan JE, Uchida H, Caprioli J: Retinal ganglion cell death in experimental glaucoma. Br J Ophthalmol, 2000. 84:303-310.

- Morgan JE, Tribble JR. Microbead models in glaucoma. Exp Eye Res 2015 (in press). DOI:10.1016/j.exer.2015.06.020.

- Morrison JC and Pollack IP, 2003. Glaucoma: Science and Practice. New York: Thieme. ISBN 0-86577-915-5. Chapter 8: Anatomy and Physiology of the optic Nerve.

- Morrison J. C., Dorman-Pease M. E., Dunkelberger G. R., Quigley H. A. Optic nerve head extracellular matrix in primary optic atrophy and experimental glaucoma. Arch Ophthalmol, 1990. 108, 1020-1024.

- Morrison, JC. Elevated intraocular pressure and optic nerve injury models in the rat. J Glaucoma. 2005. 14, 315-317.

- Morrison, J.C., et al. Understanding mechanisms of pressure-induced optic nerve damage. Prog Retin Eye Res. 2005. 24, 217-240.

- Morrison J.C, et al. Glaucoma drops control intraocular pressure and protect optic nerves in a rat model of glaucoma. Invest Ophthalmol Vis Sci; 39, 1998,526-531.

- Morrison JC, et al. Microvasculature of the rat optic nerve head. Invest Ophthalmol Vis Sci , 40, 1999, 1702-1709.

- Morrison, J.C., et al., 2011. Pathophysiology of human glaucomatous optic nerve damage: insights from rodent models of glaucoma. Exp. Eye Res. 2011, 93, 156-164.

- Morrison JC, Johnson EC and Cepurna WO. Rat models for glaucoma research. Prog. Brain Res. 2008. 173, 285-301.

- Morrison JC et al. A rat model of chronic pressure-induced optic nerve damage. 1997. Exp Eye Res 64, 1997, 85-96.

- Morrison JC et al. Modeling glaucoma in rats by sclerosing aqueous outflow pathways to elevate intraocular pressure. Exp Eye Res, 2015. In press. http://dx.doi.org/10.1016/j.exer.2015.05.012

- Mukesh BN, McCarty CA, Rait JL et al. Five-year incidence of open-angle glaucoma: the visual impairment Project. Ophthalmology, 2002. 109 (6):1047-51.

- Murphy JA et al. The role of endothelin-1 and its receptors in optic nerve head astrocyte proliferation. Br. J. Ophthalmol, 2010. 94, 1233-1238.

- Nagata A, et al. In vivo quantitative evaluation of the rat retinal nerve fiber leyer with optical coherence tomography. 2002. Invest Ophthalmol Vis Sci. 43, 2962-2968.

- Naskar R et al. Detection of early neuron degeneration and accompanying microglial responses in the retina of a rat model of glaucoma. Invest Ophthalmol Vis Sci, 2002. 43, 2962-2968.

- Nemesure B, Wu SY, Hennis A, et al. Corneal thickness and intraocular pressure in the Barbados eye studies. Arch Ophthalmol 2003; 121(2):240-244.

- Nemesure B et al. Analyses of reported family history of glaucoma: a preliminary investigation. The Barbados Eye Study Group. Ophthalmic Epiedmiol 1996; 3:135.

- Nicolela M. T., et al. Effect of moderate intraocular pressure changes on topographic measurements with confocal scanning laser tomography in patients with glaucoma. Arch Ophthalmol, 2006. 124, 633-640.

- Nicolela M. T., Drance S. M. Various glaucomatous optic nerve appearances: clinical correlations. Ophthalmology, 1996. 103, 640-649.

- Nicolela M. T., Walman B. E., Buckley A. R., Drance S. M. Various glaucomatous optic nerve appearances. A color Doppler imaging study of retrobulbar circulation. Ophthalmology, 1996b. 103, 1670-1679.

- Nicolela M. T., McCormick T. A., Drance S. M., Ferrier S. N., LeBlanc R. P., Chauhan B. C. Visual field and optic disc progression in patients with different types of optic disc damage: a longitudinal prospective study. Ophthalmology, 2003. 110, 2178-2184.

- Nicolela M. T., Walman B. E., Buckley A. R., Drance S. M. Various glaucomatous optic nerve appearances. A color Doppler imaging study of retrobulbar circulation. Ophthalmology, 1996b. 103, 1670-1679.

- Nork TM, Ver Hoeve JN, Poulsen GL, et al. Swelling and loss of photoreceptors in chronic human and experimental glaucomas. Arch Ophthalmol 2000;118:235–245. [PubMed: 10676789]

- Norman, R.E., et al., 2010. Dimensions of the human sclera: thickness measurement and regional changes with axial length. Exp. Eye Res. 90, 277-284.

- Ogden T, Duggan J, Danley K, et al. Morphometry of nerve bundle pores in the optic nerve head of the human. Exp Eye Res 1988; 46:559-568.

- Olver JM, Spalton DJ, McCartney AC. Quantitative morphology of human retrolaminar optic nerve vasculature. Invest Opthalmol Vis Sci 1994; 35: 3858.

- Onda E, Cioffi GA, Bacon DR, et al. Microvasculature of the human optic nerve. Am J Ophthalmol 1995; 120:92.

- Orgul S., Flammer J. Interocular visual-field and intraocular-pressure asymmetries in normal-tension-glaucoma. Eur J Ophthalmol, 1994. 4, 199-201.

- Panda S, Jonas JB. Decreased photoreceptor count in human eyes with secondary angle- closure glaucoma. Invest Ophthalmol Vis Sci 1992;33:2532–2536. [PubMed: 1634350]

- Pang IH et al. Elevation of intraocular pressure in rodents using viral vectors targeting the trabecular meshwork. Exp eye Res 141, 2015:33-41.

- Pang, I.H., Clark, A.F. Rodent models for glaucoma retinopathy and optic neuropathy. J. Glaucoma 2007. 16, 483-505.

- Pang, I.H., Wang, W.H. and Clark, A.F. Acute effects of glaucoma medications on rat intraocular pressure. Exp. Eye Res., 2005. 80(2): 207–214.

- Pazos M, Yang H, Gardiner SK, Cepurna WO, Johnson EC, Morrison JC, Burgoyne CF. Rat optic nerve head anatomy within 3D histomorphometric reconstructions of normal control eyes. Exp Eye Res 139 (2015): 1-12.

- Perkins ES, Phelps CD. Open-angle glaucoma, ocular hypertension, low tension glaucoma, and refraction. Arch Opthalmol 1982; 100:1464.

- Pfeiffer N., Torri V., Miglior S., Zeyen T., Adamsons I., Cunha-Vaz J. Central corneal thickness in the European Glaucoma Prevention Study. Ophthalmology, 2007. 114, 454-459.

- Phelps CD. Effect of myopia on prognosis in treated primary open-angle glaucoma. Am J Ophthalmol 1982: 92:622.

- Pierru A, et al. Measurement of subfoveal choroidal thickness after cataract surgery in enhanced depth imaging optical coherence tomography. Invest Ophthalmol Vis Sci 2014, 55, 4967-4974.

- Podos SM, Becker B, Morton WR. High myopia and primary open-angle glaucoma. Am J Ophthalmol 1966;62:1038.

- Prasanna G et al. Endothelin, astrocytes and glaucoma. Exp Eye Res, 2011. 93, 170-177.

- Quigley H, Anderson DR. The dynamics and location of axonal transport blockade by acute intraocular pressure elevation in primate optic nerve. Invest Ophthalmol. 1976; 15:606–16. [PubMed: 60300]

- Quigley HA, Addicks EM, Green WR, Maumenee AE. Optic nerve damage in human glaucoma. II.The site of injury and susceptibility to damage. Arch Ophthalmol. 1981; 99:635–49. [PubMed:6164357]

- Quigley H, Addicks E. Quantitative studies of retinal nerve fiber layer defects. Arch Ophthalmol 1982; 100:807-814.

- Quigley HA, Hohman RM, Addicks EM, et al. Morphologic changes in the lamina cribrosa correlated with neural loss in open-angle glaucoma. Am J Ophthalmol 1983; 95:673-691.

- Quigley HA, et al. The relationship between optic disc area and open-angle glaucoma: the Baltimore Eye Survey. J Glaucoma 1999; 8:347.

- Quigley HA. Glaucoma. The Lancet, 2011. 377(9774): 1367-1377.

- Quigley HA. The pathogenesis of reversible cupping in congenital glaucoma. Am J Opthhtalmol 1977;84:358).

- Quigley HA, Miller NR, George T. Clinial evaluation of nerve fiber layer atrophy as an indicator of glaucomatous optic nerve damage. Arch Ophthalmol 1980; 98:1564.

- Quigley H. A., Dorman Pease M. E., Brown A. E. Quantitative study of collagen and elastin of the optic nerve head and sclera in human and experimental monkey glaucoma. Curr Eye Res, 1991. 10, 877-888.

- Quigley H. A. Selectivity in glaucoma injury. Arch Ophthalmol, 1998. 116, 396-398.

- Quigley H. A., Sanchez R. M., Dunkelberger G. R., L'Hernault N. L., Baginski T. A. Chronic glaucoma selectively damages large optic nerve fibers. Invest Ophthalmol Vis Sci, 1987. 28, 913-920.

- Quigley H. A., Green W. R. The histology of human glaucoma cupping and optic nerve damage: clinicopathologic correlation in 21 eyes. Ophthalmology, 1979. 86, 1803-1830.

- Quigley H. A., Anderson D. R. Distribution of axonal transport blockade by acute intraocular pressure elevation in the primate optic nerve head. Invest Ophthalmol Vis Sci, 16, 1977. 640-644.

- Quigley HA, Nickells RW, Kerrigan LA, et al. Retinal ganglion cell death in experimental glaucoma and after axotomy occurs by apoptosis. Invest Ophthalmol Vis Sci 1995;36:774–786. [PubMed: 7706025]

- Quigley HA, McKinnon SJ, Zack DJ, et al. Retrograde axonal transport of BDNF in retinal ganglion cells is blocked by acute IOP elevation in rats. Invest Ophthalmol Vis Sci 2000;41:3460–3466.

- Quigley HA. Ganglion cell death in glaucoma: pathology recapitulates ontogeny. Aust N Z J Ophthalmol 1995;23:85–91. [PubMed: 7546696]

- Ramirez J, Trivino A, Ramirez A, Salazar J, Garcia-Sanchez J. Strctural specializations of human retinal glial cells. Vis Res 1996; 36:2015-2028.

- Rasker M. T., van den Enden A., Bakker D., Hoyng P. F. Deterioration of visual fields in patients with glaucoma with and without optic disc hemorrhages. Arch Ophthalmol, 1997. 115, 1257-1262.

- Read RM and Spaeth GL. The practical clinical appraisal of the optic disc in glaucoma: the natural history of cup progression and some specific disc-field correlations. Trans Am Acad Ophthalmol Otolaryngol, 1974. 78, OP255-274.

- Reis AS, Sharpe GP, Yang H, Nicolela MT, Burgoyne CF, Chauhan BC. Optic disc margin anatomy in patients with glaucoma and normal controls with spectral domain optical coherence tomography. 2012a. Ophthalmology. 119(4):738–747. [PubMed: 22222150]

- Reis AS; et al. Influence of clinically invisible, but optical coherence tomography detected, optic disc margin anatomy on neuroretinal rim evaluation. Invest Ophthalmol Vis Sci. 2012b. 53, 1852-1860.

- Ren, R., et al., Lamina cribrosa and peripapillary sclera histomorphometry in normal and advanced glaucomatous Chinese eyes with various axial length. Invest Ophthalmol. Vis. Sci. 50, 2009. 2175-2184.

- Ren R et al. Anterior lamina cribrosa surface depth, age, and visual field sensitivity in the Portland progression Project. Invest Ophthalmol Vis Sci, 2014. 55: 1531-1539.

- Repka MX, Quigley HA. The effect of age on normal human optic nerve fiber number and diameter. Ophthalmology 1989; 96:26.

- Rimmer S, Keating C, Chou T, et al. Growth of the human optic disc and nerve durging gestation, childhood, and early adulthood. Am J Ophthalmol 1993; 116:748.

- Ritch R, Shields MB, Krupin T. The Glaucomas Vol.2. Second edition. 1989. St. Louis, Missouri: Mosby.

- Roberts M. D ,et al. Remodeling of the connective tissue microarchitecture of the lamina cribrosa in early experimental glaucoma. Invest Ophthalmol Vis Sci, 2009. 50, 681-690

- Ruiz-Ederra, J., Verkman, A.S.,. Mouse model of sustained elevation in intraocular pressure produced by episcleral vein occlusion. Exp. Eye Res, 2006. 82, 879-884.

- Rosenthal AR, Perkins ES. Family studies in glaucoma. Br J Ophthalmol 1985; 69:664.

- Rosner B. 12.9. The Intraclass correlation coefficient, Fundamentals of Biostatistics, seventh ed, 2011. Harvard University. Brooks/Cole. Cengage Learning, Boston, MA, 569.

- Sawaguchi S, Yue BY, Fukuchi T, et al. Age-related changes of sulfated proteoglycans in the human lamina cribrosa. Curr Exp Eye Res 1993;12:685.

- Sappington RM, Carlson BJ, Crish SD, Calkins DJ. The microbead occlusion model: a paradigm for induced ocular hypertension in rats and mice. Invest Ophthalmol Vis Sci. 2009; 51(1):207–16.[PubMed: 19850836]

- Schlamp, C.L., et al. Progressive ganglion cell loss and optic nerve degeneration in DBA/2J mice is variable and asymmetric. BMC Neurosci. 2006. 7, 66.

- Schlamp, C.L., Johnson, E.C., Li, Y., Morrison, J.C. and Nickells, R.W. (2001) Changes in Thy1 gene expression associated with damaged retinal ganglion cells. Mol. Vis.,2001. 7: 192–201.

- Shimmyo M., Ross A. J., Moy A., Mostafavi R. Intraocular pressure, Goldmann applanation tension, corneal thickness, and corneal curvature in Caucasians, Asians, Hispanics, and African Americans. Am J Ophthalmol, 2003. 136, 603-613.

- Siegner S. W., Netland P. A. Optic disc hemorrhages and progression of glaucoma. Ophthalmology, 1996. 103, 1014-1024.

- Sigal, I.A., et al., 2005. Factors influencing optic nerve head biomechanics. Invest. Ophthalmol. Vis. Sci. 46, 4189-4199.

- Sigal, I.A., et al., 2010. 3D morphometry of the human optic nerve head. Exp. Eye Res. 90, 70-80.

- Sigal I. A., Ethier C. R. Biomechanics of the optic nerve head. Exp Eye Res, 2009. 88, 799-807

- Sommer A., Tielsch J. M., Katz J., Quigley H. A., Gottsch J. D., Javitt J., Singh K. Relationship between intraocular pressure and primary open angle glaucoma among white and black Americans. The Baltimore Eye Survey. Arch Ophthalmol, 1991. 109, 1090-1095.

- Sommer A, Miller NR, Pollack I, et al. The nerve fiber layer in the diagnosis of glaucoma. Arch Ophthalmol 1977;95:2149.

- Sommer A, Pollack I, Maumenee AE. Optic disc parameters and onset of glaucomatous field loss. II. Static screening criteria. Arch Ophthalmol 1979; 97:1449.

- Sommer A. Intraocular pressure and glaucoma. Am J Ophthalmol. 1989; 107(2):186–8. [PubMed: 2913813]

- Sonnsjo B., Dokmo Y., Krakau T. Disc haemorrhages, precursors of open angle glaucoma. Prog Retin Eye Res, 2002. 21, 35-56.

- Spaeth G. L. A new classification of glaucoma including focal glaucoma. Surv Ophthalmol, 1994. 38 Suppl, S9-17.

- Spaeth G. L., Hitchings R. A., Sivalingam E. The optic disc in glaucoma: pathogenetic correlation of five patterns of cupping in chronic open-angle glaucoma. Trans Sect Ophthalmol Am Acad Ophthalmol Otolaryngol, 1976. 81, 217-223.

- Sponsel W. E. Tonometry in question: can visual screening tests play a more decisive role in glaucoma diagnosis and management? Surv Ophthalmol, 1989: 33 Suppl, 291-300.

- Stone J, Makarov F, Hollander Ht. the glial ensheathment of the soma and axon hillock of retinal ganglion cells. Vis Neurosci 1995;12:273-279.

- Strouthidis NG and Girard MJ. Altering the way the optic nerve head responds to intraocular pressure—a potential approach to glaucoma therapy. Current Opinion in Pharmacology 2013, 13:83–89.

- Strouthidis NG, Yang H, Reynaud JF, et al. Comparison of clinical and spectral domain optical coherence tomography optic disc margin anatomy. Invest Ophthalmol Vis Sci. 2009; 50(10):4709–4718. [PubMed: 19443718]

- Strouthidis NG et al, 2010. A comparison of optic nerve head morphology viewed by spectral domain optical coherence tomography and by serial histology. Invest Ophthalmol Vis Sci, 1464-1474.

- Strouthidis NG et al. Effect of acute intraocular pressure elevation on the monkey optic nerve head as detected by spectral domain optical coherence tomography. Invest Ophthalmol Vis Sci., 2011a. 52, 1206-1219.

- Strouthidis NG. Longitudinal change detected by spectral domain optical coherence tomography in the nerve head and peripapillary retina in experimental glaucoma. Invest Ophthalmol Vis Sci, 2011b. 52, 1206-1219.

- Sugiyama K., et al. The associations of optic disc hemorrhage with retinal nerve fiber layer defect and peripapillary atrophy in normaltension glaucoma. Ophthalmology, 1997. 104, 1926-1933.

- Sugiyama K., Uchida H., Tomita G., Sato Y., Iwase A., Kitazawa Y. (1999) Localized wedgeshaped defects of retinal nerve fiber layer and disc hemorrhage in glaucoma. Ophthalmology, 1999a, 106, 1762-1767.

- Sugiyama, K., et al.,Optic nerve and peripapillary choroidal microvasculature of the rat eye. Invest. Ophthalmol. Vis. Sci. 1999b. 40, 3084-3090.

- Sun, D., Lye-Barthel, M., Masland, R.H., Jakobs, T.C., 2009. The morphology and spatial arrangement of astrocytes in the optic nerve head of the mouse. J. Comp. Neurol. 516, 1-19.

- Susanna R, Drance SM, Douglas GR. Disc hemorrhages in patients with elevated intraocualr pressure: ocurrence with and without field changes. Arch Ophthalmol 1979;97:284.

- Takayama et al. Three-Dimensioanl imaging of lamina cribrosa defects in glaucoma using swept-source optical coherence tomography. Invest Ophthalmol Vis Sci 2013; 54:4798-4807.

- Tehrani, S., Johnson, E.C., Cepurna, W.O., Morrison, J.C. Astrocyte processes label for filamentous actin and reorient early within the optic nerve head in a rat glaucoma model. Invest Ophthalmol. Vis. Sci. 2014. 55, 6945-6952.

- Tezel G and Wax MB. The immune system and glaucoma. Curr Opin Ophthalmol, 2004. 15, 80-84.

- Tezel G., Hernandez M. R., Wax M. B. In vitro evaluation of reactive astrocyte migration, a component of tissue remodeling in glaucomatous optic nerve head. Glia, 2001. 34, 178-189.

- Tham YC, Li X, Wong TY et al. Global Prevalence of glaucoma and projections of glaucoma burden through 2040. Opthahlmology 2014: 11:2081-2090.

- Thorleifsson G., et al. Common sequence variants in the LOXL1 gene confer susceptibility to exfoliation glaucoma. Science, 2007. 317, 1397-1400.

- Tielsch JM, et al. Family history and risk of primary open angle glaucoma: population-based familial aggregation study. Arch Opthhalmol 1998; 116:16410.

- Toprak AB, Yilmaz OF. Relation of optic disc topography and age to thickness of retinal nerve fiber layer as measured using scanning laser polarimetry, in normal subjects. Br J Ophthalmol 2000:84:473.

- Tseng HC et al. Visual impairment in an optineurin mouse model of primary open-angle glaucoma. Neurobiol. Aging 2015, 2201-2212.

- Tuulonen A., Airaksinen P. J. Initial Glaucomatous Optic Disk and Retinal Nerve Fiber Layer Abnormalities and Their Progression. Am J Ophthalmol, 1991. III, 485-490.

- Ueda J, Sawaguchi S, Hanyu T, Yaoeda K, Fukuchi T, Abe H, Ozawa H. Experimental glaucoma model in the rat induced by laser trabecular photocoagulation after an intracameral injection of India ink. Jpn J Ophthalmol. 1998; 42(5):337–44. [PubMed: 9822959]

- Urcola JH, Hernandez M, Vecino E. Three experimental glaucoma models in rats: comparison of the effects of intraocular pressure elevation on retinal

ganglion cell size and death. Exp Eye Res. 2006; 83(2):429–37. [PubMed: 16682027]

- Varela H. J., Hernandez M. R. Astrocyte responses in human optic nerve head with primary open-angle glaucoma. J Glaucoma, 1997. 6, 303-313.

- Vidal-Sanz M. et al. Understanding glaucomatous damage: Anatomical and functional data from ocular hypertensive rodent retinas. Prog Retin Eye Res. 2011 Sep 21. [2012] PMID: 21946033

- Vilensky J, Robertson W, Suarez-Quian C. The Clinical Anatomy of the Cranial Nerves: The Nerves of "On Olympus Towering Top". 2015. Ames, Iowa: Wiley-Blackwell. ISBN 978-1118492017.

- Votruba M et al. Optic disc morphology of patients with OPA1 autosomal dominant optic atrophy. Br J Ophthalmol, 2003. 87, 48-53.

- Wang W and Zhang X. Choroidal thickness and primary open-angle glaucoma: a cross-sectional study and meta-analysis. Invest Ophthlmol Vis Sci. 2014. 55, 6007-6014.

- Wax MB et al. Induced autoimmunity to heat shock proteins elicits glaucomatous loss of retinal ganglion cell neurons via activated T-cell-derived fas-ligand. J Neurosci, 2008. 28, 12085-12096.

- Weber AJ, Kaufman PL, Hubbard WC. Morphology of single ganglion cells in the glaucomatous primate retina. Invest Ophthalmol Vis Sci 1998;39:2304–2320. [PubMed: 9804139]

- Weih LM et al. Prevalence and predictors of open-angle glaucoma results from the visual impairment project. Opthalmology 2001, 108:1966.

- Wiggs J. L. Genetic etiologies of glaucoma. Arch Ophthalmol, 2007. 125, 30-37.

- Wilson MR et al. A case-control study of risk factors in open-angle glaucoma. Arch Ophthalmol 1987;105:1066.

- WoldeMussie E, et al. Neuroprotection of retinal ganglion cells by brimonidine in rats with laser-induced chronic ocular hypertension. 2001. Invest Ophthalmol Vis Sci. 42, 2849-2855.

- Wolfs RC e tal. Genetic risk of primary open-angle glaucoma: population-based familial aggregation study. Arch Ophthalmol 1998; 116:1640.

- Wong TY, et al. Refractive errors, intraocular pressure, and glaucoma in a white population. Ophthalmology 2003; 110:211.

- Wygnanski T, Desatnik H, Quigley HA, et al. Comparison of ganglion cell loss and cone loss in experimental glaucoma. Am J Ophthalmol 1995;120:184–189. [PubMed: 7639302]

- Yang H et al. 3-D histomorphometry of the normal and early glaucomatous monkey optic nerve head: prelaminar neural tissues and cupping. Invest Ophthalmol Vis Sci. 48, 2007a, 5068-5084.

- Yang H et al. 3-D Histomorphometry of the normal and early glaucomatous monkey optic nerve head: lamina cribrosa and peripapillary scleral position and thickness. Invest Ophthalmol Vis Sci. 48, 2007b, 4597-4607.

- Yang H et al. Physiologic intereye differences in monkey optic nerve head architecture and their relation to changes in early experimental glaucoma. Invest Ophthalmol Vis Sci. 50, 2009a, 224-234.

- Yang H et al. Deformation of the early glaucomatous monkey optic nerve head connective tissue after acute IOP elevation in 3-D histomorphometric reconstructions. Invest Ophthalmol Vis Sci. 52, 2011a, 345-363.

- Yang H, Williams G, Downs J, et al. Posterior (outward) migration of the lamina cribrosa and early cupping in monkey experimental glaucoma. Invest Opthhalmol Vis Sci. 2011b; 52:7109-7121.

- Yiu G et al. Characterization of the choroid-scleral junction and suprachoroidal layer in healthy individuals on enhanced-depth imaging optical coherence tomography. JAMA Ophthalmol. 2014. 132, 174-181.

- Yucel YH, Zhang Q, Gupta N, et al. Loss of neurons in magnocellular and parvocellular layers of the lateral geniculate nucleus in glaucoma. Arch Ophthalmol 2000;118:378–384. [PubMed: 10721961]

- Yucel YH, Zhang Q, Weinreb RN, et al. Atrophy of relay neurons in magno- and parvocellular layers in the lateral geniculate nucleus in experimental glaucoma. Invest Ophthalmol Vis Sci 2001;42:3216–3222. [PubMed: 11726625]

- Yucel YH, Zhang Q, Weinreb RN, et al. Effects of retinal ganglion cell loss on magno-, parvo-,koniocellular pathways in the lateral geniculate nucleus and visual cortex in glaucoma. Prog RetinEye Res 2003;22:465–481. [PubMed: 12742392]

- Zhang X. et al. Dual-band spectral-domain optical coherence tomography for in vivo imaging the spectral contrasts of the retinal nerve fiber layer. 2011. Opt. Express 19, 19653-19659.

- Zhi Z et al. Volumetric and quantitative imaging of retinal blood flow in rats with optical microangiography. Biomed Opt Express, 2011. 2: 579-591.

- Zhi Z et al. Impact of intraocular pressure on changes of blood flow in the retina, choroid and optic nerve head in rats investigated by optical microangiography. Biomed Opt Express, 2012. 3: 2220-2233.

- Zotter S et al. Visualization of microvasculature by dual-beam phase-resolved Doppler optical coherence tomography. Opt Express, 2011. 19:1217-1227.